

JYU DISSERTATIONS 639

Daniel Söderström

Radiation Effects on SDRAMs and Optical Fiber-Based Dosimetry of High-Energy Electrons



UNIVERSITY OF JYVÄSKYLÄ
FACULTY OF MATHEMATICS
AND SCIENCE

JYU DISSERTATIONS 639

Daniel Söderström

Radiation Effects on SDRAMs and Optical Fiber-Based Dosimetry of High-Energy Electrons

Esitetään Jyväskylän yliopiston matemaattis-luonnontieteellisen tiedekunnan suostumuksella
julkisesti tarkastettavaksi yliopiston Ylistönrinteen salissa FYS1
toukokuun 12. päivänä 2023 kello 12.

Academic dissertation to be publicly discussed, by permission of
the Faculty of Mathematics and Science of the University of Jyväskylä,
in Ylistönrinne, auditorium FYS1, on May 12, 2023 at 12 o'clock noon.



JYVÄSKYLÄN YLIOPISTO
UNIVERSITY OF JYVÄSKYLÄ

JYVÄSKYLÄ 2023

Editors

Ilari Maasilta

Department of Physics, University of Jyväskylä

Ville Korkiakangas

Open Science Centre, University of Jyväskylä

Copyright © 2023, by author and University of Jyväskylä

ISBN 978-951-39-9557-7 (PDF)

URN:ISBN:978-951-39-9557-7

ISSN 2489-9003

Permanent link to this publication: <http://urn.fi/URN:ISBN:978-951-39-9557-7>

ABSTRACT

Söderström, Daniel

Radiation effects on SDRAMs and optical fiber-based dosimetry of high-energy electrons

Jyväskylä: University of Jyväskylä, 2023, 101 p. (+included articles)

(JYU Dissertations

ISSN 2489-9003; 639)

ISBN 978-951-39-9557-7 (PDF)

This thesis work contains studies in two separate fields, unified under the topic of electron radiation. The radiation effects of electrons on electronics is a field of study that is gaining traction due to the ever smaller technology nodes found in modern electronics risk getting upset by lighter particles and through different mechanisms than historically has been observed. In this work, the response of synchronous dynamic random access memories (SDRAM) was investigated under electron irradiation with much focus on stuck bits and the evolution of data retention times of the memory bits under and after irradiation. High-energy electrons were found to be capable of inducing stuck bits as single event effects in a device under test, and large losses of retention time capability were found both in stuck bits and in bits that had bit-flips during irradiation. These radiation effects were also studied under proton irradiation as well as photon irradiation, where a large retention-time degradation was observed in both cases, which was ascribed to the effects of total ionizing dose on the device. Characterizations of optical fiber-based dosimetry systems utilizing the radiation-induced luminescence (RIL) of doped silica glasses for online dose monitoring were performed under pulsed electron beams. The RIL intensity of the fiber-based dosimeters during the delivered electron bunches was found to be linearly proportional to the dose of the electron bunches when varying the dose per electron bunch. The luminescence properties of a silica glass rod doped with Gd^{3+} -ions were investigated under electron irradiation at varying depths in an acrylic phantom. The RIL proportional to the deposited dose rate was separated from the induced Cherenkov radiation through two separate acquisition systems, one based on a monochromator and one based on a spectrometer. The decay time of the Gd^{3+} -ion luminescence was also studied through the monochromator. The presented results show that these types of optical-fiber based dosimeters can be used to efficiently monitor the dose of such a Clinac.

Keywords: dosimetry, electrons, optical fibers, photons, protons, radiation effects, radiation-induced luminescence, SDRAM, single event effects, stuck bits, total ionizing dose effects

TIIVISTELMÄ (ABSTRACT IN FINNISH)

Söderström, Daniel

Säteilyn vaikutuksia SDRAMissa ja optisiin kuituihin perustuvaa dosimetriaa suurienergisille elektroneille

Jyväskylä: University of Jyväskylä, 2023, 101 s. (+artikkelit)

(JYU Dissertations

ISSN 2489-9003; 639)

ISBN 978-951-39-9557-7 (PDF)

Tämä väitöskirjatyö sisältää tutkimuksia kahdelta erilliseltä alalta, jotka on yhdistetty elektronisäteilyn aiheen alle. Elektronisäteilyn vaikutukset elektroniikkaan on tutkimusala, joka on tulossa yhä tärkeämmäksi, koska nykyaikaisessa elektroniikassa esiintyvät aikaisempaa pienemmät rakenteet ovat vaarassa häiriintyä yhä kevyempien hiukkasten vaikutuksesta ja erilaisten mekanismien kautta kuin historiallisesti on havaittu. Tässä työssä tutkittiin elektronisäteilyn vaikutuksia aikasykronoituihin dynaamisiin hajasaantimuisteihin (SDRAM) keskittyen erityisesti muistipaikkojen jumittumiseen, ja niissä olevan tiedon säilymisaikojen muuttumiseen säteilyn aikana sekä sen jälkeen. Tutkituissa muistikomponenteissa suurenergisten elektronien havaittiin pystyvän aiheuttamaan jumittuneita bittejä yksittäistapahtumina, ja aiheuttamaan tiedon säilymisajan merkittävää lyhenemistä sekä jumittuneissa muistipaikoissa että muistipaikoissa, joissa bitti kääntyi säteilytyksen aikana. Näitä säteilyvaikutuksia tutkittiin myös protoni- ja fotonisäteilytyksessä, joissa molemmissa tapauksissa havaittiin merkittävä tiedon säilymisajan lyheneminen, joka johtui ionisoivan kokonaisannoksen vaikutuksista muistikomponenttiin. Pulssitetuilla elektronisuihkuilla tutkittiin optisiin kuituihin perustuvia annosmittausjärjestelmiä, joissa hyödynnetään seostetussa piilasissa säteilyn indusoimaa luminesenssia (Radiation-Induced Luminescence, RIL) säteilytyksen aikaiseen annosseurantaan. Valokuitupohjaisen annosmittarin tuottaman luminesenssin intensiteetin havaittiin olevan suoraan verrannollinen elektronisuihkon pulssien sisältämään annokseen, kun annosta vaihdeltiin pulssien sisältämää annosta muuttamalla. Gd^{3+} -ioneilla seostetun piilasikuidun luminesenssiominaisuuksia tutkittiin elektronisäteilyllä eri syvyyksillä akryylifantomissa. Annosnopeuteen verrannollinen RIL erotettiin indusoituneesta Cherenkov-säteilystä kahdella erillisellä, monokromaattoriin ja spektrometriin perustuvalle mittausjärjestelmällä. Gd^{3+} -ionin luminesenssin hajoamisaikaa tutkittiin myös monokromaattorin avulla. Esitetyt tulokset osoittavat, että tämän tyyppisiä optisiin kuituihin perustuvia annosmittareita voidaan käyttää tehokkaasti Clinacin tyyppisen kiihdyttimen tuottaman säteilyn annoksen seurantaan.

Suomentanut alkuperäisestä englanninkielisestä tekstistä: Heikki Kettunen

Avainsanat: dosimetria, elektronit, fotonit, ionisoivan annoksen kokonaisvaikutukset, jumittuneet bitit, protonit, SDRAM, säteilyn aiheuttama lu-

minesenssi, säteilyn vaikutuksia, valokuidut, yksittäisen hiukkasen aiheuttamat vaikutukset

Author

Daniel Söderström
Department of Physics
University of Jyväskylä
Finland
daniel.p.soderstrom@jyu.fi

Supervisors

Dr. Heikki Kettunen
Department of Physics
University of Jyväskylä
Finland

Dr. Arto Javanainen
Department of Physics
University of Jyväskylä
Finland

and

Department of Electrical and Computer Engineering
Vanderbilt University
USA

Prof. Sylvain Girard
Laboratoire Hubert Curien
Université Jean-Monnet
France

Reviewers

Dr. Jochen Kuhnenn
Fraunhofer INT
Germany

Dr. Richard Sharp
Radtest Ltd
United Kingdom

Opponent

Dr. Philippe Paillet
CEA, DAM, DIF
France

ACKNOWLEDGEMENTS

This thesis work was made within the framework of RADSAGA, an EU project which had 15 early stage researcher (ESR) positions in various Universities, institutes and companies across Europe working in the same project. RADSAGA was a Horizon 2020 research and innovation program under the Marie Skłodowska-Curie grant agreement No 721624. All ESRs and participants in the project deserve big thanks!

The reviewers of the thesis, Jochen Kuhnenn and Richard Sharp, deserve much credit for helping to improve and ensure the quality of the text, as does the opponent for the dissertation Philippe Paillet, for taking the time to come to Jyväskylä and participate in the defense to provide great expertise and fruitful discussions on the thesis subject matter.

Thanks to my research group at the University of Jyväskylä, RADEF, and everyone who was part of it for the duration of my PhD. Thanks to Sascha, RADSAGA ESR number 1 who started his PhD at the same time as me in Jyväskylä, thanks Alex who was my predecessor and early mentor at RADEF in many ways, thanks Andrea for many collaborations, much help, and good times, thanks to Corinna and Maris for good friendships, thanks Jukka and Mikko for the help in the lab, thanks Kimmo for professional collaborations and especially for getting me into playing golf, thanks Ari, for being a great group leader up until retirement, and especially thanks to Heikki and Arto, my supervisors who have provided guidance and advice throughout the whole PhD process.

I have learned many new things throughout my time as a PhD student, of which much is written down in this document. That I have managed to learn what I have, is largely thanks to the help of my collaborators, from the University Jean Monnet in Saint-Etienne I thank my supervisor Sylvain and his whole group working with optical fibers and dosimetry (among other things) who have taught me a lot. Thanks to Luigi and his group at LIRMM working with radiation effects on memories and microelectronics (among other things), who have shared their knowledge with me and who I have collaborated with on many projects, with a special mention to Lucas who I have written many papers with, and spent many long shifts with in various irradiation facilities.

In Jyväskylä I would like to thank the PhD students and post docs at the physics department throughout my years spent here, many of whom I have gotten to know and spent time with which brightens each day. The people I have gotten to know from various sports shifts of the university, from table tennis, squash, badminton, football, who have helped me to stay in relatively decent shape, deserve a big thanks as well.

Thanks also to my family who have been supportive and have come to visit me in remote Jyväskylä, and lastly as well as most importantly thanks to Marjut who I have happily shared my life with during the past years.

LIST OF INCLUDED ARTICLES

- PI Daniel Söderström, Lucas Matana Luza, Heikki Kettunen, Arto Javanainen, Wilfrid Farabolini, Antonio Gilardi, Andrea Coronetti, Christian Poivey, and Luigi Dilillo. "Electron-Induced Upsets and Stuck Bits in SDRAMs in the Jovian Environment". *IEEE Trans. Nucl. Sci.*, vol. 68, no. 5, pp. 716–723, May 2021, doi: 10.1109/TNS.2021.3068186.
- PII Daniel Söderström, Lucas Matana Luza, André Martins Pio de Matos, Thierry Gil, Heikki Kettunen, Kimmo Niskanen, Arto Javanainen, and Luigi Dilillo. "Technology Dependence of Stuck Bits and Single Event Upsets in 110, 72, and 63-nm SDRAMs". *Submitted to IEEE Trans. Nucl. Sci., under review.*
- PIII Daniel Söderström, Heikki Kettunen, Adriana Morana, Arto Javanainen, Youcef Ouerdane, Hicham El Hamzaoui, Bruno Capoen, Géraud Bouwmans, Mohamed Bouazaoui and Sylvain Girard. "Radioluminescence Response of Ce-, Cu-, and Gd-Doped Silica Glasses for Dosimetry of Pulsed Electron Beams". *MDPI Sensors*, vol. 21, no. 22, p. 7523, Nov. 2021, doi: 10.3390/s21227523.
- PIV Daniel Söderström, Oskari Timonen, Heikki Kettunen, Risto Kronholm, Hicham El Hamzaoui, Bruno Capoen, Youcef Ouerdane, Adriana Morana, Arto Javanainen, Géraud Bouwmans, Mohamed Bouazaoui and Sylvain Girard. "Properties of Gd-doped Sol-gel Silica Glass Radioluminescence under Electron Beams". *MDPI Sensors*, vol. 22, no. 23, p. 9248, Nov. 2022, doi: 10.3390/s22239248.

For the work done in these articles, the first author has written the manuscripts, planned and conducted the experiments, and performed the data analysis, interpretation, and visualization of the results. The papers are attached at the end of this thesis, and the thesis is based mainly on the results presented in those papers.

In the other publications listed on the following pages the thesis author has provided assistance during either experimental campaigns, review and editing of the paper manuscripts, analysis of experimental results, or a combination thereof.

Two data sets have been published (at the time of writing) from experimental campaigns with results included in this thesis, these are listed on the following pages as well.

List of other publications

Peer reviewed journal publications

H. El Hamzaoui, G. Bouwmans, B. Capoen, A. Cassez, R. Habert, Y. Ouerdane, S. Girard, D. Di Francesca, N. Kerboub, A. Morana, D. Söderström, A. Boukenter and M. Bouazaoui, "Gd³⁺-doped sol-gel silica glass for remote ionizing radiation dosimetry", *OSA Contin.*, vol. 3, no. 2, pp. 715–721, Mar. 2019, doi: 10.1364/OSAC.2.000715.

A. Coronetti, R. García Alía, M. Cecchetto, W. Hajdas, D. Söderström, A. Javanainen and F. Saigné, "The Pion Single-Event Effect Resonance and its Impact in an Accelerator Environment", *IEEE Trans. Nucl. Sci.*, vol. 67, no. 7, pp. 1606–1613, Jul. 2020, doi: 10.1109/TNS.2020.2978228.

A. Coronetti, R. García Alía, J. Budroweit, T. Rajkowski, I. Da Costa Lopes, K. Niskanen, D. Söderström, C. Cazzaniga, R. Ferraro, S. Danzeca, J. Mekki, F. Manni, D. Dangla, C. Virmontois, N. Kerboub, A. Koelpin, F. Saigné, P. Wang, V. Pouget, A. Touboul, A. Javanainen, H. Kettunen and R. Coq Germanicus, "Radiation Hardness Assurance Through System-Level Testing: Risk Acceptance, Facility Requirements, Test Methodology, and Data Exploitation", *IEEE Trans. Nucl. Sci.*, vol. 68, no. 5, pp. 958–969, May 2021, doi: 10.1109/TNS.2021.3061197.

A. Coronetti, R. García Alía, F. Cerutti, W. Hajdas, D. Söderström, A. Javanainen and F. Saigné, "The Pion Single-Event Latch-Up Cross Section Enhancement: Mechanisms and Consequences for Accelerator Hardness Assurance" *IEEE Trans. Nucl. Sci.*, vol. 68, no. 8, pp. 1613–1622, Aug. 2021, doi: 10.1109/TNS.2021.3070216.

L. Matana Luza, A. Ruospo, D. Söderström, C. Cazzaniga, M. Kastriotou, E. Sanchez, A. Bosio and L. Dilillo, "Emulating the Effects of Radiation-Induced Soft-Errors for the Reliability Assessment of Neural Networks", *IEEE Transactions on Emerging Topics in Computing*, vol. 10, no. 4, pp. 1867–1882, Oct. 2021, doi: 10.1109/TETC.2021.3116999.

L. Matana Luza, D. Söderström, H. Puchner, R. García Alía, M. Letiche, C. Cazzaniga, A. Bosio and L. Dilillo, "Neutron-Induced Effects on a Self-Refresh DRAM", *Microelectron. Reliab.*, vol. 128 (114406), 2022, doi: 10.1016/j.microrel.2021.114406.

M. Mounir Mahmoud, J. Prinzie, D. Söderström, K. Niskanen, V. Pouget, A. Cathelin, S. Clerc and P. Leroux, "Impact of Aging Degradation on Heavy-Ion SEU Response of 28-nm UTBB FD-SOI Technology", *IEEE Trans. Nucl. Sci.*, vol. 69, no. 8, pp. 1865–1875, Aug. 2022, doi: 10.1109/TNS.2022.3189802.

K. Niskanen, A. Javanainen, H. Kettunen, M. Lahti, M. Rossi, J. Jaatinen, D. Söder-

ström and S. Lüdeke, "Effect of 20 MeV Electron Radiation on Long Term Reliability of SiC Power MOSFETs", *IEEE Trans. Nucl. Sci.*, vol. 70, no. 4, pp. 456–461, Apr. 2023, doi: 10.1109/TNS.2023.3242335.

K. Niskanen, H. Kettunen, D. Söderström, M. Rossi, J. Jaatinen and A. Javanainen, "Proton Irradiation-Induced Reliability Degradation of SiC Power MOSFET", *IEEE Trans. Nucl. Sci.*, early access, 2023, doi: 10.1109/TNS.2023.3242829.

Conference proceedings publications

D. Söderström, L. Matana Luza, A. Bossler, T. Gil, K.-O. Voss, H. Kettunen, A. Javanainen and L. Dilillo, "Stuck and Weakened Bits in SDRAM from a Heavy-Ion Microbeam", in *Proceedings of the 2019 19th European Conference on Radiation and Its Effects on Components and Systems (RADECS)*, Sep. 2019, doi: 10.1109/RADECS47380.2019.9745715.

L. Matana Luza, D. Söderström, H. Puchner, R. García Alía, M. Letiche, A. Bosio and L. Dilillo, "Effects of Thermal Neutron Irradiation on a Self-Refresh DRAM", in *Proceedings of the 2020 15th Design & Technology of Integrated Systems in Nanoscale Era (DTIS)*, Apr. 2020, doi: 10.1109/DTIS48698.2020.9080918.

L. Matana Luza, D. Söderström, G. Tsiligiannis, H. Puchner, C. Cazzaniga, E. Sanchez, A. Bosio and L. Dilillo, "Investigating the Impact of Radiation-Induced Soft Errors on the Reliability of Approximate Computing Systems", in *Proceedings of the 2020 IEEE International Symposium on Defect and Fault Tolerance in VLSI and Nanotechnology Systems (DFT)*, Oct. 2020, doi: 10.1109/DFT50435.2020.9250865.

L. Matana Luza, D. Söderström, A. M. Pio de Mattos, E. A. Bezerra, C. Cazzaniga, M. Kastriotou, C. Poivey and L. Dilillo, "Technology Impact on Neutron-Induced Effects in SDRAMs: A Comparative Study", in *Proceedings of the 2021 16th IEEE International Conference on Design & Technology of Integrated Systems in Nanoscale Era (DTIS)*, Jun. 2021, doi: 10.1109/DTIS53253.2021.9505143.

Published data sets

D. Söderström and H. Kettunen, "Optical Fiber Based Dosimeter Data From RADEF Pulsed Electron Beams - Oscilloscope Traces", 2021, [Data set], V. 13.10.2021., University of Jyväskylä, doi: 10.17011/jyx/dataset/78578.

D. Söderström, H. Kettunen and O. Timonen, "Radiation-Induced Luminescence of Gd-Doped Sol-Gel Silica Glass under electron beams in acrylic phantoms", 2022, [Data set], Version 1, University of Jyväskylä, doi: 10.23729/e7988ecf-d719-472e-9ad7-c66d0f7c427a.

LIST OF ACRONYMS

AE8,AP8	Trapped electron and proton models
BCT	Beam current transformer
CERN	European Organization for Nuclear Research
CIS	CMOS image sensor
CLEAR	CERN linear electron accelerator for research
CME	Coronal mass ejection
CMOS	Complementary MOS
CPE	Charged particle equilibrium
CRAND	Cosmic ray albedo neutron decay
DD	Displacement damage
DDD	Displacement damage dose
DOFRS	Distributed optical fiber radiation sensor
DRAM	Dynamic random access memory
DUT	Device under test
ESA	European Space Agency
ESP	Emission of solar protons model
FLUKA	Fluktuierende kaskade (simulation toolkit)
G4SEE	GEANT4 Single Event Effect Toolkit
GCR	Galactic cosmic ray
GEANT4	Geometry and Tracking 4 (simulation toolkit)
GLONASS	Globalnaya Navigatsionnaya Sputnikovaya Sistema
GPS	Global Positioning System
GSO/GEO	Geostationary orbit
ISB	Intermittently stuck bit
ISS	International Space Station
JUICE	Jupiter Icy Moons Explorer
kerma	Kinetic energy released per unit mass
LEO	Low Earth orbit
LET	Linear energy transfer
LHC	Large Hadron Collider
MBU	Multiple bit upset
MEO	Medium Earth orbit
MOS	Metal-oxide-semiconductor
MOSFET	MOS field-effect transistor
OA	Optical absorption
OSL	Optically stimulated luminescence
PAMELA	Payload for Antimatter Matter Exploration and Light-nuclei Astro- physics
PKA	Primary knock-on atom
PMT	Photomultiplier tube

RADEF	Radiation effects facility (irradiation facility at JYU)
RCAT	Recessed channel array transistor
RIA	Radiation-induced attenuation
RIE	Radiation-induced emission
RIL	Radiation-induced luminescence
RL	Radioluminescence
RTS	Random telegraph signal
SAA	South Atlantic anomaly
SBU	Single bit upset
SDRAM	Synchronous dynamic random access memory
SEE	Single event effect
SEFI	Single event functional interrupt
SEM	Scanning electron microscopy
SEP	Solar energetic particle
SET	Single event transient
SEU	Single event upset
SPDDE	Single-particle displacement damage effect
SPE	Solar particle event
SPENVIS	Space Environment Information System
STH	Self-trapped hole
STI	Shallow trench isolation
STX	Self-trapped exciton
TID	Total ionizing dose
TL	Thermoluminescence
TLD	Thermoluminescent dosimeters
VESPER	Very energetic electron facility for space planetary exploration missions in harsh radiative environments (Electron test facility at CERN)

CONTENTS

ABSTRACT

TIIVISTELMÄ (ABSTRACT IN FINNISH)

ACKNOWLEDGEMENTS

LIST OF INCLUDED ARTICLES

LIST OF ACRONYMS

CONTENTS

1	INTRODUCTION	17
2	BACKGROUND	20
2.1	Radiation environments	20
2.1.1	Radiation in space	20
2.1.1.1	Galactic cosmic rays	20
2.1.1.2	Solar particles	21
2.1.1.3	Trapped radiation belts	21
2.1.2	Terrestrial radiation environments.....	25
2.1.2.1	Atmospheric radiation	25
2.1.2.2	Particle accelerators	25
2.2	Radiation interactions with matter	26
2.2.1	Particle-matter interactions	26
2.2.1.1	Cherenkov radiation	29
2.2.2	Photon-matter interactions	30
2.3	Dosimetry.....	30
2.3.1	Dosimetric definitions	31
2.3.2	Dosimeters.....	35
2.3.2.1	Ionization chambers.....	35
2.3.2.2	Luminescence dosimeters and optical fiber-based dosimeters	36
2.4	Radiation effects on electronics	39
2.4.1	Cumulative effects	40
2.4.1.1	Total ionizing dose.....	40
2.4.1.2	Displacement damage dose	40
2.4.2	Single event effects in SDRAM	41
2.5	Radiation effects testing facilities	45
2.5.1	RADEF	46
2.5.2	VESPER.....	50
3	RESULTS FROM RADIATION TESTS OF SDRAMs	51
3.1	Tested devices	51
3.2	Experimental setups and procedures	53
3.3	Electron-irradiation effects	55
3.3.1	SEU and stuck bits	55
3.3.2	Dose rate and annealing effects	58

3.3.3	Origins of the SEE and cumulative effects	60
3.3.4	ISB and cell damage from SEE	61
3.3.5	SEE in the Jovian environment	63
3.4	Proton-induced retention-time degradation	65
3.4.1	Comparison with photon irradiation	68
4	RESULTS OF TESTS WITH FIBER-BASED DOSIMETRY SYSTEMS	69
4.1	Tested fibers	69
4.2	Emission spectra of the RIL	69
4.3	Dosimetry of pulsed electron beams	70
4.3.1	Experimental setup and method	70
4.3.2	Dose per electron bunch measurement	71
4.4	Dose depth curves of electron beams	74
4.4.1	Oscilloscope-based acquisition setup from Section 4.3	74
4.4.2	Separating emission components using a monochromator ..	75
4.5	Luminescence properties of Gd ³⁺ -doped silica	79
4.5.1	STX decay and luminescence	81
5	CONCLUSION	84
	REFERENCES.....	86
	INCLUDED ARTICLES	

1 INTRODUCTION

Radiation is constantly present in various forms, and in a wide range of intensities at different locations. There are situations where electronic systems need to operate within environments where a large radiation background is present. To ensure that these systems work as intended, prior knowledge of the effects of the radiation on the electronics is needed, as is prior knowledge of the radiation fields present in the environment.

Radiation effects were in this thesis work studied by investigating the behavior of synchronous dynamic random access memories (SDRAM) in various radiation fields, with a focus on high-energy electron radiation. Environments containing large amounts of very high energy electrons are not very common, but one such environment is the trapped radiation fields around Jupiter, where large space missions are scheduled to be sent in the coming years. Radiation effects in a component vary with the radiation field and particle species found in the environment, making the effects of high energy electron radiation on electronics an important field of study since electron-induced radiation effects is historically less investigated than the effects of e.g. protons and heavy ions.

Dosimetry, the quantitative measurement of ionizing radiation doses, is a crucial part of defining radiation environments as well as monitoring radiation beams in accelerators. The electron accelerator at the radiation effects facility RADEF at the University of Jyväskylä was used in this thesis work to characterize optical fiber-based dosimeters which can be used to monitor the dose and dose rate through radiation-induced light emissions. The electron accelerator is a clinical linear accelerator of a type used for radiotherapy, and the dosimetry study investigated the luminescence properties and the utilization of optical fiber-based doped silica glass dosimeters for online monitoring of the dose deposition from clinical electron accelerators.

A few examples of radiation environments where systems with electronic components and/or optical fibers are used, or are envisioned to be used, are shown in Figure 1. The limits presented in the figure are approximate and many overlaps between the separated regions exist, as well as situations where much higher or lower dose rates occur within the environment than what is drawn in

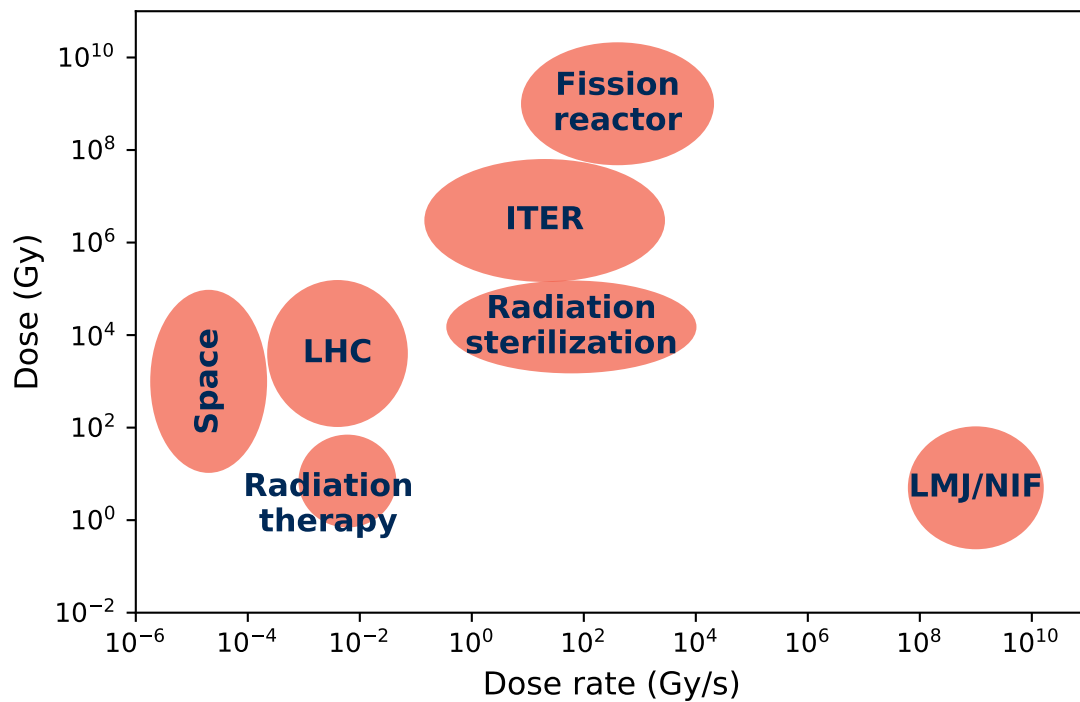


FIGURE 1 Examples of environments where enhanced levels of radiation is found, characterized by approximate typical ranges of ionizing dose rates and doses. Inspired by and adapted after [1, 2], with additional data from [3, 4, 5, 6, 7, 8, 9].

the figure. What can be seen is the wide variety of radiation doses and dose rates that can be associated with various environments, from the relatively low dose-rates associated with space missions, which over long mission durations and in certain environments can accumulate large values of total dose, to the very high dose rates associated with inertial-confinement type fusion reactor facilities such as the Laser Mégajoule (LMJ) and National Ignition Facility (NIF) but which are associated with very short active run times. Other exemplified environments are the vicinity of the beam line of the Large Hadron Collider (LHC) over the coming high-luminosity run [3], as well as common dose rates and doses for a radiotherapy treatment. Dose rates during radiation therapy is an active field of study, where e.g. flash radiotherapy is investigated where the full treatment dose can be deposited within fractions of a second and dose rates of above MGy/s can be reached [10, 11]. The oval representing the radiation sterilization is based on the sterilization of medical equipment using mainly gamma or electron radiation. It can also enclose other industrial applications, such as the radiation-based modification of polymeric materials, which also commonly utilize radiation doses in the range of tens of kGy per irradiated item [9, 12].

The contents and structure of the thesis are as follows. Chapter 2 presents the background material and underlying concepts the research is built upon. It contains descriptions of the properties and compositions of some of the radiation environments which are of concern for electronic components, and describes how

the radiation can interact with target matter and thereby transfer energy to e.g. sensitive regions of electronic components. The chapter also describes dosimetric quantities and relations that are used to describe radiation fields and to convert quantities of particle fluence and deposited dose in various materials, and then provides some descriptions of dosimeter systems relevant to this thesis work. The chapter is finalized by descriptions of various radiation effects in electronics, focused on mainly SDRAM components, and then by descriptions of irradiation facilities utilized for the experimental work for this thesis.

The results of the irradiation experiments on SDRAMs are presented and discussed in Chapter 3, based on the findings presented in the first two included articles [PI, PII] which are attached at the end of the thesis. The experimental results from the studies on optical fiber-based dosimeters are presented in Chapter 4, based on the final two included papers [PIII, PIV]. The thesis is after that concluded in Chapter 5.

2 BACKGROUND

2.1 Radiation environments

Radiation can be encountered at various places, and times, in our solar system. The types of particles that are present, and the energies of these particles, can differ greatly from one place to another, and build up radiation environments with a wide range of characteristics. We can divide these radiation environments into two main categories: radiation environments on Earth, and radiation environments in Space.

Relevant radiation environments will be presented and discussed in this section, with further information to be found in the cited material and the references therein.

2.1.1 Radiation in space

2.1.1.1 Galactic cosmic rays

The space radiation environment consists of particles produced in the sun, as well as particles originating from outside our solar system called galactic cosmic rays (GCR). The GCRs are to a large extent originating in supernova events [13], and were discovered through experiments by Victor Hess in 1912 [14]. They can reach very high energies, so that even the average GCR energy is around 1 GeV per nucleon [15, 16]. The differential particle flux spectra of a selection of GCR ion species (including protons with atomic number $Z = 1$) are shown in Figure 2, as encountered by a satellite in geosynchronous orbit (GSO) at an altitude close to 36 000 km over the equator. The figure also shows spectra of solar particles, which are discussed later in the text.

The GCRs consists of around 90% protons and 9% He ions (alpha particles), and about 1% heavier ions and electrons [16]. Since the origin of the GCRs is far away, and can even be from galaxies outside the Milky Way, the GCR flux direction is isotropic in nature. The GCR flux (especially that of the lower energy

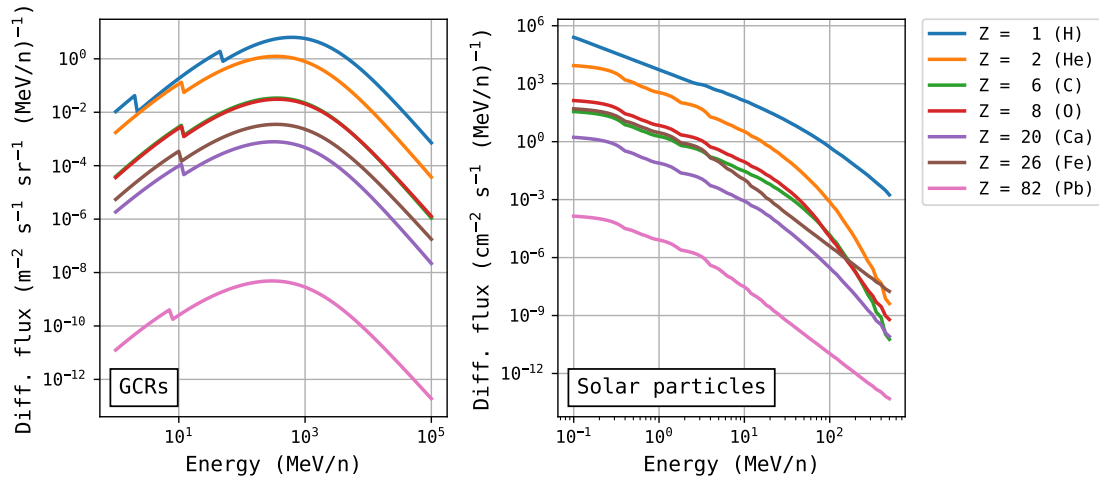


FIGURE 2 Differential flux spectra for some ion species components of GCRs, and solar particles. The spectra were simulated with the Space Environment Information System (SPENVIS) [17] using the ISO-15390 [18] and ESP-PSYCHIC [19, 20, 21] models for the GCR and solar particles respectively, encountered on average by a satellite in geosynchronous orbit (GSO) during the year 2022.

GCRs) is however dependent on the activities of the heliosphere and the sun, and of the magnetic field of the Earth. A comparison of the fluxes of GCR protons and electrons is shown in Figure 3a, containing data taken by the PAMELA Experiment [22].

2.1.1.2 Solar particles

The sun can emit large amounts of particles, solar energetic particles (SEP), through solar particle events (SPE). These events can be solar flares or coronal mass ejections (CME), where the CMEs are the most intense. These events occur fairly unpredictably and can last for periods of many days. Their frequency of occurrence is correlated to the solar cycles (which have a periodicity of around 11 years), so that SPEs are more likely to occur during the active parts of the solar cycles. The SEP consists mostly of protons, which can reach high energies of hundreds of MeV [16, 26], and even multiple GeV [27]. Also heavier ions (mostly helium), electrons, x-rays, and neutrons are emitted in the SPEs [16, 28]. The differential flux spectra of a selection of ion species are shown in Figure 2, together with those of GCRs. Note that the scales of the axes of the two figure frames are different.

A comparison of the proton and electron contents of SPEs is shown in Figure 3b. The figure shows fits of measured particle fluences over four SPEs in an especially active solar period towards the end of 2003.

2.1.1.3 Trapped radiation belts

Around planets with magnetic fields, charged particles can get trapped in specific regions. The trapped radiation belts around Earth are known as the Van Allen belts, after the observation of the radiation belts made by the Explorer satellites,

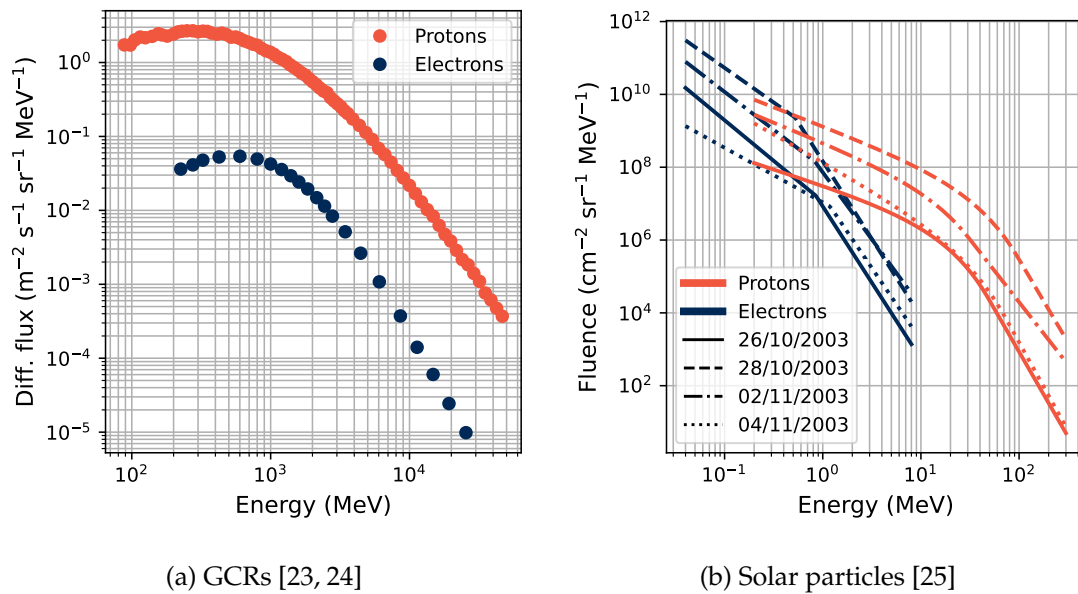


FIGURE 3 Energy spectra comparing the abundance of protons and electrons in GCRs in **a)**, and in a selection of SPEs in **b)**. The data shown in **a)** come from the in-orbit experiment PAMELA taken during 2009, with electron data from [23] and proton data from [24]. In **b)**, fits to particle fluences measured by various spacecraft during SPEs in 2003 are shown, based on data presented in [25].

and reported by James Van Allen in 1958 [29, 30]. The Van Allen belts are commonly seen as two separate radiation belts, one inner belt (“the proton belt”) and one outer belt (“the electron belt”). Despite their names, both of these belts contain electrons as well as protons (and a small part of heavier ions as well), and their positions are neither statically fixed nor always separated from each other.

In the inner belt, located from the edge of the atmosphere to within about 13 000 km above the Earth’s surface, electrons with energies < 5 MeV (typically hundreds of keV) are present, but the dominating part is protons with energies up to hundreds of MeV [31, 28]. The so called cosmic ray albedo neutron decay (CRAND) populates the inner belt with most of the protons present there [16, 31], and as well with some of the electrons of the inner belt [32]. The neutrons of the CRAND process are induced as secondary particles when GCRs collide with the Earth’s atmosphere, and the free neutrons decay with a mean lifetime of about 15 min into a proton, an electron, and an anti electron neutrino. Most of the neutron kinetic energy is maintained by the proton, while the electron from the beta decay obtains an energy of up to 782 keV [32]. It was through the detection of the showers of secondary particles that the GCRs were originally discovered [14].

In calm geomagnetic conditions the outer Van Allen belt is commonly found in the span 13 000 to 45 000 km above the Earth’s surface [31]. This radiation belt mainly contains high-energy electrons in the MeV-range (< 10 MeV), but also protons with energies of generally up to around 100 keV [31]. With changes in solar activity, such as solar flares and solar storms, the outer belt (and the magnetic field in the region of the outer belt) can however be rapidly modulated, so that the particle spectrum, shape and position of the outer belt can vary greatly [31, 28].

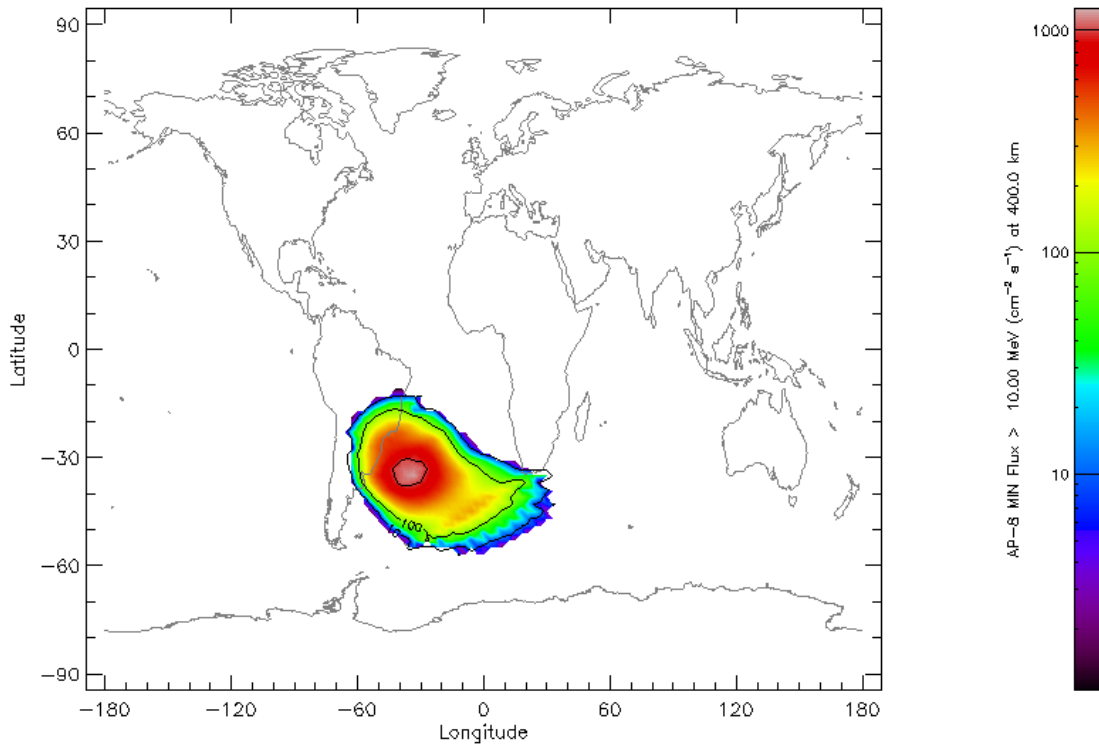


FIGURE 4 The flux of protons with energies over 10 MeV present at an altitude of 400 km over the Earth’s surface. These protons are only found in the SAA off the South American Atlantic coast. The visualization was done with SPENVIS [17], using the trapped proton environment model AP8 [33] of solar minimum (worst case for protons) conditions.

The filling of the inner belt with electrons is occurring mostly through events of high solar activity, where electrons are pushed to low altitudes. The injection events of electrons with energies above 1 MeV are rare, while injections of electrons with energies of hundreds of keV and below are more common [34]. Lower energy solar electrons can be injected through less violent solar substorms through the Earth’s magnetotail into the outer belt [31]. These can be subsequently accelerated to higher energies (into the MeV-range), through resonance interactions involving hundreds of keV electrons, and plasma waves generated by tens of keV-electrons [35].

The charged particles of the belts are trapped in the Earth’s magnetic field through three main motions. They bounce back and forth along the magnetic field lines, while undergoing a gyrating motion around those lines, and at the same time have a drifting motion around Earth: eastward for electrons and westward for protons (as well as for the small amount of other ions present in the belts, carrying a positive electric charge) [28, 31]. Further details about these motions and dynamics can be found in e.g. [36].

The Earth’s magnetic field is tilted from its axis of rotation by about 11° , as well as have an offset of about 500 km toward the west Pacific [28]. This results

in the magnetic field lines coming closer to the Earth's surface above the south Atlantic, by the South American coast. This region has a higher particle flux, most notably of high-energy protons, at lower altitudes than elsewhere on Earth, which is known as the south Atlantic anomaly (SAA). This region is visualized in Figure 4, where the flux of protons with energies above 10 MeV found at a 400 km-altitude is shown over a map of the Earth. 400 km is also the altitude of the International Space Station (ISS), flying in low Earth orbit (LEO). At these altitudes, below and around 1000 km, high-energy protons are mainly present in the SAA.

Planets with different magnetic fields will get different resulting particle spectra in their trapped radiation. An example is shown in Figure 5, where the particle environment faced by a satellite (the Galileo GSAT0221 in medium earth orbit (MEO)) in the electron (outer) belt of Earth is compared to expected environment for the European Space Agency (ESA) Jupiter Icy Moons Explorer (JUICE) mission, which will visit the Jovian environment. Navigation satellites, such as GSAT0221, as well as GPS and GLONASS satellites, are generally located in MEO, at around a 20 000 km altitude.

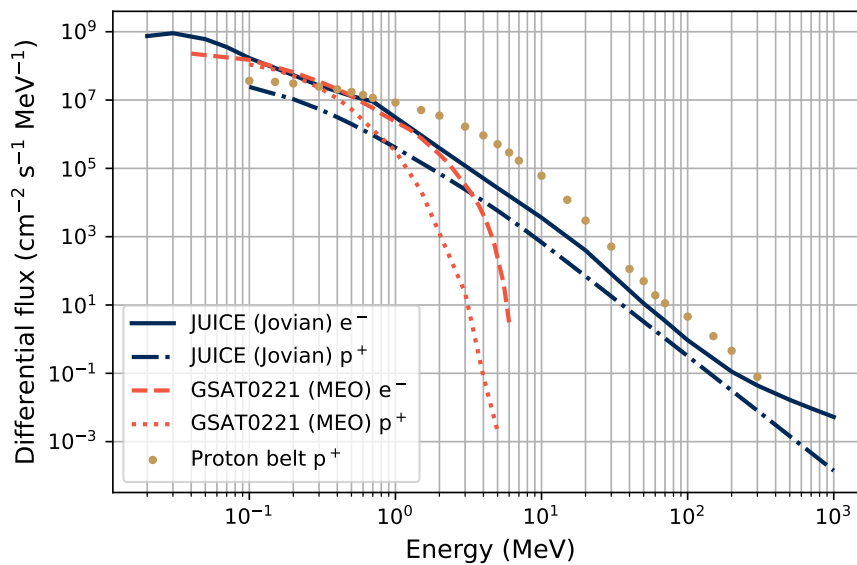


FIGURE 5 Differential trapped particle flux expected to be encountered on the ESA JUICE mission [37], compared to that faced by the Galileo satellite GSAT0221 in medium Earth orbit (MEO) as modeled by SPENVIS [17] using the trapped electron and proton models AE8 and AP8 [33] during solar maximum (worst case for electrons) conditions. This is also compared with the inner-belt protons encountered at an altitude of 7000 km, marked with gold dots.

In Figure 5 is also shown the proton environment deep in the proton (inner) belt of Earth, encountered in a circular example orbit at a 7000 km altitude, where protons with comparable energies as encountered by JUICE are found. The key difference of the trapped Jovian environment compared to the Earth's is

the presence of very-high energy electrons, up to the GeV-range in energy. These particles might produce radiation-induced effects in the spacecraft electronics not normally considered, since these high-energy electrons are not generally encountered.

2.1.2 Terrestrial radiation environments

2.1.2.1 Atmospheric radiation

As mentioned under Section 2.1.1, GCRs were first observed through the secondary particles that they induce when they collide with the atmosphere. Primary cosmic particles with high energies can result in large showers of secondary particles through spallation reactions and other nuclear reactions, through both the primary particle and its secondaries. This leads to a radiation environment in the atmosphere which is dependent on altitude, latitude, the solar activity and geomagnetic activity [16, 38, 39].

The particles present are dominantly neutrons, but also protons, electrons, photons, muons and pions are present, as well as heavier ions [16, 40]. The neutron density in the atmosphere grows with decreasing altitude as the particle showers spread, until a maximum at altitudes around 20 km [41]. The neutron component in particular, presents challenges to the safe operation of aircraft electronics [38], as well as cause elevated ionizing dose levels for aircraft crew [42].

Solar particles, as well as the GCRs, can cause increased radiation levels in the atmosphere. During severe SPEs, the solar particles can increase the dose level received by aircraft crew many times over [43]. The flux of neutrons and other particles induced by the GCRs and SEPs are attenuated when traversing further through the atmosphere, but a part of them can reach also to the ground level [44]. At ground level, the neutron density is about 500 times smaller than at the peak at 20 km [41].

2.1.2.2 Particle accelerators

There are man-made sources of radiation where the environment can be locally very harsh. These include nuclear power plants, experimental fusion reactors such as ITER [45], and particle accelerator facilities.

Accelerator facilities exist in many forms, with a wide range of potential radiation environments inside and outside of the particle beam itself. The scale is broad, from large research infrastructures like the LHC and its connected chain of accelerators at CERN [3, 46, 47], to smaller accelerators used for e.g. radiotherapy in medical facilities [48, 49].

What these have in common is when the main and intended particle beam is created and accelerated, background radiation and secondary particles are induced, which create radiation fields around the accelerator beam. Descriptions of the radiation facilities most relevant to this thesis are presented in Section 2.5.

2.2 Radiation interactions with matter

The encountered radiation might be harmful for living organisms, as well as electronic devices. The reason for this potential harm is the energy that is transferred to the target material through various interaction processes.

There are multiple ways one could categorize these interactions. Here they are separated under photon-matter interactions and interactions between other particles and matter. All types of particles are not considered in this section, and the discussion is limited to photons (γ), neutrons (n), electrons (e^-), protons (p^+ / H^+), as well as heavy ions (HI, ions heavier than H^+). Further information on the topic can be found in e.g. [50, 51, 52].

2.2.1 Particle-matter interactions

When the effects of radiation are discussed, in relation to either biological effects or electronics, it is ionizing radiation that is referred to, i.e. radiation which can directly or indirectly ionize a target material. Direct ionization occurs through charged particles such as protons, electrons and heavy ions, which directly ionize the target medium through coulomb interactions with the target material electrons. Indirectly ionizing particles are neutral particles, such as photons and neutrons. They can induce charged particles through interactions with the target material, which then in turn are directly ionizing.

For charged particles, the rate of change in energy dE per path length dx while traversing a material is defined as the stopping power S , as shown in Eq. 1. This quantity is also known as the stopping force.

$$S = -\frac{dE}{dx} \quad (1)$$

This is commonly expressed in units of MeV cm^{-1} . The stopping power divided by the density ρ of the target medium is called the mass stopping power, with e.g. the unit $\text{MeV cm}^2 \text{mg}^{-1}$.

Expressions for the mass stopping power are shown in Eqs. 2 and 3 for heavy charged particles and for electrons respectively. These equations were originally derived by Bethe, and Eq. 2 is commonly known as the Bethe-formula.

$$\left(\frac{S_{col}}{\rho}\right)_{HI,p^+} = \frac{4\pi N_A Z r_e^2 m_e c^2}{A \beta^2} z^2 \left(\ln \frac{2m_e c^2 \beta^2}{I} - \ln(1 - \beta^2) - \beta^2 \right) \quad (2)$$

$$\begin{aligned} \left(\frac{S_{col}}{\rho}\right)_{e^-} &= \frac{2\pi N_A Z r_e^2 m_e c^2}{A \beta^2} \left(\ln \frac{E_K (E_K + m_e c^2)^2 \beta^2}{2I^2 m_e c^2} + (1 - \beta^2) \right. \\ &\quad \left. - \left(2\sqrt{1 - \beta^2} - 1 + \beta^2\right) \ln 2 + \frac{1}{8} \left(1 - \sqrt{1 - \beta^2}\right)^2 \right) \end{aligned} \quad (3)$$

Here N_A is Avogadro's number, Z is the atomic number, and A the atomic mass number of the target material, m_e is the electron mass, c is the speed of light in vacuum and z is the projectile atomic number. $\beta = v/c$ is the ratio of the projectile speed v to c , I is the mean excitation energy / ionization potential of the medium, $r_e = e^2/(4\pi\epsilon_0 m_e c^2)$ is the classical electron radius, where e is the electron charge and ϵ_0 is the permittivity in vacuum, and E_K is the incident electron kinetic energy in Eq. 3.

An example of how the energy and mass stopping power vary as a Xe ion traverses a slab of Si is shown in Figure 6. The ion is continuously losing energy through coulomb interactions with the electron clouds of the target material. As the energy decreases, and the particle velocity decreases, the energy transfer per unit path length increases, until it reaches a maximum shortly before the particle is completely stopped in the target. The maximum energy transfer region is known as the Bragg peak.

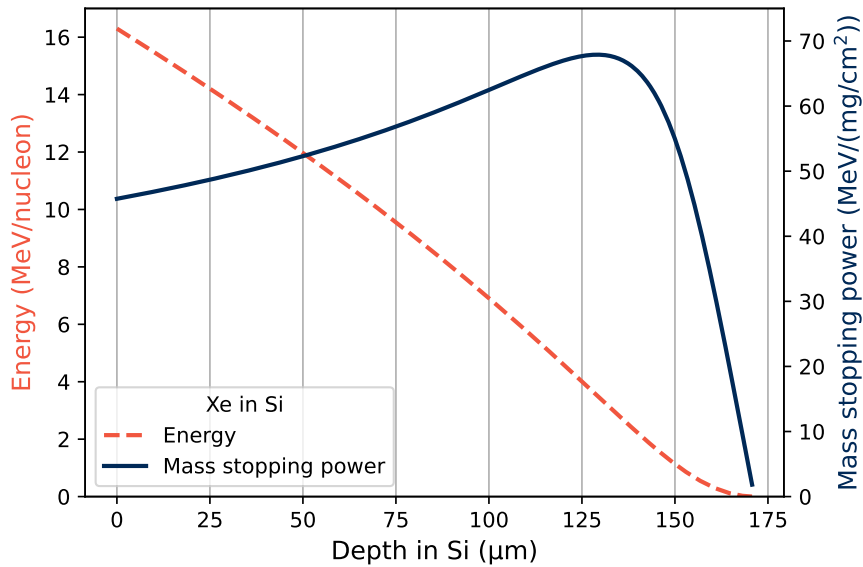


FIGURE 6 Energy and mass stopping power of 16.3 MeV/n Xe ions in Si. The evolution of the Xe energy and stopping power as the ions traverse Si is shown. The energy is steadily decreasing, while the stopping power reaches a maximum when the energy gets low, known as the Bragg peak. The data used for the figure was obtained from [53].

The collision stopping power S_{col} is mainly originating from interactions between the incident particle and the atomic electrons. For light projectiles, such as electrons, the radiative energy loss can be large, and is not negligible. Since the projectile mass is the same as the target mass when an impinging electron scatters against atomic electrons, the paths of electrons in the target material will be much more erratic, with larger scattering angles compared to those of heavier projectiles. These directional changes of charged particles lead to photon emissions called bremsstrahlung (braking radiation). The mass stopping power of electrons

due to radiative emissions is expressed by Eq. 4.

$$\left(\frac{S_{rad}}{\rho}\right)_{e^-} = \frac{N_A Z^2 r_e^2 (E_K + m_e c^2)}{137A} \left(4 \ln \frac{2(E_K + m_e c^2)}{m_e c^2} - \frac{4}{3}\right) \quad (4)$$

The total stopping power for a particle is then the sum of the collision and radiative stopping components

$$S_{tot} = S_{col} + S_{rad}. \quad (5)$$

The stopping power components from Eq. 5 are shown in Figure 7 for electrons in liquid water, Si, and Ta, with the values of the stopping powers obtained from [54]. When the electron energy increases over a few MeV the radiative stopping power becomes dominant, where the exact point in energy differs with the target material. Note the Z^2 -dependence in Eq. 4, which makes the radiative energy losses far greater for heavier target materials.

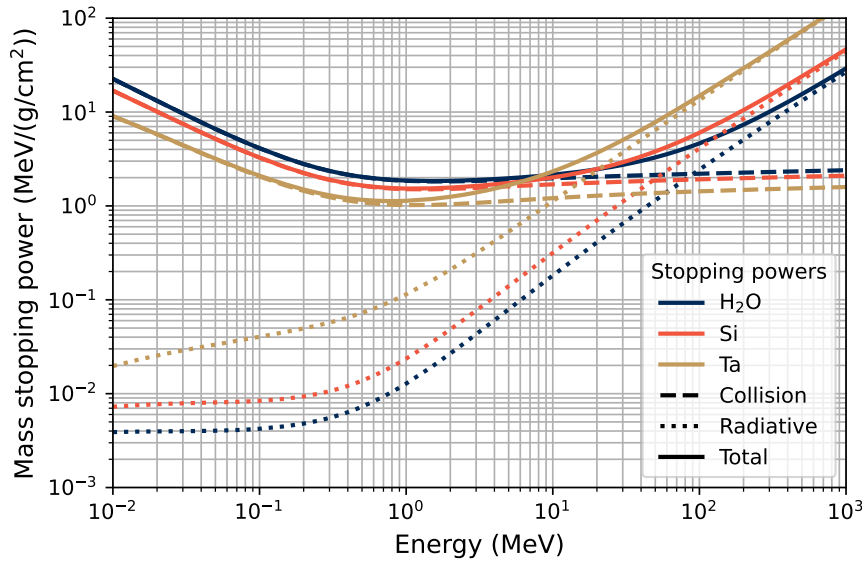


FIGURE 7 Stopping powers of electrons in Si, liquid water, and Ta. The data used for the figure was obtained from [54].

Particle projectiles can also interact with target matter through nuclear interactions, where energy can be transferred elastically or inelastically to the target nuclei, causing nuclear recoils and/or decay products. The kinematics of elastic reactions by an incident particle on a nucleus is governed by the conservation of momentum and energy in the collision, without needing to take into account nuclear excitations as needed for inelastic reactions.

For the case of electrons impinging on a nucleus, there is a very large mass difference (the ratio of the electron mass to the proton mass m_p is $m_e/m_p \approx 5 \cdot 10^{-4}$). One can therefore view the electron-nucleus scattering analogous to the

Compton scattering of a photon on an atomic electron [55]. The kinetic energy of the recoil atomic nucleus can then be expressed as

$$E_{K,r} = \frac{E_e^2}{Mc^2} \frac{2 \sin^2 \theta / 2}{1 + \frac{E_e}{Mc^2} \sin^2 \theta / 2} \quad (6)$$

where E_e is the incident electron energy, M is the recoil nucleus mass, and θ is the scattering angle of the electron. The maximum recoil energy is obtained with a backscattered electron, $\theta = \pi$.

Neutrons do not interact through Coulomb interactions since they have no net charge. They interact instead through interactions with target nuclei via the strong force in inelastic nuclear reactions. These reactions can take place at considerably lower energies for neutrons than charged particles, since the neutrons don't need to overcome the Coulomb barrier of the target nuclei.

The inelastic reactions offer many possible paths, where the interaction cross sections of possible reactions are highly dependent on the isotopes present in the target material and the incident particle species and energies. To extract the properties of the total resulting particle spectrum for an incident particle on a target, Monte-Carlo based simulation tools such as GEANT4 [56], FLUKA [57], or G4SEE [58] are useful. Examples of simulated energy spectra of generated secondaries from electron irradiation on various materials are shown in e.g. [59, 60].

2.2.1.1 Cherenkov radiation

Charged particles traversing a transparent medium at velocities larger than that of light in the material emit photons called Cherenkov radiation, named after its discoverer [61]. Along the path of the charged particle in the medium, a polarization of the surrounding medium will occur by the particles electromagnetic field, with a following electromagnetic emission upon the relaxation of the medium.

For the case of fast particles, a wavefront with positive interference emerges at an angle θ relative to the fast charged particle. The speed of light in a material is $c/n(\lambda)$, where n is the refractive index of the material and is a function of the wavelength λ of the light, and the speed of a particle is βc . The emission angle is then obtained through

$$\cos \theta = \frac{1}{\beta n(\lambda)} \quad (7)$$

which is known as the Cherenkov relation, where the particle velocity needs to be larger than the phase velocity of light in the material, i.e. $\beta n > 1$. Further information can be found in e.g. [62].

2.2.2 Photon-matter interactions

High-energy photons can originate from various sources, for instance from the acceleration and turning of charged particles (e.g. bremsstrahlung and synchrotron radiation), atomic deexcitations (X-rays), or nuclear deexcitations (γ -rays).

The secondary particles in a target material after photon interactions are mainly electrons, originating from the photoelectric effect, Compton scattering or pair production processes. Other reaction products can arise from photo-nuclear interactions, where the (γ, n)-type reactions are common for high-energy photons, and a concern when using e.g. clinical linear accelerators [63, 64].

The photoelectric effect is an atomic interaction, where the incoming photon energy is absorbed by one of the atomic electrons. The electron (called a photoelectron) will be released from the atom with a kinetic energy that is the difference between the photon energy and the electron binding energy. Also X-rays will be induced in this process, originating from the deexcitation process of the atomic electrons to fill the vacant shell position left by the ejected photoelectron (this process can also release another electron, an Auger electron, in place of an X-ray). This type of interaction is dominant for low-energy photons, and especially for absorber atoms with high Z -values.

Compton scattering occurs as the incoming photon scatters against one of the atomic electrons. In this process, a part of the photons energy and momentum is transferred to the atomic electron, which gains the kinetic energy as described in Eq. 6 (if the binding energy and initial kinetic energy of the electron is neglected). In the equation, M is exchanged to the electron mass, E_e to the photon energy, and θ is the scattering angle of the photon. This effect is dominant for photons with intermediate energies (around the MeV-range) and especially for materials with low- Z nuclei.

In the pair production effect, the photon disintegrates in the close vicinity of an atom into an electron and a positron (e^+ , anti-electron). This effect can occur for photons with energies above 1.022 MeV (since the electron and positron rest mass are of 0.511 MeV each), where the photon energy above this limit is transferred to the created particles as kinetic energy. The positron slows down in the material after it is created, and will subsequently annihilate in a reaction with an electron. The annihilation creates a pair of photons, each with an energy of 0.511 MeV emitted in opposite spatial directions. The pair production effect dominates for high-energy photons, and especially for high- Z atoms.

2.3 Dosimetry

The measurement of doses of ionizing radiation is known as dosimetry, and is central in characterizations of radiation beams and in radiation safety applications.

There are various quantities that are used for describing beams of radia-

tion, and of how much energy that is transferred from them to a target material. Some of these quantities are described in Section 2.3.1, and some examples of dosimeters are presented in Section 2.3.2. Further information can be found in e.g. [51, 65].

2.3.1 Dosimetric definitions

The number of particles that are present in a beam or radiation field is described by the particle fluence

$$\Phi = \frac{dN}{dA}, \quad (8)$$

where dN is the number of particles incident on a cross sectional area dA . The fluence has the unit m^{-2} , or more commonly used cm^{-2} since particle beam dimensions and target areas are often in the scale of cm .

If the particles in the beam have an energy E , the energy fluence Ψ is given by

$$\Psi = \frac{dN}{dA} E = \frac{dR}{dA} = \Phi E. \quad (9)$$

Here dN is the number of particles with energy E , and dR is the radiant energy incident on the area dA . Energy fluence is described in units of J m^{-2} or MeV cm^{-2} .

Particle beams are however not perfectly monoenergetic, and there is always a spread in energy. Some particle beams and radiation fields are also designed to include a range of energies. Thus an energy dependence on the quantities in Eqs. 8 and 9 can be included, and we may define the particle fluence spectrum $\Phi_E(E)$ and the energy fluence spectrum $\Psi_E(E)$ as

$$\Phi_E(E) = \frac{d\Phi}{dE}(E) \quad (10)$$

and

$$\Psi_E(E) = \frac{d\Psi}{dE}(E). \quad (11)$$

The particle flux is defined as

$$\dot{\Phi} = \frac{d\Phi}{dt} \quad (12)$$

which is the rate of particle fluence. $d\Phi$ is the increment of particle fluence in the time interval dt , and $\dot{\Phi}$ has commonly the unit $\text{cm}^{-2} \text{s}^{-1}$. The same way the energy fluence rate can be described as

$$\dot{\Psi} = \frac{d\Psi}{dt} \quad (13)$$

with the units W m^{-2} or $\text{MeV cm}^{-2} \text{s}^{-1}$.

For indirectly ionizing radiation, such as neutrons or photons (Section 2.2.1), the kinetic energy released per unit mass (kerma, K) is an important quantity. Kerma is a measure of the average amount of energy that is transferred from the indirectly ionizing radiation to secondary directly ionizing charged particles \bar{E}_{tr} , that are released in a medium following reactions of the incident particles per unit mass dm . The kerma is thus

$$K = \frac{d\bar{E}_{tr}}{dm} \quad (14)$$

and measured in the unit Gy (gray, $1 \text{ Gy} = 1 \text{ J kg}^{-1}$). In the radiation effects in electronics community however, the unit rad ($1 \text{ rad} = 0.01 \text{ Gy}$) has been, and is still, commonly used.

The secondary directly ionizing particles released in the kerma process can lose energy in the material both by collision reactions leading to ionization in the material (for the case of electrons released by incident photons as described in Section 2.2.2, c.f. Eq. 3), or through radiative processes (c.f. Eq. 4). The total kerma can then be defined as the sum

$$K = K_{col} + K_{rad}, \quad (15)$$

where collision kerma K_{col} is the kerma that leads to energy loss by the secondary particles through Coulombic interactions with the atomic electrons, and the radiative kerma K_{rad} is the part that leads to radiative energy losses. The average fraction of K that goes to K_{rad} is called the radiative fraction, and is denoted by \bar{g} . K_{col} can then be expressed as

$$K_{col} = K(1 - \bar{g}). \quad (16)$$

For photon beams, the mass attenuation coefficient μ/ρ is a factor that is dependent on the photon energy and target material properties, and is a measure of how much of an incident photon beam is lost in (or attenuated by) a target material, through interactions with a target material. It relates the incident photon beam intensity I_0 of a monoenergetic beam, to the remaining intensity $I(x)$ at a depth x in the material, by

$$I(x) = I_0 e^{-(\mu/\rho)\rho x}. \quad (17)$$

The fraction of the photon beam intensity loss that goes to the generation of charged secondary particles is described by the mass energy transfer coefficient

μ_{tr}/ρ . This coefficient is related to the mass-energy absorption coefficient μ_{en}/ρ through

$$\frac{\mu_{en}}{\rho} = \frac{\mu_{tr}}{\rho}(1 - \bar{g}), \quad (18)$$

so that μ_{en}/ρ describes the part of the photon beam which leads to collisional direct ionization in the target material, without the radiative losses of the secondary particles.

The collision kerma for photon radiation is related to the energy fluence of a monoenergetic photon beam through μ_{en}/ρ at a point in the medium, by

$$K_{col} = \Psi \frac{\mu_{en}}{\rho}. \quad (19)$$

The ratio between the collision kerma in two different materials can then be expressed as

$$\frac{K_{col,1}}{K_{col,2}} = \frac{\Psi_1(\frac{\mu_{en}}{\rho})_1}{\Psi_2(\frac{\mu_{en}}{\rho})_2}, \quad (20)$$

which, when the ratio of the energy fluences between the materials is close to 1, is equal to the fraction of the mass-energy absorption coefficients of the materials.

The absorbed dose D in a material is defined as

$$D = \frac{d\bar{\epsilon}}{dm}, \quad (21)$$

where the quantity $\bar{\epsilon}$ is known as the energy imparted, and m is a mass element of a target material. $\bar{\epsilon}$ is the measure of the total energy entering a volume, minus the energy leaving the volume.

Following the discussion of stopping power in Section 2.2.1, the quantity restricted collision stopping power is introduced as the amount of energy that is transferred to a limited target volume. A maximum energy limit Δ is introduced, so that secondary particles with energy in excess of Δ are assumed to escape the volume of interest without any interaction within the volume, and secondaries with energy below Δ are completely stopped within the volume. The restricted linear collision stopping power is denoted L_Δ and is also known as the linear energy transfer (LET). It is expressed as

$$L_\Delta = \frac{dE_\Delta}{dl} = \text{LET}, \quad (22)$$

where dE_Δ is the energy lost by a charged particle in collisions, with the sum of the energies of secondary particles with energy above Δ subtracted, and dl is the path length that the particle traveled.

The unit of LET is commonly $\text{MeV } \mu\text{m}^{-1}$, and for restricted mass collision stopping power e.g. $\text{MeV cm}^2 \text{mg}^{-1}$. Suitable values to choose for Δ depend on target material and the size of the volume of interest. In many applications, the LET is often approximated by the unrestricted collision stopping power rather than the restricted one, so that $\text{LET} \approx S_{col}$.

With the approximation that all secondary electrons are stopped in the volume of interest, and all secondary photons escape the volume, the dose from charged particles in a medium Y can be expressed using the particle fluence and the unrestricted collision stopping power

$$D_Y = \Phi_Y \left(\frac{S_{col}}{\rho} \right)_Y. \quad (23)$$

The dose can also be expressed by using the LET (by choosing a suitable value of Δ , or by using $\text{LET} \approx S_{col}$), which with commonly used units becomes

$$D[\text{Gy}] = 1.602 \times 10^{-7} \times \text{LET}[\text{MeV cm}^2 \text{mg}^{-1}] \times \Phi[\text{cm}^{-2}]. \quad (24)$$

Analogous to Eq. 20, the ratio between the doses absorbed in two different media can be expressed as

$$\frac{D_1}{D_2} = \frac{\Phi_1 \left(\frac{S_{col}}{\rho} \right)_1}{\Phi_2 \left(\frac{S_{col}}{\rho} \right)_2}. \quad (25)$$

If the ratio of the fluences in the materials is close to 1, the ratio of the doses becomes $D_1/D_2 = (S_{col}/\rho)_1/(S_{col}/\rho)_2$.

For indirectly ionizing radiation, the relation between collision kerma and deposited dose is commonly expressed by a factor

$$\beta = D/K_{col}. \quad (26)$$

This factor is equal to one under charged particle equilibrium (CPE), where the relation between the deposited dose and kerma becomes

$$D = K_{col} = K(1 - \bar{g}). \quad (27)$$

As a photon beam traverses a target material, CPE occurs at the depth in the medium where the absorbed dose is the largest. There the number of charged particles entering a volume element is equal to the number of those exiting it. At the surface of a medium, the number of photons from the beam will be the highest, and thus K_{col} will be the largest. As the photon beam goes deeper in the medium, it will attenuate, and the kerma will decrease. Since the number of charged secondaries will initially build up, the absorbed dose will also increase, until an equilibrium is reached at the maximum dose depth. Since the photon

beam attenuates along its path through the material, the deposited dose will decrease with depth beyond the maximum dose depth.

A similar dose deposition structure as a function of depth in a medium is found for electrons as with protons, with some differences. There is a similar buildup of dose and produced secondary particles in the form of lower energy electrons and photons until a maximum of deposited dose is reached. The primary electrons have an associated electronic stopping power and will interact by the Coulomb force transferring energy to the electrons in the medium. The generated secondary x-rays from bremsstrahlung can have longer range than the primary electron beam, which will result in a lingering tail of dose deposited by these x-rays after the primary electron beam is stopped.

In terms of the dose deposition as a function of depth in a material by an electron beam, the maximum dose deposited is referred to as D_{max} , and the depth in the material at which the maximum dose occur is z_{max} . The deposited dose at the surface of the material is $D_{surface}$, which is lower than D_{max} as discussed above. Other useful quantities are I_{50} , the depth at which the recorded dose has dropped to half of its maximum value, and R_p , the practical range of the electron beam calculated as where the tangent of the maximum slope of the decreasing portion of the dose depth curve intersects with the x-ray background.

2.3.2 Dosimeters

Deposited dose can be measured by different means, and many types of dosimeters exist. Which choice is the best solution varies from case to case, where considerations of radiation field, dose rate, surrounding environment, and much more can limit the suitable options. Some commonly used dosimetry systems are alanine dosimeters, film dosimeters (radiographic/radiochromic film), semiconductors (based on diodes or transistors), scintillators (plastics or crystals). These types of dosimeters have not been utilized in this work, and are described elsewhere, e.g. [51, 52, 65].

In this thesis work, luminescence dosimeters are the most used dosimeter type, specifically systems based on optical fibers were tested and characterized. These will be described in this section, along with a brief description of ionization chambers, which have been utilized here for reference dose measurements.

2.3.2.1 Ionization chambers

Ionization chambers are widely used as dosimeters in various contexts, such as radiation beam monitoring, diagnostics, and dose calibrations. They are usually constructed so that two (or more) electrodes are separated by a gas filled cavity, where the gas can be air or some different gas. As ionizing radiation passes through the gas, the gas gets ionized and the released charges are collected by the electrodes. The collected current can after calibrations be related to the deposited dose. Two common designs of ionization chamber dosimeters are cylindrical (Farmer type / thimble type), or parallel plate. Examples of these ioniza-

tion chamber types are shown in the photograph displayed in Figure 8.



FIGURE 8 Photograph showing a parallel plate ionization chamber to the left, and a Farmer type ionization chamber to the right. The Farmer chamber is covered by a protection cap (build-up cap), inside of which the cavity is located. For reference, the diameter of the top view of the white parallel plate chamber surface is 42 mm.

2.3.2.2 Luminescence dosimeters and optical fiber-based dosimeters

Dosimeters that emit luminescence, proportional to the absorbed dose or dose rate in them, are commonly divided into sub-categories of thermoluminescence (TL) dosimeters (TLD), optically stimulated luminescence (OSL) dosimeters, and radioluminescence (RL) dosimeters.

In these types of dosimeters, the incoming radiation excites the material, creating electron-hole pairs, which upon recombination emit photons. For the case of the TL and OSL dosimeters, the excited particles get trapped in metastable states. The trapped particles accumulate as the dosimeter is exposed to radiation, and after irradiation they are de-trapped by an external stimulation in the form of heating (TL) or by laser light (OSL). The de-trapped charges can then recombine in recombination centers, causing emissions of light at certain wavelengths. The energy levels associated with the trapping and recombination centers are properties of the dosimeter material and dopants added to the material, and the amount of light that is emitted in the TL and OSL processes is proportional to the ionizing dose that was deposited.

The recombination of electrons and holes, and associated light emission, can take place spontaneously and without stimuli in the RL process. Dosimeters

utilizing the radiation-induced luminescence (RIL) without TL or OSL have a light-emission intensity during irradiation which is proportional to the dose rate they are subjected to.

The TL and OSL dosimeter types should maintain their induced trapped charges over the time of irradiation, and between irradiation and the readout process, so that the detected amount of light in the readout process corresponds to the deposited dose in a consistent manner. The RL type should instead provide an output of luminescence continuously during irradiation, fast enough to be able to represent the dose-rate and potential dose-rate fluctuations of the radiation environment. Some commonly used types of TLDs are ones based on lithium fluoride with various dopants [66], while $\text{Al}_2\text{O}_3\text{:C}$ is a common OSL dosimeter material [67].

Studies of TL, OSL, and RL dosimeters based on amorphous silica glass in optical fiber-based systems have also been made, with various incorporated dopants [68, 69]. These systems are beneficial by having a small sensitive volume, not require any electric potential at the sensing area, and being more radiation hard than many similar systems based on plastic materials [68, 1, 70]. These properties make the silica fiber-based systems attractive for various applications, such as radiotherapy [71]. The remaining part of this Section 2.3.2.2 will address the topic of such optical fiber-based dosimetry systems.

A view of some optical fiber-based dosimeters is shown in Figure 9. A radiation sensitive part is located at one end of the optical fiber, in Figure 9a marked with an orange circle. This is a doped silica glass, in this case a 1 cm long and 0.5 mm wide rod doped with Ce^{3+} , which is fusion-spliced to a transport optical fiber. The transport fiber is here a pure silica core fiber, that ends as shown in Figure 9b with a bare fiber core. The sample in Figure 9a had one optical fiber spliced to it, while the sample depicted in Figure 9c has two. The doped sample, which is a rod similar to the one in Figure 9a, is located in the middle of the white plate seen in Figure 9c. This type of sample can be used for OSL dosimetry, where one of the transport fibers can be used for guiding laser light for optical stimulation to the doped region, while the other transport fiber can guide the OSL to a detection system.

The main drawbacks of the fiber-based systems are the radiation-induced attenuation (RIA) of the optical fibers, and radiation-induced emissions (RIE) of light other than the desired luminescence. The RIA is caused by damage to the pure or doped amorphous silica glass constituting the material lattice of the fiber by the incoming radiation, as the radiation can create point defects through displacing atoms, or by ionization. The different types of defects that are created are associated with specific optical absorption (OA) properties, where photons within an energy band typical for each defect can get absorbed [72].

As the RIA increases with radiation dose, the transmitted light signal gets weaker. How strong the RIA is depends on the fiber material, the dopants that are added to it, as well as irradiation conditions such as temperature and dose rate [1, 72, 73]. The RIA in optical fibers can also be exploited for use as radiation dosimeters for well characterized fibers. This can be done in e.g. distributed

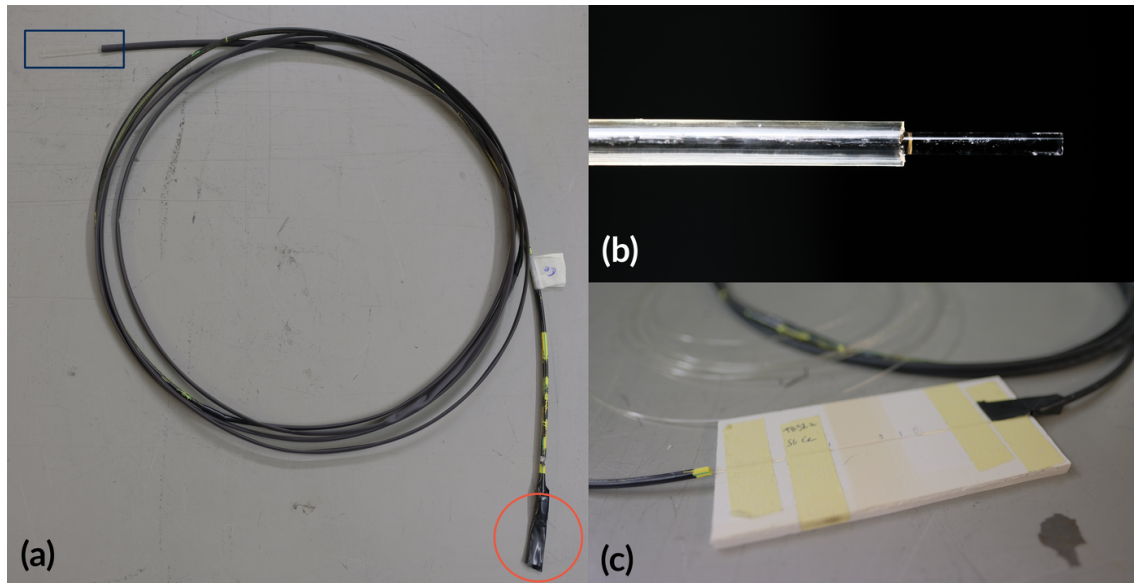


FIGURE 9 Examples of optical fiber-based dosimeter samples. **(a)** shows an optical fiber in a thin black plastic tube for protection against external light sources, with a doped silica rod in one end marked with an orange circle, and the open end of the transport fiber marked by a blue square. **(b)** depicts the end of the transport fiber, where the fiber core is bare at the fiber end to the right hand side, and is covered by the fiber cladding on the left hand side. **(c)** shows a sample that can be used for OSL, and the doped sample at the center of the white plate is fusion spliced to transport fibers in both ends, where one end can be connected to a laser for optical stimulation and the other to a photo-detection system.

optical fiber radiation sensors (DOFRS), where the measured RIA at different locations in a fiber can be used to map the radiation dose along the full fiber length. DOFRS are used for this purpose e.g. at CERN along parts of the accelerator tunnels [74].

Some induced RIA centers can anneal through processes involving heating of the sample (thermal bleaching), or through stimulation with intense light through the fiber (photobleaching) [1, 75, 76, 77]. There are also RIA processes however which are only significant during and immediately after a radiation pulse have hit the fiber, which is known as transient RIA. The transient RIA can be related to various generated non-stable defects with different absorption and decay properties, such as self-trapped holes (STH) [78, 79], self-trapped excitons (STX) [80, 81], and co-dopant related defects [82].

The major types of RIE include the luminescent decay from excited states of the material and induced Cherenkov radiation (see Section 2.2.1.1). The luminescent decays are commonly related to dopant ions, but could also be through radiation-induced (or pre-existing) point defects which can exhibit characteristic luminescence properties [72]. Examples of dopants used in silica-based optical fibers which have been investigated for RL and dosimetry based on RIL are listed

in Table 1. In the table is also listed studies found in the literature for the various dopant species, as well as the main emission bands of the RIL in terms of the main emission energy and decay time. For many of the dopants the decay time has been studied mainly under excitation by photons from lasers, i.e. through photoluminescence (PL), instead of through RL. For the cases with more than one dopant (CeTb and CuCe), the emission bands related to each dopant are specified separately.

TABLE 1 List of the main emission bands and previous studies of silica-based optical fibers with various dopants for dosimetry based on RIL.

Dopant	Main emission bands (eV)	Main RL/PL decay times	Literature
Ce	2.6–2.8 Ce: 2.6,2.8	50–60 ns Ce: 50–60 ns	[83, 84, 68, 85, 86, PIII]
CeTb	Tb: 1.99,2.11,2.28,2.54, 2.70,2.83,2.98,3.25	Tb: 2.2 ms, 1.2 ms	[87, 88, 89]
Cu	2.25 Cu: 2.28	40–50 μ s Cu: 45 μ s	[90, 91, 92, 68, 86, PIII]
CuCe	Ce: 2.75	Ce: 90 ns	[93, 86]
Ge	3.1–3.2	110 μ s	[94, 95, 96, 97]
Gd	3.95	1.2–1.8 ms	[98, 71, 99, PIII, PIV]
N	2.25,3.55	2.25 eV: ms ^a 3.55 eV: 20 ns	[100, 11, 101]
P	3.0	5–6 ms	[102, 103]

^a This emission line's properties are to the best of the author's knowledge not yet studied in the literature, but has during measurements shown signs of being long lived, on the order of multiple ms [104].

2.4 Radiation effects on electronics

The effects of radiation on electronic devices are usually divided into two main categories. These are cumulative effects and single event effects (SEE), where the cumulative effects can arise from the deposited total ionizing dose (TID) or from displacement damage dose (DDD), and in contrast the SEE arise from the interactions of single particles. The general topic of radiation effects on electronics is very wide, so this section will be centered around the effects of radiation on SDRAMs, especially the description of SEEs in Section 2.4.2.

2.4.1 Cumulative effects

2.4.1.1 Total ionizing dose

The TID effects are those which arise mainly from the ionization processes inside insulators within the electronic devices. If there is an electric field over the insulator the electrons and holes created through ionization are swept in opposite directions by the field. The charged particles which do not recombine can get trapped in different locations, commonly at defects by the material interfaces such as Si-SiO₂, creating regions with net charge that can affect the performance of the electrical device [105].

Insulators are commonly found as the oxide layer in metal-oxide-semiconductor field-effect transistors (MOSFET), where a bias voltage on the metal-side of the MOSFET is utilized to open a conductive channel in the semiconductor, close to the oxide layer. If deposited dose in the oxide layer leads to trapped charges in the oxide-semiconductor interface, the conductive channel in the semiconductor will be affected so that different voltages on the metal side are needed to open or close the channel. This is known as threshold voltage shift.

The TID effects in the oxide layers of MOSFETs are getting less and less significant, as the scaling trends of electronic components leads to ever smaller devices, and thinner oxide layers. With thin oxide layers (in the order of few nm and below) the non-recombined charges in the oxide can escape through tunneling effects [106].

In modern devices with thin gates, other isolation structures throughout the device are more important for the TID response, such as shallow trench isolation (STI) structures [107]. The STI structures can vary greatly in shape and size between different implementations in different devices, making their impact on the TID response difficult to predict. In an environment with ionizing radiation present, and with electric fields present over the insulators, net charge might accumulate in these structures and affect the device behavior.

2.4.1.2 Displacement damage dose

In contrast to the TID effects, the DDD effects are created by the displacement of the atoms of the device material rather than from interactions with the atomic electrons (which is the case in ionization) [108]. Si is a structured crystalline material, and its properties change when defects are introduced in the material lattice. Such defects can be present in pristine devices, and can also be introduced by radiation. The accumulation of point defects due to displacement damage (DD) over time due to radiation is described by the DDD.

The simplest form of defect to envision in a Si crystal lattice is the vacancy-interstitial pair (Frenkel pair), where one atom has been moved in an interaction with the incoming radiation from its original position (the vacancy), to its new position in the lattice where no atom is supposed to be present in the ordered crystal (the interstitial). The scale of complexity goes from the one displaced atom

to large clusters of displaced atoms created by cascades and chain-reactions of secondary particles. The damage clusters originate from a large collision event between the projectile particle and a primary knock-on atom (PKA), which obtain a large amount of energy in the collision.

In a semiconductor such as Si, charge carriers (electrons and holes) can move when electrons are excited to the conduction band (and holes are present in the valence band), thereby creating currents. The electrons and holes can recombine over the bandgap (between the conduction and valence band), which decreases the number of charge carriers. Defect centers can introduce energy levels within the bandgap, which can trap electrons or holes depending on the energy level. These can then facilitate the generation or recombination of electrons in the conduction band and holes in the valence band, leading to increased leakage currents or other changes of the device properties.

To compare the effects of different radiation fields on a material or electronic device, the concept of non-ionizing energy loss (NIEL) is commonly used. This quantity describes the part of energy a particle loses in the material that is transferred to the target nuclei, and that does not go to ionization of the material.

2.4.2 Single event effects in SDRAM

The set of possible SEEs can differ between different types of devices, and their impact can be more or less severe [109]. Soft errors are device upsets which are non-permanent, whereas hard errors cause permanent errors and can even cause total device failures in some cases. The upset modes most relevant to the SDRAM test results that this thesis is based on will be the focus in this section, and a few other common types of SEEs will be mentioned.

Single event upsets (SEU) are soft errors caused by single particles. In terms of SEE on memory components, the SEUs are manifested as bit-flips, i.e. transitions of one binary memory cell value (bit value) to the other ('0' \rightarrow '1' or '1' \rightarrow '0'). If one memory cell is upset, it is known as a single bit upset (SBU), and if multiple cells are upset after one particle interaction it is called a multiple bit upset (MBU).

Before going into further detail regarding SEE mechanisms in dynamic random access memories (DRAM), the operation and basic layout of the DRAM cell is introduced. A schematic of the DRAM cell layout is shown in Figure 10, which shows a simple DRAM cell with one transistor and one capacitor (1T/1C cell).

The cell can be in either of two states: have stored charge on the cell capacitor, or have no stored charge. Which of these states correspond to a value '0', and which to a value '1' depends on the programming of the device by the manufacturer. The cell value is written by opening the access transistor via a bias voltage on the gate (3) through the word line (2). The bit line (1) can then provide a voltage level, or the ground level, which will then be written to the cell capacitor (6) through the transistor contacts (4,5), where the numbers in parenthesis refers to the green numbers in Figure 10.

After the memory cell has been written, and the transistor gate closed, the

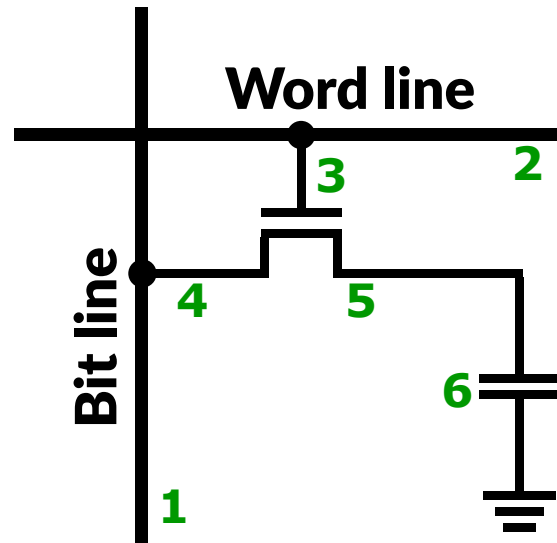


FIGURE 10 Schematic drawing of a DRAM cell. A bias on the word line causes the access transistor to open, and the charge located on the storage capacitor can be probed through the bit line.

charge will be stored on the capacitor. If the written value was to the state of zero charge (bit line on ground level), the state of the cell will remain as it is. If instead the bit value was written to a non-zero voltage level, the cell capacitor will discharge over time with a characteristic time constant

$$\tau_{cell} = R_{leak}C \quad (28)$$

where C is the cell capacitance and R_{leak} is a resistance which is governed by the leakage currents from the cell. This leakage is the combination of leakage paths of the capacitor, transistor, and other paths, such as through material defects. The parameters of Eq. 28 might differ from cell to cell in a memory due to manufacturing process variations, and local impurities in specific memory cells.

The capacitor discharge in a cell with stored charge makes it necessary to periodically refresh the data on the memory. This is commonly done every 64 ms in each of the memory's cells of newer SDRAMs (e.g. [110]). A qualitative view of the capacitor charge over time in a memory cell with stored charge is shown in Figure 11. In the event that the memory is not refreshed, the charge will decrease until it is below the limit where the sensing node in the peripheral memory electronics no longer recognizes the memory cell to be in the charged state. The amount of time it takes from the memory is written to the charged state, until the memory cell is read as being in the discharged state (without being refreshed), is known as the data retention time.

The data retention time of the memory cells within a memory component can vary by many orders of magnitude, from below 1 s up to many hours, and it can be greatly affected by radiation [PI, PII]. If the memory cell retention time is decreased so much that it loses its charge (to be in the discharged state) between the refresh events, the cell will always return the bit value corresponding to the

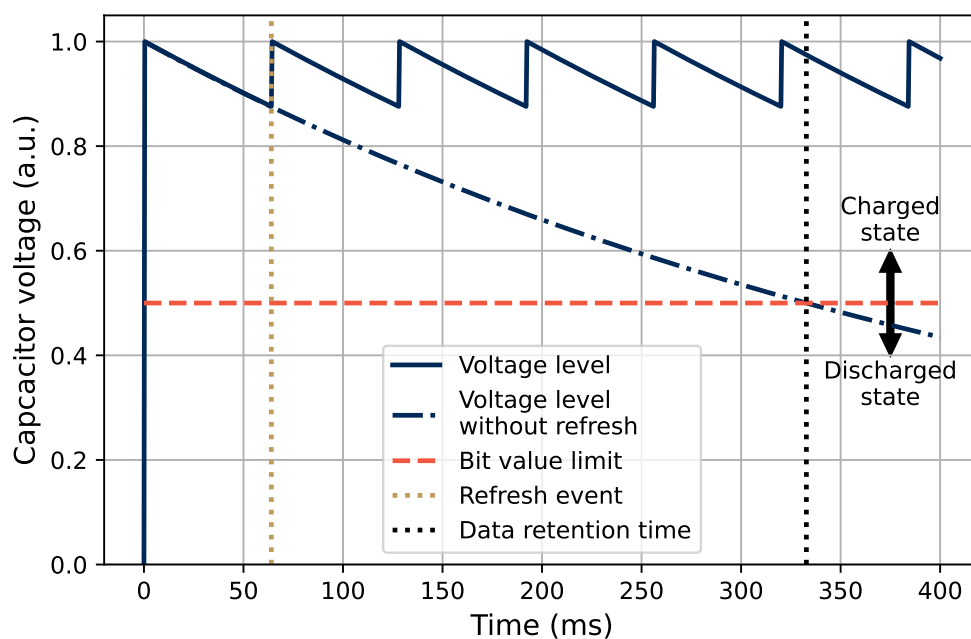


FIGURE 11 Qualitative example of the voltage level over the capacitor in the DRAM cell with stored charge, where the cell value is refreshed every 64 ms. The voltage level if no refresh operation is applied is also shown, where eventually the voltage level in the cell drops below the level which separates the regions where the sensing electronics interpret the memory cell as being in the charged state, or in the discharged state.

discharged state, no matter which value was originally written to it. These bits are known as stuck bits.

Both cumulative effects and SEE can cause stuck bits. TID effects can degrade the performance of the access transistor causing the stored charge to leak out faster, and also create regions of trapped charge around the access transistor and capacitor degrading the ability of the cell to store charge. Defects created by displacement damage might also induce leakage paths. If the defects are small (point defects) they might not individually cause a stuck bit, but the accumulation of smaller defects in the same cell could. Large displacement damage clusters created by individual particles can by themselves cause a stuck bit. This effect is known as a single-particle displacement damage effect (SPDDE) [111, 112].

Single particles can also individually cause large amounts of ionization locally. The observable radiation effects from these local dose depositions are known as microdose effects, and these effects have been discussed as the cause of stuck bits and errors in devices since the first observations of single-particle induced stuck bits [113, 114].

The stuck bits can often be intermittently stuck bits (ISB). ISBs are during some periods of time appearing as normally working bits, and in other times appearing as stuck. Two different causes of ISBs are 1) the retention time of the bit is very close to the time between data refreshes (the refresh interval), and 2) the retention time of the bit varies over time. Also a combination of the two can

be true.

If the retention time is about the same as the refresh interval, small changes in electrical noise and temperature can change the outcome of the evaluation of the cell state. The signal on the bit line when the bit value is read, is evaluated at a sensing node where the voltage level is compared to a reference value. If the voltage level on the bit line is just on the limit between being interpreted as '0' and '1', any small change in the surrounding environment can affect the resulting value.

The temperature is a factor which has a large impact on the retention time. At high temperatures the leakages from the cell increase, so that the recommended refresh interval in high temperature applications (over 85 °C) is 32 ms instead of 64 ms [115]. Testing SDRAMs at longer refresh intervals can simulate the memory operation at higher temperatures [116].

Variations in retention time can also come from variations in leakage current originating from the radiation-induced material damage sites. Similar behavior has been observed in SDRAM cells as the random telegraph signal (RTS), that exist in for instance CMOS image sensors (CIS) and charge coupled devices (CCD). The RTS is there observed as pixels in a CIS having specific discreet levels of leakage current, and switching between these levels in a random fashion resulting in blinking pixels [117, 118]. The corresponding behavior in SDRAM cells is known as variable retention time (VRT) [119], and has been suggested to originate from damage clusters switching between discreet configurations, which results in different levels of cell leakage [112, 119].

SEU in the form of bit-flips can be observed in DRAMs without the bit becoming stuck. With a particle strike and ionization in sensitive positions, and in some cases at sensitive times, the bit value that is read from the cell can differ from the one that was written. Two separate regions can be mentioned where different types of mechanisms for cell upsets are possible when they are struck by particles. These are the cell strike and bit-line strike. Strikes in the cell region are those that with the generated charge cloud from ionization directly affects the stored charge on the cell capacitor. The effect of such a strike is commonly that the stored charge dissipates, and the cell is found in its discharged state. Events of this kind were the first observed SEU in DRAMs, which were caused by alpha particles from decaying contaminants such as Th and U and their daughter nuclei in the device packages [120]. In some cases, the stored charge might instead increase after a particle impact event leading to a transition from a discharged state to a charged state, e.g. [121].

During the times that the bit is probed, also strikes on or close by the bit line and bit line contacts can cause SEUs, as can particle strikes on the sense node area. As the bit is read or being refreshed, the bit line is in a floating state to collect the charge from the cell, and during these times charges induced by particle hits could be collected on the bit line and cause the bit value to be corrupted. Also combined effects of the two types of particle impacts on cells can cause SEU, called the combined cell-bit line failure mode [122]. A few other types of SEE are presented briefly here in the coming paragraphs, which are not discussed in the

included papers, but are closely related and of general interest.

Memory devices can also be sensitive to single event functional interrupts (SEFI). These are events where the control circuitry of the memory is affected by particle strikes, and unexpected device behavior might follow. This can lead to very large numbers of errors, the device going into a different state where it is unresponsive, or to different behaviors which might differ between components or types of memories.

Another type of SEE which can occur in memories and CMOS circuits is the single event latch-up (SEL). This type of effect can cause permanent damage to a transistor structure or memory cell due to high localized currents. This effect is caused by a parasitic NPNP or PNP structure (thyristor) forming after a particle hit, where a current path opens, and if not externally limited or turned off, might cause device failure.

In general terms, parts of circuits which are commonly sensitive to particle strikes are semiconductor junctions with reverse bias. There the generated electron-hole pairs are swiftly collected and separated, generating potentially large transient voltage pulses. This is the same mechanism as the one used in diode particle detectors. If such events take place in a part of an electronic device or circuit, the charge pulse created by the individual radiation strike can be transmitted through a circuit as a voltage spike, known as a single event transient (SET). The SET can cause issues in logical circuitry if its size is large enough (in terms of peak voltage and time width), and if it is occurring at a time and place where the circuit is sensitive to voltage perturbations [123].

2.5 Radiation effects testing facilities

There is a great diversity in the types of radiation fields that can be used for the testing of radiation effects on electronics or on other materials. The suitable facility to use is then chosen based on the purposes of the test. Test facilities based on sources of radioactive isotopes, nuclear reactors, X-ray tubes, and particle accelerators all exist. Heavy ion beams can be used for estimating the behavior of a device in an environment with a known LET spectrum, while tests with beams of high energy protons or neutrons can be used to estimate the response to high-energy hadrons (HEH). HEHs such as neutrons and protons of high kinetic energy have similar characteristics to each other in the way they cause upsets in electronic devices, by causing secondary recoil ions within the device materials, as well as generally similar error cross sections [124, 125].

Facilities with mixed radiation fields can be used to directly simulate the target environment if a similar radiation field is found in the facility. One example of such a test facility is CHARM at CERN, where different facility configurations and test positions exist, resulting in a variety of possible resulting radiation environments [126]. Radiation facilities that simulate the energy spectrum of neutrons in the atmosphere exist as well, where ISIS at RAL in Didcot, UK, is an example

of such a facility in Europe [127, 128].

For specific cases, radiation fields and test facilities not normally used for the testing of electronic components have to be used. An example of this is the component testing for the interplanetary space missions to Jupiter, and into the Jovian trapped radiation environment where a harder energy spectrum of electrons is found than normally encountered elsewhere (see Section 2.1.1). The response of the electronic components to high-energy electrons is not commonly characterized and the possible effects encountered not very well known. In the included paper [PI], the Very energetic electron facility for space planetary exploration missions in harsh radiative environments (VESPER) at CERN, as well as the Varian clinical linear accelerator (Clinac) at the Radiation Effects Facility (RADEF) in the University of Jyväskylä, Finland, were used to investigate the response of some models of SDRAMs to high-energy electrons. These facilities are described in more detail in the following Sections 2.5.1 and 2.5.2. The SDRAMs were also further characterized at the Proton Irradiation Facility (PIF) at the Paul Scherrer Institute (PSI), Switzerland, as well as in the proton beam at RADEF, as described in [PII]. At the Clinac at RADEF, the characterizations of doped silica glass dosimeters described in [PIII] and [PIV] were also performed.

2.5.1 RADEF



FIGURE 12 A photograph of the RADEF Clinac. The beam direction is downwards in the picture, coming from the accelerator head towards the so called couch where a block of acrylic can be seen in the beam window position.

RADEF is primarily a heavy ion facility, utilizing various cocktail beams from the K130 cyclotron at the University of Jyväskylä accelerator laboratory. The separate ion cocktails consist of selections of ions with close to the same mass to charge ratio, and thus with a constant energy per nucleon. Within a cocktail one

can quickly (generally on the order of 10 to 15 min) change between the available ions, to be able to characterize component and device behavior at different particle LET values. The (currently) available ion cocktails have energies of 9.3, 10, 16.3 and 22 MeV/n respectively [129, 130].

Proton beams are also accelerated by the cyclotron [131], with proton energies of up to about 55 MeV. The proton beams are directed to a target area where samples can be irradiated in air, where the resulting proton energy at the DUT position is around 52 MeV. To lower the proton beam energies, aluminium plates can be introduced to degrade the beam. As the protons exit the beam line, which is kept in vacuum, they pass through an ionization chamber which is used to monitor the proton flux. At the target area, the beam diameter can be up to about 10 cm, and the proton flux can be up to around $3 \times 10^8 \text{ cm}^{-2} \text{ s}^{-1}$. High energy protons can cause large material activation, by causing the creation of radioactive isotopes as they collide with materials in the irradiation area, which limits the usable beam flux. Also low energy proton beams are available at RADEF [132], with energies of 0.4 to 8 MeV. The beam target area for the low energy protons is in vacuum and not in air.

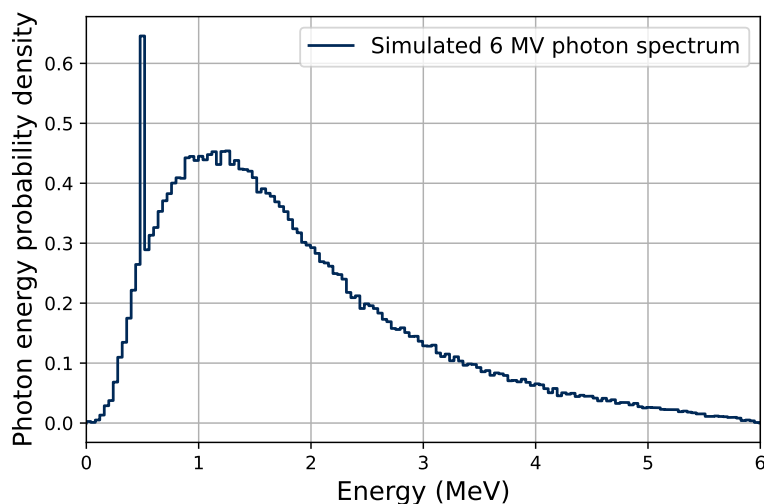


FIGURE 13 Energy spectrum of the 6 MV photon beam, simulated using GEANT4. Adapted with permission from [PI] © 2021, IEEE.

A Varian Clinac 2100C/D linear electron accelerator is located at RADEF [133], that was previously used in a hospital as a radiotherapy accelerator and is shown in Figure 12. The Clinac can produce electrons with energies 6, 9, 12, 16 and 20 MeV, as well as 6 and 15 MV photon beams. The photon beams are produced by placing a heavy metal (Ta) target in the beam of 6 and 15 MeV electrons for the 6 and 15 MV photon beams respectively. This creates a spectrum of photons consisting of bremsstrahlung radiation from the electrons. The resulting energy spectrum is shown in Figure 13 for the 6 MV case (also shown in [PI]), simulated using GEANT4 [56, 134]. The continuous energy spectrum of the bremsstrahlung up to the maximum energy located at the incident electron energy 6 MeV is seen, as well as a peak at 511 keV from the annihilation

of positrons from pair-production interactions of the photons. The maximum intensity is located around 1 MeV, which is a similar energy as gammas from ^{60}Co sources. These ^{60}Co sources are commonly used for TID testing, and apart from the energy spectrum differ mainly from the 6 MV Clinac beam in the pulsed beam structure of the Clinac, compared to the constant dose rate provided by ^{60}Co sources.

In the normal clinical operation mode of the Clinac, the dose rate of the electron beams can be varied from 1 to 10 Gy(H₂O)/min, while the photon beams have dose rates from 1 to 6 Gy(H₂O)/min. The beam of electrons from the accelerator is pulsed, where the sizes of the individual electron bunches from the machine is fixed. In the normal clinical operation, changing the dose rate modulates the frequency of the bunches and not their sizes, so that the average dose rate is changed, but the instantaneous dose rate is fixed. This mode of dose rate change is shown in Figure 14.

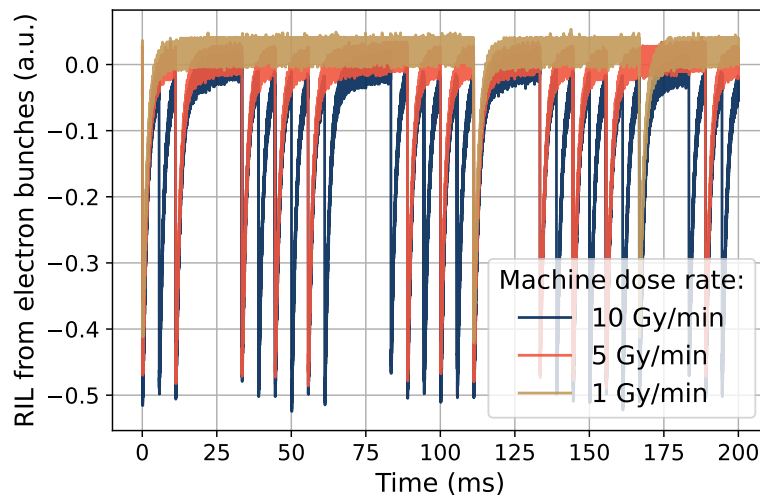


FIGURE 14 A higher dose-rate setting of the RADEF Clinac corresponds to a higher frequency of electron bunches from the machine. The data used for the figure was measured using the RIL from a doped silica glass rod. The pulses in the figure are wider in time than the electron bunches due to the decay time of the RIL, and the high impedance of the oscilloscope used to record the signal. Adapted from [PIII] under the license CC BY 4.0.

The length of the electron bunches is around 3 μs , and the bunch frequency of electron beams at 1 Gy(H₂O)/min is close to 20 Hz. This corresponds to a dose per bunch of 0.83 mGy(H₂O), and an instantaneous dose rate of around 280 Gy(H₂O)/s. It is however possible to alter the dose per electron bunch, if the Clinac is used in a mode where some of the machine beam control systems have been disabled. This allows the bunch frequency and the spacing between the bunches to be fixed to a constant value, and the amount of electrons per bunch to be tuned. This mode of operation was used in some of the tests of optical fiber-based dosimeters in Chapter 4, and in the studies presented in [PIII] where the mode of operation of the accelerator during those tests are described in more de-

tail. For the experiments of SDRAMs using the Clinac described in Chapter 3, the normal clinical mode of operation was used.

The Clinac beam dose and dose rate are monitored by in-beam ionization chambers. These parameters are given in units of Gy(H₂O), since the beams of the machine are calibrated in water phantoms using external dosimeters. A parallel plate IBA PPC40 dosimeter [135] is used for electrons, and a Farmer chamber IBA FC65-P dosimeter [135] for photons (these two dosimeter models are shown in Figure 8). The dose rates are given at the depth of maximum dose in water. This depth, along with the fraction of the maximum dose that is deposited at the water surface, and the mass collision stopping powers of the primary beam electrons in water and Si (with values from [54]), are shown in Table 2. Using Eq. 23, the fluence of electrons on a sample in air can be estimated from the surface dose factor and collision stopping power value. In Table 3, similar data for the photon beams are shown, but with the mass energy-absorption coefficients instead of the stopping powers. Since the main photon intensities are around 1 and 2 MeV for the 6 and 15 MV beams respectively, these coefficients are given for these two photon energy values.

TABLE 2 Properties of the electron beams at the RADEF Clinac, with S_{coll}/ρ values obtained from [54].

Energy (MeV)	Surface dose rate (fraction of max)	Maximum dose depth (cm H ₂ O)	S_{coll}/ρ (MeV cm ² g ⁻¹ (H ₂ O))	S_{coll}/ρ (MeV cm ² g ⁻¹ (Si))
6	0.78	1.19	1.911	1.639
9	0.83	1.96	1.956	1.685
12	0.89	2.61	1.989	1.716
16	0.94	2.40	2.021	1.746
20	0.91	1.58	2.046	1.796

TABLE 3 Properties of the photon beams at the RADEF Clinac, with μ_{en}/ρ values obtained from [136].

Photon beam	Surface dose rate (fraction of max)	Maximum dose depth (cm H ₂ O)	μ_{en}/ρ (cm ² /g (H ₂ O))	μ_{en}/ρ (cm ² /g (Si))
6 MV	0.47	1.56	3.10×10^{-2} (a)	2.78×10^{-2} (a)
15 MV	0.32	2.87	2.61×10^{-2} (b)	2.35×10^{-2} (b)

^a value for 1 MeV photons

^b value for 2 MeV photons

The accelerator head is rotatable around the machine isocenter, located at a distance of 1 m from the head of the accelerator. All calibrations of the beam were done at the isocenter position, as well as all measurements done using the

Clinac. Typical sizes of the beam area at the machine isocenter is a square with sides ranging from 5 to 20 cm.

2.5.2 VESPER

VESPER is a facility located at the CERN Linear Electron Accelerator for Research (CLEAR) [137, 138]. Typically, the accelerator can accelerate electrons to energies of 60 to 220 MeV, and has a pulsed beam structure with short electron bunches of 1 to 4 ps. These bunches are grouped together in bunch trains containing 1 to 200 bunches, with a bunch frequency within a train of 1.5 GHz, and a bunch train frequency of 0.8 to 10 Hz. The charge per electron bunch can be varied in the range 10 pC to 2 nC.

The electron beam at VESPER is monitored by a beam current transformer (BCT), which monitors the total current of the electron beam over time, while the shape of the beam spot is monitored by a scintillating yttrium aluminium garnet (YAG) screen. The beam spot at the test position is approximated to be Gaussian, and the 2D shape of the beam during the experiments is described by the beam center position $\mu_{x,y}$ and the standard deviation of the beam intensity profile $\sigma_{x,y}$, where the beam size is of the order of up to a few cm in diameter.

The experiments presented in [PI] utilized 100 bunches per bunch train and a bunch train frequency of 10 Hz, with beam sizes of around $\sigma_{x,y} = 12\text{--}15$ mm. The average electron flux that was used was generally around $2\text{--}3 \times 10^8 \text{ cm}^{-2} \text{ s}^{-1}$, which was rather low compared to the capability of the facility, where electron fluxes of up to the order of a few $10^{12} \text{ cm}^{-2} \text{ s}^{-1}$ are possible. The monitored beam profile at lower fluxes, such as was used in the experiments presented in this thesis, was rather diffuse using the YAG screen. This made the beam spot shape and position difficult to exactly estimate in the recorded beam logs, and the uncertainty of the resulting flux and fluence was estimated to be around 20% instead of the 10% that is commonly used [139].

The beam shape was approximately Gaussian at the facility, and the beam spot position was slightly drifting during the runs, by a few mm in horizontal or vertical directions. The electron fluence on the DUT of the irradiations were estimated as the average fluence in the center of the Gaussian beam, within one σ in the x and y directions.

3 RESULTS FROM RADIATION TESTS OF SDRAMs

3.1 Tested devices

The devices under test (DUT) were 512 Mb SDRAMs from the same manufacturer, but of different generations built using three separate technology nodes. The oldest device referred to as model B, is a 110 nm device built using a planar transistor technology, while the two newer ones, model D and model F, are of 72 nm and 63 nm technology nodes respectively, and constructed using a recessed channel array transistor (RCAT) technology [140]. These devices are listed in Table 4, and the cell layouts of the models are displayed in Figure 15. The devices were opened, and their layouts were studied using scanning electron microscopy (SEM) imaging, to observe differences in the memory cell structures which can be related to differences in the radiation responses of the devices.

TABLE 4 The tested SDRAMs in the described experiments.

Memory model	Technology	Node size (nm)
Model B	Planar	110
Model D	RCAT	72
Model F	RCAT	63

The numbers in Figure 15 are showing the functionality of the different parts of the cells, with corresponding numbers seen in the electrical schematic sketch in Figure 10. The bit (1) and word (2) lines are shown with gold colors in the figures, where the active word line(s) in the cell shown in the figure is marked with a number, while the non-active word lines which operate other cells behind or in front of the depicted cell in the figure are not. The contact to the applied gate voltage of the access transistor from the word line is marked 3 in the figures.

The cell structure of SDRAM model B depicted in Figure 15a is based on a planar device structure of the access transistor, with the bit line contact (4) connected to the storage capacitor (5-6) through a straight conducting channel

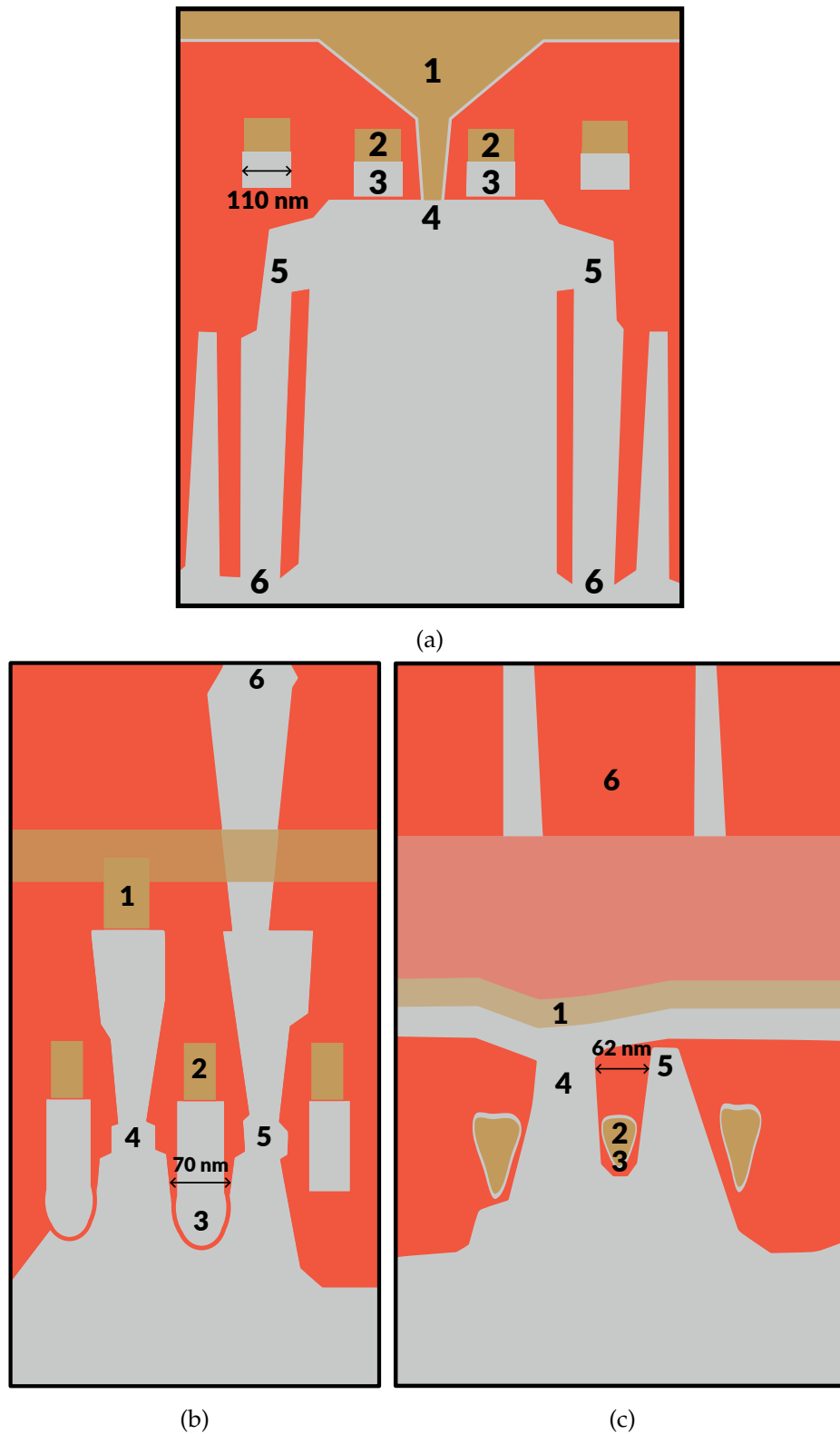


FIGURE 15 Schematic cross-sectional views of the memory cells of the tested SDRAM models, based on SEM images. The figure frames show unit cells of model B (a), model D (b), and model F (c). The numbers in the images refer to the different parts of the cell as shown in Figure 10, and the colors show metal contacts in gold, insulating layers in orange, and silicon or poly-silicon in grey.

opened under the access transistor gate. The storage capacitor is buried in the silicon bulk, below the word and bit lines.

In contrast, the model D and F cells in Figures 15b and 15c utilize an RCAT structure of the access transistors, where a curved channel is formed to connect the bit line with the storage capacitor when the word line is biased. The storage capacitors in these devices are formed by tubes located above the word and bit lines. In Figure 15b the bottom of the capacitor tube is located just above the schematic view, and in Figure 15c the capacitor tube is shown in orange and marked with 6.

The device of model B was envisioned to fly on the JUICE space mission to Jupiter. Therefore its response to high-energy electron radiation is of interest due to the hard energy spectrum of electrons in the trapped Jovian radiation environment, as discussed in Section 2.1.1. This model, along with models D and F, was tested under electron irradiation at VESPER and RADEF to investigate its expected behavior in the Jovian electron environment. These experiments are described in [PI] and Section 3.3. In those tests, stuck bits from the high-energy electrons were observed, and the radiation-induced retention-time degradation was studied. The formation of stuck bits and the degradation of the retention time were further studied using proton irradiation. Those results are described in [PII] and Section 3.4. In both papers, the results were compared to irradiations with photon beams for comparison, highlighting effects of TID.

3.2 Experimental setups and procedures

The DUTs were packaged in plastic housing, and not opened before irradiation, due to the long range of the high-energy electron and proton beams. During the irradiation experiments, the DUTs were mounted on irradiation test boards where the DUTs were placed under the radiation beams, and controlling electronics kept outside of the radiation field to as large extent as possible. For the experiments, a Terasic DE0-CV FPGA development board was used as a test controller board. This control board is shown in Figure 16 displaying the irradiation location at VESPER. The DUTs were soldered on daughter boards (green in the figure) that were connected to the control boards (blue in the figure). The figure shows also some of the dosimetry devices used at VESPER described in Section 2.5.2. The BCT is shown in the bottom right corner of the picture through which the electron beam is directed before reaching the DUTs, and the scintillating YAG screen is the yellow screen in front of the DUT on the left hand side in the figure.

During irradiation, the DUTs were tested in either static or dynamic modes. In static mode tests, a test pattern was written to the memory before irradiation, then the stored data on the DUT was read back after the irradiation run. During the dynamic tests, read and write operations were continuously performed on the DUT. When testing SDRAMs, tests are however not completely static since

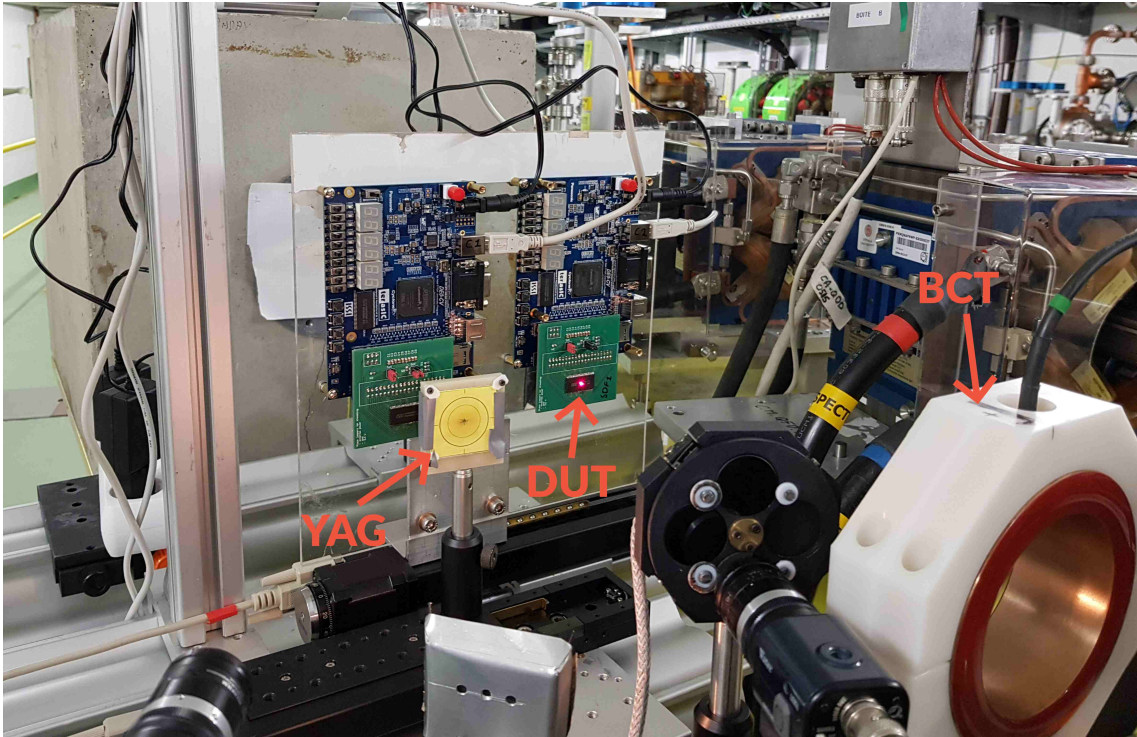


FIGURE 16 A photograph of the test boards and DUTs used at VESPER. Two setups are shown in the figure, where the DE0-CV test boards have blue background, daughter boards are in green, and the DUTs are soldered to the daughter boards.

the memory array is periodically refreshed (as shown schematically in Figure 11), and the cells are rewritten at each refresh event.

The dynamic tests that were performed during irradiation tests were variations of writing and then reading data patterns of all '0' and all '1' to the DUT. One such dynamic test procedure that was often used in the irradiation tests was the March C- test

$$\begin{aligned} & \uparrow (w0); \{ \uparrow (r0, w1); \uparrow (r1, w0); \\ & \downarrow (r0, w1); \downarrow (r1, w0); \} \uparrow (r0), \end{aligned}$$

where w and r signifies write and read operations of '0's or '1's, and the operations in parentheses are applied to the whole tested memory portion where the addressing order is specified the arrows \uparrow and \downarrow . For example the segment $\uparrow (r0, w1)$ means that a read operation with all '0' expected as return value is performed starting at the word with the lowest logical address, then all '1' is written to the same word. Then the same $r0, w1$ procedure is applied to all words in the tested memory at increasing logical word addresses. The operations within the brackets were looped over when multiple iterations of the test were performed after each other, to not repeat the stand-alone read or write elements in the loop.

The irradiation tests were in all cases performed using a beam direction perpendicular to the device surface, i.e. in a normal incidence angle. The irradiation tests, as well as storage of the devices before and after irradiation, were done in room temperature. The analysis and visualization of the data were done using python code.

The radiation-induced retention-time degradation is an important part of the experimental work and analysis presented in this Chapter. To properly investigate retention-time changes of the memory cells the time intervals between memory refresh operations should be tuneable. This functionality was implemented for the memory controller so that the refresh interval could be changed or fully disabled. The retention time of the bits can then be investigated by setting a refresh time interval, then, after writing the memory, waiting for some time corresponding to multiple refresh cycles before reading the memory array back. This approach was used for the characterizations done for the electron-irradiated DUTs. An updated approach that was used for the proton irradiated DUTs, was to keep a constant nominal refresh operation, then, some time after writing the memory, disabling the memory refresh for a specified time interval, after which the refresh operations are again applied before the memory is read back. Repeating such tests at various refresh time intervals or time periods with refresh operations disabled makes it possible to study the retention time distributions of the memory cells. The retention time characterizations were not done during irradiation, but in between and after radiation tests, as well as after periods of annealing.

3.3 Electron-irradiation effects

3.3.1 SEU and stuck bits

During the irradiation tests with electrons the March C- dynamic test loop was used. One of each memory models was initially tested at VESPER using a beam of 200 MeV electrons, up to electron fluences of $1\text{--}2 \times 10^{12} \text{ cm}^{-2}$. During these tests, SEU (bit-flips) and stuck bits were observed in the model B DUT, but no errors were observed in models D or F. Therefore the following irradiation tests were focused on the model B devices. Irradiation tests using electrons with energies of 123 and 61 MeV in addition to 200 MeV were performed at VESPER, and 20 and 6 MeV electron irradiations were performed at RADEF where also the 6 MV photon beam was used. The nominal refresh frequency was used in these tests, so the data in the bits of the DUTs were refreshed every 64 ms. The irradiation tests with model B devices are summarized in Table 5, where the DUT IDs (used to refer to the DUT in figures and discussion) are presented, along with the irradiation conditions in terms of the particle energy, species, and dose rate. The presented dose rate values are approximate, since some fluctuations and changes of dose rate (beam flux) occurred during some of the tests.

In the table are also shown the numbers of bit-flips (SEU) and stuck bits that were observed before the error rate increase, which is listed in the right-most column of Table 5. After a certain electron fluence the number of observed errors in the DUT as a function of fluence showed a distinct increase, which is shown in Figure 17a, where the number of stuck bits follows a linear trend up to

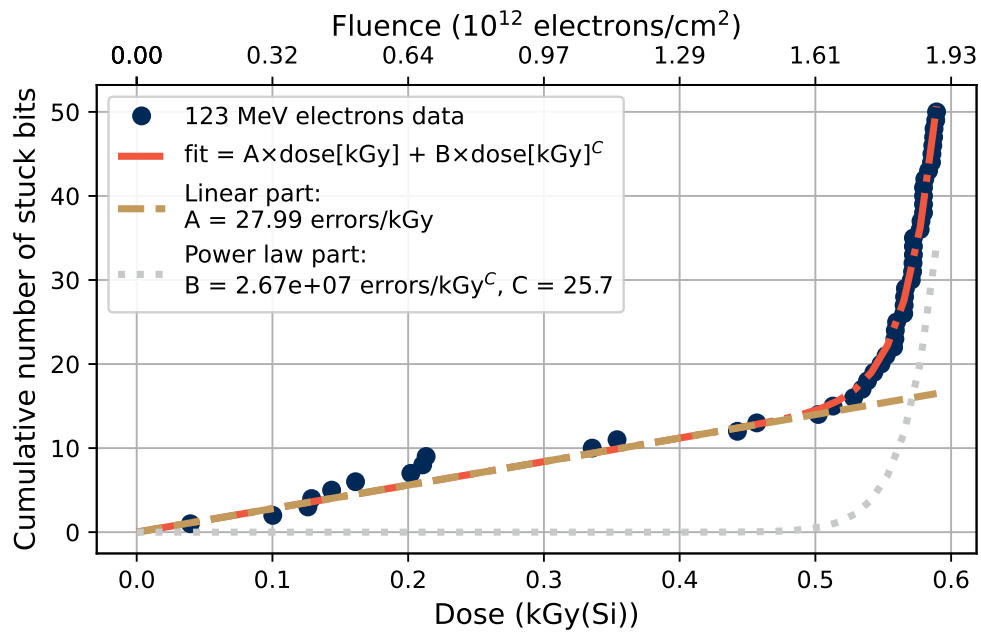
TABLE 5 Summary of the irradiation tests with electron and photon beams using DUTs of SDRAM model B. The number of observed bit-flips and stuck bits before the fluence or dose specified in the last column is shown for each DUT. Adapted with permission from [PI] © 2021, IEEE.

DUT ID	Particle	Energy	Dose rate (Gy(Si)/min)	Bit-flips	Stuck bits	Onset of error rate increase
SDF1	Electrons	200 MeV	1.9	10	11	1.58×10^{12} e/cm ²
SDF3	Electrons	123 MeV	5.6	10	13	1.61×10^{12} e/cm ²
SDF4	Electrons	61 MeV	7.2	10	13	3.33×10^{12} e/cm ²
SDF5	Electrons	20 MeV	5.7	6	6	2.78×10^{12} e/cm ²
SDG1	Electrons	20 MeV	8.2	2	5	2.95×10^{12} e/cm ²
SDG3	Electrons	6 MeV	6.7	0	0	2.67×10^{12} e/cm ²
SDG4	Electrons	20 MeV	25	2	6	2.43×10^{12} e/cm ²
SDG5	Electrons	20 MeV	4.1	4	7	4.52×10^{12} e/cm ²
SDG6	Photons	6 MV	4.5	0	0	0.5 kGy(Si)

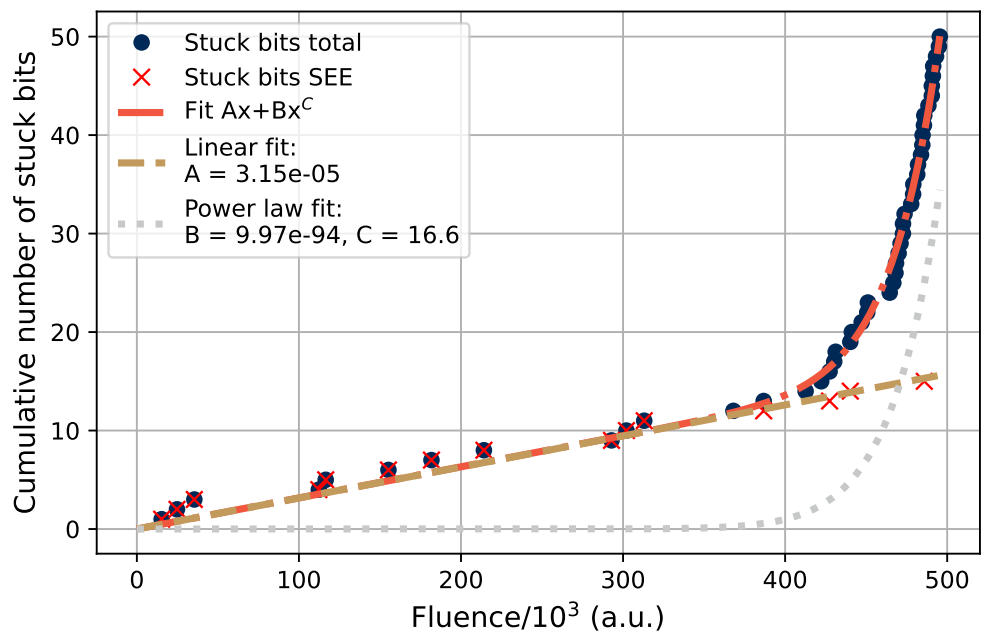
around 1.6×10^{12} e/cm² or 0.5 kGy(Si) after which the number of induced stuck bits increased steeply. Conversion between electron fluence and dose was done by using Eq. 23, with values of S_{col}/ρ for each electron energy in Si obtained from [54].

The observed errors in the DUT before the error rate increase are occurring randomly and follow a linear trend with the dose and electron fluence. These errors are attributed to an SEE phenomenon, where individual electrons are causing the upsets in the device. After large electron fluences and amounts of deposited dose in the DUTs, cumulative radiation effects start to show and the error rate increases to higher order dependencies, following a power law function. For the case of Figure 17a, this power is fitted to 25.7, which is a value representing the number of particle interactions required for the stuck bits to form if the stuck bit events are Poisson distributed.

The error trend, and the origins of the different types of observed errors following linear and power law functions were verified by simulation as shown in Figure 17b. The simulation was performed using Python by defining a bit array of 100×100 bits, then simulating random hit positions by particles on the bit array. If the particle hit was close to a bit location, there was a certain probability that the particle would induce a stuck bit immediately as an SEE, and a different, larger probability, of inducing a small amount of damage to the bit. These small amounts of damage accumulated in the bits over the simulation run, and when the damage amount reached over a threshold the bit was defined as stuck. The stuck bits from SEE as a function of the simulated fluence are marked as red crosses in the figure, and the total amount of stuck bits are marked as blue dots. The generation of the experimentally observed stuck bits in Figure 17a corresponds well to this simulated behavior resulting in the error generation as seen in Figure 17b.



(a) The cumulative number of induced stuck bits in the DUT SDF3 under irradiation by 123 MeV electrons. The data is fitted to a function consisting of a sum of a linear part fitting the errors from SEEs, and a power law part fitting the stuck bits from cumulative effects. Adapted with permission from [PI] © 2021, IEEE.



(b) The cumulative number of induced stuck bits in a simulated case. Each simulated particle hit had a probability to induce a stuck bit directly, or to deposit a smaller amount of damage in the cell, requiring multiple particle hits to cause a stuck bit. The trends of this simple case follow the experimental observations.

FIGURE 17 The trends of induced stuck bits as a function of fluence as observed experimentally, and by simulation.

Based on the number of stuck bits and bit-flips from SEEs as listed in Table 5, the SEE cross sections for bit-flips and stuck bits as a function of electron energy were calculated. These cross sections are shown in Figure 18 together with fits to the data using Weibull functions. No SEEs were observed during irradiation with 6 MeV electrons, so this data point is only represented by the upper limit of the error bars. The error bars are constructed using Poisson statistics with 95 % confidence limits, combined with the estimated error of the fluence measurements. In irradiation facilities used for irradiation of electronic components, the estimated value of uncertainty in the measured particle fluence is commonly 10 %, and this is the value used for the beams at RADEF. For the electron beams at VESPER 20 % was used as the fluence uncertainty value as described in Section 2.5.2.

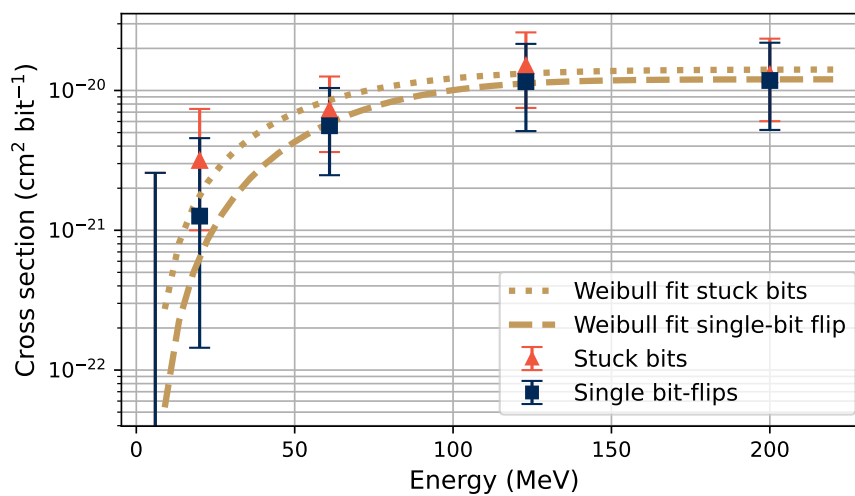


FIGURE 18 Electron SEE cross sections for stuck bits and bit-flips for 6, 20, 61, 123 and 200 MeV electrons, from data of DUTs SDG3, SDG1, SDF4, SDF3 and SDF1. Adapted with permission from [PI] © 2021, IEEE.

3.3.2 Dose rate and annealing effects

The point of onset of the observed error rate increase is related to the dose rate of the beam. This was investigated by testing DUTs using 20 MeV electrons with three separate dose rates, and the induced stuck bits as a function of dose and dose rate in the DUTs are shown in Figure 19. The dose rates that are reported are average dose rates, not instantaneous dose rates during the radiation pulses. The dose rate dependence suggests an ongoing annealing process, where the impinging radiation induces effects on the device which accumulate, but also anneal over time. During irradiation with the smaller dose rates, more time is available for the cumulative radiation effects to anneal, and the onset of the error rate increase is delayed.

The annealing of the stuck bits was investigated using retention-time distributions of the bits in the devices. This is shown in Figure 20, where the retention times of bits were investigated at different times of annealing. The DUT was kept

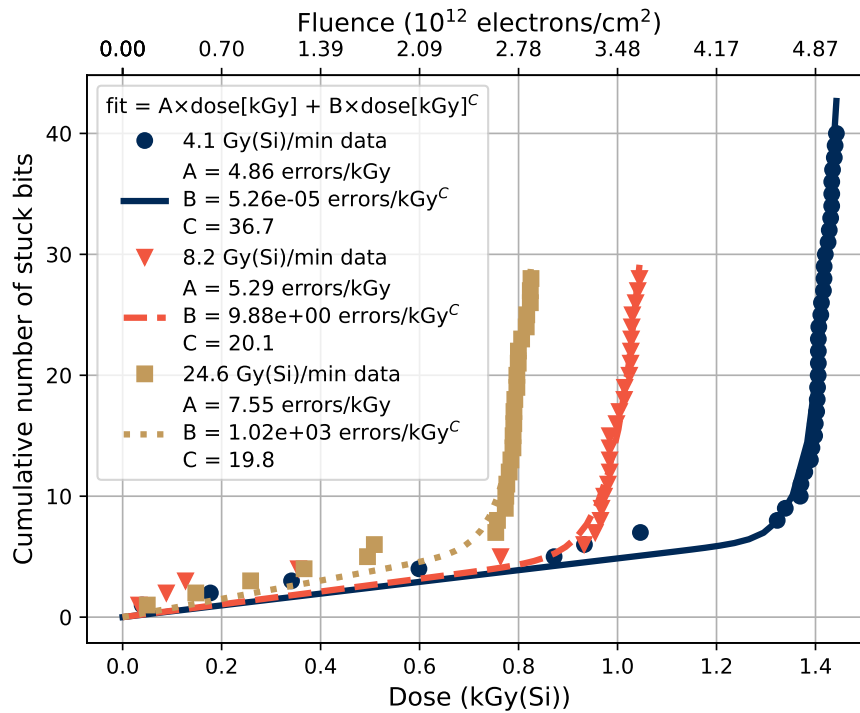


FIGURE 19 Induced stuck bits from 20 MeV electron beams at three different dose rates, with fits to the data to a sum of a linear function and a power law function. The error rate increase occurs earlier for higher dose rates. Adapted with permission from [PI] © 2021, IEEE.

unbiased in ambient room temperature during the annealing periods. The retention time test was performed by setting the desired refresh period of the memory, writing a data pattern of all '0' to the DUT, then waiting one minute before reading it back, then repeating the write-wait-read cycle with an all '1' pattern. The errors from these two memory readings were summed up, and the result is shown on the y-axis of the figure.

After the irradiation was stopped, and the DUT in Figure 20 recently had experienced the steep error rate increase as seen in Figure 19 for the SDG5 DUT irradiated at 4.1 Gy(Si)/min, many bits were stuck at the nominal refresh time period of 64 ms. Note that the errors in Figure 19 (and in figures presenting similar data) are cut in the y-axis direction so that both the linear and power-law parts of the data can be viewed. The irradiation runs were continued to slightly higher doses, as seen when comparing with Figure 20 where the number of errors after the irradiation end was around 10^3 . This number of errors at fast refresh frequencies around the nominal value dropped quickly after the irradiation, while the retention times of bits with intermediate to long retention times stayed fairly constant. After longer annealing times, the number of errors at long times between refresh events even started to increase. This retention time decrease as a function of annealing has also been reported in e.g. [141].

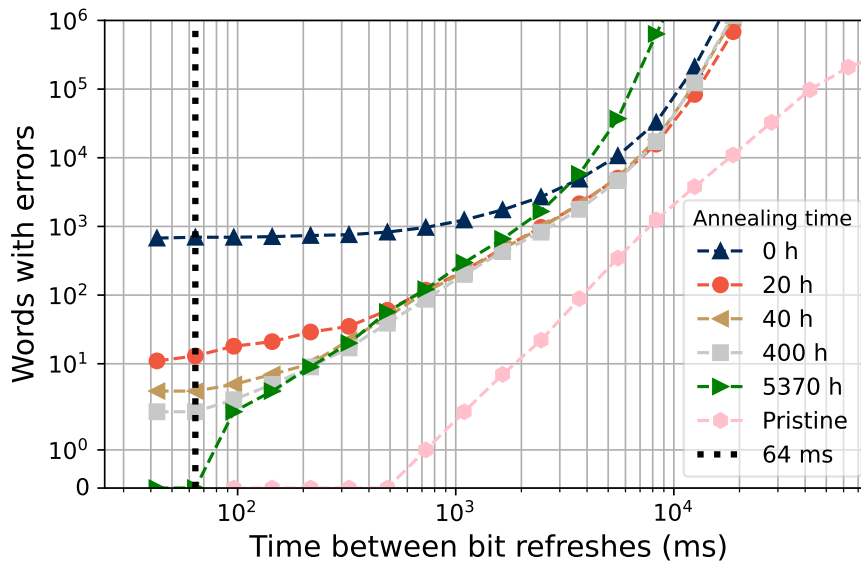


FIGURE 20 The evolution of retention times of bits in DUT SDF5 after irradiation by 20 MeV electrons at various times of annealing. Adapted with permission from [PI] © 2021, IEEE.

3.3.3 Origins of the SEE and cumulative effects

The response of the devices to 6 MeV electrons was compared with the 6 MV photon beam from the RADEF Clinac. No upsets due to SEEs were observed for either of the cases, and in both cases a steep onset of errors occurred, after 0.5 kGy(Si) for the 6 MV case (at 6.7 Gy(Si)/min) and 0.75 kGy(Si) for the 6 MeV case (at 4.5 Gy(Si)/min), as shown in Figure 21. In the figure only the power-law increase of the error rate is observed. The suspected cause for the stuck bits due to SEE are particle collisions involving a large transfer of energy to the target device, at a sensitive location in the device, creating displacement damage clusters where the stored charge on the memory cell can leak out, i.e., SPDDs. The high-energy electrons are then able to induce such displacement damage clusters through interactions with PKAs, while the lower energy electrons and photon beams can not create energetic enough PKAs.

The cumulative radiation damage leading to that the error rate increases as a power law function could in principle occur due to either DDD or TID. In the DDD process the accumulation of smaller defect centers over the irradiation runs could occur, and in the TID process the radiation effects would originate from the accumulation of charges in the oxides present around the memory cells, such as in STIs, as well as the increase of interface states and defects at the border regions between the silicon and the insulators. The likely dominant effect for the cumulative radiation effects should in this case come from TID. The retention time decrease of many of the cells after long annealing times observed in Figure 20 for the bits with long retention times, could then be explained by the slow migration of charges in the oxides. As they reach and get trapped in interface regions, they can negatively affect the retention capabilities of the bits. Also po-

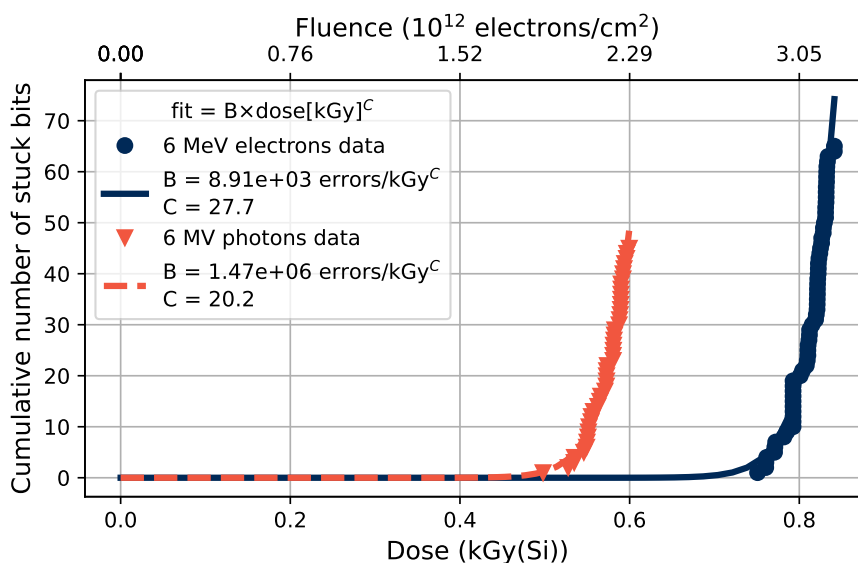


FIGURE 21 The induced stuck bits from 6 MeV electron and 6 MV photon beams, together with fits to the data to a power law function. The data for the 6 MV photon beam is only related to the bottom axis and deposited dose, while the scales of both dose and fluence apply to the 6 MeV electron data. Adapted with permission from [PI] © 2021, IEEE.

tential evolution of the induced interface defects to more severe states associated with higher cell leakage currents could cause a decrease of retention times and a negative annealing trend, and vice versa for evolution towards less severe defect configurations. The similar behavior observed in Figure 21 between DUTs irradiated by 6 MV photons and 6 MeV electrons, as well as the similar power-law trends seen for higher energy electrons (e.g. the 123 MeV electrons in Figure 17a) speak for a TID origin of the cumulative effects. The dose rates used for the DUTs shown in Figures 17a and 21 were rather similar, where the photon-irradiated DUT experienced the cumulative error onset at a similar or earlier stage than the electron-irradiated DUTs. The photons at energies primarily around 1 MeV should not be able to induce larger lattice displacements than the higher energy electrons. Irradiation by such photons results however in a low rate of recombination of generated electron-hole pairs in the presence of an electric field compared to many other radiation sources [142, 105], and thus has a strong ability to induce TID effects. However, the difference in this regard should be small compared to the electron beams, since the fraction of holes escaping recombination is fairly similar for irradiations with ^{60}Co and high-energy electrons [105].

3.3.4 ISB and cell damage from SEE

All observed stuck bits were intermittently stuck bits (ISBs), so that they were stuck over some periods of time and then were able to operate normally at other times. An example of this is shown in Figure 22. The figure shows the amount of time each stuck bit spent in its stuck state compared to in a normally func-

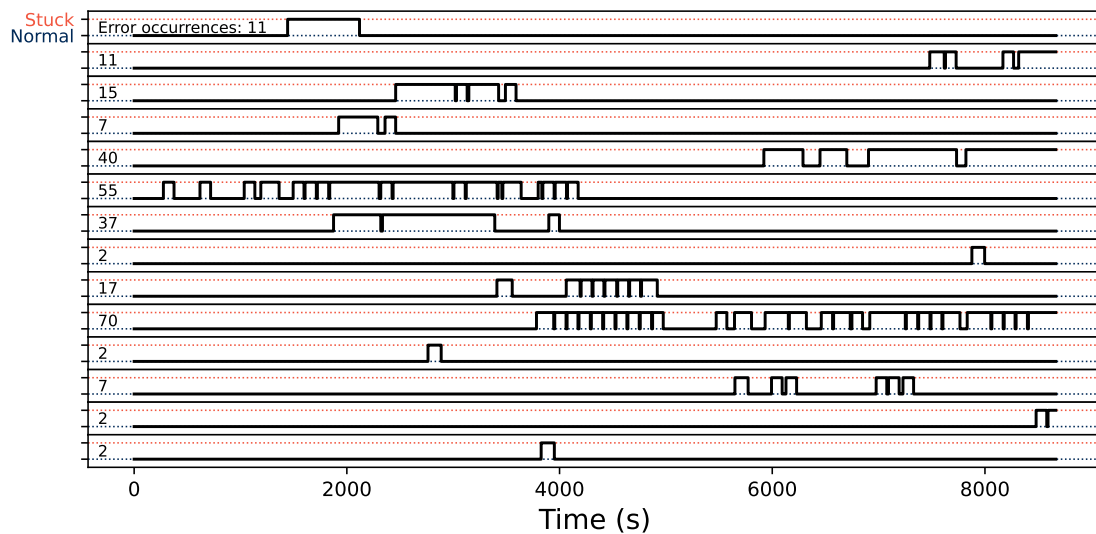


FIGURE 22 The error intermittency of the stuck bits in DUT SDF3 irradiated by 123 MeV electrons. All stuck bits were intermittently stuck, with periods during which they were stuck and other periods during which they behaved normally and returned the expected value when read. Adapted with permission from [PI] © 2021, IEEE.

tioning state in DUT SDF3 during irradiation. Each bit is represented with a line that goes up to a level representing a stuck state when errors are detected in the bit, and then goes down to the normal state when a correct reading is performed of the charged state of the bit. Since a loop of the March C- test was run during the irradiation, the memory was alternately written to its charged and discharged states, but only the ability to read back the bit value corresponding to the charged state was of interest regarding the stuck bits. Thus a correct reading of the discharged state does not make the line go down to the normal state in Figure 22. Since the definition of stuck bits in this work are bits where reoccurring errors were observed, bits with only two error occurrences would be counted as stuck. The number of error occurrences for each bit during the irradiation is written on the left side of each line in the figure, where a few of the bits were returning errors only twice.

Retention time distributions of bits that had stuck bits and bit flips as SEEs during irradiation, as well as of the full bit populations are shown in Figure 23 for DUTs of model B tested at different electron energies. The data for the figure were generated after irradiation, by the same procedure as the one described for Figure 20. Bits that had bit flips, as well as bits that were stuck during irradiation show a decrease in data retention time compared to the bits without errors. The data retention time trends in the two bit-populations that had SEEs are fairly similar to each other, and show similar degrees of degradation compared to the all-bits population. The same trend has also been shown for a different model of DRAM in [143].

The similarities between the bits with bit-flips and bits that were stuck during irradiation in terms of retention time degradation, as well as the intermittency

of the stuck bits shown in Figure 22, suggest that the mechanism causing them in this type of memory could be the same. Since there are stuck bits with only two error occurrences, the same type of event in the DUT could result also in only one error occurrence. The proposed mechanism for stuck bits by SEE in the current literature revolves around single particles creating clusters of lattice displacement in a sensitive region of the memory cell as an SPDDE. This lattice damage structure can be more or less stable, so that stuck bits can anneal and disappear. The cluster could also evolve between different configurations through e.g. thermal excitations, which may cause varying leakage currents from the memory cells and thus variations in the data retention times leading to intermittently stuck bits [111, 112].

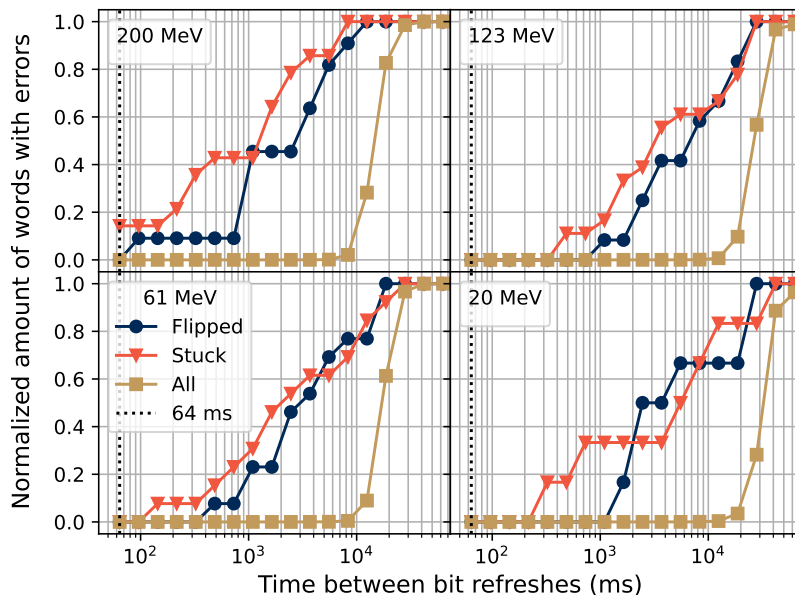


FIGURE 23 Retention time distributions of bits which had SEE in the form of stuck bits and bit flips in the irradiated DUTs, compared to the retention time population of the full bit population in the respective DUTs. Adapted with permission from [PI] © 2021, IEEE.

3.3.5 SEE in the Jovian environment

The Jovian electron environment shown in Figure 5 can be compared to the cross sections in Figure 18 to estimate the number of SEEs the model B DUT would experience due to the electron radiation if it flew on the JUICE mission. The cross sections with the associated Weibull fits are shown together with the electron energy spectrum in Figure 24. In the figure is also shown the resulting electron spectrum after it has been transported through 15 mm Al, simulating the material of a spacecraft wall. The transported electron fluence was simulated using GEANT4.

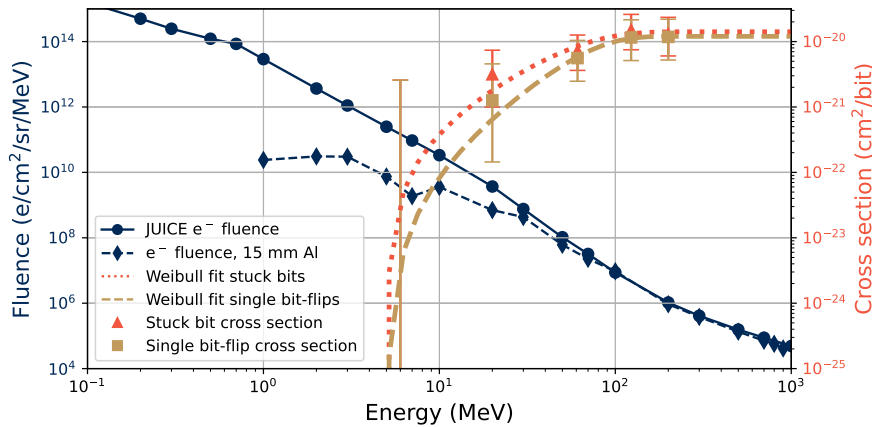


FIGURE 24 The electron fluence encountered by JUICE, along with the transported fluence through 15 mm Al, is shown together with the electron SEE cross sections of SDRAM model B as a function of electron energy. Adapted with permission from [PI] © 2021, IEEE.

The DUTs were only tested at normal incidence angle, so when calculating the expected number of SEEs the differential fluence was multiplied with 4π , approximating an isotropic fluence as well as an isotropic device response. Folding the resulting fluence between the cutoff energy of the Weibull fit and the maximum energy in the fluence spectrum 1 GeV, results in the estimated number of stuck bits and bit flips. The resulting number of SEEs is sensitive to the final fitted curve representing the cross-section data, where variations in the Weibull cutoff energy and the shape of the curve can yield a varying number of calculated errors. The fitting procedure was redone again for this document compared to the presented values in [PI] where a corresponding table to Table 6 is shown with slightly different values presented. The largest difference between the two is the non-shielded stuck bits which in [PI] was calculated to be 2.7 instead of 1.7.

TABLE 6 Estimated amount of electron-induced SEE in SDRAM model B in flight on the 11 year JUICE mission.

Error type	Errors without shielding	With 15 mm Al shielding
Stuck bits	1.7	0.5
Bit flips	0.6	0.2
Total	2.2	0.7

There is also a large expected TID associated with the electron fluence. The TID during the JUICE mission is in [37] expected to be around 2.3 kGy(Si) using a shielding of 10 mm Al, and 1.2 kGy(Si) when using 14 mm Al, with the majority of the dose originating from the electron environment. In Figure 19, the lowest tested average dose rate was 4.1 Gy(Si)/min, while the average dose rate of the 11 year JUICE mission would be 0.39 mGy(Si)/min and 0.21 mGy(Si)/min for the 10 and 14 mm cases respectively. The much lower dose rates in flight

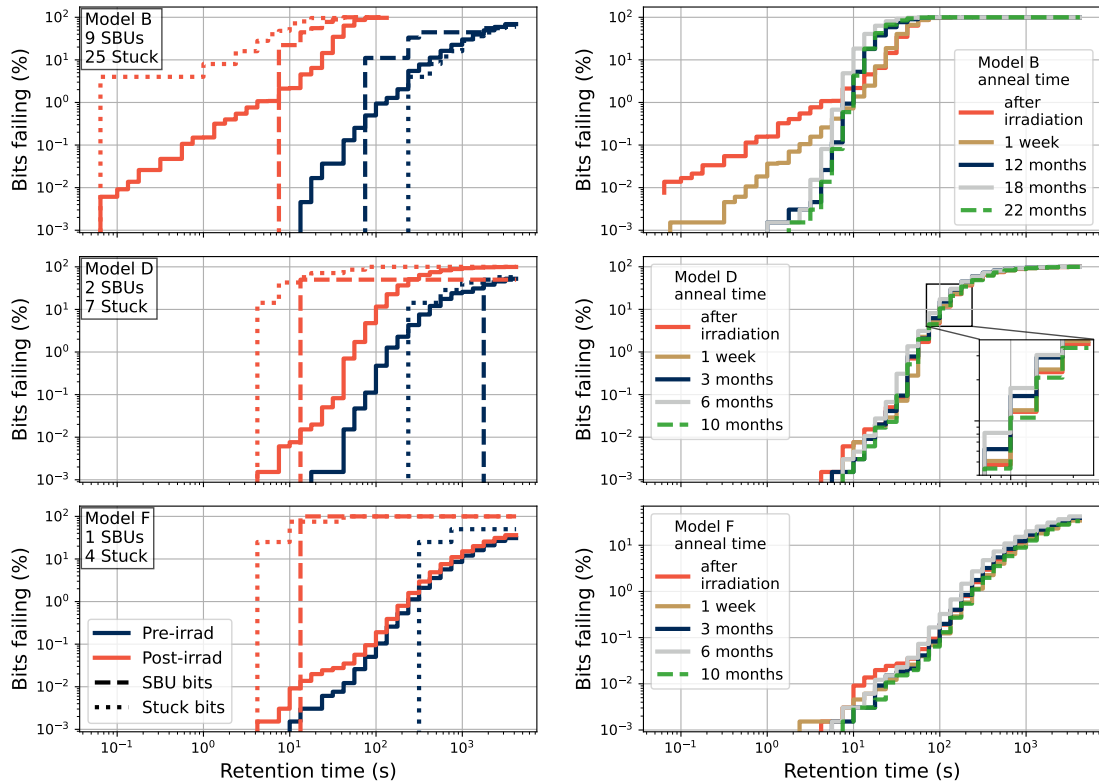
compared to the tested cases might cause the cumulative effects of the electron radiation to be different than described here, and likely much less severe.

The low error cross section for SEEs caused by electrons of the DUTs, and the number of errors estimated in Table 6, show that these types of events are likely not a big issue in flight. The cumulative radiation effects could instead be a larger issue, affecting the whole bit array and potentially causing multiple stuck bits at the TID levels encountered during the mission, but low dose-rate tests would be needed to be performed for better estimations of the in-flight TID behavior.

3.4 Proton-induced retention-time degradation

For the tests conducted with 52 MeV protons at RADEF, a part of the memory array was characterized in detail in terms of the retention time of the bits before and after irradiation. A memory portion of 128 kb was used, and the irradiation of the DUTs was performed under a lowered refresh frequency to increase the SEE cross sections. Each bit was refreshed every 8 s (much longer than the nominal value of 64 ms), and no errors were observed in the memory portion before irradiation at this refresh interval. The data pattern AA_h (hexadecimal 'AA', corresponding to '1010' repeated over the memory portion) was used for all tests, during irradiation and for characterization. Half of the used bits were in the charged state using this pattern, so effectively 64 kb were tested for and susceptible to stuck bits. One sample of each SDRAM model from Table 4 was irradiated, and the retention time distributions of the memory arrays before and after irradiation between the nominal refresh time interval of 64 ms up to around 4.3×10^3 s are shown in Figure 25a. During irradiation, the test pattern (AA_h) was read and rewritten every 60 s. The DUT of model B was irradiated first, until a power-law increase of the error rate was observed, along the same trends as presented in Figure 17. The total proton fluence on the DUT was $5 \times 10^{11} \text{ cm}^{-2}$, and the following two DUTs of models D and F were irradiated up to the same fluence, to compare the responses of the three DUTs. No error rate increase was observed in models D or F.

In Figure 25a are also shown the retention time distributions of the populations of bits which had SEE during irradiation, with the number of detected stuck bits (at the tested refresh frequency) and bit flips (SBUs) displayed in the figure frames. A shift to shorter retention times is seen for all three DUTs, with the largest effect seen in the model B DUT and the smallest in the model F DUT. The bits with SEEs during irradiation had large retention-time shifts towards shorter retention times after irradiation, but the bits which had SEEs did not necessarily have the shortest retention times of the tested memory portion before irradiation. This makes a pre-irradiation screening process very difficult to put in place to identify the most sensitive bits to SEE. The retention time distributions of the bits which became stuck during irradiation are shown as dotted lines in blue as they were before irradiation and in orange after irradiation. The same is shown for



(a) Retention times before and after irradiation. (b) Retention times after various times of annealing in room temperature. The retention time of the bits with SEE during irradiation is shown specifically as well, both before and after irradiation.

FIGURE 25 The cumulative retention time distributions in 128 kb of the three different irradiated SDRAM models irradiated by a proton fluence of $5 \times 10^{11} \text{ cm}^{-2}$. Some of the data shown in the figures are also presented in [PII].

the bits with bit flips (SBU) with dashed lines. The one bit with an SBU during irradiation of the model F DUT had longer retention time before irradiation than the maximum tested value, so the blue dashed line is missing in Figure 25a for model F.

General shifts of the full tested cell populations toward shorter retention times are seen in Figure 25, most notably for the model B DUT but also clearly for the DUT of model D. This is not clearly observed for the model F DUT, except for an increase of cells with shorter retention times (below 100 s). Relating this to the device cell structures shown in Figure 15, there are more and larger insulating structures present around the storage capacitor and access transistor regions for models D and B compared to F. Deposition of TID in these insulating structures can affect the cell operation by the accumulation of parasitic charges close to the locations of the cell charge storage and the conducting path to the bit line, causing cumulative effects on the full cell populations.

The time evolution of the retention time distributions after the irradiation is presented for the irradiated DUTs in Figure 25b. No drastic changes are seen for the DUTs of models D and F, where the model D device retention time dis-

tribution stayed close to the distribution seen directly after irradiation. For the model F DUT the retention time decrease observed around 10 s after irradiation was seen to anneal, and the distribution was approaching the pre-irradiation distribution. The same trend as was seen for electrons in Figure 20 is seen for the annealing after proton irradiation for the model B DUT. The most affected bits with the shortest retention times after irradiation are seen to anneal to longer retention times, and at the same time the bits with the longest retention times show a retention-time decrease. This creates a more vertical distribution where the bits have retention times within a fairly small range compared to the distributions of Figure 25a.

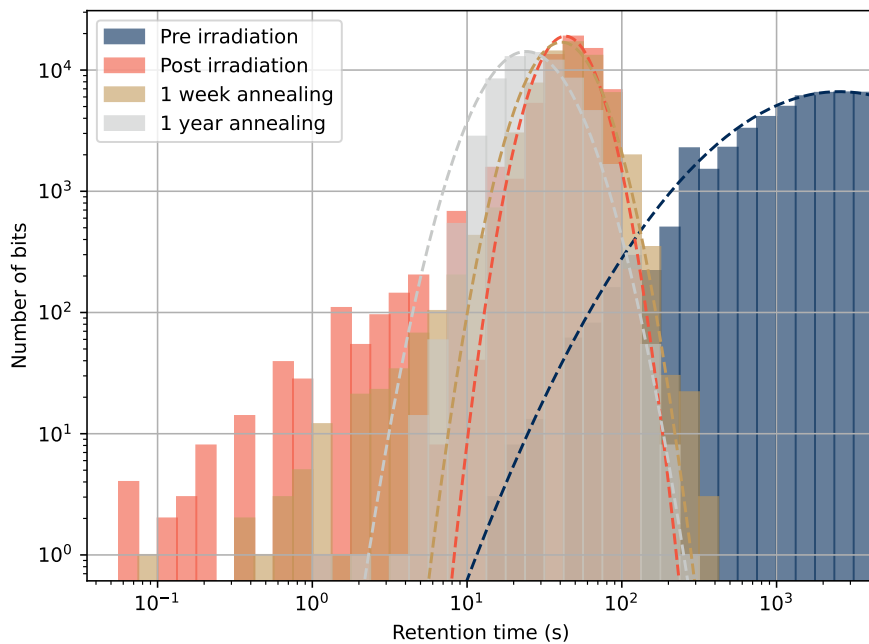


FIGURE 26 The retention times of the bits in the proton irradiated DUT of SDRAM model B. The bar heights signify the number of bits with retention times within the width of the bar.

A different view of the retention time distributions is shown in Figure 26, where the retention times of the bits in the DUT are shown in a non-cumulative plot. After 12 months of annealing, the retention times are seen to be grouped around a maximum at about 30 s. The included fits to the retention time data in Figure 26 are of lognormal distributions, fitted to the points at the top left corners of the bars in the figure. The fitted lines show the behavior of the retention times of the main part of the bits, i.e. not following the tail of bits with short retention times after irradiation. The fitted lines follow the trends of the full distributions well before irradiation, as well as after a long time of annealing after irradiation. Just after irradiation, there is a tail present of the distribution towards shorter retention times, seen also in Figure 25 for the model B DUT. This tail is seen to anneal over time, so that the distribution of retention times in the memory portion after one year of annealing is that shown in gray in Figure 26.

3.4.1 Comparison with photon irradiation

The dominance of the TID effects can be seen comparing the post-irradiation retention-time distributions of the proton irradiated DUT of model B with a DUT irradiated with photons. This is shown in Figure 27, where the retention time curve of the proton irradiated DUT is the same as the top frames in Figure 25, and representing the same data as in Figure 26 after irradiation. This is compared to a DUT irradiated by 6 MV photons up to a similar dose as that obtained during the proton irradiation. The distributions in the figure are very similar to each other, and since the displacement damage induced by the protons is considerably larger than that of the photons it seems the TID is responsible for most of the retention time degradation.

The deposited dose in Si by the proton irradiation was around 0.77 kGy(Si), and the photon irradiation was performed up to 0.80 kGy(H₂O) using the RADEF Clinac 6 MV beam with a 1.5 cm buildup layer of acrylic over the DUT. Converting the 0.80 kGy(H₂O) to dose in Si using Eq. 20 (at CPE), with values of μ_{en}/ρ from Table 3, this is estimated to be around 0.72 kGy(Si).

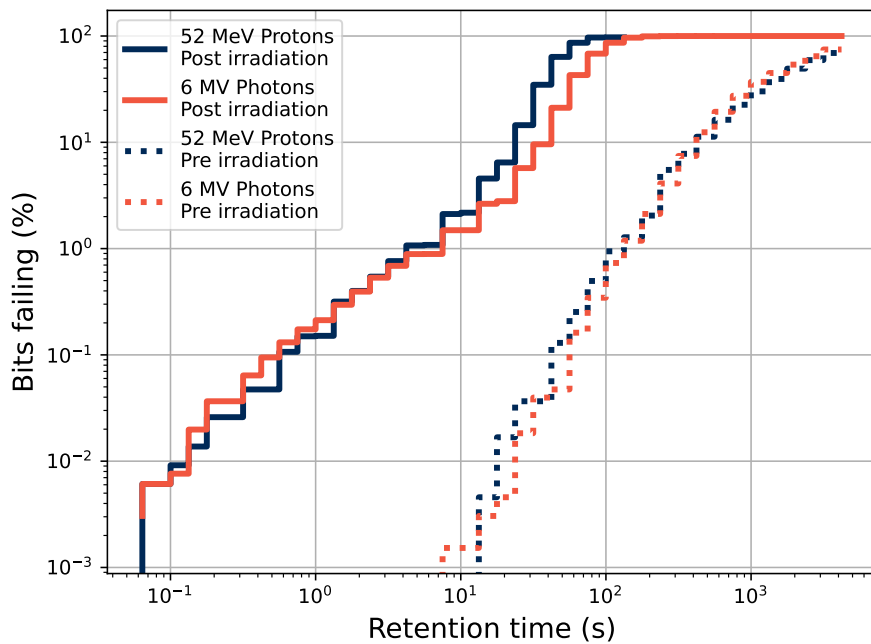


FIGURE 27 Retention time distributions post irradiation from DUTs irradiated by protons and photons up to a similar level of dose. The data shown in the figure are also presented in [PII].

4 RESULTS OF TESTS WITH FIBER-BASED DOSIMETRY SYSTEMS

4.1 Tested fibers

Silica glass rods doped with Ce^{3+} -, Cu^{+} -, and Gd^{3+} -ions were tested for use as dosimeters in the pulsed electron beams of the RADEF Clinac, described in Section 2.5.1. The tested rods were 1 cm long with a diameter of 0.5 mm, and fusion spliced to 5 m long, 0.5 mm wide pure silica core optical fibers used to transport the RIE from the irradiation area for detection. The samples are listed in Table 7 along with their dopant concentrations. The fabrication of the tested samples was not part of this work, nor was the development of the fabrication procedure. Further information on the samples and the fabrication process of them can be found in e.g. [PIII, PIV, 144, 145].

TABLE 7 The three tested fiber samples. The table data is also presented in [PIII].

Sample	Dopant	Concentration (wt%)
Ce-rod	Ce^{3+}	0.07
Cu-rod	Cu^{+}	0.07
Gd-rod	Gd^{3+}	0.1

4.2 Emission spectra of the RIL

Each dopant from Table 7 in the silica matrix has its associated characteristic emission bands under excitation by ionizing radiation. These emissions are shown in Figure 28 under excitation by the 20 MeV electron beam, detected utilizing an Ocean Optics USB2000+ UV-VIS-ER spectrometer [146] for light detection at the end of the transport fibers.

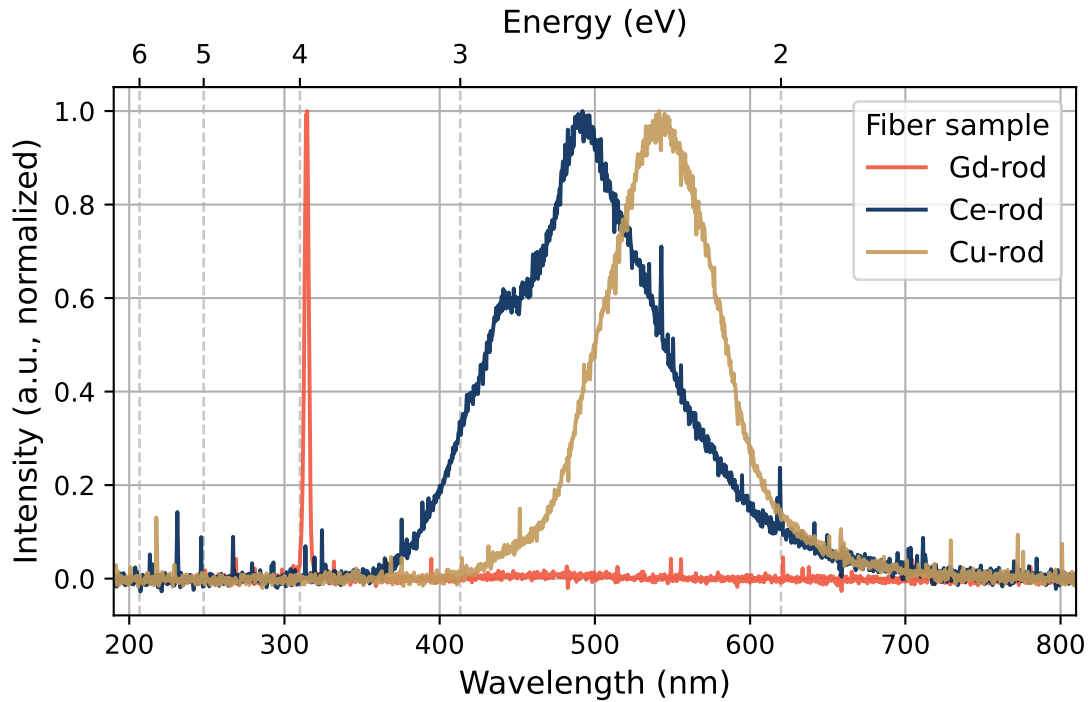


FIGURE 28 The emission spectra of the three tested samples under excitation by 20 MeV electrons, where the peak heights have been normalized to one. Adapted from [PIII] under the license CC BY 4.0.

The observed emission bands agree with those presented in Table 1, with the Gd^{3+} -emission peaking narrowly around 314 nm (3.95 eV) [98], the Ce^{3+} -emission having peaks around 440 nm (2.8 eV) and 490 nm (2.5 eV) [89, 85], and the wide Cu^{+} -emission being centered around 543 nm (2.3 eV) [90].

4.3 Dosimetry of pulsed electron beams

The capabilities of the fiber-based dosimeters to measure dose in pulsed electron beams were tested by varying the dose delivered per electron bunch by the Clinac, and detecting the pulses of RIE by the samples under irradiation. The method of varying the Clinac electron bunch doses is described in Section 2.5.1, and in detail in [PIII], using a different mode of operation than normally used in Clinacs.

4.3.1 Experimental setup and method

The experimental setup that was used is also described in detail in [PIII], and will only be described briefly here. The RIE of the tested samples was directed to a photomultiplier tube (PMT) away from the irradiation area by the transport fiber. The PMT was a Hamamatsu H9305-13 [147], and it was encased in a dark

aluminium casing to shield the system from parasitic light. Also the sample and transport fiber was enclosed and shielded from outside light by a thin black plastic tube. The PMT output signal was sent to an oscilloscope with $1\text{ M}\Omega$ input impedance, and all tests described in this chapter were performed at room temperature. The data analysis and visualization were performed using Python code.

For each of the tested settings of dose per electron bunch, a fixed dose corresponding to circa 30 s of irradiation was delivered to the sample, and the PMT signal during irradiation was recorded on the oscilloscope. Two different bunch frequencies were used, at around 200 Hz and 20 Hz, where the higher frequency was used for the cases with a dose per electron bunch lower than around 1 mGy. An example of a part of a recorded run can be seen in Figure 29, where also the height and area of the recorded pulses are visualized. The height and area integration of the pulses were done relative to the zero-level shown in the figure inset, calculated immediately before each new pulse.

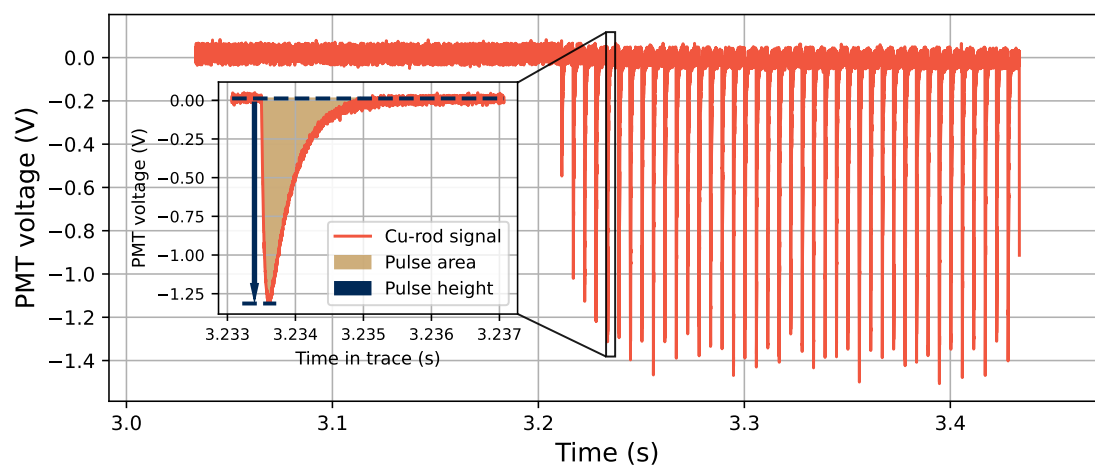


FIGURE 29 An example of the start of a recorded trace of RIL pulses in an oscilloscope. The figure shows the case of the Cu-rod under 20 MeV electrons at a dose rate of 5 Gy/min and a bunch frequency of around 200 Hz. The figure inset shows a schematic view of the calculations of pulse height and pulse area. The variations of these properties of the output pulses were compared to variations of the dose per electron bunches.

4.3.2 Dose per electron bunch measurement

All detected pulses recorded in the oscilloscope for each run were characterized in terms of their height and area. The average values of these parameters were compared to the average dose per electron bunch, which is shown in Figure 30a for the pulse height and Figure 30b for the pulse area. The error bars in the y-axis direction are the standard deviation of the pulse parameters, while the error bars in the x-axis direction are 10 % of the measured average dose per bunch value. In Figure 30c, the total integrated oscilloscope trace area is plotted against the total run dose.

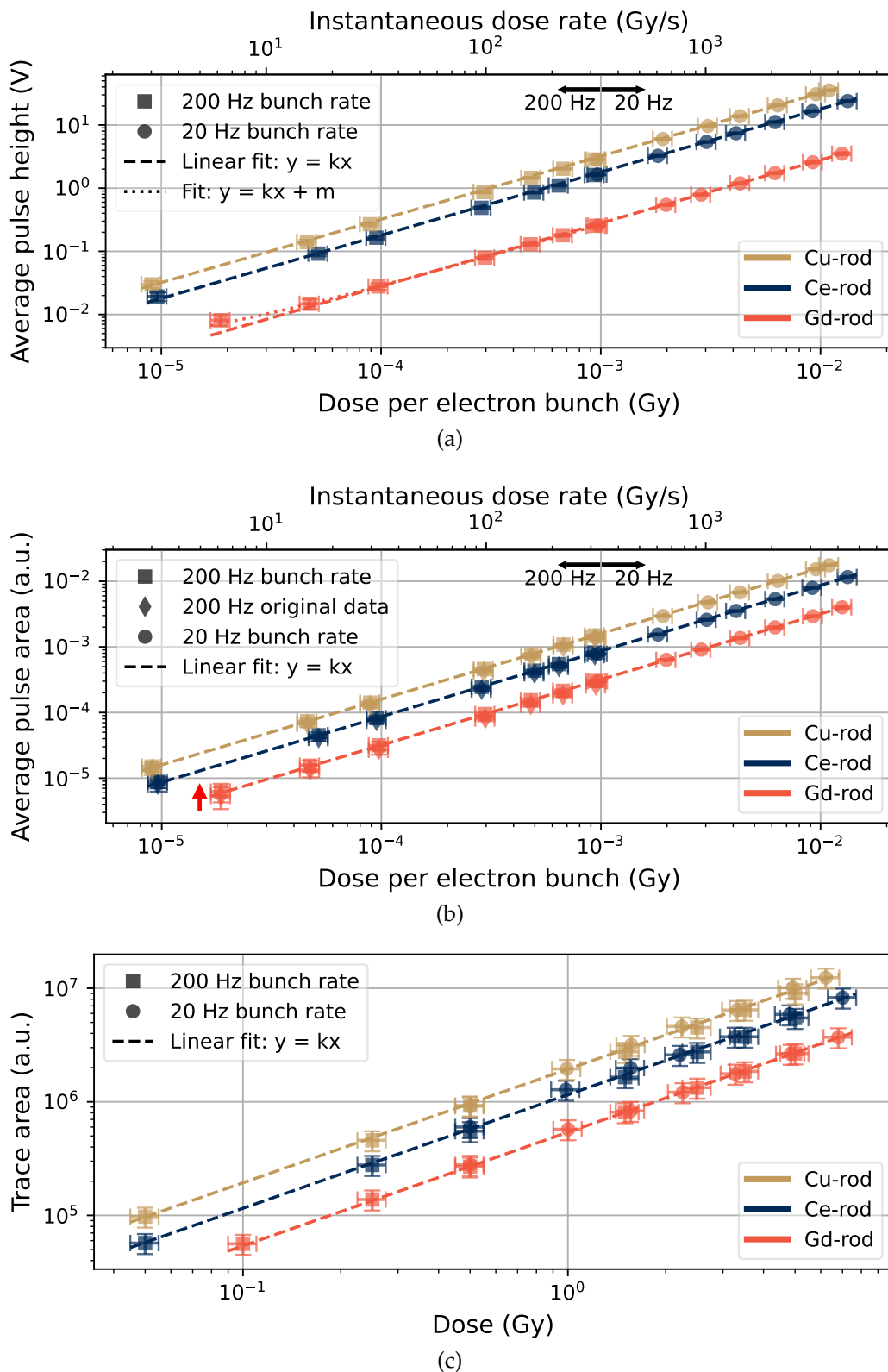


FIGURE 30 The linearities of the recorded light-emission pulses from the doped silica rods as a function of dose per electron bunch are shown for the pulse height (a) and pulse area (b), as well as the integrated area of the total collected trace in the oscilloscope as a function of the run dose (c). The average values of the pulse parameters are used, where the y-axis error bars are the standard deviations of the parameters, and the x-axis error bars are 10% of the estimated dose value. Adapted from [PIII] under the license CC BY 4.0.

All data in Figure 30 are from irradiation by a 20 MeV electron beam at a normal incidence angle, without any dose buildup layers present above the samples. The dose values that are presented are not the deposited dose in the silica, instead the samples were irradiated by a fluence of 20 MeV electrons which correspond to the given dose at maximum dose depth in water. The data points at a dose per bunch close to 1 mGy are overlapping points from frequencies of both 20 and 200 Hz.

For the case of the pulse heights shown in Figure 30a, there is a good linearity observed for the Ce and Cu rods for electron bunch doses between about 10^{-5} Gy and 10^{-2} Gy. For the case of the Gd-rod, the pulse heights are considerably smaller than the other samples, and for the lowest dose per pulse the noise level in the recorded signal starts to affect the pulse-height measurement. The point at the lowest dose per bunch for the Gd sample is because of this above the linear fit line, and a fit containing an added constant representing the noise level of the system is able to better follow the trend of the full data set.

The trends of the pulse areas versus the dose per pulse in Figure 30b show also a good linearity. This is expected since the pulse shapes of the signals from the samples at the different tested dose per pulse values are constant, and the pulse heights show a good linearity. The noise level of the detected signal does not have the same effect as in Figure 30a, since the noise is symmetric around the signal level and cancels out during the integration. Instead the pulse area linearity is affected by the change of the bunch frequency, and the figure shows the 200 Hz data shifted upwards by a constant to fit with the trend of the 20 Hz data. The unshifted original data points are shown as diamond markers visible at the lower edge of the square 200 Hz markers. The shifting is due to the long decay times of the collected pulses caused by the large input impedance of the oscilloscope, where during a high bunch frequency the signal level does not have sufficient time to decay down to the original zero level, and the new pulse is located on the tail of the previous pulse. The calculated pulse areas are in these cases slightly below the linear trend of the low frequency bunch data. This effect is the biggest for the Gd-rod, since the decay time of the Gd^{3+} -luminescence is considerably longer than that of the Ce^{3+} and Cu^{+} -ions as seen from the listed luminescence decay times in Table 1.

The full dose of the measurement runs are compared to the total integrated recorded trace areas in Figure 30c. These show a linear relationship over the tested range from a few cGy to around 7 Gy. The luminescence of all three samples is thus able to represent the dose delivered by the pulsed Clinac beam for different amounts of dose per pulse.

4.4 Dose depth curves of electron beams

4.4.1 Oscilloscope-based acquisition setup from Section 4.3

All tests of Figure 30 were performed under the same conditions, with the 20 MeV electron beam at a normal angle. Using the oscilloscope-based setup as was described in Section 4.3.1, the Gd-rod sample was also irradiated at various depths in water. The ability to measure dose accurately in water is important for dosimetry in clinical environments, since a water phantom can be used to simulate the dose depth behavior in a human body. The recorded pulse heights of the Gd-rod as a function of depth in water under irradiation by 20 MeV electrons are shown in Figure 31, together with the dose measured by an IBA PPC40 dosimeter ([135]) for reference.

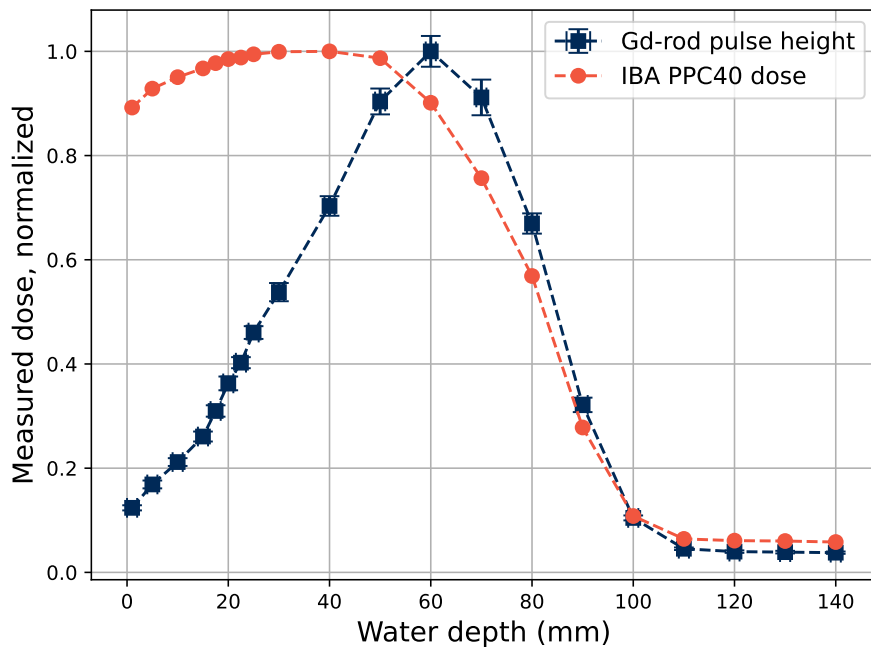


FIGURE 31 Dose depth curve measured with an IBA PPC40 reference dosimeter, along with the recorded pulse heights of the luminescence from the Gd-rod as a function of depth in water for 20 MeV electrons.

In this case the recorded pulse heights of the Gd-rod luminescence are not able to follow the curve of the deposited dose, and the initial relative pulse height at the water surface is considerably below the surface dose measured by the reference dosimeter. A closer look at the recorded peak shapes of the data in Figure 31 is shown in Figure 32. This reveals a varying pulse shape with increasing water depth, where the average pulses of the 30 s irradiation at each tested depth are shown. The pulse shape at the water surface shows a relatively larger signal tail than what is seen as the water depth increases. This suggests an increase of the prompt signal component relative to the luminescence tail as the water depth increases, caused by an increase of Cherenkov radiation at larger water depths. The

scattering of the electron beam increases as the water depth increases, which lead to more electrons traversing the sample at larger angles. This causes an increase of the generation of Cherenkov radiation along the direction of the sample and transport fiber. The shape of the Gd-rod pulse height curve in Figure 31 is very similar to previously measured curves of Cherenkov radiation measurements using optical fibers in water, e.g. in [148], which suggests that Cherenkov radiation is the cause of the luminescence profile seen in Figure 31.

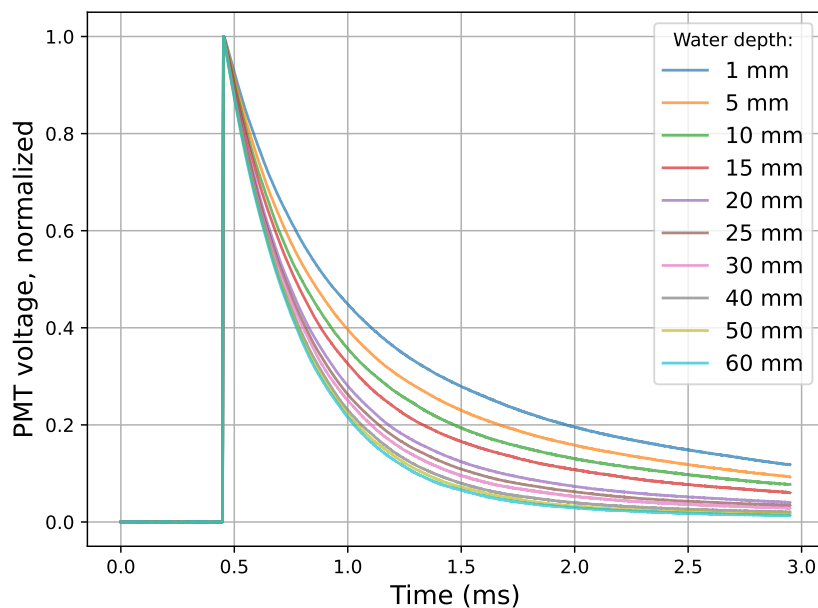


FIGURE 32 Shapes of the Gd-rod pulses in the oscilloscope as a function of depth in water under irradiation by 20 MeV electrons. The peaks are seen to get sharper as the water depth increases, with smaller pulse tails relative to the peak height.

4.4.2 Separating emission components using a monochromator

To separate and further analyze the different components of the RIE, a monochromator setup was used. This allowed narrow wavelength bands of the RIE to be investigated separately. At the end of the transport fiber, a pair of aspheric lenses were used to focus the light emission from the sample onto the end of a guide fiber bundle used as the monochromator input light guide. The monochromator was of Fastie-Ebert type with a focal length of 996 mm, and is described in further detail in [149, 150]. The transmitted light emission was detected using a R9880U-110 PMT [151], where the resulting light spectrum segment had an FWHM of about 3.5 nm.

The signal from the PMT was recorded using the digitizer module CAEN N6751 [152], in which a sampling interval of 0.5 ns in traces with lengths of up to 1 ms was used. Parallel to the sample in the beam window was a Si diode detector, which was used to generate an acquisition trigger signal to the digitizer. The resulting PMT signal of each electron bunch was saved as a digitized trace

using this procedure, each in the same time frame relative to the electron bunch. Details of this experimental setup is described in [PIV].

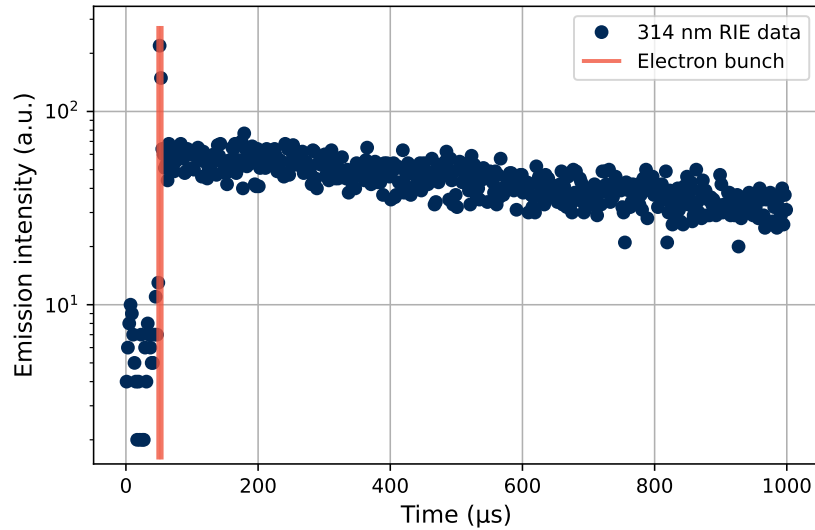


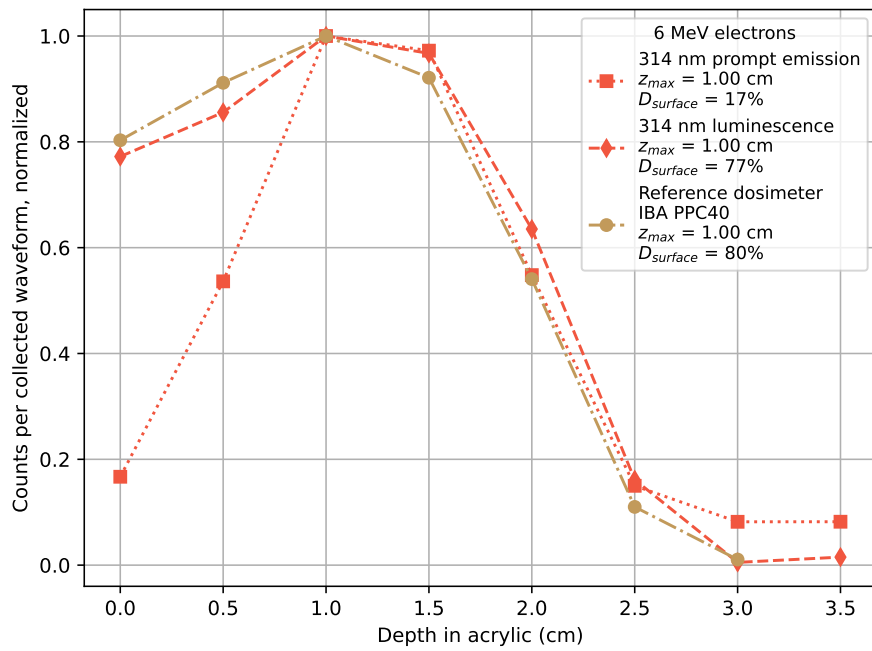
FIGURE 33 The RIE at 314 nm of the Gd-rod under irradiation by 20 MeV electrons over time relative to the 3 μs long electron bunch. Adapted from [PIV] under the license CC BY 4.0.

The time of each detected light quantum in the PMT after the RIE passed through the monochromator was recorded, and the light intensity over time in relation to the electron bunch position can be visualized through histograms, as is done in Figure 33 with the monochromator set to 314 nm. The time of the electron bunch is shown by orange lines, showing a prompt emission response during the electron bunch, followed by a long luminescence tail composed by the slow Gd^{3+} decay at 314 nm. A short period of time before the electron bunch is also included as an estimation and visualization of the noise level.

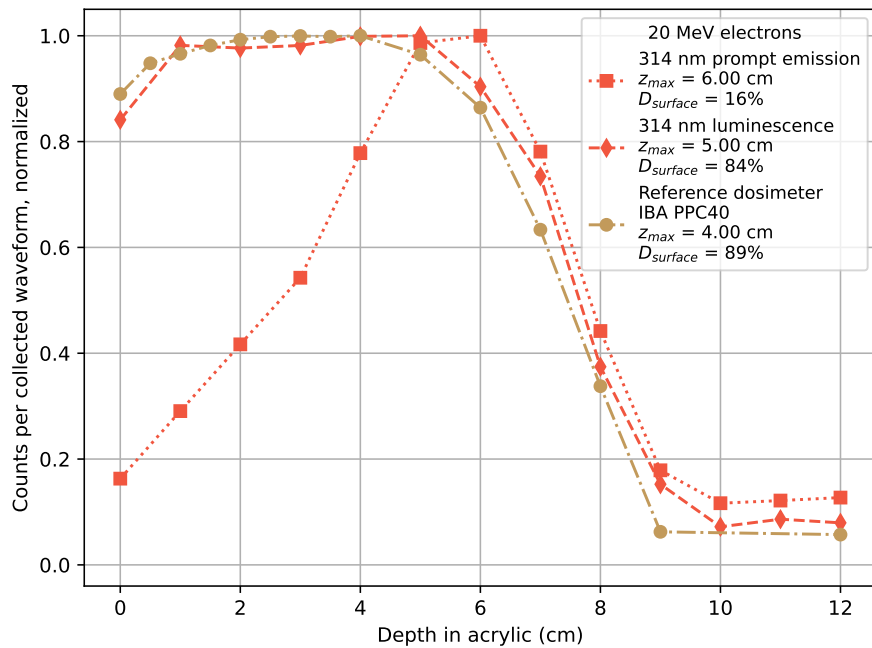
The detected light emissions as exemplified in Figure 33 can then be separated in prompt emissions during the electron bunch, and luminescence after the electron bunch. Investigating dose depth curves in an acrylic phantom using these two separated emission components results in the curves seen in Figure 34. Data using electron beams of 6 MeV and 20 MeV are shown in Figures 34a and 34b respectively. The prompt emission curves are similar to the results shown in Figure 31. They are caused by the induced Cherenkov radiation, while the luminescence components follow the shapes of the reference dosimeter curves.

In the figure legends the quantities z_{max} and $D_{surface}$ are also shown for each curve. These values signify the depth of the signal maximum, z_{max} , and the fraction of the signal at the water surface (at 0 cm depth) and the signal at the depth z_{max} .

Data at different depths of acrylic were also obtained using a spectrometer in addition to the monochromator setup, using the same spectrometer system as described in Section 4.2. The RIL signal can in this case be separated from the Cherenkov background using the emission spectrum. An example of the



(a)



(b)

FIGURE 34 Dose depth measurements of electron beams in acrylic for the electron energies 6 MeV in a) and 20 MeV in b). The prompt and fluorescent emissions at 314 nm are shown separately in the figures. Adapted from [PIV] under the license CC BY 4.0.

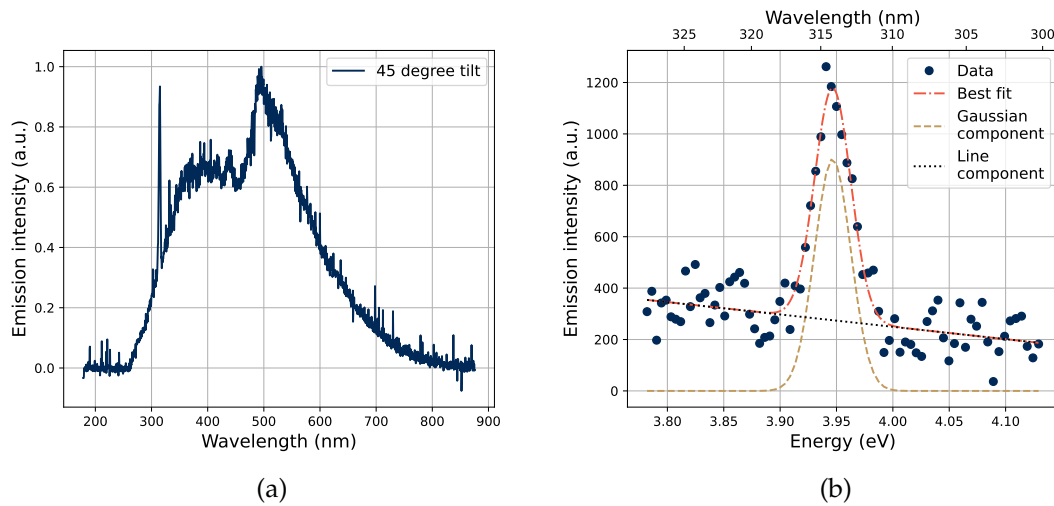


FIGURE 35 RIE spectra of the Gd-rod irradiated by 20 MeV electrons at a beam angle of 45° in a), and in b) by 12 MeV electrons at a depth of 2.5 cm in acrylic. The 314 nm luminescence peak is shown in both figures, along with a background of Cherenkov radiation. Adapted from [PIV] under the license CC BY 4.0.

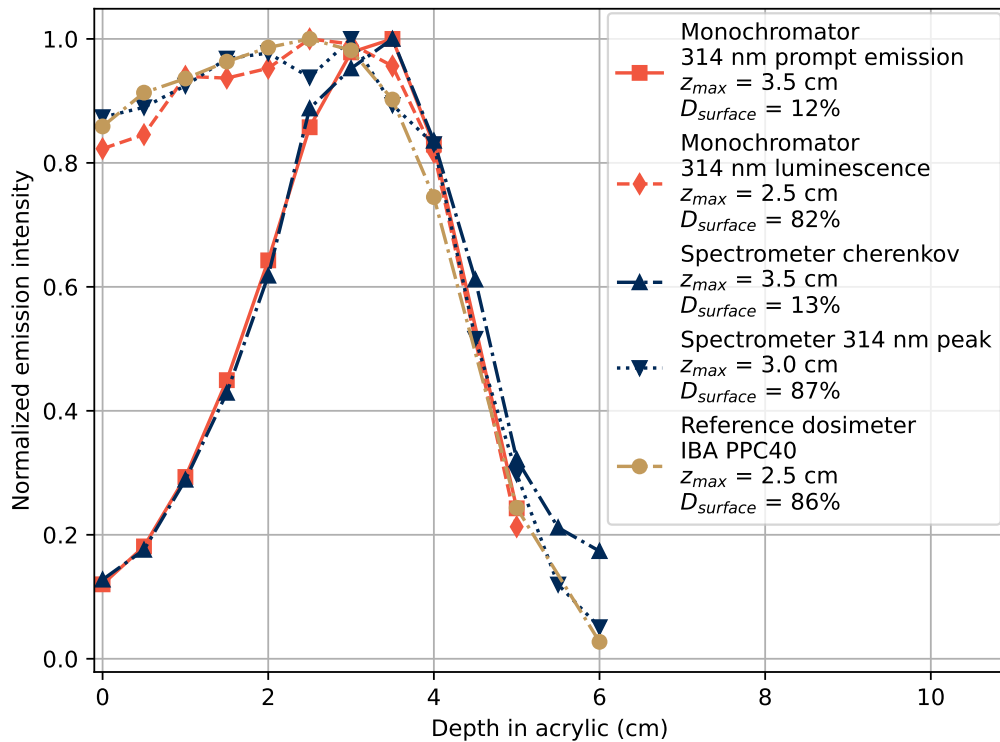


FIGURE 36 Dose depth measurements of a 12 MeV electron beam in acrylic. Prompt and fluorescent emissions at 314 nm measured using the monochromator setup are shown, as well as the 314 nm RIL peak along with the total integrated Cherenkov emission measured using the spectrometer. Adapted from [PIV] under the license CC BY 4.0.

emission spectrum containing a considerable amount of Cherenkov radiation is shown in Figure 35a, which was measured by tilting the electron beam in relation to the sample. In this case the beam was tilted 45° compared to the normal incidence angle to increase the amount of Cherenkov radiation transported through the fiber. The RIL peak at 314 nm is still clearly visible, but the spectrum is dominated by the Cherenkov radiation. The 314 nm peak can be separated from the Cherenkov background by the procedure visualized in Figure 35b, where the RIL peak at 314 nm was fitted with a Gaussian and the Cherenkov background in a narrow region around the 314 nm emission line was fitted by a straight line.

The dose depth curve for 12 MeV electrons in acrylic is shown in Figure 36, with the prompt and luminescence component at 314 nm obtained by the monochromator setup as was done also in Figure 34, but also with the separated RIL and Cherenkov components from data measured using the spectrometer. The extracted Gd^{3+} -luminescence from both acquisition methods capture the shape of the dose depth profile measured by the reference dosimeter well.

4.5 Luminescence properties of Gd^{3+} -doped silica

Data in the form shown in Figure 33 can be used to calculate the decay time of the luminescence. A fitted exponential decay curve is presented in Figure 37a, where the function

$$I(t) = Ae^{-t/\tau} + C \quad (29)$$

describing the emission intensity as a function of time $I(t)$ with one decay time component τ was used, where A is a constant describing the intensity amplitude, and C is a constant describing the background intensity. The resulting fitted decay time τ is here 1.3 ms, similar to previously reported values [98]. The decay curves show however a tendency to have an increase in luminescence intensity shortly after the electron bunch. A fit taking this effect into account with a term added for a signal buildup according to

$$I(t) = A \left(e^{-t/\tau_1} - e^{-t/\tau_2} \right) + C \quad (30)$$

is presented in Figure 37b, where τ_2 signifies the time constant of the signal increase early after the electron bunch and τ_1 describes the luminescence decay time.

Fits on the form of Eq. 30 were performed for the electron energies 6, 12 and 20 MeV, at the various tested depths of acrylic. The fitted values of τ_1 and τ_2 were similar to each other across the energies and depths, and the averages of the fitted values at various depths of acrylic for each energy are listed in Table 8. The estimated standard deviation of the averages shown in Table 8 in parentheses are

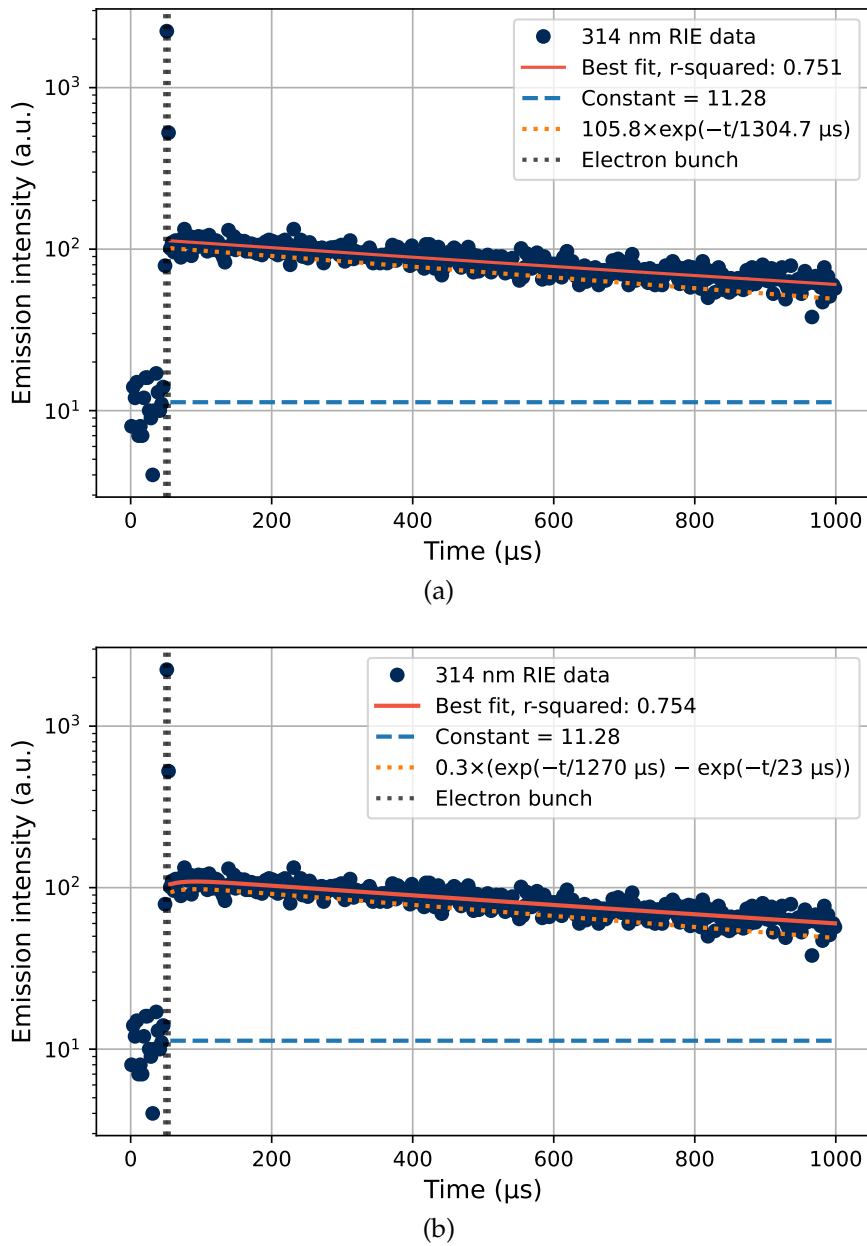


FIGURE 37 The luminescence decay of the Gd-rod under irradiation by 20 MeV electrons at a depth of 5 cm of acrylic. a) shows the decay fitted to one decay time component according to Eq. 29, while in b) the decay fit includes also a buildup term according to Eq. 30 accounting for the initial increase of luminescence observed after the electron bunch arrival. The constant background term shown by a blue dashed line is fitted to the initial noise level before the electron bunch arrival. Adapted from [PIV] under the license CC BY 4.0.

including the averages of the estimated error of each fitted decay time, based on the covariance matrix from fitting procedure.

The cause of the initial increase in luminescence after the radiation pulse can be a transient RIA phenomenon, where the high level of radiation causes a strong RIA by a modification of the material matrix, which leads to absorption bands in the silica glass. If these defects are non-permanent and decay, the RIA is transient with some decay time constant, here described by τ_2 . One type of transient effect which could have this impact at emissions around 4 eV is the STX, which is discussed further in Section 4.5.1.

TABLE 8 RIL decay times of Gd^{3+} -doped silica at 314 nm with time constants fitted according to Eq. 30. The average of the fitted values at different depths are shown for each energy, with an estimation of the standard deviation of the average fitted value in parentheses after each value. Adapted from [PIV] under the license CC BY 4.0.

Electron energy (MeV)	RIL decay time τ_1 (μs)	RIL buildup time constant τ_2 (μs)
6	1257 (43)	22 (4)
12	1267 (44)	28 (5)
20	1257 (44)	22 (9)

4.5.1 STX decay and luminescence

The STX is a defect which has an absorption band centered at 4.2 eV, and which covers the 314 nm emission line of Gd^{3+} at 3.95 eV, as well as an absorption band at slightly higher energies, observed at 5.3 eV [80, 153, 1]. The STX centers were in [154] suggested to be formed by the rupture of a Si-O bond as an electron is excited, and the excited electron and hole pair getting trapped on the broken apart Si and O atoms respectively. A luminescent decay of the STX was observed in [153], with an emission around 2.4 eV (517 nm). This emission was there observed to exhibit a blue-shift, with slightly shorter wavelengths of the emissions as the time after the radiation pulse causing the STX formation increases, moving from around 2.05 eV towards 2.4 eV at the temperature 80 K which was used under those experiments. In [80], this luminescence was observed around 2.8 eV with a decay time at around 1 ms at temperatures below 170 K, with decreasing decay times as the temperature increased above 170 K.

In tests at RADEF, as presented in [PIV], the emission spectrum shown in Figure 38 was collected using the Gd-rod sample under 20 MeV electrons at 0° beam angle without acrylic above the sample. The irradiation conditions were similar to those when the Gd-rod spectrum in Figure 28 was collected, but in Figure 38 an emission structure around 500 nm (2.4 to 2.8 eV) is clearly visible, which is not clear in the spectrum in Figure 28. In between the spectra taken for Figure 28 and Figure 38, many experiments were conducted with a fairly large

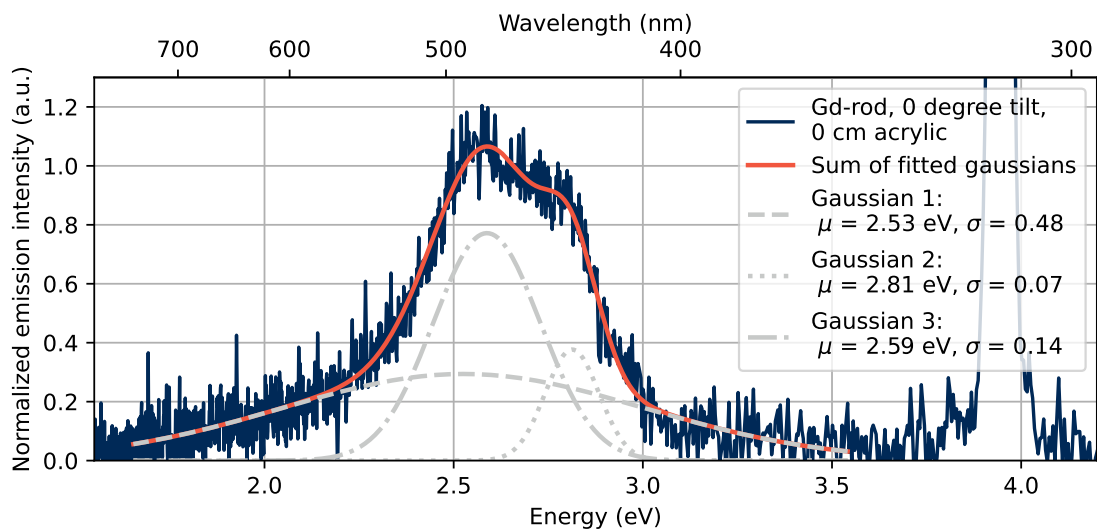


FIGURE 38 The emission spectrum of the Gd-sample under 20 MeV electron irradiation at normal incidence angle without acrylic covering the sample. The emission structure around 2.4 to 2.8 eV is fitted with a sum of three Gaussian components. The 314 nm (3.95 eV) peak has a height of around 10 in the scale of the figure for reference. Adapted from [PIV] under the license CC BY 4.0.

total dose on the sample (multiple kGy), which suggests that the visible emission structure in Figure 38 could be dependent on the dose history of the sample, and that the emissions at 2.4 to 2.8 eV increases with increasing dose history.

The transient RIA observed at 314 nm, in combination with the emissions at 2.4 to 2.8 eV shown in Figure 38 suggest a creation of STX defects in the Gd-rod during the radiation pulses. The difference between the Gd-rod emission spectra of Figures 28 and 38 suggests an evolution of the STX defect creation with dose history on the sample.

The fitted Gaussian components of the spectrum in Figure 38 are specified with their peak position μ and width parameter σ . Three components were needed to recreate the shape of the observed peak, with components centered close to 2.5, 2.6 and 2.8 eV, agreeing well with the previously reported luminescence of the STX decay. Noteworthy is however that the acquired spectrum is not corrected by the spectral response of the used setup, i.e. the transport fiber and spectrometer, so the measured spectra is not necessarily exactly the one of the material, but is convoluted by the transfer function of the parts of the measurement setup.

The decay time of the luminescence in the observed peak structure of Figure 38 was investigated in the same manner as was done in Figure 37. The monochromator was then tuned to select wavelengths within the peak, resulting in measured decay curves as exemplified in Figure 39 where the emissions around the radiation pulse at the wavelength 475 nm are shown.

The emission structure in Figure 38 was investigated under irradiation by 20 MeV electrons at a normal angle of incidence without acrylic covering the sam-

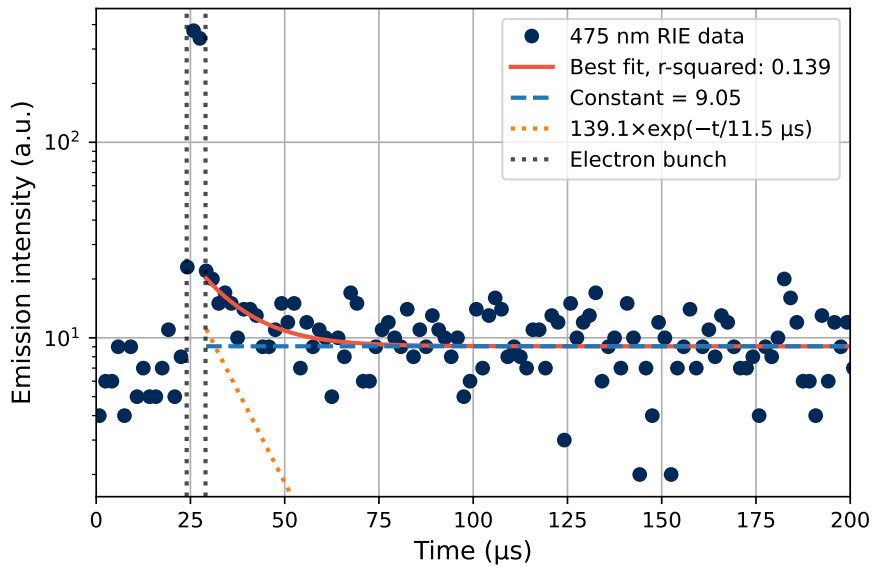


FIGURE 39 A decay time curve measured at 475 nm under irradiation by 20 MeV electrons. The data was fitted to one decay time component according to Eq. 29. Adapted from [PIV] under the license CC BY 4.0.

TABLE 9 Fitted decay time values of the luminescence after the radiation pulse at different wavelengths under irradiation by 20 MeV electrons. The values in parentheses are the estimated standard error based on the covariance matrix from the fitting procedure. Adapted from [PIV] under the license CC BY 4.0.

Wavelength (nm)	Decay Time τ (μs)
425	12.6 (3.7)
450	16.7 (3.3)
475	11.5 (3.5)
500	8.3 (2.8)

ple, and the fitted decay time parameters at the investigated wavelengths are presented in Table 9. The decay times are observed to be in the vicinity of 10 to 15 μs , where the observed decay times at the different tested wavelengths show similar results to each other. The estimated standard error at each wavelength is reported in parentheses, based on the resulting covariance matrix from the fitting procedure.

5 CONCLUSION

This thesis work contains two fairly separate topics of investigation: the topic of radiation effects on SDRAMs, and the topic of dosimetry using the RIL of doped silica glasses. The SDRAMs were initially investigated under electron beams, to observe what radiation effects were induced by high-energy electrons in the context of upcoming space missions to Jupiter and to the especially harsh electron environment found there. In those experiments, described in [PI], it was found that stuck bits could be induced by single high-energy electrons in one of the tested components. It was also found that a comparable retention time degradation was observed in bits which were stuck, and bits which had SBUs, indicating that the two fault modes were induced by a similar upset mechanism. The SDRAMs were later studied also under proton irradiation, for a more detailed investigation of the retention-time degradation induced by the irradiation that was presented in [PII]. The observed retention-time degradation was there discussed in the context of variations in the memory cell layouts between the tested component types. The observed collective degradation of retention time of the memory array caused by cumulative radiation effects was found to originate from the deposition of TID. The presented results show that also high-energy electrons when present need to be considered for potentially causing SEE and stuck bits in SDRAMs, as protons and heavy ions for a long time have been known to be capable of. For smaller technology nodes, and smaller critical charges and perturbances necessary for causing upsets, electrons might pose increasingly important threats to causing upsets in various technologies.

On the topic of optical-fiber based dosimetry, the capability of three differently doped sol-gel silica glass rods to represent the dose of a pulsed electron beam was investigated in [PIII]. The tested rods were doped with Ce^{3+} , Cu^+ , and Gd^{3+} , each exhibiting different luminescence properties. It was found that all samples could well monitor the dose on a pulse-by-pulse manner from the medical electron accelerator that was used, when the luminescence decay time and pulse frequency were taken into account. When measuring dose-depth curves of electron beams in water however, the Cherenkov radiation background needs to be considered. The RIL and Cherenkov components of the RIE were investigated

for the Gd^{3+} -doped sample in [PIV], where the two emission components could be separated using two different measurement setups. In that study it was also found that the pulsed radiation induced a transient RIA affecting the main RIL component of Gd^{3+} , which was likely caused by generation of STX centers. These results show that the tested systems are viable candidates for dosimeters to monitor pulsed electron beams, and that the RIL proportional to the deposited dose can be separated from the background Cherenkov emission providing a parasitic light emission.

Some questions are left open after these conducted studies. One is regarding the clearer appearance of the emission structure at 2.6 to 2.8 eV in the Gd^{3+} -doped sample over time, and after an increasing dose history. The evolution of this emission structure, along with that of the transient RIA observed at the main emission line at 314 nm, as a function of deposited dose in the sample should be studied, potentially also revealing further details on the formation of STX centers.

Studying retention-time distributions of the memory arrays is a powerful way of observing radiation-induced degradation of the memory performance in DRAM-type devices. Continued studies of the radiation-induced retention-time degradation on modern device technologies and under various types of radiation beams can give a good measure of how susceptible the device cells are towards specific radiation fields. These studies in combination with annealing properties of the radiation damage, also under elevated temperatures, are valuable future investigations.

REFERENCES

- [1] S. Girard, J. Kuhnenn, A. Gusarov, B. Brichard, M. van Uffelen, Y. Ouerdane, A. Boukenter, and C. Marcandella, "Radiation effects on silica-based optical fibers: Recent advances and future challenges," *IEEE Trans. Nucl. Sci.*, vol. 60, no. 3, pp. 2015–2036, Jun. 2013.
- [2] A. Fernandez Fernandez, H. Ooms, B. Brichard, M. Coeck, S. Coenen, F. Berghmans, and M. Decréton, "SCK·CEN gamma irradiation facilities for radiation tolerance assessment," in *IEEE Radiation Effects Data Workshop*, 2002, pp. 171–176, doi: 10.1109/REDW.2002.1045549.
- [3] R. García Alía, M. Brugger, F. Cerutti, S. Danzeca, A. Ferrari, S. Gilar-doni, Y. Kadi, M. Kastriotou, A. Lechner, C. Martinella, O. Stein, Y. Thurel, A. Tsinganis, and S. Uznanski, "LHC and HL-LHC: present and future radiation environment in the high-luminosity collision points and RHA implications," *IEEE Trans. Nucl. Sci.*, vol. 65, no. 1, pp. 448–456, Jan. 2018, doi: 10.1109/TNS.2017.2776107.
- [4] S. Delepine-Lesoille, S. Girard, M. Landolt, J. Bertrand, I. Planes, A. Boukenter, E. Marin, G. Humbert, S. Leparmentier, J.-L. Auguste, and Y. Ouerdane, "France's state of the art distributed optical fibre sensors qualified for the monitoring of the french underground repository for high level and intermediate level long lived radioactive wastes," *Sensors*, vol. 17, no. 6, p. 1377, 2017, doi: 10.3390/s17061377.
- [5] S. Girard, A. Morana, A. Ladaci, T. Robin, L. Mescia, J.-J. Bonnefois, M. Boutillier, J. Mekki, A. Paveau, B. Cadier, E. Marin, Y. Ouerdane, and A. Boukenter, "Recent advances in radiation-hardened fiber-based technologies for space applications," *J. Opt.*, vol. 20, no. 9, p. 093001, Aug. 2018, doi: 10.1088/2040-8986/aad271.
- [6] S. Yamamoto, T. Shikama, V. Belyakov, E. Farnum, E. Hodgson, T. Nishitani, D. Orlinski, S. Zinkle, S. Kasai, P. Stott, K. Young, V. Zaveriaev, A. Costley, L. deKock, C. Walker, and G. Janeschitz, "Impact of irradiation effects on design solutions for ITER diagnostics," *J. Nucl. Mater.*, vol. 283–287, no. 1, pp. 60–69, Nov. 2000, doi: 10.1016/S0022-3115(00)00157-4.
- [7] J. L. Bourgarde, R. Marmoret, S. Darbon, R. Rosch, P. Troussel, B. Villette, V. Glebov, W. T. Shmayda, J. C. Gomme, Y. Le Tonqueze, F. Aubard, J. Baggio, S. Bazzoli, F. Bonneau, J. Y. Boutin, T. Caillaud, C. Chollet, P. Combis, L. Disdier, J. Gazave, S. Girard, D. Gontier, P. Jaanimagi, H. P. Jacquet, J. P. Jadaud, O. Landoas, J. Legendre, J. L. Leray, R. Maroni, D. D. Meyerhofer, J. L. Miquel, F. J. Marshall, I. Masclet-Gobin, G. Pien, J. Raimbourg, C. Reverdin, A. Richard, D. Rubin de Cervens, C. T. Sangster, J. P. Seaux, G. Soullie, C. Stoeckl, I. Thfoin, L. Videau, and C. Zuber, "Diagnostics

- hardening for harsh environment in Laser Mégajoule (invited)," *Rev. Sci. Instrum.*, vol. 79, no. 10, p. 10F301, Oct. 2008, doi: 10.1063/1.2991161.
- [8] A. G. Chmielewski, M. Al-Sheikhly, A. J. Berejka, M. R. Cleland, and M. Antoniak, "Recent developments in the application of electron accelerators for polymer processing," *Rad. Phys. Chem.*, vol. 94, pp. 147–150, Jan. 2014, doi: 10.1016/j.radphyschem.2013.06.024.
- [9] M. R. Cleland, "Industrial applications of electron accelerators," in *CAS - CERN Accelerator School : small accelerators*, Zeegse, Netherlands, Jun. 2005, pp. 383–416, doi: 10.5170/CERN-2006-012.383.
- [10] J. D. Wilson, E. M. Hammond, G. S. Higgins, and K. Petersson, "Ultra-high dose rate (FLASH) radiotherapy: Silver bullet or fool's gold?" *Front. Oncol.*, vol. 9, p. 1563, Jan. 2020, doi: 10.3389/fonc.2019.01563.
- [11] J. Vidalot, C. Campanella, J. Dachicourt, C. Marcandella, O. Duhamel, A. Morana, D. Poujols, G. Assailit, M. Gaillardin, A. Boukenter, Y. Ouerdane, S. Girard, and P. Paillet, "Monitoring of ultra-high dose rate pulsed x-ray facilities with radioluminescent nitrogen-doped optical fiber," *Sensors*, vol. 22, no. 9, p. 3192, Apr. 2022, doi: 10.3390/s22093192.
- [12] *Guidelines for Industrial Radiation Sterilization of Disposable Medical Products (Cobalt-60 Gamma Irradiation)*, ser. TECDOC. Vienna, Austria: INTERNATIONAL ATOMIC ENERGY AGENCY, 1990, no. 539, available from https://inis.iaea.org/collection/NCLCollectionStore/_Public/21/042/21042969.pdf, accessed on 2023-04-18.
- [13] M. Ackermann *et al.*, "Detection of the characteristic pion-decay signature in supernova remnants," *Science*, vol. 339, no. 6121, pp. 807–811, Dec. 2012, doi: 10.1126/science.1231160.
- [14] V. F. Hess, "Über Beobachtungen der durchdringenden Strahlung bei sieben Freiballonfahrten," *Z. Phys.*, vol. 13, p. 1084, 1912.
- [15] R. A. Mewaldt, "Galactic cosmic ray composition and energy spectra," *Advances in Space Research*, vol. 14, no. 10, pp. 737–747, 1994, doi: 10.1016/0273-1177(94)90536-3.
- [16] G. Santin, P. Truscott, R. Gaillard, and R. García Alía, "Radiation environments: space, avionics, ground and below," in *Short Course notes of the European Conference on Radiation and Its Effects on Components and Systems*, Geneva, Switzerland, Oct. 2017.
- [17] The Royal Belgian Institute for Space Aeronomy (BIRA-IASB), "Space environment information system (SPENVIS)," European Space Agency (ESA), Ringlaan 3 Avenue Circulaire, 1180 Brussels, Belgium, 2022, <https://www.spennis.oma.be/>.

- [18] International Organization for Standardization, "ISO 15390:2004, space environment (natural and artificial) — galactic cosmic ray model," 2004.
- [19] M. A. Xapsos, G. P. Summers, J. L. Barth, E. G. Stassinopoulos, and E. A. Burke, "Probability model for worst case solar proton event fluences," *IEEE Trans. Nucl. Sci.*, vol. 46, no. 6, pp. 1481–1485, Dec. 1999, doi: 10.1109/23.819111.
- [20] —, "Probability model for cumulative solar proton event fluences," *IEEE Trans. Nucl. Sci.*, vol. 47, no. 3, pp. 486–490, Jun. 2000, doi: 10.1109/23.856469.
- [21] M. A. Xapsos, C. Stauffer, T. Jordan, J. L. Barth, and R. A. Mewaldt, "Model for cumulative solar heavy ion energy and linear energy transfer spectra," *IEEE Trans. Nucl. Sci.*, vol. 54, no. 6, pp. 1985–1989, Dec. 2007, doi: 10.1109/TNS.2007.910850.
- [22] P. Picozza *et al.*, "PAMELA – a payload for antimatter matter exploration and light-nuclei astrophysics," *Astropart. Phys.*, vol. 27, no. 4, pp. 296–315, Apr. 2007, doi: 10.1016/j.astropartphys.2006.12.002.
- [23] R. Munini *et al.*, "Solar modulation of GCR electrons over the 23rd solar minimum with PAMELA," *J. Phys.: Conf. Ser.*, vol. 632, no. 1, p. 012073, Jul. 2015, doi: 10.1088/1742-6596/632/1/012073.
- [24] O. Adriani *et al.*, "Time dependence of the proton flux measured by PAMELA during the 2006 July–2009 December solar minimum," *The Astrophysical Journal*, vol. 765, no. 2, p. 91, Feb. 2013, doi: 10.1088/0004-637X/765/2/91.
- [25] R. A. Mewaldt, C. M. S. Cohen, A. W. Labrador, R. A. Leske, G. M. Mason, M. I. Desai, M. D. Looper, J. E. Mazur, R. S. Selesnick, and D. K. Haggerty, "Proton, helium, and electron spectra during the large solar particle events of October–November 2003," *J. Geophys. Res.*, vol. 110, p. A09S18, 2005, doi: 10.1029/2005JA011038.
- [26] M. A. Xapsos, J. L. Barth, E. G. Stassinopoulos, S. R. Messenger, R. J. Walters, G. P. Summers, and E. A. Burke, "Characterizing solar proton energy spectra for radiation effects applications," *IEEE Trans. Nucl. Sci.*, vol. 47, no. 6, pp. 2218–2223, Dec. 2000, doi: 10.1109/23.903756.
- [27] J. L. Lovell, M. L. Duldig, and J. E. Humble, "An extended analysis of the september 1989 cosmic ray ground level enhancement," *J. Geophys. Res.*, vol. 103, no. A10, pp. 23 733–23 742, 1998, doi: 10.1029/98JA02100.
- [28] E. Stassinopoulos and J. Raymond, "The space radiation environment for electronics," *Proceedings of the IEEE*, vol. 76, no. 11, pp. 1423–1442, 1988, doi: 10.1109/5.90113.

- [29] J. A. van Allen, G. H. Ludwig, E. C. Ray, and C. E. McIlwain, "Observation of high intensity radiation by satellites 1958 alpha and gamma," *J. Jet Propulsion*, vol. 28, no. 9, pp. 588–592, 1958, doi: 10.2514/8.7396.
- [30] J. A. Van Allen, C. E. McIlwain, and G. H. Ludwig, "Radiation observations with satellite 1958 ϵ ," *J. Geophys. Res. (1896-1977)*, vol. 64, no. 3, pp. 271–286, 1959, doi: 10.1029/JZ064i003p00271.
- [31] J.-F. Ripoll, S. G. Claudepierre, A. Y. Ukhorskiy, C. Colpitts, X. Li, J. F. Fennell, and C. Crabtree, "Particle dynamics in the earth's radiation belts: Review of current research and open questions," *J. Geophys. Res. Space Physics*, vol. 125, no. 5, p. e2019JA026735, 2020, doi: 10.1029/2019JA026735.
- [32] X. Li, R. Selesnick, Q. Schiller, K. Zhao, D. N. Baker, and M. A. Temerin, "Measurement of electrons from albedo neutron decay and neutron density in near-earth space," *Nature*, vol. 552, no. 7685, pp. 382–385, Dec. 2017, doi: 10.1038/nature24642.
- [33] D. M. Sawyer and J. I. Vette, "Ap-8 trapped proton environment for solar maximum and solar minimum. [AP8MAX and AP8MIN]," National Aeronautics and Space Administration, Greenbelt, MD (USA). Goddard Space Flight Center, Tech. Rep. N-77-18983; NASA-TM-X-72605, Dec. 1976. [Online]. Available: <https://www.osti.gov/biblio/7094195>
- [34] D. N. Baker, P. J. Erickson, J. F. Fennell, J. C. Foster, A. N. Jaynes, and P. T. Verronen, "Space weather effects in the earth's radiation belts," *Space Sci. Rev.*, vol. 214, p. 17, Dec. 2017, doi: 10.1007/s11214-017-0452-7.
- [35] A. N. Jaynes, D. N. Baker, H. J. Singer, J. V. Rodriguez, T. M. Loto'aniu, A. F. Ali, S. R. Elkington, X. Li, S. G. Kanekal, S. G. Claudepierre, J. F. Fennell, W. Li, R. M. Thorne, C. A. Kletzing, H. E. Spence, and G. D. Reeves, "Source and seed populations for relativistic electrons: Their roles in radiation belt changes," *J. Geophys. Res. Space Physics*, vol. 120, no. 9, pp. 7240–7254, 2015, doi: 10.1002/2015JA021234.
- [36] T. G. Northrop and E. Teller, "Stability of the adiabatic motion of charged particles in the earth's field," *Phys. Rev.*, vol. 117, pp. 215–225, Jan. 1960, doi: 10.1103/PhysRev.117.215.
- [37] JUICE Team, "JUICE environment specification," European Space Agency (ESA)/ESTEC, Revision 5 Issue 5, Feb. 2017, reference JS-14-09.
- [38] E. Normand and T. J. Baker, "Altitude and latitude variations in avionics SEU and atmospheric neutron flux," *IEEE Trans. Nucl. Sci.*, vol. 40, no. 6, pp. 1484–1490, Dec. 1993, doi: 10.1109/23.273514.
- [39] P. Goldhagen, J. M. Clem, and J. W. Wilson, "The energy spectrum of cosmic-ray induced neutrons measured on an airplane over a wide range

- of altitude and latitude," *Radiat. Prot. Dosim.*, vol. 110, no. 1-4, pp. 387–392, Aug. 2004, doi: 10.1093/rpd/nch216.
- [40] S. N. Clucas, C. S. Dyer, and F. Lei, "The radiation in the atmosphere during major solar particle events," *Space Res.*, vol. 36, no. 9, pp. 1657–1664, Sep. 2005, doi: 10.1016/j.asr.2005.08.013.
- [41] J. L. Barth, C. S. Dyer, and E. G. Stassinopoulos, "Space, atmospheric, and terrestrial radiation environments," *IEEE Trans. Nucl. Sci.*, vol. 50, no. 3, pp. 466–482, Jun. 2003, doi: 10.1109/TNS.2003.813131.
- [42] L. Lindborg, D. Bartlett, P. Beck, I. McAulay, K. Schnuer, H. Schraube, and F. Spurny, "Cosmic radiation exposure of aircraft crew: compilation of measured and calculated data," *Radiat. Prot. Dosim.*, vol. 110, no. 1-4, pp. 417–422, Aug. 2004, doi: 10.1093/rpd/nch232.
- [43] R. Bütikofer and E. O. Flückiger, "Radiation doses along selected flight profiles during two extreme solar cosmic ray events," *Astrophys. Space Sci. Trans.*, vol. 7, no. 2, pp. 105–109, Apr. 2011, doi: 10.5194/astra-7-105-2011.
- [44] M. S. Gordon, P. Goldhagen, K. P. Rodbell, T. H. Zabel, H. H. K. Tang, J. M. Clem, and P. Bailey, "Measurement of the flux and energy spectrum of cosmic-ray induced neutrons on the ground," *IEEE Trans. Nucl. Sci.*, vol. 51, no. 6, pp. 3427–3434, Dec. 2004, doi: 10.1109/TNS.2004.839134.
- [45] M. Bagatin, A. Coniglio, M. D'Arienzo, A. De Lorenzi, S. Gerardin, A. Paccagnella, R. Pasqualotto, S. Peruzzo, and S. Sandri, "Radiation environment in the iter neutral beam injector prototype," *IEEE Trans. Nucl. Sci.*, vol. 59, no. 4, pp. 1099–1104, Aug. 2012, doi: 10.1109/TNS.2012.2187461.
- [46] K. Røed, V. Boccone, M. Brugger, A. Ferrari, D. Kramer, E. Lebbos, R. Losito, A. Mereghetti, G. Spiezia, and R. Versaci, "FLUKA simulations for SEE studies of critical LHC underground areas," *IEEE Trans. Nucl. Sci.*, vol. 58, no. 3, pp. 932–938, Jun. 2011, doi: 10.1109/TNS.2010.2097605.
- [47] A. Infantino, D. Björkman, L. Elie, M. Maietta, C. Tromel, and H. Vincke, "Radiation protection at the large hadron collider: Problematics, challenges and advanced monte carlo simulation techniques," *Environments*, vol. 9, no. 5, pp. 387–392, Apr. 2022, doi: 10.3390/environments9050054.
- [48] E. J. Axton and A. G. Bardell, "Neutron production from electron accelerators used for medical purposes," *Phys. Med. Biol.*, vol. 17, no. 2, p. 293, Dec. 1972, doi: 10.1088/0031-9155/17/2/015.
- [49] C. E. Cardenas, P. L. Nitsch, R. J. Kudchadker, R. M. Howell, and S. F. Kry, "Out-of-field doses and neutron dose equivalents for electron beams from modern Varian and Elekta linear accelerators," *J. Appl. Clin. Med. Phys.*, vol. 17, no. 4, pp. 442–455, Jul. 2016, doi: 10.1120/jacmp.v17i4.6216.

- [50] K. S. Krane, *Introductory Nuclear Physics*. 111 River Street, Hoboken, NJ 07030, USA: John Wiley & Sons, Inc., 1988.
- [51] E. B. Podgorsak *et al.*, *Radiation Oncology Physics: A Handbook for Teachers and Students*. Wagramer Strasse 5, P.O. Box 100, A-1400 Vienna, Austria: International Atomic Energy Agency (IAEA), 2005.
- [52] G. F. Knoll, *Radiation Detection and Measurement*, 4th ed. 111 River Street, Hoboken, NJ 07030-5774, USA: John Wiley & Sons, Inc., 2010.
- [53] “European component irradiation facilities cocktail calculator,” University of Jyväskylä, Online stopping power calculator tool, Nov. 2019, <http://research.jyu.fi/radef/ECIFcalc/dedx.html>.
- [54] M. J. Berger, J. S. Coursey, M. A. Zucker, and J. Chang, “Stopping-power & range tables for electrons, protons, and helium ions,” NIST, Physical Measurement Laboratory, NIST Standard Reference Database 124, Jul. 2017, doi: 10.18434/T4NC7P.
- [55] R. Hofstadter, “Nuclear and nucleon scattering of high-energy electrons,” *Annual Rev. Nucl. Sci.*, vol. 7, no. 1, pp. 231–316, Dec. 1957, doi: 10.1146/annurev.ns.07.120157.001311.
- [56] S. Agostinelli *et al.*, “GEANT4—a simulation toolkit,” *Nucl. Instrum. Methods Phys. Res. A*, vol. 506, no. 3, pp. 250–303, 2003, doi: 10.1016/S0168-9002(03)01368-8.
- [57] T. T. Böhlen, F. Cerutti, M. P. W. Chin, A. Fassò, A. Ferrari, P. G. Ortega, A. Mairani, P. R. Sala, G. Smirnov, and V. Vlachoudis, “The fluka code: Developments and challenges for high energy and medical applications,” *Nuclear Data Sheets*, vol. 120, pp. 211–214, 2014, doi: <https://doi.org/10.1016/j.nds.2014.07.049>.
- [58] D. Lucsányi, R. García Alía, K. Biłko, M. Cecchetto, S. Fiore, and E. Pirovano, “G4see: A geant4-based single event effect simulation toolkit and its validation through monoenergetic neutron measurements,” *IEEE Trans. Nucl. Sci.*, vol. 69, no. 3, pp. 273–281, Mar. 2022, doi: 10.1109/TNS.2022.3149989.
- [59] M. Tali, R. G. Alía, M. Brugger, V. Ferlet-Cavrois, R. Corsini, W. Farabolini *et al.*, “High-energy electron-induced SEUs and jovian environment impact,” *IEEE Trans. Nucl. Sci.*, vol. 64, no. 8, pp. 2016–2022, Aug. 2017, doi: 10.1109/TNS.2017.2713445.
- [60] M. Tali, “Single-event radiation effects in hardened and state-of-the-art components for space and high-energy accelerator applications,” Ph.D. dissertation, University of Jyväskylä, 2019, available: <https://jyx.jyu.fi/handle/123456789/64284>.

- [61] P. A. Čerenkov, *Dokl. Akad. Nauk. SSSR*, vol. 2, p. 451, 1934.
- [62] J. V. Jelley, "Čerenkov radiation and its applications," *Br. J. Appl. Phys.*, vol. 6, no. 7, pp. 227–232, Jul. 1955.
- [63] E. J. Hall, S. G. Martin, H. Amols, and T. K. Hei, "Photoneutrons from medical linear accelerators—radiobiological measurements and risk estimates," *Int. J. Radiation Oncology Biol. Phys.*, vol. 33, no. 1, pp. 225–230, Aug. 1995, doi: 10.1016/0360-3016(95)00092-D.
- [64] H. R. Vega-Carrillo, S. A. Martínez-Ovalle, A. M. Lallena, G. A. Mercado, and J. L. Benites-Rengifo, "Neutron and photon spectra in LINACs," *Appl. Radiat. Isot.*, vol. 71, pp. 75–80, Dec. 2012, doi: 10.1016/j.apradiso.2012.03.034.
- [65] F. Ravotti, "Dosimetry techniques and radiation test facilities for total ionizing dose testing," *IEEE Trans. Nucl. Sci.*, vol. 65, no. 8, pp. 1440–1464, Aug. 2018, doi: 10.1109/TNS.2018.2829864.
- [66] P. Bilski, "Lithium fluoride: from LiF:Mg,Ti to LiF:Mg,Cu,P," *Radiat. Prot. Dosim.*, vol. 100, no. 1-4, pp. 199–205, Jul. 2002, doi: 10.1093/oxfordjournals.rpd.a005847.
- [67] E. G. Yukihara, S. W. S. McKeever, and M. S. Akselrod, "State of art: Optically stimulated luminescence dosimetry – frontiers of future research," *Radiation Measurements*, vol. 71, pp. 15–24, 2014, doi: 10.1016/j.radmeas.2014.03.023.
- [68] S. Girard, B. Capoen, H. El Hamzaoui, M. Bouazaoui, G. Bouwmans, A. Morana, D. Di Francesca, A. Boukenter, O. Duhamel, P. Paillet, M. Raine, M. Gaillardin, M. Trinczek, C. Hoehr, E. Blackmore, and Y. Ouerdane, "Potential of copper- and cerium-doped optical fiber materials for proton beam monitoring," *IEEE Trans. Nucl. Sci.*, vol. 64, no. 1, pp. 567–573, Jan. 2017.
- [69] M. Benabdesselam, F. Mady, S. Girard, Y. Mebrouk, J. B. Duchez, M. Gaillardin, and P. Paillet, "Performance of Ge-doped optical fiber as a thermoluminescent dosimeter," *IEEE Trans. Nucl. Sci.*, vol. 60, no. 6, pp. 4251–4256, Dec. 2013.
- [70] M. Kovačević, S. Savović, A. Djordjevich, J. Bajić, D. Stupar, M. Kovačević, and S. Simić, "Measurements of growth and decay of radiation induced attenuation during the irradiation and recovery of plastic optical fibres," *Optics & Laser Technology*, vol. 47, pp. 148–151, 2013, doi: 10.1016/j.optlastec.2012.09.019.
- [71] C. Hoehr, A. Morana, O. Duhamel, B. Capoen, M. Trinczek, P. Paillet, C. Duzenli, M. Bouazaoui, G. Bouwmans, A. Cassez, Y. Ouerdane, A. Boukenter, H. El Hamzaoui, and S. Girard, "Novel Gd³⁺-doped silica-based optical fiber material for dosimetry in proton therapy," *Sci. Rep.*, vol. 9, no. 1, p. 16376, Nov. 2019.

- [72] S. Girard, A. Alessi, N. Richard, L. Martin-Samos, V. De Michele, L. Giacomazzi, S. Agnello, D. Di Francesca, A. Morana, B. Winkler, I. Reghioua, P. Paillet, M. Cannas, T. Robin, A. Boukenter, and Y. Ouerdane, "Overview of radiation induced point defects in silica-based optical fibers," *Rev. Phys.*, vol. 4, p. 100032, Nov. 2019.
- [73] T. Wijnands, K. Aikawa, J. Kuhnenn, D. Ricci, and U. Weinand, "Radiation tolerant optical fibers: From sample testing to large series production," *Journal of Lightwave Technology*, vol. 29, no. 22, pp. 3393–3400, 2011, doi: 10.1109/JLT.2011.2168512.
- [74] D. Di Francesca, I. Toccafondo, G. Li Vecchi, S. Calderini, S. Girard, A. Alessi, R. Ferraro, S. Danzeca, Y. Kadi, and M. Brugger, "Distributed optical fiber radiation sensing in the proton synchrotron booster at CERN," *IEEE Trans. Nucl. Sci.*, vol. 65, no. 8, pp. 1639–1644, Aug. 2018, doi: 10.1109/TNS.2018.2818760.
- [75] R. A. B. Devine, "On the physical models of annealing of radiation induced defects in amorphous SiO_2 ," *Nucl. Instrum. Meth. Phys. Res. B*, vol. 46, no. 1-4, pp. 261–264, Feb. 1990, doi: 10.1016/0168-583X(90)90709-4.
- [76] H. Henschel and O. Kohn, "Regeneration of irradiated optical fibres by photobleaching?" in *Fifth European Conference on Radiation and Its Effects on Components and Systems. RADECS 99*, Fontevraud, France, Sep. 1999, pp. 502–507, doi: 10.1109/RADECS.1999.858632.
- [77] C. Campanella, A. Morana, V. De Michele, J. Vidalot, E. Marin, A. Boukenter, Y. Ouerdane, P. Paillet, and S. Girard, "Photobleaching effect on the radiation-induced attenuation of an ultralow loss optical fiber at telecommunication wavelengths," *Physica Status Solidi A*, vol. 219, no. 3, p. 2100518, Jan. 2022, doi: 10.1002/pssa.202100518.
- [78] S. Girard, D. L. Griscom, J. Baggio, B. Brichard, and F. Berghmans, "Transient optical absorption in pulsed-x-ray-irradiated pure-silica-core optical fibers: Influence of self-trapped holes," *J. Non-Cryst. Solids*, vol. 352, no. 23-25, pp. 2637–2642, Jul. 2006.
- [79] D. L. Griscom, "Self-trapped holes in pure-silica glass: A history of their discovery and characterization and an example of their critical significance to industry," *J. Non-Cryst. Solids*, vol. 352, no. 23-25, pp. 2601–2617, Jul. 2006.
- [80] K. Tanimura, T. Tanaka, and N. Itoh, "Creation of quasistable lattice defects by electronic excitation in SiO_2 ," *Phys. Rev. Lett.*, vol. 51, no. 5, p. 423, Aug. 1983.
- [81] G. H. Siegel Jr., "Ultraviolet spectra of silicate glasses: A review of some experimental evidence," *J. Non-Cryst. Sol.*, vol. 13, pp. 372–398, Mar. 1974, doi: 10.1016/0022-3093(74)90002-7.

- [82] S. Girard, J. Keurinck, A. Boukenter, J. P. Meunier, Y. Ouerdane, B. Azais, P. Charre, and M. Vié, "Gamma-rays and pulsed x-ray radiation responses of nitrogen-, germanium-doped and pure silica core optical fibers," *Nucl. Inst. Meth. Phys. Res. B*, vol. 215, no. 1–2, pp. 187–195, Jan. 2004.
- [83] A. Vedda, N. Chiodini, D. Di Martino, M. Fasoli, S. Keffer, A. Lauria, M. Martini, F. Moretti, G. Spinolo, M. Nikl, N. Solovieva, and G. Brambilla, "Ce³⁺-doped fibers for remote radiation dosimetry," *Appl. Phys. Lett.*, vol. 85, no. 26, p. 6356, Dec. 2004.
- [84] H. El Hamzaoui, B. Capoen, N. Al Helou, G. Bouwmans, Y. Ouerdane, A. Boukenter, S. Girard, C. Marcandella, O. Duhamel, G. Chadeyron, R. Mahiou, and M. Bouazaoui, "Ce-activated sol-gel silica glasses for radiation dosimetry in harsh environment," *Mater. Res. Express*, vol. 3, no. 4, p. 046201, Apr. 2016, doi: 10.1088/2053-1591/3/4/046201.
- [85] N. Al Helou, H. El Hamzaoui, B. Capoen, G. Bouwmans, A. Cassez, Y. Ouerdane, A. Boukenter, S. Girard, G. Chadeyron, R. Mahiou, and M. Bouazaoui, "Radioluminescence and optically stimulated luminescence responses of a cerium-doped sol-gel silica glass under x-ray beam irradiation," *IEEE Trans. Nucl. Sci.*, vol. 65, no. 8, pp. 1591–1597, Aug. 2018, doi: 10.1109/TNS.2017.2787039.
- [86] N. Kerboub, D. Di Francesca, S. Girard, A. Morana, H. El Hamzaoui, Y. Ouerdane, G. Bouwmans, R. Habert, A. Boukenter, B. Capoen, E. Marin, M. Bouazaoui, Y. Kadi, D. Ricci, R. García Alía, J. Mekki, and M. Brugger, "Temperature effect on the radioluminescence of cu-, ce-, and cuce-doped silica-based fiber materials," *IEEE Trans. Nucl. Sci.*, vol. 68, no. 8, pp. 1782–1787, Aug. 2021, doi: 10.1109/TNS.2021.3075481.
- [87] W. Chewpraditkul, Y. Shen, D. Chen, B. Yu, P. Prusa, M. Nikl, A. Beitlerova, and C. Wanarak, "Luminescence and scintillation of Ce³⁺-doped high silica glass," *Opt. Mater.*, vol. 34, pp. 1762–1766, May 2012, doi: 10.1016/j.optmat.2012.04.012.
- [88] W. Chewpraditkul, Y. Shen, D. Chen, A. Beitlerova, and M. Nikl, "Luminescence of Tb³⁺-doped high silica glass under UV and X-ray excitation," *Opt. Mater.*, vol. 35, no. 3, pp. 426–430, Jan. 2013, doi: 10.1016/j.optmat.2012.09.012.
- [89] J. Bahout, "Fibres optiques dédiées à la détection de rayonnements ionisants : vers une dosimétrie aux extrêmes," Ph.D. dissertation, Université de Lille, 2020, available: <https://pepite-depot.univ-lille.fr/LIBRE/EDSMRE/2020/50376-2020-Bahout.pdf>, accessed on 10 Jan. 2023.
- [90] H. El Hamzaoui, Y. Ouerdane, L. Bigot, G. Bouwmans, B. Capoen, A. Boukenter, S. Girard, and M. Bouazaoui, "Sol-gel derived ionic copper-doped microstructured optical fiber: a potential selective ultraviolet radia-

- tion dosimeter," *Opt. Express*, vol. 20, no. 28, pp. 29 751–29 760, Dec. 2012, doi: 10.1364/OE.20.029751.
- [91] B. Capoen, H. El Hamzaoui, M. Bouazaoui, Y. Ouerdane, A. Boukenter, S. Girard, C. Marcandella, and O. Duhamel, "Sol-gel derived copper-doped silica glass as a sensitive material for x-ray beam dosimetry," *Opt. Mater.*, vol. 51, pp. 104–109, Jan. 2016.
- [92] N. Al Helou, H. El Hamzaoui, B. Capoen, Y. O. A. Boukenter, S. Girard, and M. Bouazaoui, "Effects of ionizing radiations on the optical properties of ionic copper-activated sol-gel silica glasses," *Opt. Mater.*, vol. 75, pp. 116–121, Jan. 2018, doi: 10.1016/j.optmat.2017.09.049.
- [93] J. Bahout, Y. Ouerdane, H. El Hamzaoui, G. Bouwmans, M. Bouazaoui, A. Cassez, K. Baudelle, R. Habert, A. Morana, A. Boukenter, S. Girard, and B. Capoen, "Cu/ce-co-doped silica glass as radioluminescent material for ionizing radiation dosimetry," *Materials*, vol. 13, no. 11, p. 2611, Jun. 2019, doi: 10.3390/ma13112611.
- [94] A. K. M. Mizanur Rahman, M. Begum, H. T. Zubair, H. A. Abdul-Rashid, Z. Yusoff, N. M. Ung, and D. A. Bradley, "Ge-doped silica optical fibres as RL/OSL dosimeters for radiotherapy dosimetry," *Sens. Actuators A Phys.*, vol. 264, pp. 30–39, Sep. 2017, doi: 10.1016/j.sna.2017.07.038.
- [95] A. K. M. Mizanur Rahman, M. Begum, M. Begum, H. T. Zubair, H. A. Abdul-Rashid, Z. Yusoff, and D. A. Bradley, "Radioluminescence of Ge-doped silica optical fibre and Al₂O₃:C dosimeters," *Sens. Actuators A Phys.*, vol. 270, pp. 72–78, Feb. 2018, doi: 10.1016/j.sna.2017.12.032.
- [96] V. B. Neustruev, "Colour centres in germanosilicate glass and optical fibres," *J. Phys.: Condens. Matter*, vol. 6, pp. 6901–6936, 1994, doi: 10.1088/0953-8984/6/35/003.
- [97] L. Skuja, "Isoelectronic series of twofold coordinated Si, Ge, and Sn atoms in glassy SiO₂: a luminescence study," *J. Non-Cryst. Solids*, vol. 149, no. 1, pp. 77–95, 1992, doi: 10.1016/0022-3093(92)90056-P.
- [98] H. El Hamzaoui, G. Bouwmans, B. Capoen, A. Cassez, R. Habert, Y. Ouerdane, S. Girard, D. Di Francesca, N. Kerboub, A. Morana, D. Söderström, A. Boukenter, and M. Bouazaoui, "Gd³⁺-doped sol-gel silica glass for remote ionizing radiation dosimetry," *OSA Contin.*, vol. 2, no. 3, pp. 715–721, Mar. 2019, doi: 10.1364/OSAC.2.000715.
- [99] D. Di Martino, N. Chiodini, M. Fasoli, F. Moretti, A. Vedda, A. Baraldi, E. Buffagni, R. Capelletti, M. Mazzera, M. Nikl, G. Angella, and C. B. Azzoni, "Gd-incorporation and luminescence properties in sol-gel silica glasses," *J. Non-Cryst. Sol.*, vol. 354, pp. 3817–3823, Jul. 2008.

- [100] S. Girard, D. Di Francesca, A. Morana, C. Hoehr, P. Paillet, C. Duzenli, N. Kerboub, I. Reghioua, G. Li Vecchi, A. Alessi, O. Duhamel, M. Trinczek, E. Marin, A. Boukenter, Y. Ouerdane, J. Mekki, R. García Alía, Y. Kadi, and M. Brugger, "X-rays, γ -rays, and proton beam monitoring with multimode nitrogen-doped optical fiber," *IEEE Trans. Nucl. Sci.*, vol. 66, no. 1, pp. 306–311, Jan. 2019, doi: 10.1109/TNS.2018.2879791.
- [101] E. M. Dianov, K. M. Golant, R. R. Khrapko, O. I. Medvedkov, A. L. Tomashuk, and S. A. Vasil'ev, "UV absorption and luminescence in silicon oxynitride prepared by hydrogen-free SPCVD-process," *Opt. Mater.*, vol. 5, pp. 169–173, Mar. 1996, doi: 10.1016/0925-3467(95)00047-X.
- [102] G. Origlio, F. Messina, M. Cannas, R. Boscaino, s. Girard, A. Boukenter, and Y. Ouerdane, "Optical properties of phosphorus-related point defects in silica fiber preforms," *Phys. Rev. B*, vol. 80, no. 20, p. 205208, Nov. 2009, doi: 10.1103/PhysRevB.80.205208.
- [103] D. A. Bradley, H. T. Zubair, A. Oresgun, G. T. Louay, A. Ariffin, M. U. Khandakera, K. S. Alzimamid, and H. A. Abdul-Rashid, "Radioluminescence sensing of radiology exposures using p-doped silica optical fibres," *Appl. Rad. Isotopes*, vol. 141, pp. 176–181, Nov. 2018, doi: 10.1016/j.apradiso.2018.02.025.
- [104] S. Girard, personal communication, 2023-02-24.
- [105] T. R. Oldham and F. B. McLean, "Total ionizing dose effects in MOS oxides and devices," *IEEE Trans. Nucl. Sci.*, vol. 50, no. 3, pp. 483–499, Jun. 2003, doi: 10.1109/TNS.2003.812927.
- [106] J. M. Benedetto, H. E. Boesch, F. B. McLean, and J. P. Mize, "Hole removal in thin-gate MOSFETs by tunneling," *IEEE Trans. Nucl. Sci.*, vol. 32, no. 6, pp. 3916–3920, Dec. 1985, doi: 10.1109/TNS.1985.4334043.
- [107] F. Faccio and G. Cervelli, "Radiation-induced edge effects in deep submicron CMOS transistors," *IEEE Trans. Nucl. Sci.*, vol. 52, no. 6, pp. 2413–2420, Dec. 2005, doi: 10.1109/TNS.2005.860698.
- [108] J. R. Srour, C. J. Marshall, and P. W. Marshall, "Review of displacement damage effects in silicon devices," *IEEE Trans. Nucl. Sci.*, vol. 50, no. 3, pp. 653–670, Jun. 2003, doi: 10.1109/TNS.2003.813197.
- [109] P. E. Dodd and L. W. Massengill, "Basic mechanisms and modeling of single-event upset in digital microelectronics," *IEEE Trans. Nucl. Sci.*, vol. 50, no. 3, pp. 583–602, Jun. 2003, doi: 10.1109/TNS.2003.813129.
- [110] JEDEC Standard, "Double data rate (DDR) SDRAM environment specification, JESD79," JEDEC Solid State Technology Association, 3103 North 10th Street, Suite 240 South, Arlington, VA 22201-2107, USA, Revision F, Feb. 2008.

- [111] A. M. Chugg, A. J. Burnell, P. H. Duncan, S. Parker, and J. J. Ward, "The random telegraph signal behavior of intermittently stuck bits in SDRAMs," *IEEE Trans. Nucl. Sci.*, vol. 56, no. 6, pp. 3057–3064, Dec. 2009, doi: 10.1109/TNS.2009.2032184.
- [112] A. M. Chugg, J. McIntosh, J. Burnell, P. H. Duncan, and J. J. Ward, "Probing the nature of intermittently stuck bits in dynamic RAM cells," *IEEE Trans. Nucl. Sci.*, vol. 57, no. 6, pp. 3190–3198, Dec. 2010, doi: 10.1109/TNS.2010.2084103.
- [113] G. M. Swift, D. J. Padgett, and A. H. Johnston, "A new class of single event hard errors," *IEEE Trans. Nucl. Sci.*, vol. 41, no. 6, pp. 2043–2048, Dec. 1994, doi: 10.1109/23.340540.
- [114] T. R. Oldham and J. M. McGarrity, "Ionization of SiO₂ by heavy charged particles," *IEEE Trans. Nucl. Sci.*, vol. 28, no. 6, pp. 3975–3980, Dec. 1981, doi: 10.1109/TNS.1981.4335658.
- [115] JEDEC Standard, "DDR2 SDRAM specification JESD79-2B," JEDEC Solid State Technology Association, 2500 Wilson Boulevard, Arlington, VA 22201-3834, USA, Tech. Rep., Jan. 2005.
- [116] M. Amrbar and S. M. Guertin, "Total ionizing dose response of SDRAM, DDR2 and DDR3 memories," pp. 199–204, Jul. 2016, doi: 10.1109/NSREC.2016.7891750.
- [117] I. H. Hopkins and G. R. Hopkinson, "Random telegraph signals from proton-irradiated CCDs," *IEEE Trans. Nucl. Sci.*, vol. 40, no. 6, pp. 1567–1574, Dec. 1993, doi: 10.1109/23.273552.
- [118] V. G. P. Magnan, P. Martin-Gonthier, C. Virmontois, and M. Gaillardin, "Evidence of a novel source of random telegraph signal in CMOS image sensors," *IEEE Electron Device Lett.*, vol. 32, no. 6, pp. 773–775, Jun. 2011, doi: 10.1109/LED.2011.2125940.
- [119] V. Goiffon, T. Bilba, T. Deladerrière, G. Beaugendre, A. Le-Roch, A. Dion, C. Virmontois, J.-M. Belloir, M. Gaillardin, A. Jay, and P. Paillet, "Radiation induced variable retention time in dynamic random access memories," *IEEE Trans. Nucl. Sci.*, vol. 67, no. 1, pp. 234–244, Jan. 2020, doi: 10.1109/TNS.2019.2956293.
- [120] T. C. May and M. H. Woods, "Alpha-particle-induced soft errors in dynamic memories," *IEEE Trans. Electron Devices*, vol. 26, no. 1, pp. 2–9, Jan. 1979, doi: 10.1109/T-ED.1979.19370.
- [121] E. Takeda, K. Takeuchi, D. Hisamoto, T. Toyabe, K. Ohshima, and K. Itoh, "A cross section of α -particle-induced soft-error phenomena in VLSI's," *IEEE Trans. Electron Devices*, vol. 36, no. 11, pp. 2567–2575, Nov. 1989, doi: 10.1109/16.43681.

- [122] T. V. Rajeevakumar, N. C. C. Lu, W. H. Henkels, W. Hwang, and R. Franch, "A new failure mode of radiation-induced soft errors in dynamic memories," *IEEE Electron Device Lett.*, vol. 9, no. 12, pp. 644–646, Dec. 1988, doi: 10.1109/55.20423.
- [123] L. W. Massengill, A. E. Baranski, D. O. Van Nort, J. Meng, and B. L. Bhuvu, "Analysis of single-event effects in combinational logic—simulation of the AM2901 bitslice processor," *IEEE Trans. Nucl. Sci.*, vol. 47, no. 6, pp. 2609–2615, Dec. 2000, doi: 10.1109/23.903816.
- [124] K. Røed, M. Brugger, D. Kramer, P. Peronnard, C. Pignard, G. Spiezia, and A. Thornton, "Method for measuring mixed field radiation levels relevant for SEEs at the LHC," *IEEE Trans. Nucl. Sci.*, vol. 59, no. 4, pp. 1040–1047, Aug. 2012, doi: 10.1109/TNS.2012.2183677.
- [125] H. H. K. Tang, "Nuclear physics of cosmic ray interaction with semiconductor materials: Particle-induced soft errors from a physicist's perspective," *IBM J. Res. Develop.*, vol. 40, no. 1, pp. 91–108, Jan. 1996.
- [126] J. Mekki, M. Brugger, R. García Alía, A. Thornton, N. C. Dos Santos Mota, and S. Danzeca, "CHARM: a mixed field facility at CERN for radiation tests in ground, atmospheric, space and accelerator representative environments," *IEEE Trans. Nucl. Sci.*, vol. 63, no. 4, pp. 2106–2114, Aug. 2016, doi: 10.1109/TNS.2016.2528289.
- [127] C. Cazzaniga and C. D. Frost, "Progress of the scientific commissioning of a fast neutron beamline for chip irradiation," *J. Phys.: Conf. Ser.*, vol. 1021, p. 012037, 2018, doi: 10.1088/1742-6596/1021/1/012037.
- [128] C. Cazzaniga, M. Bagatin, S. Gerardin, A. Costantino, and C. D. Frost, "First tests of a new facility for device-level, board-level and system-level neutron irradiation of microelectronics," *IEEE Transactions on Emerging Topics in Computing*, vol. 9, no. 1, pp. 104–108, Jan.–March 2021, doi: 10.1109/TETC.2018.2879027.
- [129] H. Kettunen, *Heavy ion cocktails available at RADEF*, University Of Jyväskylä, Oct. 2021, accessed on: November 16, 2022. [Online]. Available: <https://www.jyu.fi/science/en/physics/research/infrastructures/accelerator-laboratory/radiation-effects-facility/heavy-ion-cocktails>
- [130] A. Virtanen, R. Harboe-Sørensen, A. Javanainen, H. Kettunen, H. Koivisto, and I. Riihimäki, "Upgrades for the RADEF facility," in *IEEE Radiation Effects Data Workshop*, Honolulu, HI, USA, Jul. 2007, pp. 38–41, doi: 10.1109/REDW.2007.4342538.
- [131] H. Kettunen, *Proton beams at RADEF*, University Of Jyväskylä, May 2021, accessed on: November 16, 2022. [Online]. Available: <https://www.jyu.fi/science/en/physics/research/infrastructures/accelerator-laboratory/radiation-effects-facility/proton-beams>

- [132] H. Kettunen, V. Ferlet-Cavrois, P. Roche, M. Rossi, A. Bosser, G. Gasiot, F.-X. Guerre, J. Jaatinen, A. Javanainen, F. Lochon, and A. Virtanen, "Low energy protons at radeF – application to advanced esrams," in *Proceedings of the 2014 IEEE Radiation Effects Data Workshop (REDW)*, Paris, France, Jul. 2014, pp. 1–4, doi: 10.1109/REDW.2014.7004577.
- [133] H. Kettunen, *Linear electron accelerator*, University Of Jyväskylä, Apr. 2020, accessed on: November 16, 2022. [Online]. Available: <https://www.jyu.fi/science/en/physics/research/infrastructures/accelerator-laboratory/radiation-effects-facility/linear-electron-accelerator>
- [134] J. Allison *et al.*, "Recent developments in GEANT4," *Nucl. Instrum. Methods Phys. Res. A*, vol. 835, pp. 186–225, Nov. 2016, doi: 10.1016/j.nima.2016.06.125.
- [135] IBA, *DETECTORS For Relative and Absolute Dosimetry - Ionization chambers and diode detectors*, IBA Dosimetry GmbH, Bahnhofstr. 5, 90592 Schwarzenbruck, Germany, 2018, https://www.iba-dosimetry.com/fileadmin/user_upload/products/02_radiation_therapy/_Detectors/Detectors-RD_-AD_Rev.3_0718_E.pdf, Accessed on: October 1, 2020.
- [136] J. H. Hubbell and S. M. Seltzer, "X-ray mass attenuation coefficients," NIST, Radiation Physics Division, NIST Standard Reference Database 126, NISTIR 5632, Jul. 2004, doi: 10.18434/T4D01F.
- [137] K. N. Sjobak, E. Adli, C. A. Lindstrom, M. Bergamaschi, S. Burger, R. Corsini, S. Döbert, W. Farabolini, D. Gamba, L. Garolfi, A. Gilardi, I. Gorgisyan, E. Granados, H. Guerin, R. Kieffer, M. Krupa, T. Lefèvre, C. Lindstrøm, A. Lyapin, S. Mazzoni, G. McMonagle, J. Nadenau, H. Panuganti, S. Pitman, V. Rude, A. Schlogelhofer, P. Skowronski, M. Wendt, and A. Zemanek, "Status of the CLEAR electron beam user facility at CERN," in *Proceedings of the 10th International Particle Accelerator Conference (IPAC'19), Melbourne, Australia, 19-24 May 2019*, ser. International Particle Accelerator Conference, no. 10, Jun. 2019, pp. 983–986, doi: 10.18429/JACoW-IPAC2019-MOPTS054.
- [138] D. Gamba, R. Corsini, S. Curt, S. Doebert, W. Farabolini, G. Mcmonagle, P. K. Skowronski, F. Tecker, S. Zeeshan, E. Adli, C. A. Lindstrøm, A. Ross, and L. M. Wroe, "The CLEAR user facility at CERN," *Nucl. Inst. Meth. Phys. Res. A*, vol. 909, pp. 480–483, Nov. 2018, doi: 10.1016/j.nima.2017.11.080.
- [139] European Space Component Coordination (ESCC), "Single event effects test method and guidelines," European Space Agency (ESA), ESCC Basic Specification No. 25100, Oct. 2014, <https://escies.org/>.
- [140] J. Y. Kim, C. S. Lee, S. E. Kim, I. B. Chung, Y. M. Choi, B. J. Park *et al.*, "The breakthrough in data retention time of DRAM using Recess-Channel-Array Transistor (RCAT) for 88nm feature size and beyond," in *2003 Symposium*

- on *VLSI Technology*, Kyoto, Japan, Jun. 2003, pp. 11–12, doi: 10.1109/VLSIT.2003.1221061.
- [141] J. P. David, F. Bezerra, E. Lorfèvre, T. Nuns, and C. Inguibert, “Light particle-induced single event degradation in SDRAMs,” *IEEE Trans. Nucl. Sci.*, vol. 53, no. 6, pp. 3544–3549, Dec. 2006, doi: 10.1109/TNS.2006.886210.
- [142] T. R. Oldham and J. M. McGarrity, “Comparison of ^{60}Co response and 10 KeV X-Ray response in MOS capacitors,” *IEEE Trans. Nucl. Sci.*, vol. NS-30, no. 6, pp. 4377–4381, Dec. 1983, doi: 10.1109/TNS.1983.4333141.
- [143] L. Matana Luza, D. Söderström, H. Puchner, R. G. Alía, M. Letiche, C. Cazzaniga, A. Bosio, and L. Dilillo, “Neutron-induced effects on a self-refresh DRAM,” *Microelectronics Reliability*, vol. 128, p. 114406, 2022, doi: 10.1016/j.microrel.2021.114406.
- [144] H. El Hamzaoui, L. Courthéoux, V. N. Nguyen, E. Berrier, A. Favre, L. Bigot, M. Bouazaoui, and B. Capoen, “From porous silica xerogels to bulk optical glasses: The control of densification,” *Mater. Chem. Phys.*, vol. 121, no. 1-2, pp. 83–88, May 2010, doi: 10.1016/j.matchemphys.2009.12.043.
- [145] H. El Hamzaoui, G. Bouwmans, B. Capoen, Y. Ouerdane, G. Chadeyron, R. Mahiou, S. Girard, A. Boukenter, and M. Bouazaoui, “Effects of densification atmosphere on optical properties of ionic copper-activated sol-gel silica glass: towards an efficient radiation dosimeter,” *Mater. Res. Express*, vol. 1, no. 2, p. 026203, Jun. 2014, doi: 10.1088/2053-1591/1/2/026203.
- [146] Ocean Optics, Inc., *USB2000+ Fiber Optic Spectrometer Installation and Operation Manual*, 830 Douglas Ave., Dunedin, FL 34698, USA, <https://www.oceaninsight.com/globalassets/catalog-blocks-and-images/manuals--instruction-old-logo/spectrometer/usb2000-operating-instructions1.pdf>, Accessed on: August 26, 2021.
- [147] Hamamatsu, *Photosensor modules H9305 series*, Hamamatsu Photonics K.K., 314-5, Shimokanzo, Iwata City, Shizuoka Pref., 438-0193, Japan, 2020, https://www.hamamatsu.com/resources/pdf/etd/H9305_TPMO1065E.pdf, Accessed on: May 26, 2021.
- [148] A. S. Beddar, T. R. Mackie, and F. H. Attix, “Cerenkov light generated in optical fibres and other light pipes irradiated by electron beams,” *Phys. Med. Biol.*, vol. 37, no. 4, pp. 925–935, 1992.
- [149] R. Kronholm, T. Kalvas, H. Koivisto, and O. Tarvainen, “Spectroscopic method to study low charge state ion and cold electron population in ECRIS plasma,” *Rev. Sci. Instrum.*, vol. 89, no. 4, p. 043506, Apr. 2018.
- [150] R. Kronholm, T. Kalvas, H. Koivisto, J. Laulainen, M. Marttinen, M. Sakildien, and O. Tarvainen, “Spectroscopic study of ion temperature in

- minimum-B ECRIS plasma," *Plasma Sources Sci. Technol.*, vol. 28, no. 7, p. 075006, Jul. 2019.
- [151] Hamamatsu, *Metal Package Photomultiplier Tube R9880U Series*, Hamamatsu Photonics K.K., 314-5, Shimokanzo, Iwata City, Shizuoka Pref., 438-0193, Japan, 2022, https://www.hamamatsu.com/content/dam/hamamatsu-photonics/sites/documents/99_SALES_LIBRARY/etd/R9880U_TPMH1321E.pdf, Accessed on: Aug 15, 2022.
- [152] CAEN, *N6751*, CAEN S.p.A., Via Vetraia, 11, 55049, Viareggio (LU), Italy, 2022, <https://www.caen.it/products/n6751/>, Accessed on: Aug 15, 2022.
- [153] K. Tanimura, C. Itoh, and N. Itoh, "Transient optical absorption and luminescence induced by band-to-band excitation in amorphous SiO₂," *J. Phys. C: Solid State Phys.*, vol. 21, p. 1869, Nov. 1988.
- [154] S. Ismail-Beigi and S. G. Louie, "Self-trapped excitons in silicon dioxide: Mechanism and properties," *Phys. Rev. Lett.*, vol. 95, no. 15, p. 156401, Oct. 2005.



ORIGINAL PAPERS

PI

ELECTRON-INDUCED UPSETS AND STUCK BITS IN SDRAMs IN THE JOVIAN ENVIRONMENT

by

Daniel Söderström, Lucas Matana Luza, Heikki Kettunen, Arto Javanainen, Wilfrid Farabolini, Antonio Gilardi, Andrea Coronetti, Christian Poivey, and Luigi Dilillo

IEEE Trans. Nucl. Sci., vol. 68, no. 5, pp. 716–723, May 2021

<https://doi.org/10.1109/TNS.2021.3068186>

© 2021 IEEE. Reprinted with permission.

Electron-Induced Upsets and Stuck Bits in SDRAMs in the Jovian Environment

Daniel Söderström, *Student Member, IEEE*, Lucas Matana Luza, *Student Member, IEEE*, Heikki Kettunen, *Member, IEEE*, Arto Javanainen, *Member, IEEE*, Wilfrid Farabolini, Antonio Gilardi, Andrea Coronetti, *Student Member, IEEE*, Christian Poivey, *Member, IEEE* and Luigi Dilillo, *Member, IEEE*

Abstract—This study investigates the response of synchronous dynamic random access memories to energetic electrons, and especially the possibility of electrons to cause stuck bits in these memories. Three different memories with different node sizes (63, 72 and 110 nm) were tested. Electrons with energies between 6 MeV and 200 MeV were used at RADEF in Jyväskylä, Finland, and at VESPER in CERN, Switzerland. Photon irradiation was also performed in Jyväskylä. In these irradiation tests, stuck bits originating from electron-induced single event effects were found, as well as single bit-flips from single electrons. To the best knowledge of the authors, this is the first time that stuck bits from single electron-events has been reported in the literature. It is argued in the paper that the single event bit-flips and stuck bits are caused by the same mechanism, large displacement damage clusters, and that they represent different amounts of damage to the memory cell. After a large particle fluence, a rapid increase in the error rate was observed, originating from the accumulation of smaller displacement damage clusters in the memory cells. The 110 nm memory was a candidate component to fly on the ESA JUICE mission, so the single event effect cross section as a function of electron energy was compared to the expected electron environment encountered by JUICE to estimate the error rates during the mission.

Index Terms—Electron radiation, radiation effects, single event upsets, stuck bits, total ionizing dose

I. INTRODUCTION

RADIATION effects in electronic components caused by energetic electrons is of higher concern in the Jovian radiation environment than in the radiation belts surrounding Earth, due to the harder energy spectrum present around

Manuscript submitted October 1, 2020.

The results presented here are part of the RADSAGA project that has received funding from the European Union's Horizon 2020 research and innovation program under the Marie Skłodowska-Curie grant agreement No 721624.

This work was also supported by the European Space Agency (ESA) under contract 4000124504/18/NL/KML/zk, the Van Allen Foundation under contract no. UM 181387, and Region Occitane under contract no. UM 181386.

D. Söderström, H. Kettunen, A. Javanainen and A. Coronetti are with the Department of Physics at the University of Jyväskylä, Finland. Contact: daniel.p.soderstrom@jyu.fi.

L. Matana Luza and L. Dilillo are with Laboratoire d'Informatique, de Robotique et de Microélectronique de Montpellier (LIRMM), Montpellier, France.

A. Javanainen is also with the Electrical Engineering and Computer Science Department at Vanderbilt University, Nashville, TN 37235, USA.

A. Gilardi is with the University of Napoli Federico II, DIETI, Napoli, Italy.

W. Farabolini, A. Gilardi and A. Coronetti are with CERN, CH-1211 Geneva 23, Switzerland.

C. Poivey is with the European Space Agency (ESA), ESTEC, 2201 Noordwijk, The Netherlands

Thanks to ESA and 3D+ for providing memory samples tested in this work.

Jupiter [1]–[3]. This study is motivated by the European Space Agency's (ESA) JUPITER ICY moons Explorer (JUICE) mission in the Jovian environment, and focuses on electron-induced radiation effects in synchronous dynamic random access memories (SDRAM), where one of the tested components was a candidate to be used on board JUICE.

One of the main points of interest of this work was to investigate the possibility of stuck bits being induced by single electrons. This has, to the best of the authors' knowledge, not previously been observed or reported.

Previous studies of single event effects (SEE) caused by energetic electrons have been reported in e.g. [4]–[9], where single event upsets (SEU) and single event latch-up (SEL) were investigated mainly in static random access memories (SRAM). In [4] SEUs from secondary electrons induced by X-rays were studied, while in [5] and [6] SEUs in FPGA embedded and configuration RAM were studied. In [7] SEUs in SRAMs operated at a low voltage were observed. SEUs from high energy electrons were studied in [8], and the same authors studied electron-induced SEL in [9].

In this work concerning SDRAM, stuck bits are defined as bits with reoccurring errors, so that the memory cell is returning the same data when it is read ('0' or '1'), independent of the value which was written to the cell. This behaviour is different from typical SEU, which manifest themselves as a bit-flip, only present in a single reading of the bit in question, but not in any consecutive reads of the cell after it had been rewritten.

Stuck bits in SDRAM have been studied in irradiation experiments using different particle species, such as protons and ions, e.g. in [10]–[13]. There, a common suggested cause for the stuck bits is single particles creating leakage paths from the cell capacitor by displacement damage. In [13], as well as in [14], [15], intermittently stuck bits (ISB) are discussed, which deals with the phenomenon of bits appearing as stuck in some periods of time, when otherwise they can operate normally and return the correct value which was written to the memory cell. Stuck bits are discussed in [16] under the terminology weakened cells, where flight data and ground data are presented. Here displacement damage from single particles is also identified as the cause for the upsets.

In this paper, experimental SEE results from electrons, resulting in stuck bits and bit-flips are presented and discussed. No new interpretation of the mechanism causing stuck bits or ISBs in SDRAMs is presented, but the cause of stuck bits is put in relation to that of single bit-flips. The degradation of the

TABLE I
SUMMARY OF SPECIMEN USED IN THE EXPERIMENTS.

Memory	Node size (nm)	DUT IDs
IS42S86400B	110	SDF1, SDF3, SDF4, SDF5, SDG1, SDG3, SDG4, SDG5, SDG6
IS42S16320D	72	SDB1
IS42S16320F	63	SDE1

cells subject to SEE is studied, and implications of the usage of the studied SDRAM in the JUICE mission are discussed.

II. TESTED COMPONENTS AND EXPERIMENTAL PROCEDURE

The tested components are described in Table I, where the ISSI 512 Mb SDRAM IS42S86400B [17] was a candidate to be flown on the JUICE mission when the irradiation tests were performed.

The tested memory devices were all ISSI 512 Mb Single Data Rate (SDR) SDRAMs, with 536,870,912 bits separated on four banks. The IS42S86400B memory banks are organized into 8192 rows by 2048 columns of 8 bits, while the IS42S16320D/F [18], [19] memories have 8192 rows of 1024 columns by 16 bits in their banks. They all have an operating frequency of up to 143 MHz, with a 3.3 V bias, and were packaged in 54-pin TSOP-II packages. None of the devices were delidded for the irradiation experiments, and no further information about the memory layout in terms of physical structure or physical mapping of the memory bits are known to the authors.

A Terasic DE0-CV FPGA development board [20] was used as a memory control board during the experiments, and the samples were mounted on daughter boards connected to the control board through a GPIO pin interface. Only the device under test (DUT) was placed in the radiation field during irradiation, and the control board was kept outside the beam.

The components were running dynamic tests during irradiation, with read and write operations carried out continuously. The memories were running a March C- test, which was slightly modified so that it would not have any stand-alone write or read elements [21]. The dynamic test cycle of read and write operations for the DUTs during irradiation is shown in (1).

$$\begin{aligned} & \uparrow (w0); \{ \uparrow (r0, w1); \uparrow (r1, w0); \\ & \quad \downarrow (r0, w1); \downarrow (r1, w0) \} \end{aligned} \quad (1)$$

The operations within the brackets $\{ \}$ in (1) were looped over during irradiation, the r and w are read and write operations respectively, the ‘0’ and ‘1’ are data patterns of all ‘0’ and all ‘1’, and the arrows represent the address accessing order in the operation, starting from either the lowest address and stepping upwards (\uparrow), or vice versa (\downarrow). The IS42S86400B memories were operated at 100 MHz, while the IS42S16320D/F memories were operated at 75 MHz, because the D/F memories could not operate without issues at higher frequencies with the cabling and set-up used in the experiment. During all runs, the memories were operated

with their nominal refresh frequency 128 kHz. This frequency is based on the auto refresh command, which automatically defines the row address to refresh. At 128 kHz, this command is executed 8192 times every 64 ms [17] so that every row of the memory is refreshed once per 64 ms. This refresh frequency was altered during analysis procedures to investigate data retention times of the memories’ bits.

III. TEST FACILITIES

The tests with high-energy electrons (60 - 200 MeV) were performed at VESPER (the Very energetic Electron facility for Space Planetary Exploration missions in harsh Radiative environments) [22] at CERN (The European Organization for Nuclear Research). Lower energy electron (up to 20 MeV) and photon exposures were performed at RADEF (RADiation Effects Facility) at the University of Jyväskylä, Finland, with a Varian Clinac (Clinical LINEar ACcelerator) 2100 CD [23].

A. VESPER

The VESPER beam is pulsed, and the electrons arrive in short bunches (< 10 ps) at a frequency of 3 GHz. The electron bunches were arranged in trains of 100 electron bunches each, and the trains were arriving at a 10 Hz frequency.

A beam current transformer (BCT) was used to monitor the beam current during the runs, and an Yttrium Aluminium Garnet (YAG) screen was used to monitor the beam spot shape. A camera was filming the scintillating YAG-screen to monitor the beam profile during the run. The beam spot was approximated to be of Gaussian shape, and the shape parameters of the beam centre and standard deviation ($\mu_{x,y}$ and $\sigma_{x,y}$) were logged in real time while performing the experiment.

This system for beam monitoring worked rather well with a high intensity beam. As the beam intensity gets lower, and as the beam energy gets lower, the beam profile and charge is monitored less efficiently. Since the irradiation was done in air, with the beam having to pass through an exit window as well as a scattering screen to enlarge the beam spot, a more diffuse and scattered beam would reach the scintillating screen when a beam with lower energy and penetration power is used for a given beam intensity. The DUTs were unable to operate under high electron fluxes without large portions of the memory being corrupted, so a rather low flux (in general about $2 - 3 \cdot 10^8$ e/cm²/s, which is low in relation to what the facility could provide) had to be chosen. The beam spot was thus rather diffuse, and the exact beam position difficult to recreate. In combination with this, the beam spot was drifting (generally < 5 mm) vertically and horizontally during the runs.

To calculate the electron fluence on the DUT, the beam charge and measured shape ($\sigma_{x,y} = 12 - 15$ mm depending on beam energy) were used. The fluence on the DUT was assumed as the average fluence within the area $\sigma_x \times \sigma_y$ and with an estimated uncertainty 20 % due to drifting of the electron beam position during irradiation and the diffuse beam spot.

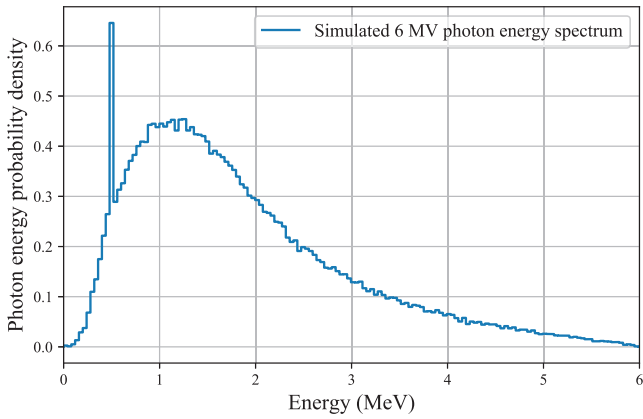


Fig. 1. Simulated photon energy spectrum of the 6 MV photon mode of the RADEF Clinac.

B. RADEF

Electrons with energies of 6, 9, 12, 16 and 20 MeV are available at the Clinac at RADEF. This electron beam is also pulsed and consists of 5 μ s long pulses every 5 ms (pulse frequency of 200 Hz). Furthermore, the radiation from the machine is provided in runs of up to 10 krad(H_2O) each, so the irradiation has to be restarted every 10 krad(H_2O). This is however a fast procedure, taking only a few seconds of time. 6 MeV and 20 MeV electrons were used for tests discussed in this paper.

The Clinac can be run in electron mode or in photon mode. In photon mode, a target is placed within the electron beam, converting the incident electrons to a bremsstrahlung spectrum of photons. In photon mode, the Clinac can be run at 6 MV or 15 MV, which means that the resulting photon spectrum is that of the bremsstrahlung from electrons accelerated over a 6 MV or 15 MV electric field (electrons with energies 6 MeV and 15 MeV) respectively. The 6 MV mode were used for photon-tests with results presented in this paper.

The photon energy spectrum for the 6 MV operating mode is a smooth continuous distribution from 0 to 6 MeV, with an intensity maximum at about 1 MeV, and can be seen in Fig. 1. The spectrum is the result of a Geant4-simulation [24] where 6 MeV electrons were impinging on a 2.5 mm thick Ta-target. The bremsstrahlung photons generated in the target was transported through a tungsten flattening filter, which is present in the beam line to create a spatially homogeneous photon field, and a 1 m air column, after which the photon energy spectrum was recorded. The sharp peak in the spectrum located at 0.511 MeV consists of annihilation photons.

The beam was monitored with in-beam ionization chambers, which were calibrated against a dosimeter in the beam centre at maximum dose depth in water (i.e., at the water depth where the dose rate is the highest). An IBA PPC40 dosimeter [25] was used for electrons and an IBA FC65-P dosimeter [25] for photons.

At the facility, the dose at maximum dose depth in water is measured and recorded. In addition, the water surface dose was also measured, so the dose rate ratio between the maximum

TABLE II
PARAMETERS OF THE USED BEAMS AT THE RADEF CLINAC.

Energy (MeV)	Surface dose rate (fraction of max)	Max dose depth (cm H_2O)	S_{coll} (MeV cm^2/g (H_2O))	S_{coll} (MeV cm^2/g (Si))
6	0.78	1.19	1.911	1.639
20	0.91	1.58	2.046	1.796
6 MV ^a	0.47	1.56	-	-

S_{coll} values obtained from [26]

^a Photon radiation field

depth and surface is known. From this, the electron fluence on the DUT was calculated as the surface dose in water, divided by the collision stopping power (S_{coll}) in water (using appropriate units). The surface dose factors and S_{coll} for the electron energies used at RADEF are shown in Table II.

When values of deposited dose are presented for electrons in this paper, it is the surface dose in Si. This is calculated from the electron fluence, by multiplying the fluence with S_{coll} in Si for the electron energy in question. For photon irradiation, the surface dose is as seen in Table II much smaller than the dose at maximum dose depth in water. The irradiation with photons was performed with 6 MV photons with the DUT covered by 1.5 cm of acrylic (polymethyl methacrylate), and with 2 cm of acrylic below the DUT. This was done so that the dose level in the DUT would correspond to the dose at maximum dose depth in water.

Another factor that was taken into account was the surface homogeneity. No electron applicator was used during the irradiation, which makes the beam surface slightly less homogeneous. The electron fluence at the DUT position was measured to be the fractions 0.79 and 0.88 of the fluence at the beam centre for 6 MeV and 20 MeV electrons respectively, and the presented fluences was corrected with these factors. For the photon mode operation, the inhomogeneities were negligible. The uncertainty of the calculated electron fluence is estimated to be less than 10 %.

The memory dies are encapsulated in a plastic package, and part of the die is covered by the metal bonding. Metal could have an impact on the absorbed dose in the Si die due to dose enhancements present in the interface regions between Si and high-Z materials [27]. The interior design of the memory is not known, in terms of the location of possible metallic material in relation to sensitive die regions. The dose enhancement effect is largest for photons of lower energy, due to the dominance of the photoelectric effect as a photon interaction mode at lower energies. Low energy electrons that are released from the high-Z material can then cause a dose enhancement effect in the interface regions. For higher energy photons, like the ones present here (Fig. 1), this effect is not as big [27]. In this work, the displacement damage effects are also more important than the total dose, and the low energy secondaries are not as important in this regard as the higher energy particles, so no modifications to the value of the absorbed dose was made due to dose enhancement effects.

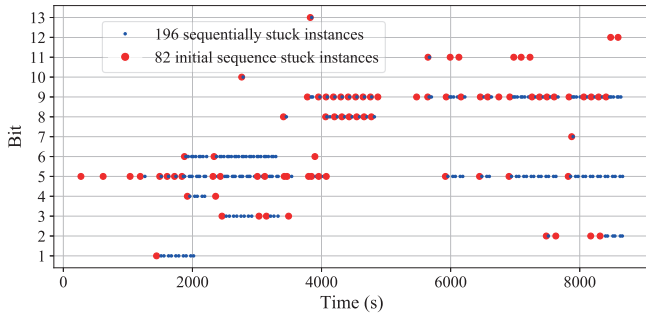


Fig. 2. Time structure of the errors from stuck bits in memory SDF3 under 123 MeV electron irradiation during modified March C- test loops. The bits are numbered as 1 - 13, with each row displaying the behaviour of one of the observed stuck bits.

IV. RESULTS AND DISCUSSION

A. Observed errors

The memory models with smaller node sizes (72 nm and 63 nm, Table I) were only tested at VESPER with 200 MeV electrons. They did not show any response to the energetic electrons during the irradiation, and they were not subjected to irradiation tests with lower energy electrons.

During the irradiation tests, two types of errors attributed to SEE were observed in memory type IS42S86400B. One type manifested themselves as bit-flips, which resulted in a single recoverable erroneous read of a bit in a word. The other type was stuck bits. These were bits that returned faulty values more than once, while the bit had been rewritten in between the read operations. They were however generally stuck only for a few write/read cycles. An example of the pattern of errors in the stuck bits can be seen in Fig. 2. In the figure, the red dots represent initial errors, with the previous write and read of the same value in the bit not resulting in an error. The blue dots represent an error in the memory where also the previous write and read cycle of the same value in the bit did give an error. Note that the abscissa of Fig. 2 is irradiation time, since the write/read cycles are periodic in time and the pattern of recurring errors is more clearly visible like this, and is independent of flux fluctuations.

Many of these stuck bits in Fig. 2 were ISBs, i.e. bits that switch between being stuck, and being normally operational. This effect has been discussed e.g. in [13]–[15] with stuck bits observed during irradiation with other particle types than electrons. ISBs discussed in these publications have, like the ones found here, long periods of time where they are not stuck.

The number of detected errors during the tests present a sudden increase at a certain dose level (electron fluence). An example of this is shown in Fig. 3 for the SDF3 memory under 123 MeV electron irradiation after 50 krad(Si). Up to this dose level the errors follow a linear trend with the electron fluence. The same effect was seen in all memories of this model (IS42S86400B), and the point of onset of this error increase is displayed in Table III. The errors up to this point, following a linear trend with the electron fluence, are assumed to originate from SEE induced by the impinging electrons.

TABLE III
SUMMARY OF IRRADIATION RESULTS. THE OBSERVED ERRORS OCCURRING BEFORE THE FLUENCE LIMIT IN THE RIGHTMOST COLUMN ARE PRESENTED FOR EACH DUT.

ID	Electron energy (MeV)	Dose rate (rad(Si)/min)	Bit-flips	Stuck bits	Fluence at onset of error rate increase (e/cm ²)
SDF1	200	$1.9 \cdot 10^2$	10	11	$1.58 \cdot 10^{12}$
SDF3	123	$5.6 \cdot 10^2$	10	13	$1.61 \cdot 10^{12}$
SDF4	61	$7.2 \cdot 10^2$	10	13	$3.33 \cdot 10^{12}$
SDF5	20	$5.7 \cdot 10^2$	6	6	$2.78 \cdot 10^{12}$
SDG1	20	$8.2 \cdot 10^2$	2	5	$2.95 \cdot 10^{12}$
SDG3	6	$6.7 \cdot 10^2$	0	0	$2.67 \cdot 10^{12}$
SDG4	20	$2.5 \cdot 10^3$	2	6	$2.43 \cdot 10^{12}$
SDG5	20	$4.1 \cdot 10^2$	4	7	$4.52 \cdot 10^{12}$
SDG6	6 MV ^a	$5.0 \cdot 10^2$	0	0	50 krad(H ₂ O) ^a
SDB1	200	$1.9 \cdot 10^2$	0	0	$1.0 \cdot 10^{12}$ ^b
SDE1	200	$3.8 \cdot 10^2$	0	0	$1.8 \cdot 10^{12}$ ^b

^a Tested with 6 MV photon radiation field.

^b Total fluence on DUT, no errors observed.

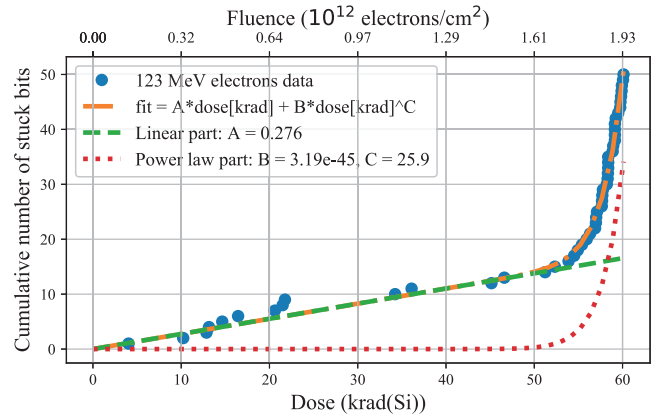


Fig. 3. Errors during irradiation with 123 MeV electrons at VESPER in memory SDF3. The figure shows the onset of new stuck bits in the memory as a function of the surface dose in Si and electron fluence. The trend of new errors has been shown with a fitted function, that is a sum of a linear part and a power law part. The fitting function is $errors = A \cdot dose[krad(Si)] + B \cdot dose[krad(Si)]^C$, where A , B and C are fitted parameters.

The number of such errors in each DUT is also presented in Table III.

Similar errors to the electron stuck bit SEEs observed here, are in e.g. [13], [14] discussed as single particle displacement damage effects (SPDDEs), where the errors are induced by single protons and neutrons that create damage clusters in a depletion region of the memory cells, increasing the leakage from the stored charge in the cells and causing the bits to become stuck. In [14] a power law dependency on the stuck bits as a function of particle fluence is also discussed, where the exponent (C in Fig. 3) according to Poisson statistics correspond to the number of single particle interactions in a sensitive region that are required to cause a stuck bit.

For the 123-MeV electron case in Fig. 3, there is an initial linear slope with single particle interactions causing stuck bits, followed by the error rate increase where around 26 particle

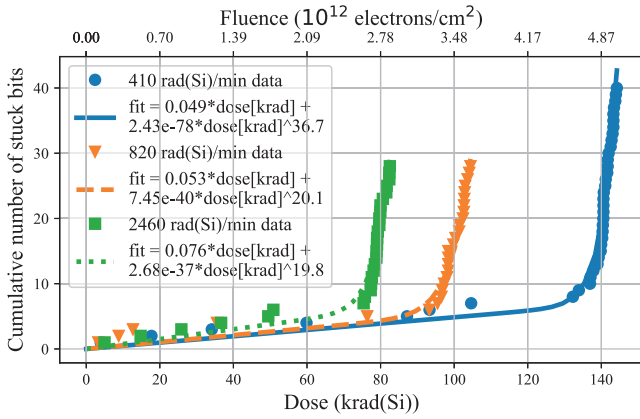


Fig. 4. Stuck bits found in DUTs SDG1, SDG4 and SDG5 at different dose rates of 20 MeV electrons, with fits to the data to show the initial linear region with errors originating from SEE, and the subsequent increase in errors due to the cumulative effects.

interactions are needed to induce the errors. This suggests that rare events induced by single electrons are capable of creating large enough damage clusters to create a stuck bits, while more common, smaller displacement damage complexes can accumulate, and eventually become large enough to also create a stuck bit.

The fitted factor C varied between 19 and 37 in the fits to the stuck bit data for all tested IS42S86400B devices. The fitted variable C seems to be quite sensitive to the fitting procedure, with fluctuations on the fitted values that were rather independent on particle type and energy, and should rather be viewed as a qualitative measure than an exact numerical value to rely on.

The error rate increase, and the consecutive annealing of the stuck bits discussed later in the paper, present competing effects. In Table III, the reported dose rate is the approximate median for most DUTs, and variations in dose rate occurred during the irradiation. However, in DUTs SDG1, SDG4 and SDG5 the dose rate was kept constant throughout the tests with 20 MeV electrons. The induced stuck bits for the different dose rates in these memories are shown in Fig. 4. In the figure it can be seen that the sharp increase in error rate occurs earlier at higher dose rates, when less time is allowed for the annealing to happen. At a low enough dose rate, the memory might thus not necessarily suffer this kind of break-down from the accumulated damage at all, if the annealing is faster than the damage cluster accumulation.

No SEEs were observed during the tests with 6 MeV electrons or 6 MV photons. Only the error increase due to the cumulative damage was observed. The stuck bits as a function of deposited dose for these tests are shown in Fig. 5. The dose level in this figure is calculated as described in Section III-B, with dose in Si for the electrons, and a water equivalent dose for photons. These results with no errors found before the sharp increase in errors for the cases with low-energy electrons and with photons suggest that these individual particles are not capable of inducing large enough damage clusters to cause stuck bits, but they can still induce smaller damage clusters

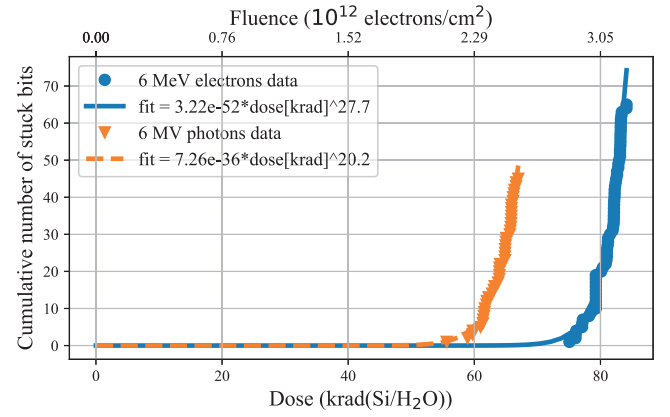


Fig. 5. Stuck bits found in DUTs SDG3 and SDG6 during the tests with 6 MeV electrons and 6 MV photons. Only the sharp increase in errors due to the cumulative damage is seen, and no SEEs before this increase is observed. The dose level is specified in krad(Si) for the electrons and krad(H₂O) for the photons.

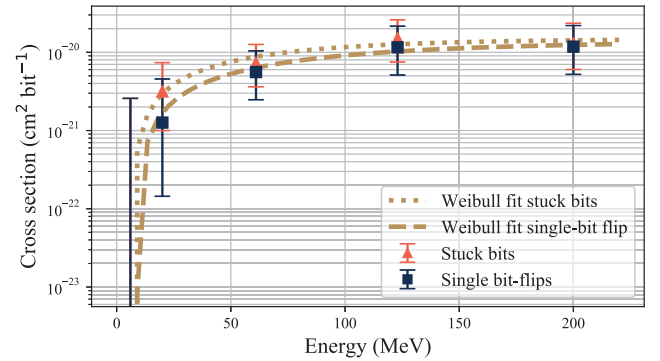


Fig. 6. Stuck bits and single bit-flip cross sections of electron irradiation under dynamic testing. The Weibull fits of the cross sections are also presented, which will be used later for a discussion of the memory behaviour in the Jovian environment. No events were observed for 6 MeV electrons, and only the upper limit is shown.

that may accumulate to large enough complexes which causes the bits to become stuck.

No errors were observed in the IS42S16320D/F memories during the irradiation with 200 MeV electrons. This could be due to a lower error cross section due to the smaller node sizes of the memories, but also due to other design changes between the different memory versions which are unknown to the authors.

B. Stuck bit and single bit-flip cross section

The calculated cross sections for the errors obtained before the increase in error rate are presented in Fig. 6. The error bars in the figure represent a 95 % confidence interval with a 20 % beam fluence uncertainty for the data points at energies over 20 MeV, and 10 % at 20 MeV and below. A similar number of stuck bits and single bit-flips were observed at each of the tested energies, and thus the cross sections for the two failure modes are similar.

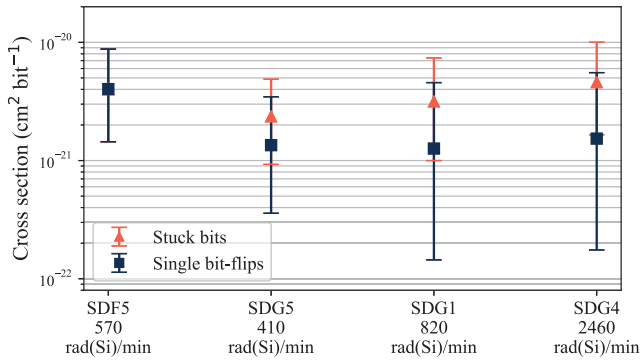


Fig. 7. Stuck bit and single bit-flip cross sections from tests with 20 MeV electrons at different dose rates. The dose rate on DUT SDF5 was varied during the test, while the dose rates for SDG5, SDG1 and SDG4 was kept constant.

In Fig. 6, the 20 MeV point is from the test with SDG1, which was tested at a dose rate of 820 rad(Si)/min. DUTs SDG4, SDG5 and SDF5 were also tested with 20 MeV electron irradiation, but at different dose rates. The resulting SEE cross sections from these tests are shown in Fig. 7, where all tests resulted in similar results for the calculated cross section independent of dose rate, with largely overlapping error bars as would be expected for SEE.

C. Damage in memory cells subject to SEE

The bits that are stuck have been damaged by the incident radiation, so that the storage capacitors in the memory cells are not anymore able to hold its charge during the refresh cycles of the memory, and the bits get stuck to their discharged state. For the cells exhibiting single bit-flips, the memory cell storage capacitor has been discharged due to the electron strike, but the cell can still hold the stored charge during the refresh cycles in the following write and read cycles of the test. Fig. 8 shows how the retention time distributions of the cells that have been subject to SEE during irradiation, compared to the total distribution of retention times of all the cells in the memory. This study was made for the memories SDF1, SDF3, SDF4 and SDF5 post-irradiation, with three different cell populations considered in each memory: all cells (All), cells that got stuck during irradiation (Stuck), and cell that exhibited a single bit-flip (Flipped).

The different populations of each memory were for each tested refresh frequency separately checked for failing bits. For the cells that had been subject to SEE during irradiation, the same words which contained the errors during irradiation were written with the same value as when the error occurred ('0' or '1') to the memory. One minute later, the data was read back, and the fraction of the population exhibiting errors at the reading of the data is displayed in Fig. 8. The same was done for all words in the memory, where the fraction of the total number of words failing at patterns of either all '0' or all '1' is displayed.

The population of cells that had SEEs fail earlier, at lower refresh frequencies, than the rest of the memory (i.e. all bit

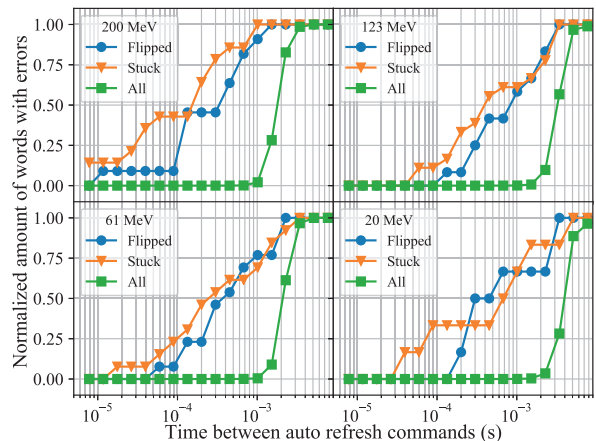


Fig. 8. The amount of words with bits that fail at given refresh frequencies, as a function of auto refresh command frequency of the memory (abscissa is $1/F_R$). The populations that are shown are the bits which had only one bit-flip during irradiation, bits that were stuck, and all bits in the memory. Data taken post irradiation for the four tested SDF# memories (see Table III).

population). Also, the population of bits that were stuck during irradiation seem, in general, to fail at lower refresh frequencies than the ones that had a bit-flip. Still, the behaviour of the stuck and the flipped populations, as seen in Fig. 8, are similar.

This can indicate that the mechanisms behind the different failure modes are similar, but differ mainly in the severity. The suggestion that displacement damage caused by single particles creating leakage paths, e.g. in a depletion region common to the storage capacitor and the access transistor [12], [14] (depending on the specific memory layout), is the cause for the stuck bits from SEE in this study is a likely case. This displacement damage would be caused by reaction products from nuclear interactions involving the energetic electrons [8], [9].

Since the cells that exhibited only a single bit-flip display similar behaviour in Fig. 8 to the bits that were stuck, and they display a worse data retention capability than the population of all cells, it is possible that the cause for the single bit-flips found in this study is the same as for the stuck bits. Looking at the behaviour in Fig. 2, some bits are stuck only twice or a few times, while others are stuck in many more instances. It is therefore reasonable that the same kind of failure could result in an error at only one occasion.

D. Retention time distributions and annealing

The retention time distribution of the words in the SDF5 memory during irradiation with 20 MeV electrons is presented in Fig. 9. This figure shows the number of words with bits that are stuck at different refresh frequencies at increasing dose levels. The nominal refresh frequency of the memories, 128 kHz, is marked in the figure with a dotted black line.

These distributions were produced by changing the auto refresh command frequency F_R of the memories (the abscissas in the figures are the inverse of this, $1/F_R$), then writing the memory with all '0' pattern, waiting 60 s, then reading back

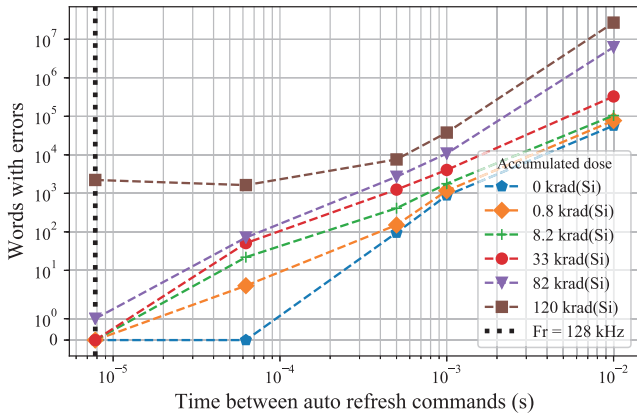


Fig. 9. Retention time distribution of the words in the SDF5 memory during 20 MeV electron irradiation at 5 different refresh frequencies at different deposited doses.

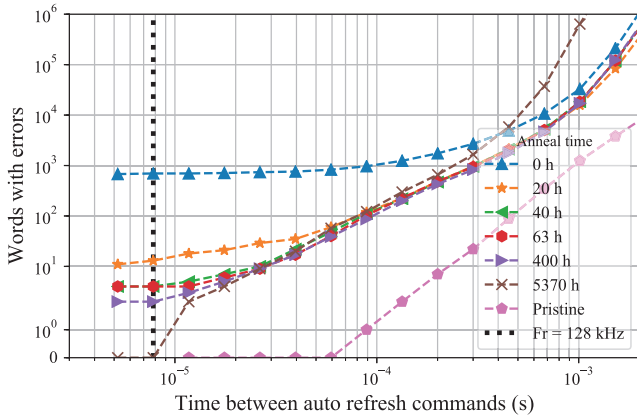


Fig. 10. Retention time distribution of the words in the SDF5 memory after 20 MeV electron irradiation after different annealing times.

the memory. Thereafter the procedure was repeated for an all '1' pattern. The sum of the words with errors in these tests is presented on the vertical axis.

The retention time distribution of the words in the SDF5 memory post-irradiation with 20 MeV electrons is presented in Fig. 10, where the annealing of the memory is shown. The memories were kept in room temperature (only room-temperature annealing was performed), and without bias when not characterized. A complete recovery to the pristine case is not observed in the annealing. Instead, the distribution of retention times is approaching one which is shifted upwards, with more words containing failing bits at each measurement point compared to the pristine case. As a comparison, this is the same type of data as is shown in Fig. 8 for the population of all bits in the SDF5 memory.

After the annealing time is in the time-scale of thousands of hours, the amount of errors at lower refresh frequencies start to increase dramatically, while the number of errors at high F_R continues to decrease. This is consistent with results in e.g. [11]. This behaviour, with a continuing decrease of errors at high F_R , and an increase of errors at low F_R after 10^3 h

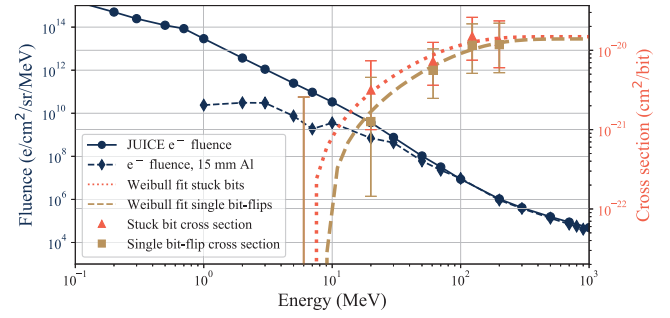


Fig. 11. The total differential electron fluence of the JUICE mission from [1], as well as the transported electron fluence through 15 mm Al. The Weibull fits of the electron cross sections from Fig. 6 are also presented.

of annealing time, is consistent in the tested memories in this study, both for memories tested with electrons and photons.

The increase in errors at low F_R might be due to an increase of interface traps, accumulating over the annealing time by the access transistor, storage capacitor, or closely located dielectric allowing the storage capacitor to leak its charge faster and reduce the retention time of the bits. At least up to the doses applied in this work, this effect has not been observed to affect the normal operation of the cells at 128 kHz.

V. IN-FLIGHT PREDICTIONS

Based on the cross sections presented in Fig. 6, and the expected electron environment during the JUICE mission [1] which is depicted in Fig. 11 along with the cross section Weibull fits, an estimation of the number of upsets the IS42S86400B memory would have during the JUICE mission was made. The mission duration is in total planned to be 11.1 years, with different phases of the mission receiving different fluxes of particles [1].

As an estimation, the presented differential fluence was multiplied with 4π to assume an isotropic radiation field, and also as an approximation an isotropic sensitivity of the component. The component has only been tested with electrons at a normal incidence angle, so the normal incidence angle sensitivity is used for the whole isotropic fluence. The cross section was then folded with the electron fluence over the energies between the cross section cut-off energy and 1 GeV, and multiplied with the number of bits in the memory to obtain an estimation of the number of upsets.

Geant4 was also used to simulate the resulting electron fluence after the original electron fluence had passed through a spacecraft shielding of 15 mm Al. The estimated errors from the shielded and non-shielded electron fluence are shown in Table IV. Due to the low error cross section very few electron-induced SEEs would be expected: 4 for the non-shielded case and 1 for the shielded. In a memory using an error detection and correction system, this low number would not present a problem in the usage.

Shielding thicknesses of 10 mm Al and 14 mm Al during the JUICE mission would result in a TID of 227 krad(Si) and 120 krad(Si) respectively [1], of which a large majority would originate from the trapped electron environment. These doses

TABLE IV
ESTIMATED NUMBER OF SEE FROM ELECTRONS IN IS42S86400B
DURING THE JUICE MISSION.

Fault	Non-shielded errors	15 mm Al-shielded errors
Stuck bits	2.7	0.6
Single bit-flips	1.1	0.4
Total	3.8	1.0

would translate to average dose rates of about 39 mrad(Si)/min and 21 mrad(Si)/min, instead of the $10^2 - 10^3$ rad(Si)/min which was used in the testing in this work. The memory tested at the lowest dose rate 410 rad(Si)/min in Fig. 4 failed due to the accumulated radiation damage after about 130 krad(Si). However, with the much lower dose rate encountered on the JUICE mission, it is not clear if the small damage clusters would anneal before accumulating and being capable to induce stuck bits even at 227 krad(Si). If a thicker shielding than 10 mm Al is used (e.g. 14 mm), then the mission dose values are comparable to the ones reached during some of the tests presented here.

VI. CONCLUSION

In this paper, high-energy electron irradiation is demonstrated to cause stuck bits and bit-flips in SDRAMs as SEEs, and cross sections for these failure modes are determined. These cross sections are put in relation to the Jovian environment, and a number of expected SEEs from electrons if the memory was to be used on the JUICE mission is estimated. The estimated number is low, 3.8 in total without shielding and 1.0 with 15 mm of Al shielding, and electron-induced SEEs are not expected to be a large problem if the memory is to be used on the mission.

The mechanism behind the two observed SEE failure modes stuck bits and single bit-flips is suggested to be the same. This is based on the similarity of the degraded retention time distributions of the cell populations consisting of bits that were stuck, and those that had bit-flips, compared to that of the total cell population.

The electron irradiation is found to degrade the memory cells on a long time scale. Annealing of the cell damage was observed, but also an increase in failing cells at low refresh rates was observed after long annealing times.

In these accelerated tests, where high dose rates and electron fluxes were utilized, a sharp increase in the number of errors in the memory was observed. This effect is attributed to the accumulation of smaller damage clusters, and occurs at lower dose levels for higher dose rates, when less time is allowed for annealing in between events.

To estimate the total performance of the memory in the JUICE environment, it would be needed to perform tests at low electron fluxes and dose rates. This because of the dose rate dependence on the memory response observed in this study. The temperatures effect on the annealing properties would also have to be investigated to be able to predict the memory response on board JUICE.

REFERENCES

- [1] JUICE Team, "JUICE environment specification," European Space Agency (ESA)/ESTEC, Revision 5 Issue 5, Feb. 2017, reference JS-14-09.
- [2] I. de Pater and D. E. Dunn, "VLA observations of Jupiter's synchrotron radiation at 15 and 22 GHz," *Icarus*, vol. 163, no. 2, pp. 449–455, Jun. 2003, doi: [https://doi.org/10.1016/S0019-1035\(03\)00068-X](https://doi.org/10.1016/S0019-1035(03)00068-X).
- [3] M. de Soria-Santacruz, H. B. Garrett, R. W. Evans, I. Jun, W. Kim, C. Paranicas, and A. Drozdov, "An empirical model of the high-energy electron environment at Jupiter," *J. Geophys. Res. Space Phys.*, vol. 121, no. 10, p. 9732–9743, Oct. 2016, doi: <https://doi.org/10.1002/2016JA023059>.
- [4] M. P. King, R. A. Reed, R. A. Weller, M. H. Mendenhall, R. D. Schrimpf, B. D. Sierawski *et al.*, "Electron-induced single-event upsets in static random access memory," *IEEE Trans. Nucl. Sci.*, vol. 60, no. 6, pp. 4122–4129, Dec. 2013, doi: [10.1109/TNS.2013.2286523](https://doi.org/10.1109/TNS.2013.2286523).
- [5] A. Samaras, P. Pourrouquet, N. Sukhaseum, L. Gouyet, B. Vandeveld, N. Charty *et al.*, "Experimental characterization and simulation of electron-induced SEU in 45-nm CMOS technology," *IEEE Trans. Nucl. Sci.*, vol. 61, no. 6, pp. 3055–3060, Dec. 2014, doi: [10.1109/TNS.2003.820727](https://doi.org/10.1109/TNS.2003.820727).
- [6] M. J. Gadlage, A. H. Roach, A. R. Duncan, M. W. Savage, and M. J. Kay, "Electron-induced single-event upsets in 45-nm and 28-nm bulk CMOS SRAM-based FPGAs operating at nominal voltage," *IEEE Trans. Nucl. Sci.*, vol. 62, no. 6, pp. 2717–2724, Dec. 2015, doi: [10.1109/TNS.2015.2491220](https://doi.org/10.1109/TNS.2015.2491220).
- [7] J. M. Trippe, R. A. Reed, R. A. Austin, B. D. Sierawski, R. A. Weller, E. D. Funkhouser *et al.*, "Electron-induced single event upsets in 28 nm and 45 nm bulk SRAMs," *IEEE Trans. Nucl. Sci.*, vol. 62, no. 6, pp. 2709–2716, Dec. 2015, doi: [10.1109/TNS.2015.2496967](https://doi.org/10.1109/TNS.2015.2496967).
- [8] M. Tali, R. G. Alía, M. Brugger, V. Ferlet-Cavrois, R. Corsini, W. Farabolini *et al.*, "High-energy electron-induced SEUs and jovian environment impact," *IEEE Trans. Nucl. Sci.*, vol. 64, no. 8, pp. 2016–2022, Aug. 2017, doi: [10.1109/TNS.2017.2713445](https://doi.org/10.1109/TNS.2017.2713445).
- [9] —, "Mechanisms of electron-induced single-event latchup," *IEEE Trans. Nucl. Sci.*, vol. 66, no. 1, pp. 437–443, Jan. 2019.
- [10] H. Shindou, S. Kuboyama, N. Ikeda, T. Hiraio, and S. Matsuda, "Bulk damage caused by single protons in SDRAMs," *IEEE Trans. Nucl. Sci.*, vol. 50, no. 6, pp. 1839–1845, Dec. 2003, doi: [10.1109/TNS.2003.820727](https://doi.org/10.1109/TNS.2003.820727).
- [11] J. P. David, F. Bezerra, E. Lorfèvre, T. Nuns, and C. Inguibert, "Light particle-induced single event degradation in SDRAMs," *IEEE Trans. Nucl. Sci.*, vol. 53, no. 6, pp. 3544–3549, Dec. 2006, doi: [10.1109/TNS.2006.886210](https://doi.org/10.1109/TNS.2006.886210).
- [12] L. D. Edmonds and L. Z. Scheick, "Physical mechanisms of ion-induced stuck bits in the hyundai 16M x 4 SDRAM," *IEEE Trans. Nucl. Sci.*, vol. 55, no. 6, pp. 3265–3271, Dec. 2008, doi: [10.1109/TNS.2008.2006902](https://doi.org/10.1109/TNS.2008.2006902).
- [13] A. M. Chugg, J. McIntosh, J. Burnell, P. H. Duncan, and J. J. Ward, "Probing the nature of intermittently stuck bits in dynamic RAM cells," *IEEE Trans. Nucl. Sci.*, vol. 57, no. 6, pp. 3190–3198, Dec. 2010, doi: [10.1109/TNS.2010.2084103](https://doi.org/10.1109/TNS.2010.2084103).
- [14] A. M. Chugg, A. J. Burnell, P. H. Duncan, S. Parker, and J. J. Ward, "The random telegraph signal behavior of intermittently stuck bits in SDRAMs," *IEEE Trans. Nucl. Sci.*, vol. 56, no. 6, pp. 3057–3064, Dec. 2009, doi: [10.1109/TNS.2009.2032184](https://doi.org/10.1109/TNS.2009.2032184).
- [15] V. Goiffon, T. Bilba, T. Deladerrière, G. Beaugendre, A. Le-Roch, A. Dion *et al.*, "Radiation induced variable retention time in dynamic random access memories," *IEEE Trans. Nucl. Sci.*, vol. 67, no. 1, pp. 234–244, Jan. 2020, doi: [10.1109/TNS.2019.2956293](https://doi.org/10.1109/TNS.2019.2956293).
- [16] A. Samaras, B. Vandeveld, N. Sukhaseum, N. Charty, A. Rodriguez, F. Wrobel *et al.*, "Experimental characterization and in-flight observation of weakened cell in SDRAM," in *2015 15th European Conference on Radiation and Its Effects on Components and Systems (RADECS)*, 2015, pp. 110–117, doi: [10.1109/RADECS.2015.7365611](https://doi.org/10.1109/RADECS.2015.7365611).
- [17] ISSI, *IS42S86400B, IS42S16320B, IS45S16320B - 64M x 8, 32M x 16, 512Mb SYNCHRONOUS DRAM, Rev. H*, Integrated Silicon Solution, Inc., Dec. 2011, accessed on: August 31, 2020. [Online]. Available: <http://www.issi.com/WW/pdf/42S16320B-86400B.pdf>
- [18] —, *IS42/45R86400D/16320D/32160D IS42/45S86400D/16320D/32160D - 16Mx32, 32Mx16, 64Mx8 512Mb SDRAM, Rev. B*, Integrated Silicon Solution, Inc., May 2015, accessed on: October 1, 2020. [Online]. Available: http://www.issi.com/WW/pdf/42-45R-S_86400D-16320D-32160D.pdf

- [19] —, *IS42R86400F/16320F, IS45R86400F/16320F, IS42S86400F/16320F, IS45S86400F/16320F - 32Mx16, 64Mx8 512Mb SDRAM, Rev. B1*, Integrated Silicon Solution, Inc., Jul. 2017, accessed on: October 1, 2020. [Online]. Available: http://www.issi.com/WW/pdf/42-45R-S_86400F-16320F.pdf
- [20] Terasic, *DE0-CV User Manual*, Terasic Inc., May 2015, accessed on: October 1, 2020. [Online]. Available: <https://www.terasic.com.tw/cgi-bin/page/archive.pl?Language=English&CategoryNo=167&No=921&PartNo=4>
- [21] L. Dilillo, G. Tsiligiannis, V. Gupta, A. Bosser, F. Saigne, and F. Wrobel, "Soft errors in commercial off-the-shelf static random access memories," *Semiconductor Science and Technology*, vol. 32, no. 1, p. 013006, dec 2016, doi: 10.1088/1361-6641/32/1/013006.
- [22] K. Sjobak, E. Adli, C. A. Lindstrom, M. Bergamaschi, S. Burger, R. Corsini *et al.*, "Status of the CLEAR Electron Beam User Facility at CERN," in *Proc. 10th International Particle Accelerator Conference (IPAC'19), Melbourne, Australia, 19-24 May 2019*, ser. International Particle Accelerator Conference, no. 10, Geneva, Switzerland, Jun. 2019, pp. 983–986, <https://doi.org/10.18429/JACoW-IPAC2019-MOPTS054>.
- [23] H. Kettunen, *Varian Clinac linear accelerator*, University Of Jyväskylä, Aug. 2020, accessed on: October 1, 2020. [Online]. Available: <https://www.jyu.fi/science/en/physics/research/infrastructures/research-instruments/miscellaneous-instruments/clinac>
- [24] S. Agostinelli, J. Allison, K. Amako, J. Apostolakis, H. Araujo, P. Arce *et al.*, "Geant4—a simulation toolkit," *Nucl. Instrum. Methods Phys. Res. A, Accel. Spectrom. Detect. Assoc. Equip.*, vol. 506, no. 3, pp. 250–303, 2003.
- [25] IBA, *DETECTORS For Relative and Absolute Dosimetry - Ionization chambers and diode detectors*, IBA Dosimetry, 2018, accessed on: October 1, 2020. [Online]. Available: https://www.iba-dosimetry.com/fileadmin/user_upload/products/02_radiation_therapy/_Detectors/Detectors-RD-_-AD_Rev.3_0718_E.pdf
- [26] M. J. Berger, J. S. Coursey, M. A. Zucker, and J. Chang, "Stopping-power & range tables for electrons, protons, and helium ions," NIST, Physical Measurement Laboratory, NIST Standard Reference Database 124, Jul. 2017, DOI: <https://dx.doi.org/10.18434/T4NC7P>.
- [27] D. M. Long, D. G. Millward, R. L. Fitzwilson, and W. L. Chadsey, "Handbook for dose enhancement effects in electronic devices," Technical Report, Science Applications, Incorporated, Mar. 1983.



PII

**TECHNOLOGY DEPENDENCE OF STUCK BITS AND SINGLE
EVENT UPSETS IN 110, 72, AND 63-NM SDRAMs**

by

Daniel Söderström, Lucas Matana Luza, André Martins Pio de Mattos, Thierry Gil,
Heikki Kettunen, Kimmo Niskanen, Arto Javanainen, and Luigi Dilillo

Submitted to IEEE Trans. Nucl. Sci., under review.

Request a copy from author.



PIII

RADIOLUMINESCENCE RESPONSE OF CE-, CU-, AND GD-DOPED SILICA GLASSES FOR DOSIMETRY OF PULSED ELECTRON BEAMS

by

Daniel Söderström, Heikki Kettunen, Adriana Morana, Arto Javanainen, Youcef Ouerdane, Hicham El Hamzaoui, Bruno Capoen, Géraud Bouwmans, Mohamed Bouzaoui and Sylvain Girard

MDPI Sensors, vol. 21, no. 22, p. 7523, Nov. 2021

<https://doi.org/10.3390/s21227523>

© CC BY 4.0.

Article

Radioluminescence Response of Ce-, Cu-, and Gd-Doped Silica Glasses for Dosimetry of Pulsed Electron Beams

Daniel Söderström ^{1,*}, Heikki Kettunen ¹, Adriana Morana ², Arto Javanainen ^{1,3}, Youcef Ouerdane ², Hicham El Hamzaoui ^{4,*}, Bruno Capoen ⁴, Géraud Bouwmans ⁴, Mohamed Bouazaoui ⁴ and Sylvain Girard ²

¹ Department of Physics, University of Jyväskylä, Surfontie 9D, 40500 Jyväskylä, Finland; heikki.i.kettunen@jyu.fi (H.K.); arto.javanainen@jyu.fi (A.J.)

² UJM, CNRS, IOGS, Laboratoire Hubert Curien, University of Lyon, UMR 5516, 18 rue Prof. B. Laurus, F-42000 Saint-Etienne, France; adriana.morana@univ-st-etienne.fr (A.M.); ouerdane@univ-st-etienne.fr (Y.O.); sylvain.girard@univ-st-etienne.fr (S.G.)

³ Department of Electrical and Computer Engineering, Vanderbilt University, Nashville, TN 37235, USA

⁴ Univ-Lille, CNRS, UMR 8523-PhLAM-Physique des Lasers Atomes et Molécules, F-59000 Lille, France; bruno.capoen@univ-lille.fr (B.C.); geraud.bouwmans@univ-lille.fr (G.B.); mohamed.bouazaoui@univ-lille.fr (M.B.)

* Correspondence: daniel.p.soderstrom@jyu.fi (D.S.); hicham.el-hamzaoui@univ-lille.fr (H.E.H.)



Citation: Söderström, D.; Kettunen, H.; Morana, A.; Javanainen, A.; Ouerdane, Y.; El Hamzaoui, H.; Capoen, B.; Bouwmans, G.; Bouazaoui, M.; Girard, S. Radioluminescence Response of Ce-, Cu-, and Gd-Doped Silica Glasses for Dosimetry of Pulsed Electron Beams. *Sensors* **2021**, *21*, 7523. <https://doi.org/10.3390/s21227523>

Academic Editors: Flavio Esposito, Agostino Iadicco, Stefania Campopiano, Andrei Stancalie and Flavio Esposito

Received: 13 October 2021

Accepted: 8 November 2021

Published: 12 November 2021

Publisher's Note: MDPI stays neutral with regard to jurisdictional claims in published maps and institutional affiliations.



Copyright: © 2021 by the authors. Licensee MDPI, Basel, Switzerland. This article is an open access article distributed under the terms and conditions of the Creative Commons Attribution (CC BY) license (<https://creativecommons.org/licenses/by/4.0/>).

Abstract: Radiation-induced emission of doped sol-gel silica glass samples was investigated under a pulsed 20-MeV electron beam. The studied samples were drawn rods doped with cerium, copper, or gadolinium ions, which were connected to multimode pure-silica core fibers to transport the induced luminescence from the irradiation area to a signal readout system. The luminescence pulses in the samples induced by the electron bunches were studied as a function of deposited dose per electron bunch. All the investigated samples were found to have a linear response in terms of luminescence as a function of electron bunch sizes between 10^{-5} Gy/bunch and 1.5×10^{-2} Gy/bunch. The presented results show that these types of doped silica rods can be used for monitoring a pulsed electron beam, as well as to evaluate the dose deposited by the individual electron bunches. The electron accelerator used in the experiment was a medical type used for radiation therapy treatments, and these silica rod samples show high potential for dosimetry in radiotherapy contexts.

Keywords: dosimetry; electron accelerator; optical fiber; point dosimeter; pulsed electron beam; radiation-induced luminescence

1. Introduction

A large part of the previous studies on radiation-induced luminescence (RIL) of doped silica glasses for ionizing radiation dosimetry has been done under X-ray irradiation. Regarding particle beams, most of the studies focused on proton beams. Examples of such studies are reported in [1], where Ce³⁺- and Cu⁺-doped samples were evaluated for proton therapy dosimetry purposes, and in [2], where Gd³⁺-doped silica glass was also studied. In these studies, a dose rate range of about 0.02–0.30 Gy/s from a continuous beam was used, and proton energies between 8 and 63 MeV were investigated. In [2], dose-depth profiles were also studied using Gd-, Cu-, and Ce-doped samples. A further review of optical fibre-based dosimetry for radiotherapy is reported in [3].

Ce-doped silica glass has been studied under X-ray irradiation in e.g., [4], where the optically stimulated luminescence (OSL) and RIL properties of the sample were investigated, and a linear RIL output for continuous dose rates between at least 26 and 1187 mGy/s was found. The electronic transition 4f–5d in Ce³⁺ ions is the basis for RIL emission, which is discussed in e.g., [4–6].

Ce-activated silica glass was also studied in [5]. The doped glass was tested with a continuous X-ray beam up to a dose rate of 50 Gy/s, with a linear output up to 30 Gy/s. At dose rates higher than 30 Gy/s, a luminescence response over the linear trend was observed.

Silica glass doped with Gd^{3+} -ions has been studied in [7], where the RIL response under steady-state X-ray irradiation was found to be linear between at least $125 \mu Gy(SiO_2)/s$ and $12.25 Gy(SiO_2)/s$. The RIL of Gd^{3+} ions is ascribed to the transition between the ${}^6P_{7/2}$ and ${}^8S_{7/2}$ levels [2,7,8].

Cu-doped silica samples were studied in e.g., [9], in the shape of a photonic crystal fibre (PCF) under UV light excitation, and in [10], under X-ray irradiation. In [10], a linear trend of the luminescence response was also reported up to a dose rate of $30 Gy/s$, and then a response over the linear trend above $30 Gy/s$, as was the case for Ce-doped samples in [5]. In Cu^+ ions, the transitions responsible for the RL emission are those from the state $3d^94s$ to the ground state $3d^{10}$ [9,11].

Very limited results of doped silica glass RIL responses to pulsed electron beams exist in the literature. In [12], a scintillating material (terbium-activated gadolinium oxysulfide) was placed in contact with a light-guiding fibre. The sample was then subjected to a beam of pulsed X-rays from a clinical linear accelerator (Clinac[®]). Studies of electron beams include those of thermoluminescence (TL) of Ge-doped optical fibers, such as in [13,14], and the same type of samples has been tested with other particles in e.g., [15]. The scintillation and OSL response of a Cu^+ -doped quartz glass was investigated in electron and X-ray beams from a Clinac in [16,17], where the sample was used to measure the total dose deposited during radiation runs.

In this paper, the RIL responses of Ce-, Cu-, and Gd-doped sol-gel silica glasses under a pulsed electron beam are investigated. The emission properties, and possibilities of monitoring the beam pulse-by-pulse with these samples are presented.

The interest and possibility of using these types of samples for dosimetry in the context of radiation therapy [1,2] makes the investigation of their responses to pulsed electron beams highly relevant. The particle accelerator used for irradiation tests in this study is a Clinac, and a characterization of the doped sol-gel silica rods in the pulsed Clinac electron beam opens the prospect of using the doped rods for dosimetry in a wider range of radiation therapy contexts.

2. Materials and Methods

2.1. Tested Samples

The tested materials were sol-gel glass rods. Further information regarding the production and fabrication of these samples can be found in previous publications, e.g., in [18,19]. Each sample, consisting of a rod drawn from doped silica glass, was fusion-spliced to $500\text{-}\mu m$ core multimode pure-silica core optical fibers (here referred to as transport fibers) to guide the induced RIL to the read-out electronics. The radioluminescent rods were approximately 1 cm long and 0.5 mm thick. Information about the tested samples and their doping concentrations are listed in Table 1.

Table 1. Summary of tested samples

Sample	Dopant	Dopant Concentration (wt%)
Ce-rod	Ce^{3+}	0.07
Cu-rod	Cu^+	0.07
Gd-rod	Gd^{3+}	0.1

2.2. Test Setup

At the end of the transport fiber, the signal readout system was located. For the tests of the response of the fibers as a function of electron pulse size, the readout system consisted of a photomultiplier tube (PMT) to convert the incident light to a voltage pulse, which was collected in an oscilloscope with high input impedance (1 M Ω).

The PMT, a Hamamatsu H9305-13 [20], was encased in a dark metal casing where the luminescent light from the sample could be collected from the transport fiber in the PMT window without background light contamination. A schematic of the PMT setup and a sample is shown in Figure 1, where the whole system was kept in darkness to

shut out parasitic light. The transport fibers were running through a black tube, and the samples were covered with dark tape. Between the transport fiber and the PMT, an optical band-pass filter was placed to select a relevant wavelength span that included the RIL. The used filter was thus specific for each sample.

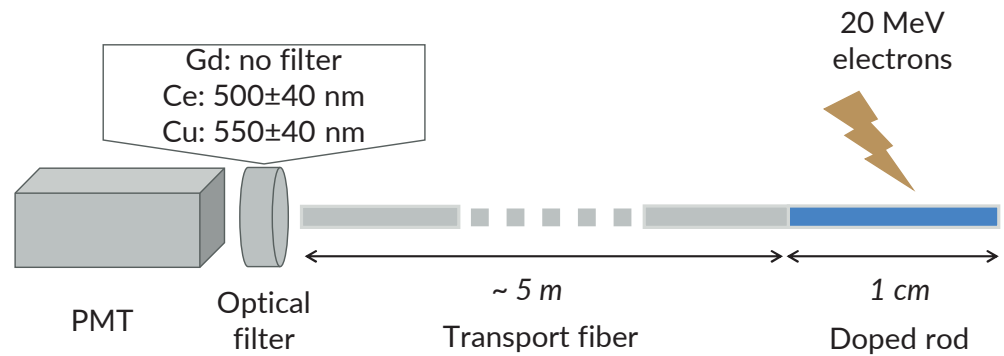


Figure 1. Schematic overview of the setup, where radiation-induced luminescence (RIL) in the doped rods are transported to a photomultiplier tube (PMT) through an optical filter.

To measure the optical emission spectra from the samples, an Ocean Optics USB2000+ UV-VIS-ER spectrometer [21] was used. The transport fiber was then placed directly against the spectrometer window, which thus replaces the optical filter and PMT in Figure 1.

2.3. Test Methodology

To investigate the RIL response of the samples when subjected to a pulsed beam, a large number of RIL pulses were collected at a fixed beam setting. Then, the properties of the collected pulses in the oscilloscope were investigated after irradiation. The experimental procedure was the following for the different samples:

1. Fix a constant electron bunch size and frequency in the accelerator;
2. Start irradiation and keep on for circa 30 s, by irradiating until a fixed dose value;
3. Save the collected trace from the oscilloscope containing RIL pulses from the 30 s of irradiation;
4. Tune to a different electron bunch size and repeat.

During irradiation, a Si-diode detector was also located in the beam. The signal from this detector was saved as well, and used to identify electron bunches also in certain beam configurations where the signal in the tested sample was small. Such configurations consist, for example, in a shielded sample, in a sample positioned outside of the beam, or for very small bunch sizes.

The saved traces of pulses were analyzed post-irradiation in terms of the height and area of the separate pulses. One pulse from a run with the Ce-rod sample is shown in Figure 2, where the separate procedures for determining the height and area of the pulses are presented. The baseline for the pulse was calculated as the average signal level immediately before the pulse, and the height of the pulse was recorded as the absolute difference between the pulse maximum and the calculated baseline, as shown in orange in the figure. The area was calculated as the absolute value of the integral of the pulse with respect to the calculated baseline, so that effectively the pulse area below the zero level was counted as positive, and the area above the zero level as negative.

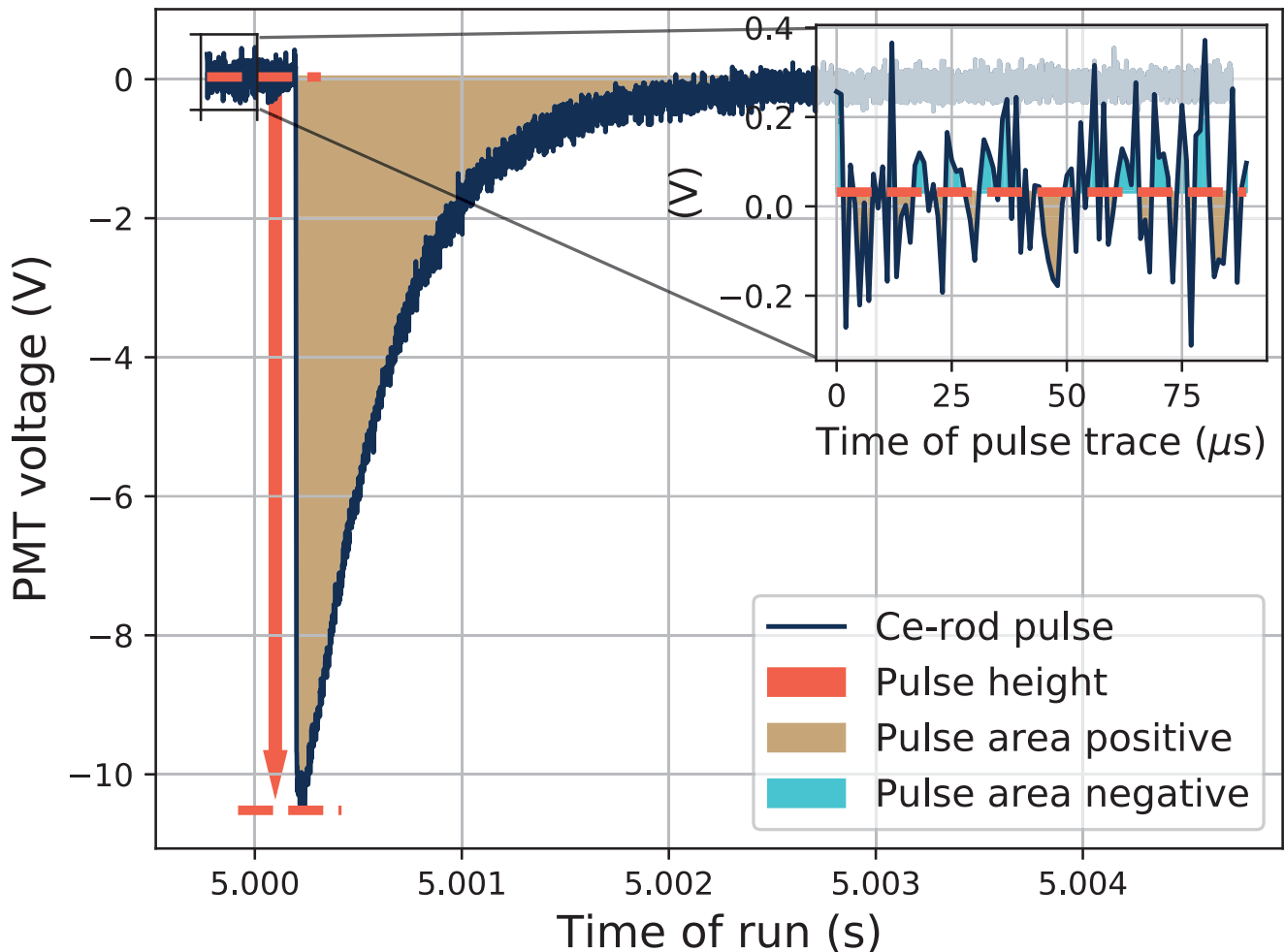


Figure 2. Example of one recorded pulse from a test using the Ce-rod, where the methods of calculating the height and area of the pulses are presented.

2.4. Irradiation Facility, RADEF

The irradiation experiments presented in this paper were performed at the radiation effects facility (RADEF) at the accelerator laboratory of the University of Jyväskylä, Finland. A Varian Clinac 2100C/D [22] was used to generate the electron beam that was used in the experiments. At the facility, 6, 9, 12, 16, and 20 MeV electrons are available, with dose rates between 1 and 10 Gy(H₂O)/min in standard operation. The dose rates mentioned here correspond to the dose rate at maximum dose depth in water. The machine was, however, not utilized in the standard mode of operation during the experiments presented in this paper, but instead used in a manner allowing for manual tuning of the amount of electrons present in the separate electron bunches from the machine.

In the standard mode of operation (which was not utilized here), 5- μ s long electron bunches are delivered at a frequency of up to 200 Hz when the machine is set to a dose rate of 10 Gy(H₂O)/min. When the dose rate is lowered, an increasing number of 5- μ s electron bunches are removed, so that when, e.g., running at 1 Gy(H₂O)/min, 10 times fewer bunches are present than in the 10 Gy(H₂O)/min operation, but the sizes of the individual electron bunches stay the same. This is shown for a few dose rate settings in Figure 3a, and is also discussed in e.g., [12]. In Figure 3, the PMT signal from consecutive electron bunches collected in an oscilloscope are shown (see Section 2.2) for different

operating modes and different dose rates. The figures are made using the signal from a Cu-doped rod.

In this work, 20-MeV electrons were used at different dose rates, where the dose rate was modulated in a different manner than described above. Here the automatic dose rate regulation of the machine was turned off, and a certain bunch frequency was fixed. The bunch frequencies that were used were 20 and 200 Hz, corresponding to electron bunches delivered every 50 ms and 5 ms. Then the sizes of the electron bunches at the fixed frequency could be manually tuned by changing the current to the electron gun. This way, the responses of the samples to different sizes of electron bunches could be investigated. The dose rate tuning in this operating mode is shown in Figure 3b.

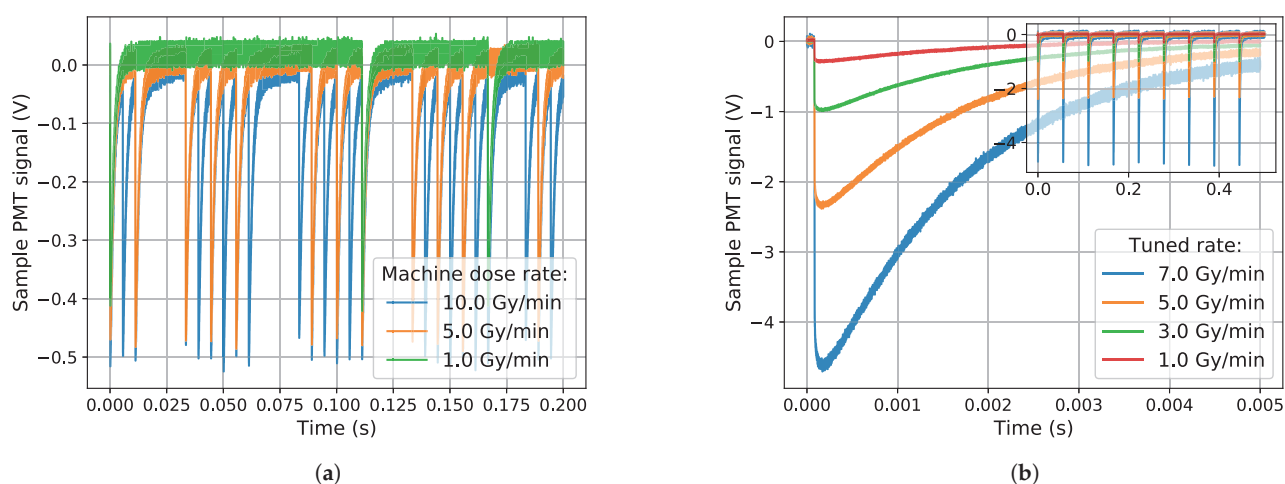


Figure 3. Dose rate tuning of the electron machine in different operating modes, recorded using a Cu-doped rod. (a) The standard dose rate tuning scheme is shown in the figure, where the bunch frequency is automatically modulated while the bunch sizes are kept constant. (b) The operation mode used in the experiments, where the bunch frequency is kept constant (shown in the figure inset) while the electron bunch size is tuned (see the varying size of the PMT pulses).

Changing the electron bunch sizes, so they become larger than normal, affects the functionality of the built-in dosimetry system of the electron accelerator. In the accelerator, there are ionization chambers which monitor the outgoing accelerator beam, which are meant to handle electron bunches of a certain size as shown in Figure 3a. As the bunches get larger, non-linearities in the built-in dosimeters are observed. This can be seen in Figure 4, where the nominal bunch size of the machine corresponds to a dose rate of 1 Gy(H₂O)/min.

The saturation of the Clinacs internal ionization chambers at large bunch sizes is shown in Figure 4a, comparing the dose recorded by the machine with an external dosimeter (IBA PPC40 dosimeter [23]) at a maximum dose depth in water. Comparing this external dosimeter with a second one (IBA FC65-P [23]) located in the beam periphery in air, results in a linear relationship as seen in Figure 4b. The external dosimeters were used to ensure that the correct values of dose and dose rate were recorded, and they were used as the reference dosimeters during the experiments in the tests where electron bunches larger than nominally was used.

The values of dose and dose per electron bunch that are reported in this study refers to the electron fluence, which corresponds to said dose at maximum dose depth in water, and not the absorbed dose in the tested samples. During irradiation, the samples were located under a thin layer of darkening material (a black plastic sheet and a layer of black tape), but it can be approximated as the samples being located in air and being subjected to the immediate electron beam.

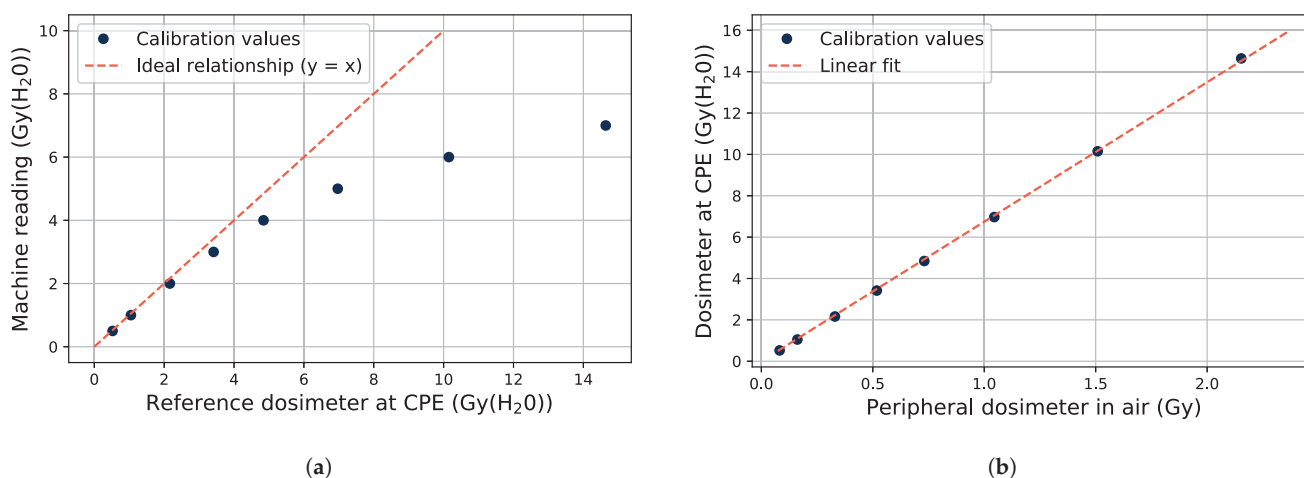


Figure 4. Response of the built-in dosimetry of the accelerator and external dosimeters when the electron bunch sizes are changed. The data points are each taken at a fixed dose rate (bunch size) for one minute of irradiation at a bunch frequency of 20 Hz. At this setting, the bunch size corresponding to the nominal machine value is 1 Gy/min. (a) Accelerator internal dosimetry against an external dosimeter at maximum dose depth in water. (b) Dosimeter at maximum dose depth in water against a peripheral dosimeter in air.

3. Results and Discussion

3.1. Emission Spectra of the Samples

The measured RIL emission spectra of the samples are shown in Figure 5 for the different types of samples under 20-MeV electron irradiation. The emission spectra for the three different dopants correspond well to previously reported RIL emission spectra in the literature where X-rays were used as the excitation source. The reported spectra are all dominated by the expected RIL wavelengths without visible contamination from other sources such as Čerenkov radiation. No optical filters were used while obtaining the spectra presented in Figure 5.

The emission spectrum of the Gd-doped sample is a narrow peak at 314 nm. This is the same result as was discussed in [7], where a narrow emission peak at 314 nm was found under both X-ray and 275-nm UV excitation. The emission spectra of a Cu-doped sample under X-ray and 325-nm UV excitation was compared in e.g., [24], where the UV excited spectra was seen to be slightly broadened. This was ascribed to an increased emission from non-bridging oxygen hole centers (NBOHC) in the UV excitation case. The corresponding spectrum in Figure 5 peaks at 543 nm, and does not show this broadening. It is similar to the reported X-ray excited spectrum in [24].

This same comparison was done for a Ce-doped sample in [4] between X-ray and a 351-nm UV excited emission spectra. The X-ray emission spectrum in that study corresponds well to the one in Figure 5, however the knee structure around 450 nm is slightly less pronounced in [4] than it is here. Such differences can however be masked or amplified depending on the total transfer function of the detection system that was used (the combination of transport fiber and spectrometer), on calibrations of the spectrometer, and on potential post-processing of the data.

For the following tests, optical band-pass filters at 500 ± 40 nm and 550 ± 40 nm were used for the Ce-rod and the Cu-rod respectively, in front of the PMT window. No optical band-pass filter was used for the Gd-rod tests, since none were available that could cover the 314-nm emission peak of Gd.

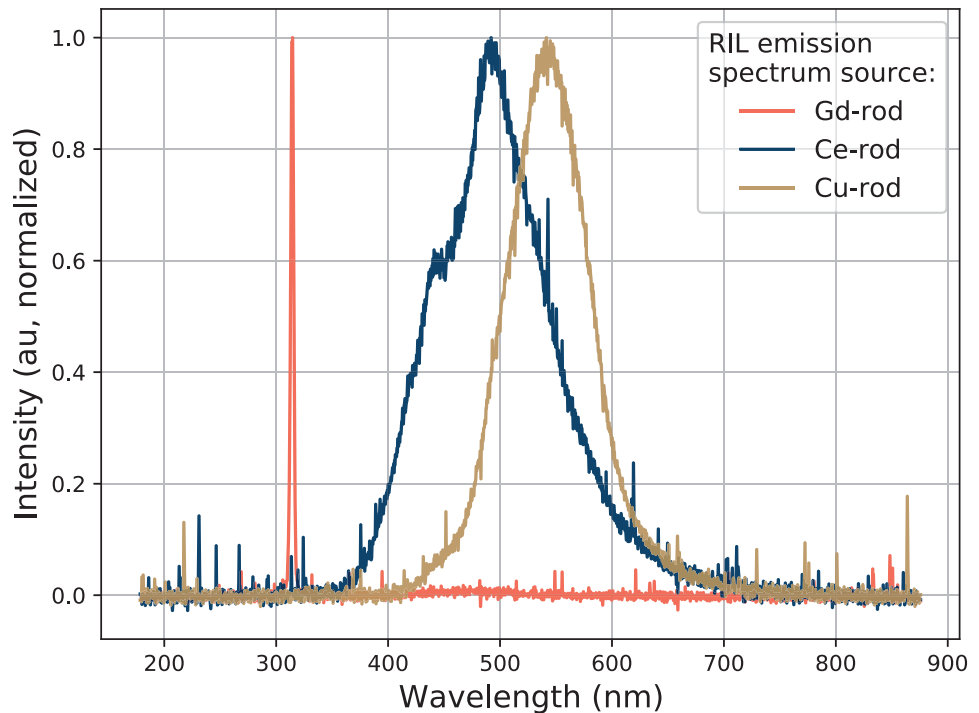


Figure 5. RIL emission spectra taken from the different sample types.

3.2. Sample Response to Varying Electron Pulse Sizes

3.2.1. Variations of Output Pulse Height

Examples of collected pulses in the oscilloscope are shown in Figure 6. All the resulting pulses from the PMT for half a minute of irradiation at a fixed electron bunch frequency of 20 Hz, and at constant electron bunch sizes of 9.7×10^{-4} Gy/bunch impinging on the Ce-doped sample are displayed in the figure. The electron bunch that resulted in the pulse at 1.0 V in pulse height was the first recorded bunch of the run. This is a common behavior among all the runs in that the machine reaches the set bunch size after one or two smaller initial bunches.

The relation between the height of the pulses and the size of the electron bunches is seen in Figure 7 for different sample dopants, and for dose rates up to 1.5×10^{-2} Gy/bunch. A note to keep in mind is that this dose rate corresponds to an instantaneous dose rate during a 5- μ s pulse of 3 kGy/s. The data is based on 30-s irradiation runs at each electron bunch size, and the data points are located at the average pulse height (see Figures 2 and 6). The error bars represent, in the y -axis direction, the standard deviation of the pulse height, and in the x -axis direction, 10% of the reported dose per pulse.

The results in Figure 7 show a linear trend over the whole tested range of bunch sizes for the Ce- and Cu-doped rods. For the Gd-doped rod, the point at 2×10^{-5} Gy/bunch is slightly above the fitted linear slope. The signal light output was smaller from this sample than the others in terms of the pulse height, and at smaller electron bunches, the signal was influenced by noise. Thus a fit to the data containing a constant factor taking into account the background noise level in the signal gives a better representation of the sample response for small electron bunches. The constant factor (m in the figure legend) in the dotted line was fitted to a value of $3.8 \times \sigma_{noise}$, where $\sigma_{noise} = 0.6$ mV was the calculated standard deviation of the signal noise in the data point at 2×10^{-5} Gy/bunch.

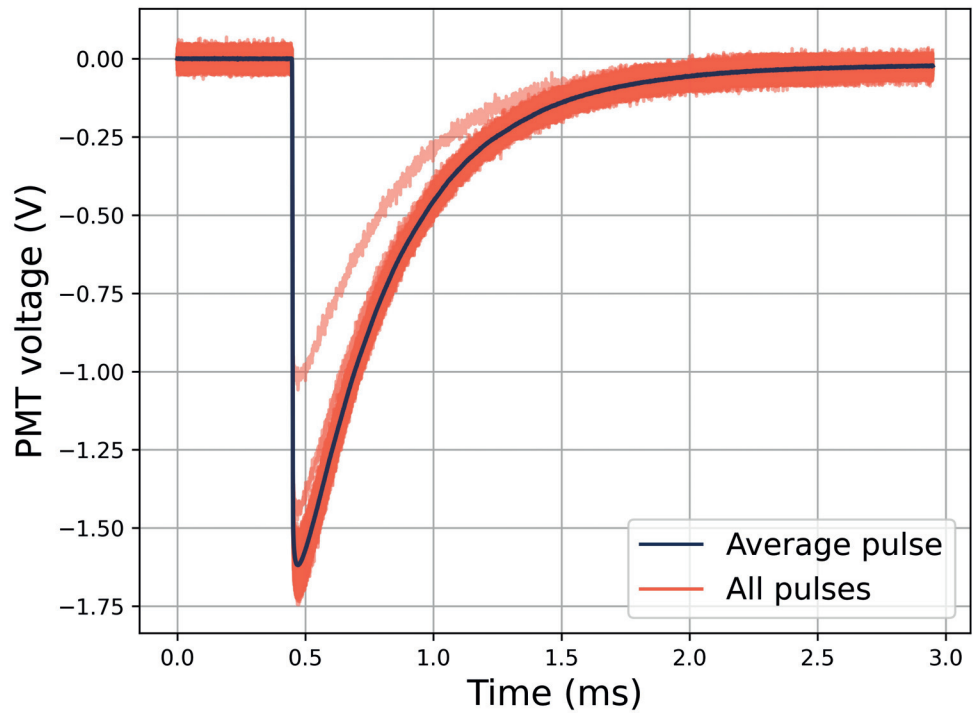


Figure 6. Collected pulses in the oscilloscope from 20-Hz electron bunch irradiation of the Ce-doped rod sample at 9.7×10^{-4} Gy/bunch.

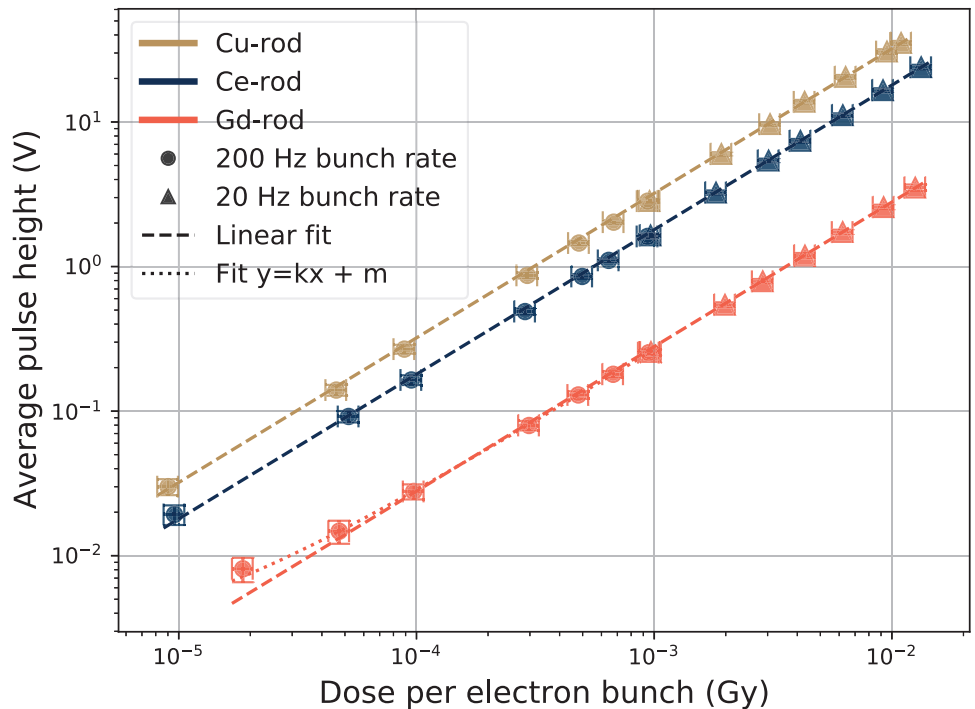


Figure 7. Pulse height as a function of electron bunch size in the different samples. The average pulse height is shown for electron bunch rates of 20 Hz and 200 Hz.

The actual magnitude of the data points in Figure 7 depend on many parameters. Luminescence properties of the sample is one of these parameters, but PMT gain voltage,

the thickness of transport fiber, and relative orientation between the transport fibers end and PMT window are examples of parameters that will have an influence on the signal level. Thus, a test setup like this will have to be re-calibrated each time the setup is constructed. However, for a product where all relevant parameters can be kept constant or accounted for, this would not be necessary.

Adding a term to the fit to account for the background for the Gd-rod data in Figure 7, provides a better representation for the points with low dose per bunch. The effect of varying the PMT gain voltage during tests with the Gd-rod is shown in Figure 8, where data sets taken at 200-Hz bunch frequencies with PMT gains of 0.7 and 0.9 V are shown. When increasing the gain voltage from 0.7 V to 0.9 V, the signal from the low dose pulses gets represented better by the linear fit to the data. The error bars, i.e., the variations of the height of the pulses, are still large at the low dose per pulse point with 0.9 V PMT gain. Thus, the Ce- or Cu-rods, providing larger output pulses, are better suited to monitor small radiation pulses in this manner than the Gd-rod.

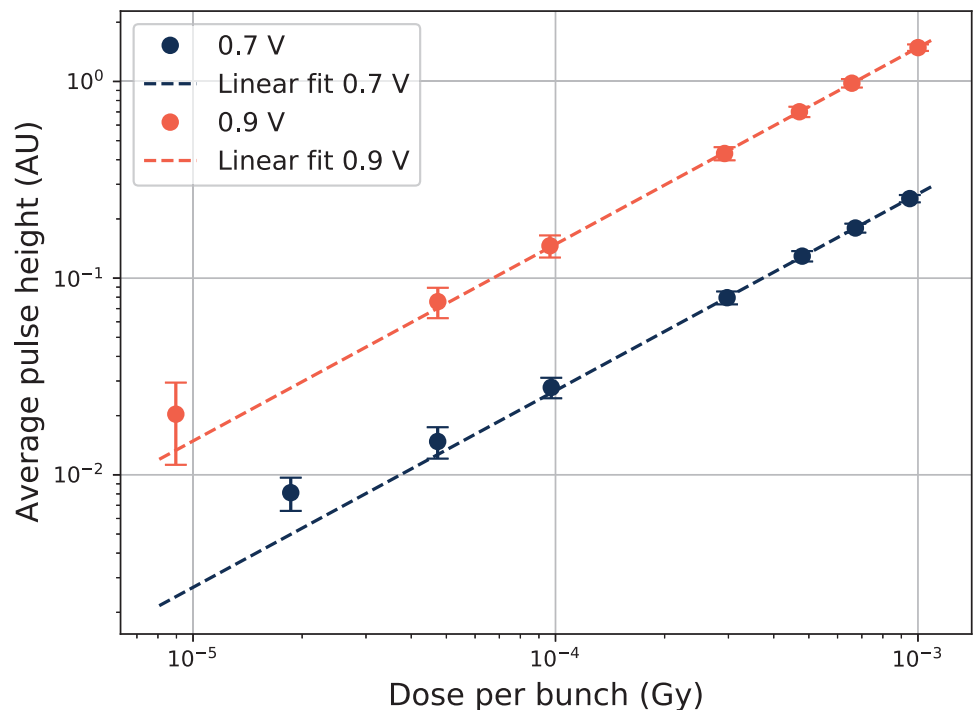


Figure 8. Pulse height as a function of electron bunch size in the Gd-doped sample at varying PMT gain voltages.

In Figure 9, three different shielding configurations were used to study where the light emission was induced in the Gd-doped sample, since no optical filter was used for this one. The *no shielding* option is the same as shown in previous figures, where the sample was in the beam center and no lead was present.

To shield different parts of the sample, 5-cm thick lead bricks were used, and when the transport fiber is put under lead, the signal decreases slightly. Čerenkov radiation is a possible source for light induced in the transport fiber, since it can be induced by 20-MeV electrons in silica. However, it has a maximum emission angle at about 45° [25], and thus much of the induced Čerenkov light would not be transmitted, as the angle between the transport fiber direction and the beam direction was 90°, and no visible Čerenkov component could be seen in Figure 5.

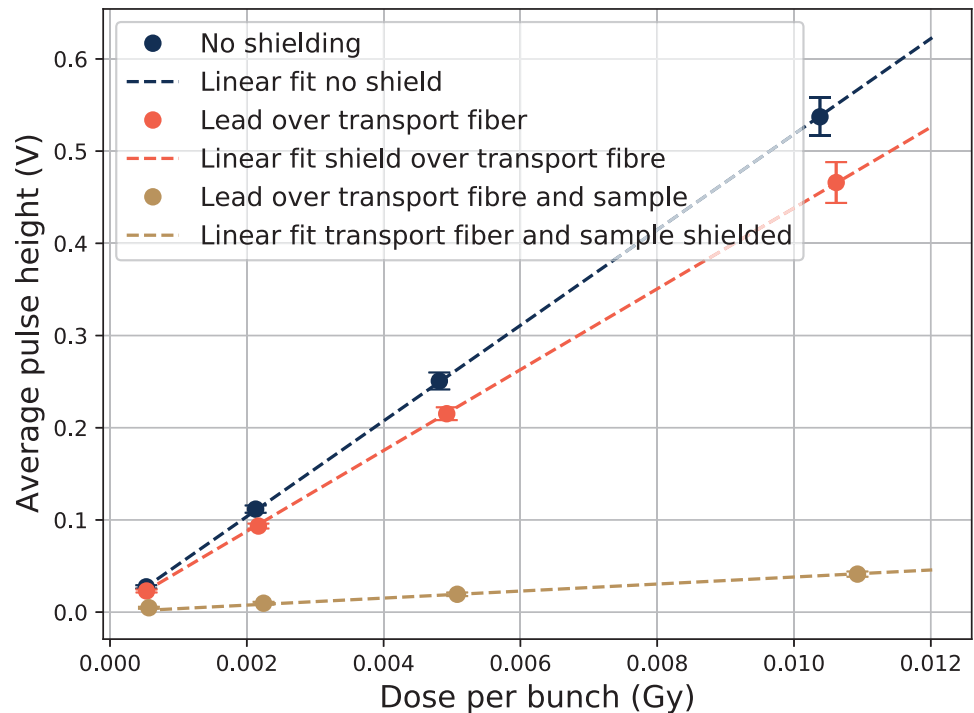


Figure 9. Pulse height as a function of electron bunch size in the Gd-doped sample at different shielding configurations using 5-cm thick lead bricks.

When also shielding the sample, there is still a signal in the system proportional to the electron bunch size, as can be seen in Figure 9. To further examine this, the pulse height of the signal as a function of the sample position is shown in Figure 10, where the beam profile can be seen. No electron applicator was used for these tests, which would make the beam edges sharper if it was used. Even when the sample is positioned outside of the beam, as well as when the transport fiber (TF in the figure legend) is laid out beside the accelerator (about 1 m below and beside the beam area), there is some signal in the system. This shows that there is some radiation background present far from the beam, which can explain the presence of the signal in the fully shielded case in Figure 9, in which the unshielded transport fiber far from the beam has a similar position as the transport fiber laying beside the Clinac in Figure 10.

In the sample position beside the Clinac, the whole transport fiber and rod was stretched out on the floor of the irradiation hall, about 1 m from the irradiation window. The signal that is present when the sample is outside of the beam is however not likely induced in, or by, the electronics, because when the sample was located at the same position as the PMT (the green datum point in Figure 10), the signal was at the noise level. In the fully shielded case of Figure 9, some of the signal that is present will likely also come from electrons and photons penetrating the Pb shield, since the high energy electrons and the bremsstrahlung produced within the shielding material is highly penetrating.

3.2.2. Variations of Pulse Area

The output pulses from the PMT have the same shape for a given sample at varying bunch sizes, and thus the area of the PMT pulses (the integrated voltage over time of the PMT pulse duration) is also proportional to the electron bunch size, since the pulse height is. The average PMT pulse area (c.f. Figure 2) as a function of electron bunch size is shown in Figure 11.

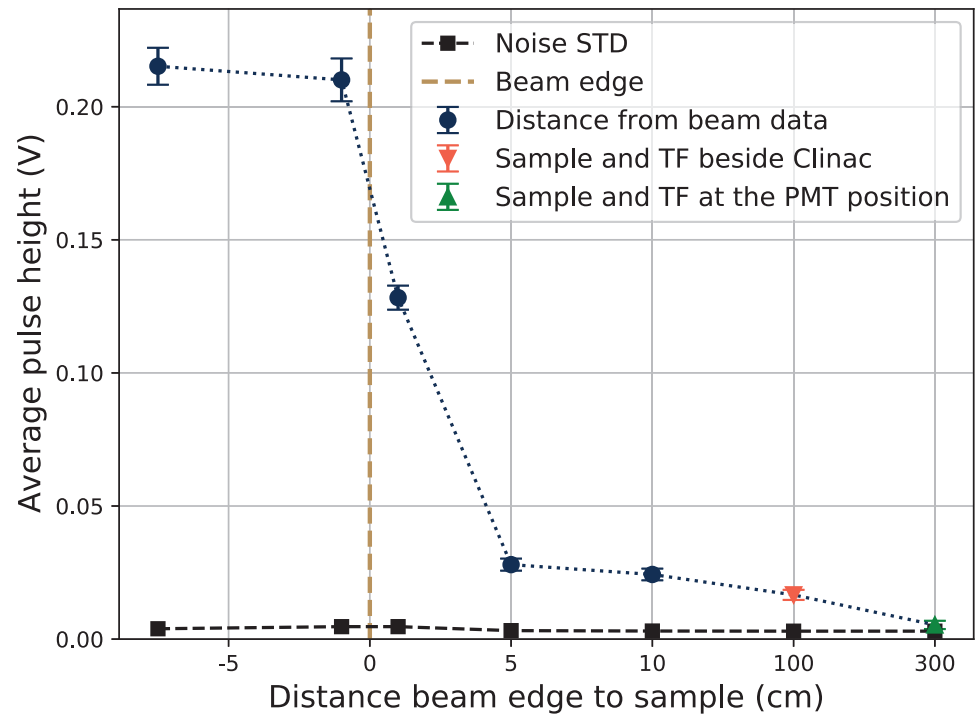


Figure 10. Pulse height as a function of the Gd-doped samples position relative to the edge of the electron beam. The beam spot was a square with 15-cm sides, and the point at -7.5 cm is taken in the beam center. At the point at a 300-cm distance, the sample was laying at a position beside the PMT and electronics. Electron bunches of 5 mGy/bunch at 20 Hz were used to produce this data.

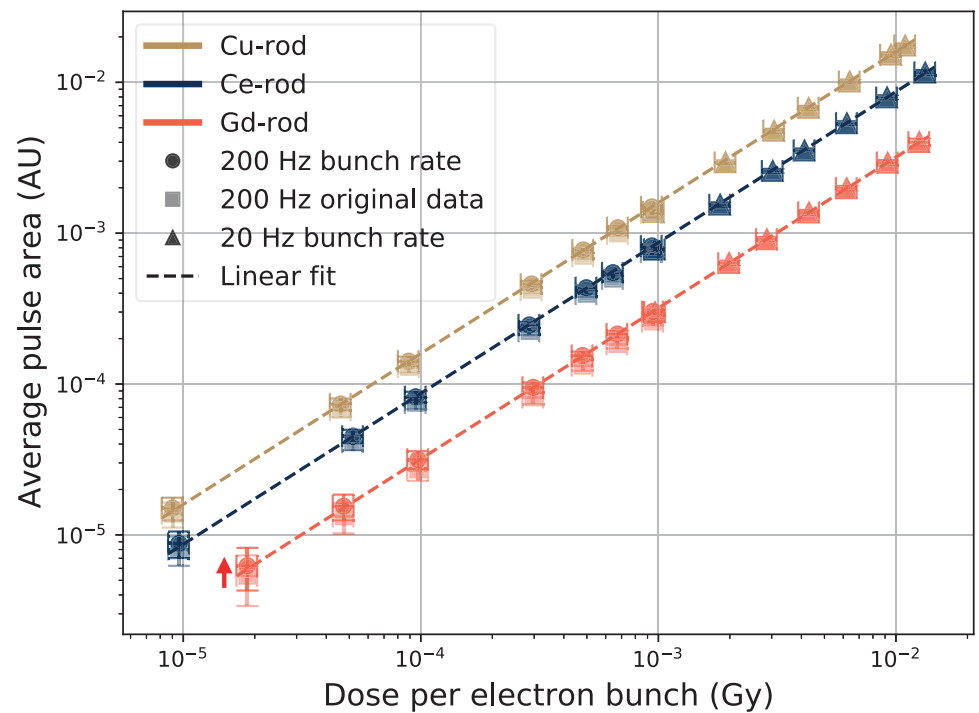


Figure 11. Pulse area as a function of electron bunch size in the samples. The average pulse area is shown for electron bunch rates of 20 Hz and 200 Hz.

In Figure 11, the data taken at different bunch frequencies are scaled to match with each other. There is an offset between the data at the different frequencies for the case of the pulse area, which is shown with an arrow beside the Gd-rod data in Figure 11, and faint square markers for the original 200-Hz data points. This offset is compensated with a constant factor, and it comes from the fact that the signal from the previous pulses has not yet been able to reach the baseline level when the electron bunch frequency is high. The arriving pulses are thus located on the tail of the previous pulse (illustrated in Figure 12), and this tail is then decaying, moving the baseline lower over the duration of the new pulse, thereby decreasing the effective area of the pulses.

The tails of the Gd-sample are the longest due to the long decay time of the Gd luminescence. The main decay time component of the Gd^{3+} ions luminescence is about 1.8 ms (see e.g., [26]) compared with Cu^+ ions and Ce^{3+} ions where the decay times are on the order of 40–50- μs and 50 ns respectively [6,9,27]. The shift factor for the high-rate points was also noted to be most apparent for the Gd-doped sample. The factors used to scale the 200 Hz data to the 20 Hz data were 1.17 for the Gd-rod, and 1.10 and 1.09 for the Ce-rod and Cu-rod, respectively.

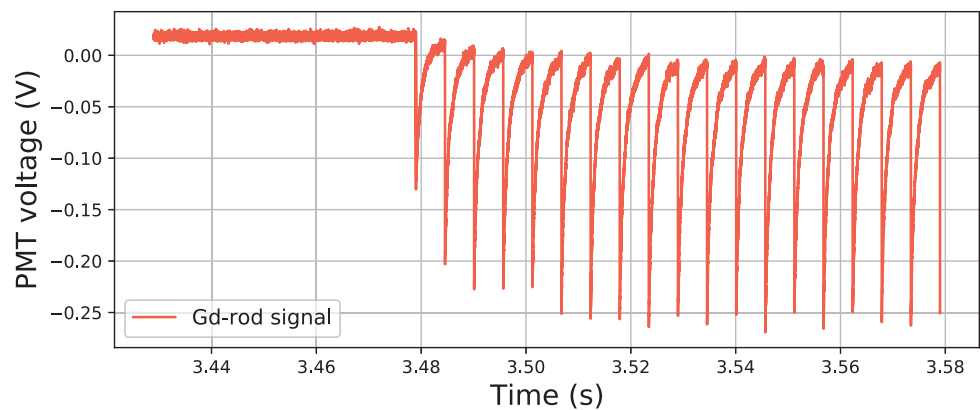


Figure 12. Signal from the Gd-doped sample when subjected to a pulsed beam with a frequency of 200 Hz at 1 mGy/bunch. The signal does not have time to fall back to the baseline, and the consecutive pulses are located on the tails of the previous ones.

The decay times of the pulses in e.g., Figures 6 and 12 differ from the decay times of the luminescence of the dopant ions. This is because they were collected with a 1-M Ω input impedance in the oscilloscope, which affects the signal pulses relaxation time. As a comparison for these samples, the fall times of the recorded pulses (here time from the peak value V_{peak} to the value V_{peak}/e) were about 0.95 ms for the Gd-rod, 0.41 ms for the Ce-rod, and 0.40 ms for the Cu-50 sample. These are approximate values observed for the pulses behind the data in Figure 11, and are presented in Table 2 along with the decay times of the dopant ions obtained from the literature.

Table 2. Time structure of the pulses from the samples.

Sample	Dopant	Dopant Decay Time (s)	PMT Pulse Fall Time to V_{peak}/e (s)
Ce-rod	Ce^{3+}	50×10^{-9} [6,27]	4.1×10^{-4}
Cu-rod	Cu^+	$40\text{--}50 \times 10^{-6}$ [9]	4.0×10^{-4}
Gd-rod	Gd^{3+}	1.8×10^{-3} [26]	9.5×10^{-4}

From the tabulated decay and fall times in Table 2, it can be seen that the Ce^{3+} and Cu^+ ions have shorter dopant decay times than the fall time of the pulse seen in the 1-M Ω impedance oscilloscope as would be expected. Moreover, the samples containing these dopants were used with optical filters selecting the corresponding RIL emission spectral

domain. Hence, the exact values of the PMT pulse fall time will depend on the total relaxation times of each of the systems, which might differ from the specific decay time of the dopant ions, along with the input impedance of the oscilloscope. For the Gd^{3+} -doped rod, the dopant decay time is instead longer than the PMT pulse fall time. For the Gd-rod, no optical filter was used, and the prompt response of the sample (originating from e.g., Čerenkov light) might have a larger impact. The prompt response of the sample will quickly vanish, which for this case would make the resulting response time faster than the decay time of the dopant.

The different properties of the samples will have implications in what bunch frequencies can be resolved: A faster RIL decay makes it possible to use in a higher bunch frequency. The pulse duration could also be further adapted to the bunch frequency in the desired application, by tuning the input impedance of the readout system.

Using the pulse area instead of the pulse heights makes the noise level less significant, as uniform noise around the zero-level cancels out to zero when integrating the PMT pulse over time. Thus, no added constant factor to the linear fit, accounting for the signal noise, is needed. The error bars are however still large for signals, which are close to the noise, as seen for the Gd-rod sample at 10^{-5} Gy/bunch in Figure 11.

3.2.3. Total Area of Traces with Many Pulses

Since the area of the individual pulses are proportional to the electron bunch sizes, the area of the whole recorded trace should be proportional to the dose of the full run. This is shown in Figure 13, where the y -axis direction error bars represent 10% of the numeric value of the trace area as a guidance value, and the x -axis direction error bars represent 10% of the reported dose value.

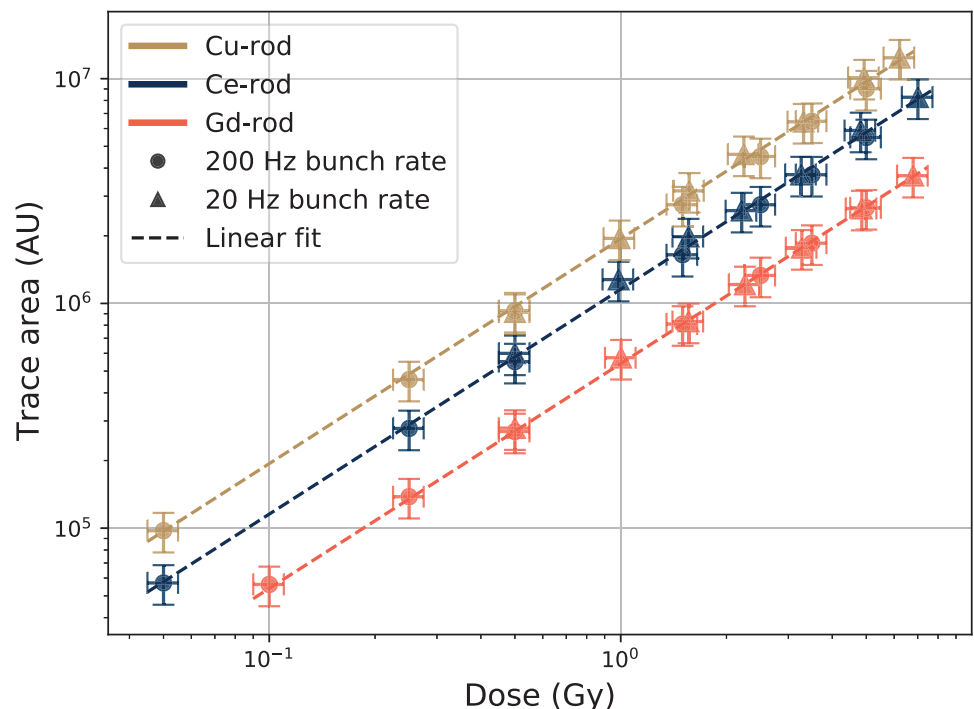


Figure 13. Total area of the recorded pulse traces as a function of run dose in the samples, from the same data sets as in Figures 7 and 11.

When comparing the trace area values, no correction between high and low frequency data points is needed, as the piling up of the individual pulses at high electron bunch frequencies does not change the total trace area, as seen in Figure 13, where the high and

low frequency data points follow the same linear trend over the tested dose range from 5×10^{-2} Gy to about 6.5 Gy.

The noise is in Figure 13, as in Figure 11, uniform around the signal level and cancels out when the trace area is calculated (signal trace is integrated over time). For each tested rod, the data shows a good linearity between the dose absorbed by the sample and the total signal area. Compared with Figure 2, the zero level of the trace was calculated only in the beginning of each run to obtain the total trace area, and the separate pulses were not specifically taken into account.

4. Conclusions

In this study, the RIL response of doped sol-gel silica glass samples to a pulsed electron Clinac beam was investigated for the first time to the best of our knowledge. In effect, studies addressing the RIL from luminescent glassy materials in a fibered system to probe electron beams are scarce. Moreover, the doped sol-gel silica used here is quite different from materials appearing in references [12–17]. The response of the tested samples was also studied in a pulse-by-pulse manner for each impinging electron bunch. It was found that the height and area of the output PMT pulses were proportional to the dose of the impinging electron bunches in the range 10^{-5} Gy/bunch— 1.5×10^{-2} Gy/bunch. The total integrated trace areas of the irradiation runs were also found to be proportional to the dose from the electron beam during the runs. Based on these results, it is concluded that these samples have strong potential to be used for radiation monitoring of electron Clinac beams.

These observations were true for all tested samples. However, choosing an appropriate sample with properties matching the desired beam parameters is necessary. The sample needs to have a high enough light output so the signal from the bunches is visible. In this case, parameters regarding sample geometry and doping are important to consider, as well as signal amplification such as the PMT gain. Further care should be taken at high bunch frequencies of irradiation, so that the RIL in the sample can fully decay between consecutive bunches. Alternatively, this could be compensated if necessary by applying an offset factor depending on the bunch frequency and sample that is used.

Part of the induced signal was found to originate within the transport fibers, and not from the RIL of the dopant ions in the samples. A linear agreement between the induced signal and the dose of the electron bunches was still observed, but an important consideration is to keep a controlled transport fiber orientation relative to the beam, to minimize variations in, for example, induced Čerenkov radiation between runs.

In a radiation environment from a Clinac in use for radiotherapy, the variation of electron bunch sizes would be much smaller than the range studied in this paper. The variations of the bunch sizes in a Clinac in operation could originate from varying depth in a target material or possible variations between different accelerator models. These variations would occur within the central region of the studied range, where the tested samples would be well suited to monitor the dose deposited by each electron bunch, or the total dose during a run with many consecutive bunches.

Author Contributions: Conceptualization, D.S., H.K. and S.G.; methodology, D.S. and H.K.; software, D.S.; validation, A.M., Y.O., H.E.H., B.C., M.B. and S.G.; formal analysis, D.S.; investigation, D.S. and H.K.; resources, H.K., A.J., H.E.H., B.C., G.B., M.B. and S.G.; data curation, D.S.; writing—original draft preparation, D.S.; writing—review and editing, D.S., H.K., A.M., H.E.H., B.C., M.B. and S.G.; visualization, D.S.; supervision, H.K., A.J. and S.G.; project administration, D.S., H.K., A.J. and S.G.; funding acquisition, H.K., A.J. and S.G. All authors have read and agreed to the published version of the manuscript.

Funding: The results presented here have been conceived within the RADSAGA ITN, which has received funding from the European Union's Horizon 2020 Research and Innovation Programme under the Marie Skłodowska-Curie Grant Agreement No. 721624. This work was also supported by the European Space Agency (ESA) under contract 4000124504/18/NL/KML/zk, by the ANR: LABEX CEMPI (ANR-11-LABX-0007), the Equipex Flux (ANR-11-EQPX-0017), by the Ministry of Higher Education and Research, and the Hauts-de-France Regional Council and the European Regional Development Fund (ERDF) through the Contrat de Projets Etat-Region (CPER Photonics for Society P4S).

Institutional Review Board Statement: Not applicable.

Informed Consent Statement: Not applicable.

Data Availability Statement: The data that were analyzed to produce this publication are available through the JYX database (<https://jyx.jyu.fi/handle/123456789/78578>, accessed on 7 November 2021).

Acknowledgments: This work has been supported by the IRCICA institute and the FiberTech Lille platform (<https://fibertech.univ-lille.fr/en/>, accessed on 7 November 2021) of the University of Lille.

Conflicts of Interest: The authors declare no conflict of interest.

References

1. Girard, S.; Capoen, B.; El Hamzaoui, H.; Bouazaoui, M.; Bouwmans, G.; Morana, A.; Di Francesca, D.; Boukenter, A.; Duhamel, O.; Paillet, P.; et al. Potential of Copper- and Cerium-Doped Optical Fiber Materials for Proton Beam Monitoring. *IEEE Trans. Nucl. Sci.* **2017**, *64*, 567–573. [[CrossRef](#)]
2. Hoehr, C.; Morana, A.; Duhamel, O.; Capoen, B.; Trinczek, M.; Paillet, P.; Duzenli, C.; Bouazaoui, M.; Bouwmans, G.; Cassez, A.; et al. Novel Gd³⁺-doped silica-based optical fiber material for dosimetry in proton therapy. *Sci. Rep.* **2019**, *9*, 16376. [[CrossRef](#)] [[PubMed](#)]
3. O'Keefe, S.; McCarthy, D.; Woulfe, P.; Grattan, M.W.D.; Hounsell, A.R.; Sporea, D.; Mihai, L.; Vata, I.; Leen, G.; Lewis, E. A review of recent advances in optical fibre sensors for in vivo dosimetry during radiotherapy. *Br. J. Radiol.* **2015**, *88*, 20140702. [[CrossRef](#)] [[PubMed](#)]
4. Al Helou, N.; El Hamzaoui, H.; Capoen, B.; Bouwmans, G.; Cassez, A.; Ouerdane, Y.; Boukenter, A.; Girard, S.; Chadeyron, G.; Mahiou, R.; et al. Radioluminescence and optically stimulated luminescence responses of a cerium-doped sol-gel silica glass under X-ray beam irradiation. *IEEE Trans. Nucl. Sci.* **2018**, *65*, 1591–1597. [[CrossRef](#)]
5. El Hamzaoui, H.; Capoen, B.; Al Helou, N.; Bouwmans, G.; Ouerdane, Y.; Boukenter, A.; Girard, S.; Marcandella, C.; Duhamel, O.; Chadeyron, G.; et al. Ce-activated sol-gel silica glasses for radiation dosimetry in harsh environment. *Mater. Res. Express* **2016**, *3*, 046201. [[CrossRef](#)]
6. Chewpraditkul, W.; Shen, Y.; Chen, D.; Yu, B.; Prusa, P.; Nikl, M.; Beitlerova, A.; Wanarak, C. Luminescence and scintillation of Ce³⁺-doped high silica glass. *Opt. Mater.* **2012**, *34*, 1762–1766. [[CrossRef](#)]
7. El Hamzaoui, H.; Bouwmans, G.; Capoen, B.; Cassez, A.; Habert, R.; Ouerdane, Y.; Girard, S.; Di Francesca, D.; Kerboub, N.; Morana, A.; et al. Gd³⁺-doped sol-gel silica glass for remote ionizing radiation dosimetry. *OSA Contin.* **2019**, *2*, 715–721. [[CrossRef](#)]
8. He, J.; Wang, Y.; Steigenberger, S.; Macpherson, A.; Chiodini, N.; Brambilla, G. Intense ultraviolet photoluminescence at 314 nm in Gd³⁺-doped silica. In Proceedings of the Conference on Lasers and Electro-Optics: Applications and Technology 2016, Optical Society of America, San Jose, CA, USA, 14–19 May 2016; p. JTh2A.86. [[CrossRef](#)]
9. El Hamzaoui, H.; Ouerdane, Y.; Bigot, L.; Bouwmans, G.; Capoen, B.; Boukenter, A.; Girard, S.; Bouazaoui, M. Sol-gel derived ionic copper-doped microstructured optical fiber: A potential selective ultraviolet radiation dosimeter. *Opt. Express* **2012**, *20*, 29751–29760. [[CrossRef](#)]
10. Capoen, B.; El Hamzaoui, H.; Bouazaoui, M.; Ouerdane, Y.; Boukenter, A.; Girard, S.; Marcandella, C.; Duhamel, O. Sol-gel derived copper-doped silica glass as a sensitive material for X-ray beam dosimetry. *Opt. Mater.* **2016**, *51*, 104–109. [[CrossRef](#)]
11. Borsella, E.; Dal Vecchio, A.; Garcia, M.A.; Sada, C.; Gonella, F.; Polloni, R.; Quaranta, A.; van Wilderen, L.J.G.W. Copper doping of silicate glasses by the ion-exchange technique: A photoluminescence spectroscopy study. *J. Appl. Phys.* **2002**, *91*, 90–98. [[CrossRef](#)]
12. O'Keefe, S.; Zhao, W.; Sun, W.; Zhang, D.; Qin, Z.; Chen, Z.; Ma, Y.; Lewis, E. An Optical Fibre-Based Sensor for Real-Time Monitoring of Clinical Linear Accelerator Radiotherapy Delivery. *IEEE J. Sel. Top. Quantum Electron.* **2016**, *22*, 5600108. [[CrossRef](#)]
13. Abdul Rahman, A.T.; Nisbet, A.; Bradley, D.A. Dose-rate and the reciprocity law: TL response of Ge-doped SiO₂ optical fibers at therapeutic radiation doses. *Nucl. Inst. Meth. Phys. Res. A* **2011**, *652*, 891–895. [[CrossRef](#)]
14. Ghomeshi, M.; Amouzad Mahdiraji, G.; Mahamd Adikan, F.R.; Ung, N.M.; Bradley, D.A. Sensitive Fibre-Based Thermoluminescence Detectors for High Resolution In-Vivo Dosimetry. *Sci. Rep.* **2015**, *5*, 13309. [[CrossRef](#)] [[PubMed](#)]
15. Benabdesselam, M.; Mady, F.; Girard, S.; Mebrouk, Y.; Duchez, J.B.; Gaillardin, M.; Paillet, P. Performance of Ge-Doped Optical Fiber as a Thermoluminescent Dosimeter. *IEEE Trans. Nucl. Sci.* **2013**, *60*, 4251–4256. [[CrossRef](#)]

16. Huston, A.L.; Justus, B.L.; Falkenstein, P.L.; Miller, R.W.; Ning, H.; Altemus, R. Optically Stimulated Luminescent Glass Optical Fibre Dosimeter. *Radiat. Prot. Dosim.* **2002**, *101*, 23–26. [[CrossRef](#)] [[PubMed](#)]
17. Justus, B.L.; Falkenstein, P.; Huston, A.L.; Plazas, M.C.; Ning, H.; Miller, R.W. Gated fiber-optic-coupled detector for in vivo real-time radiation dosimetry. *Appl. Opt.* **2004**, *43*, 1663–1668. [[CrossRef](#)]
18. El Hamzaoui, H.; Courthéoux, L.; Nguyen, V.N.; Berrier, E.; Favre, A.; Bigot, L.; Bouazaoui, M.; Capoen, B. From porous silica xerogels to bulk optical glasses: The control of densification. *Mater. Chem. Phys.* **2010**, *121*, 83–88. [[CrossRef](#)]
19. El Hamzaoui, H.; Bouwmans, G.; Capoen, B.; Ouerdane, Y.; Chadeyron, G.; Mahiou, R.; Girard, S.; Boukenter, A.; Bouazaoui, M. Effects of densification atmosphere on optical properties of ionic copper-activated sol-gel silica glass: Towards an efficient radiation dosimeter. *Mater. Res. Express* **2014**, *1*, 026203. [[CrossRef](#)]
20. Hamamatsu. *Photosensor Modules H9305 Series*; Hamamatsu Photonics K.K.: Iwata City, Japan, 2020. Available online: https://www.hamamatsu.com/resources/pdf/etd/H9305_TPMO1065E.pdf (accessed on 26 May 2021).
21. Ocean Optics, Inc. *USB2000+ Fiber Optic Spectrometer Installation and Operation Manual*; 830 Douglas Ave.: Dunedin, FL, USA, 2010. Available online: <https://www.oceaninsight.com/globalassets/catalog-blocks-and-images/manuals--instruction-old-logo/spectrometer/usb2000-operating-instructions1.pdf> (accessed on 26 August 2021).
22. Kettunen, H. *Varian Clinac Linear Accelerator*; University of Jyväskylä: Jyväskylän Yliopisto, Finland, 2020. Available online: <https://www.jyu.fi/science/en/physics/research/infrastructures/research-instruments/miscellaneous-instruments/clinac> (accessed on 19 March 2021).
23. IBA. *DETECTORS For Relative and Absolute Dosimetry—Ionization Chambers and Diode Detectors*; IBA Dosimetry GmbH: Schwarzenbruck, Germany, 2018. Available online: https://www.iba-dosimetry.com/fileadmin/user_upload/products/02_radiation_therapy/_Detectors/Detectors-RD-_-AD_Rev.3_0718_E.pdf (accessed on 1 October 2020).
24. Al Helou, N.; El Hamzaoui, H.; Capoen, B.; Bouwmans, G.; Cassez, A.; Ouerdane, Y.; Boukenter, A.; Girard, S.; Bouazaoui, M. Optical responses of a copper-activated sol-gel silica glass under low-dose and low-dose rate X-ray exposures. *OSA Contin.* **2019**, *2*, 563–571. [[CrossRef](#)]
25. Beddar, A.S.; Mackie, T.R.; Attix, F.H. Cerenkov light generated in optical fibres and other light pipes irradiated by electron beams. *Phys. Med. Biol.* **1992**, *37*, 925–935. [[CrossRef](#)]
26. Di Martino, D.; Chiodini, N.; Fasoli, M.; Moretti, F.; Vedda, A.; Baraldi, A.; Buffagni, E.; Capelletti, R.; Mazzer, M.; Nikl, M.; et al. Gd-incorporation and luminescence properties in sol-gel silica glasses. *J. Non-Cryst. Sol.* **2008**, *354*, 3817–3823. [[CrossRef](#)]
27. Chiodini, N.; Fasoli, M.; Martini, M.; Rosetta, E.; Spinolo, G.; Vedda, A.; Nikl, M.; Solovieva, N.; Baraldi, A.; Capelletti, R. High-efficiency SiO₂:Ce³⁺ glass scintillators. *Appl. Phys. Lett.* **2002**, *81*, 4374. [[CrossRef](#)]



PIV

**PROPERTIES OF GD-DOPED SOL-GEL SILICA GLASS
RADIOLUMINESCENCE UNDER ELECTRON BEAMS**

by

Daniel Söderström, Oskari Timonen, Heikki Kettunen, Risto Kronholm, Hicham El Hamzaoui, Bruno Capoen, Youcef Ouerdane, Adriana Morana, Arto Javanainen, Géraud Bouwmans, Mohamed Bouazaoui and Sylvain Girard

MDPI Sensors, vol. 22, no. 23, p. 9248, Nov. 2022

<https://doi.org/10.3390/s22239248>

© CC BY 4.0.

Article

Properties of Gd-Doped Sol-Gel Silica Glass Radioluminescence under Electron Beams

Daniel Söderström ^{1,*} , Oskari Timonen ¹, Heikki Kettunen ¹, Risto Kronholm ¹, Hicham El Hamzaoui ^{2,*}, Bruno Capoen ² , Youcef Ouerdane ³ , Adriana Morana ³ , Arto Javanainen ¹ , Géraud Bouwmans ², Mohamed Bouzaoui ² and Sylvain Girard ³

¹ Accelerator Laboratory, Department of Physics, University of Jyväskylä, FI-40014 Jyväskylä, Finland

² Univ-Lille, CNRS, UMR 8523-PhLAM-Physique des Lasers Atomes et Molécules, 59000 Lille, France

³ Univ Lyon, Laboratoire H. Curien, UJM-CNRS-IOGS, 18 Rue du Pr. Benoît Laurus, 42000 Saint-Etienne, France

* Correspondence: daniel.p.soderstrom@jyu.fi (D.S.); hicham.el-hamzaoui@univ-lille.fr (H.E.H.)

Abstract: The radiation-induced emission (RIE) of Gd³⁺-doped sol-gel silica glass has been shown to have suitable properties for use in the dosimetry of beams of ionizing radiation in applications such as radiotherapy. Linear electron accelerators are commonly used as clinical radiotherapy beams, and in this paper, the RIE properties were investigated under electron irradiation. A monochromator setup was used to investigate the light properties in selected narrow wavelength regions, and a spectrometer setup was used to measure the optical emission spectra in various test configurations. The RIE output as a function of depth in acrylic was measured and compared with a reference dosimeter system for various electron energies, since the dose–depth measuring abilities of dosimeters in radiotherapy is of key interest. The intensity of the main radiation-induced luminescence (RIL) of the Gd³⁺-ions at 314 nm was found to well represent the dose as a function of depth, and was possible to separate from the Cherenkov light that was also induced in the measurement setup. After an initial suppression of the luminescence following the electron bunch, which is ascribed to a transient radiation-induced attenuation from self-trapped excitons (STEX), the 314 nm component was found to have a decay time of approximately 1.3 ms. An additional luminescence was also observed in the region 400 nm to 600 nm originating from the decay of the STEX centers, likely exhibiting an increasing luminescence with a dose history in the tested sample.

Keywords: dosimetry; electron accelerator; optical fiber; point dosimeter; pulsed electron beam; radiation-induced attenuation; radiation-induced luminescence



Citation: Söderström, D.; Timonen, O.; Kettunen, H.; Kronholm, R.; El Hamzaoui, H.; Capoen, B.; Ouerdane, Y.; Morana, A.; Javanainen, A.; Bouwmans, G.; et al. Properties of Gd-Doped Sol-Gel Silica Glass Radioluminescence under Electron Beams. *Sensors* **2022**, *22*, 9248. <https://doi.org/10.3390/s22239248>

Academic Editors: Kan Wu and Xing Li

Received: 13 October 2022

Accepted: 16 November 2022

Published: 28 November 2022

Publisher's Note: MDPI stays neutral with regard to jurisdictional claims in published maps and institutional affiliations.



Copyright: © 2022 by the authors. Licensee MDPI, Basel, Switzerland. This article is an open access article distributed under the terms and conditions of the Creative Commons Attribution (CC BY) license (<https://creativecommons.org/licenses/by/4.0/>).

1. Introduction

Silica glass doped with Gd³⁺-ions fabricated through the sol-gel process has been shown to be suitable for use in dosimeters for X-ray beams [1], proton beams [2], and electron beams [3]. The radiation-induced luminescence (RIL) generated in the doped silica glass has in these studies been shown to be proportional to the ionizing dose on the tested samples, by studying the light generated in the doped glass, which was transported away from the irradiation area through an optical fiber, fusion-spliced to the doped glass.

The RIL response under steady-state irradiation was studied using X-rays in [1]. There, the response was found to be at least linear in the dose rate range 125 μGy(SiO₂)/s to 12.25 Gy(SiO₂)/s. In the study using proton irradiation [2], the sample was irradiated by the proton beams of energies between 6 MeV and 63 MeV, with dose rates from 0.02 Gy/s to 0.30 Gy/s. The dose profile of the proton beams in water was also investigated in the study, along with the samples doped with Ce³⁺-ions and Cu⁺-ions. The doped glass samples' ability to resolve the proton Bragg peak was compared with a reference Markus chamber, where the Gd³⁺-doped sample came close to the performance of the Markus chamber, and showed better capabilities in this aspect than the samples with other dopants. The response to the electron radiation of doped silica glasses was tested in [3], where

samples doped with Ce^{3+} -ions, Cu^{+} -ions, and Gd^{3+} -ions were investigated. In that study, a pulsed beam was used and the RIL response to the variations of the electron bunch sizes were studied. The tested samples showed a linear RIL response in the dose-per-bunch range 10^{-5} Gy/bunch– 1.5×10^{-2} Gy/bunch, for the 3 μs long electron bunches. The RIL of Gd^{3+} -ions is ascribed to the transition between the ${}^6\text{P}_{7/2}$ and ${}^8\text{S}_{7/2}$ levels [1,2,4]. This transition produces a narrow emission peak at 314 nm [1,3,4]. The decay time of this transition is fairly long, and has been measured to be 1.80 ms in [5] for the comparable doping level of 0.05 mol%, and to 1.35 ms in [1], a similar sample as the one tested in this paper, with a dopant level of 0.1 wt% \approx 0.04 mol%.

SiO_2 also has radiation-induced absorption (RIA) and RIL bands, which are not related to the Gd^{3+} -dopant ions. Studies of the transient RIA was performed on amorphous SiO_2 samples using pulsed electron beams in [6], where transient absorption bands were observed at 5.3 eV (234 nm), and at 4.2 eV (295 nm). These absorption bands are ascribed to the metastable centers formed after electron–hole pair generation, called self-trapped excitons (STEXs) [6,7]. The STEX centers in [8] were found to be formed by an Si–O bond breaking when an electron was excited, and the lattice subsequently distorting, trapping the excited electron and the hole, respectively, on the broken apart Si and O atoms. The STEXs causing the transient RIA were in [6] found to have a luminescent decay by emission energies around 2.4 eV (517 nm), also exhibiting a blue-shift over the time of the decay. The luminescence in [9] was measured to have a peak energy around 2.8 eV, and a decay time close to 1 ms when the sample was cooled down to temperatures below 170 K. At temperatures above 170 K, the decay time was found to decrease with increasing temperature.

An important quality for dosimeter systems used in radiotherapy contexts is the ability to represent dose as a function of depth in water, since the dose deposited in human tissue is the key parameter for radiotherapy. For the Gd^{3+} -doped silica glass dosimeters studied in this paper, the ability to measure the dose–depth curves of protons in water has been previously demonstrated [2]. The corresponding dose–depth curves of electron beams measured with this type of sample have not yet been studied in the literature to the best of the authors' knowledge.

When measuring the light output of an optical fiber irradiated by electrons at a depth in water or another material, a signal from Cherenkov light will be induced with increasing intensity as a function of depth, as the electrons scatter more frequently at larger angles [10]. The depth profile of emitted Cherenkov light in an optical fiber differs from the depth profile of an ionizing dose. The dose–depth profile from electron beams displays an initial increase due to the generation of secondary particles up to the maximum dose value, then a decrease of deposited dose due to the decrease in the primary beam intensity, and finally, a longer tail by induced X-ray secondaries (see, e.g., [11] for further descriptions).

The dose–depth profiles of electron beams in an acrylic phantom, measured using a Gd^{3+} -doped silica glass sample, were studied in this paper. Acrylic is commonly used as a substitute to water in the dosimetric measurements of clinical beams due to its similar properties to water [12], and thus, provides a good understanding of the behavior of the Gd^{3+} -doped sample under electron beams in tissue for medical applications. The sample was also studied under electron beams at varying angles relative to the sample to further study the properties of the induced Cherenkov emission. The properties of the RIL from the Gd^{3+} -doped glass was also investigated in narrow wavelength regions selected with a monochromator setup, where the decay times of the RIL emissions were measured.

2. Materials and Methods

2.1. Tested Sample

A Gd^{3+} -doped sol–gel silica glass rod was tested. The rod was 1 cm-long and had a diameter of approximately 500 μm , and a dopant concentration of 0.1 wt% Gd^{3+} -ions. The descriptions of the fabrication process of this type of sample were found in, e.g., [13,14]. The Gd^{3+} -doped rod, drawn at a temperature of approximately 2000 $^\circ\text{C}$, was fusion-spliced

to a 500 μm pure-silica core multimode optical fiber, with a numerical aperture of 0.4. This optical fiber was used to transport the RIL to the signal analysis and read-out systems described in Section 2.2.

2.2. Test Setup

A monochromator was used to select specific wavelength regions of the RIL for analysis. The monochromator was a 996 mm focal length Fastie–Ebert type monochromator with a 2200 grooves/mm holographic diffraction grating, which was further described in [15]. The RIL-light from the 500 μm transport fiber was sent to the monochromator through two aspheric lenses, which converted the numerical aperture and focused the light to fit a fiber bundle which led the light into the monochromator.

At the output end of the monochromator, the light was detected by a Hamamatsu R9880U-110 photomultiplier tube (PMT) [16]. The spectral resolution of a monochromator is partly determined by the width of its output aperture, and the total photon flux measured at the output is determined by the aperture area. Typically, a narrow slit is used in front of the output aperture in order to achieve the desired spectral resolution, at the expense of measured light intensity. However, in order to obtain a detectable light signal in these experiments, no exit slit was used and the detection resolution was limited by the 8 mm-diameter photosensitive area of the PMT window, resulting in an instrumental FWHM of approximately 3.5 nm.

The output wavelength of the monochromator was selected by rotating the diffraction grating with a stepping motor. The stepper motor was driven by an ST-7128 Microstep Driver, and controlled by an Arduino UNO. The amount of steps taken was set with the measurement PC via a USB serial connection using Python. The same Python program also controlled the data transfer to the PC of the digitized PMT signal through a CAEN N6751 digitizer module [17].

The PMT signal was sent to a fast linear amplifier then to the digitizer. The electron beam used for the tests was pulsed (further described in Section 2.3), and the digitizer acquisition was controlled by a trigger signal coming from an external Si-diode detector in the electron beam. The induced signal from the Si diode when it was struck by an electron bunch was sent to a single channel analyzer, which generated a trigger signal transmitted to the digitizer. Upon the trigger signal arrival, the digitizer acquired a signal trace consisting of a predefined length of the PMT signal. The trace was up to 1 ms-long, with a sampling interval of 0.5 ns within the trace. This allowed the detection of emitted photons by the sample at a specific wavelength, and with a known timing relative to the electron bunch.

To take wider emission spectra, an Ocean Optics USB2000+ UV–VIS–ES spectrometer [18] was used. When the spectrometer was used, the end of the transport fiber was directly fixed by the spectrometer input window.

2.3. Irradiation Facility

The irradiation tests were carried out at the Radiation Effects Facility (RADEF), in the accelerator laboratory of the University of Jyväskylä, Finland. A Varian Clinac 2100C/D linear electron accelerator [3,19] was used to generate the electron beam for the experiments. Electrons with energies of 6, 9, 12, 16, and 20 MeV are available from the Clinac, along with 6 and 15 MV photon beams, consisting of photons with energy spectra, respectively, reaching up to 6 and 15 MeV. The photon beams are bremsstrahlung spectra generated by electrons with energies of 6 and 15 MeV impinging on a metal target.

This study focuses on electron beams, where the energies 6, 12, and 20 MeV were used. The dose rates of the electron beams can be set between 100 rad(H_2O)/min and 1 krad(H_2O)/min, corresponding to average dose rates of 17 mGy(H_2O)/s–0.17 Gy(H_2O)/s. The dose rate was monitored by an internal ionization chamber in the machine, which was calibrated against an external ionization chamber at the maximum dose–depth in water. The dose and dose rate levels set by the machine therefore refer to the dose in water.

When changing the dose rate, the electron bunch frequency is modulated, but the size of the bunches stays the same. A ten-fold increase in dose rate thus corresponds to a ten-fold higher bunch frequency. At the lowest dose rate setting from the machine, 100 rad(H₂O)/min, the average electron bunch frequency is approximately 20 Hz. This means that the dose per electron bunch is approximately 0.83 mGy, and the instantaneous dose rate from the machine is close to 280 Gy/s during the approximately 3 μs-long electron bunches.

The Clinac at RADEF is an accelerator that was previously used in a hospital for radiotherapy purposes. The gantry is rotatable around the machine isocenter, which is the position at which the dosimetry calibration of the machine is performed, and the location where the tested sample was positioned.

2.4. Test Methodology

When using the monochromator setup, in combination with the PMT and digitizer, the lowest available dose rate of 100 rad(H₂O)/min (17 mGy(H₂O)/s) from the machine was always used. This was due to the long data traces saved through the digitizer (up to 1 ms), which was associated with a long data processing and transfer time. The digitizer was always busy when recording the data; thus, a higher bunch frequency would not have resulted in any benefits regarding the data collection rate.

The total light transfer efficiency from the doped sample to the PMT was not measured explicitly. The amount of emitted light on the PMT was, however, not large, and irradiation runs of approximately 1 h were utilized for each measurement point and test configuration. To be able to compare the results between different test configurations, the number of detected photon signals per saved digitizer trace were used as a comparable metric. Here, one trace in the digitizer corresponds to one electron bunch from the accelerator.

With the spectrometer setup, the dose rate from the electron accelerator that was used was instead the highest available, 1 krad(H₂O)/min (0.17 Gy(H₂O)/s). In this case, the acquired spectra were generated by summing up the emitted photons from the sample during 20 s-long time intervals. Three such intervals were used for each irradiation configuration, reaching 1 min of irradiation per tested configuration.

The deposited dose as a function of depth in acrylic was tested, and discussed in Section 3.2. This was performed by placing the sample in the machine isocenter on top of a 5 cm thick block of acrylic, and placing the sample and transport fiber between two sheets of acrylic with a thickness of 2 mm. The depth in acrylic was then varied by placing layers of acrylic sheets of 5 and 10 mm thickness on top of the sample.

Tests at different beam rotation angles were performed as well, as shown in Section 3.3. These were performed by suspending the sample freely in air, only supported by a thin plastic sheet. The amount of material surrounding the tested sample was minimized to lessen the scattering of electrons onto the sample from varying angles, potentially producing additional Cherenkov radiation. The transport fiber was oriented away from the beam tilting direction, which is schematically shown in Figure 1a, where ϕ is the tilt angle of the gantry.

A beam window size of 15 cm × 15 cm was used for the tests at the normal incidence angle ($\phi = 0$, and for dose–depth tests in acrylic), which is shown in Figure 1b, where the sample is seen in the center of the beam window. The total length of sample and transport fiber in the beam is thus 8 cm. After beam rotation, the beam area was changed so that the portion of the sample and transport fiber that was irradiated was always the same. This is shown in Figure 1a, where the 15 cm × 15 cm beam after rotation is drawn with a dashed line, and the corrected beam after rotation is marked by full blue lines.

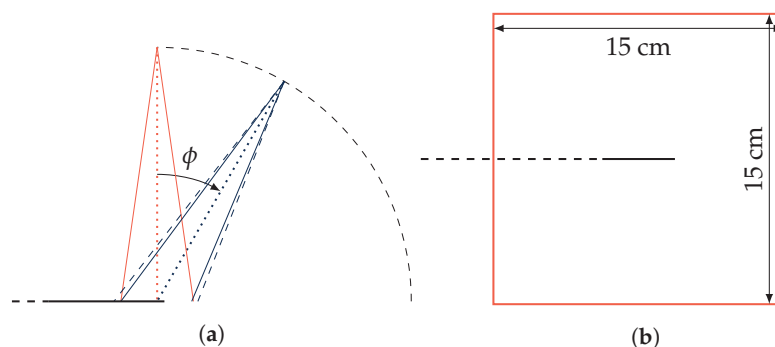


Figure 1. Schematic view of the beam tilting procedure. (a) View from the side, where ϕ is the tilting angle of the beam, and the sample with the transport fiber is marked by the horizontal black line ending in a dashed line. (b) View from the top, with the sample laying in the center of the beam window marked in orange, and the transport fiber directed to the left of the figure along the black dashed line. The beam tilting direction is towards the right.

3. Results and Discussion

3.1. RIL at Selected Wavelengths

From the digitized traces of collected photons in the PMT, histograms of the times of detected photons relative to the electron bunch can be constructed. From such histograms, the RIL can be seen, as shown in Figure 2. In Figure 2a, the luminescence of the main 314 nm emission line of Gd^{3+} is shown. If a different wavelength is selected from the monochromator, the RIL after the electron pulse is gone, but the prompt luminescence response during the electron bunch is still present, as shown for 300 nm in Figure 2b.

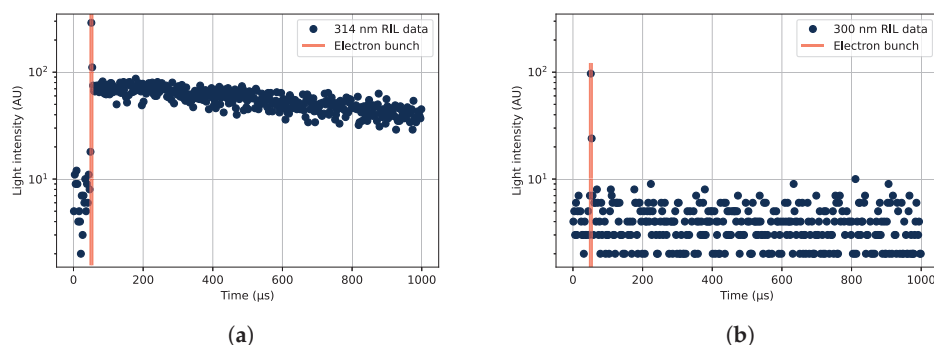


Figure 2. Examples of the time structure of the radiation-induced emission (RIE), as detected at different wavelengths under irradiation by a pulsed 20 MeV electron beam. (a) The radiation-induced luminescence (RIL) of the Gd^{3+} -ions at 314 nm, along with the prompt radiation response during the electron bunch, marked with orange lines around 50 μs into the collected digitized data traces. (b) Detected photons at 300 nm, consisting of a prompt response but no visible RIL component.

To generate the data shown in Figure 2, the sample was placed under the beam covered with a thin black plastic tube to shield the sample from outside light sources, and without any acrylic covering the sample. Under these irradiation conditions, the RIL was investigated at different wavelengths, which is shown in Figure 3. The prompt responses to the electron beam as well as the luminescence occurring after the electron bunch at different wavelengths are displayed in the figure. The different parts of the detected luminescence can be seen in Figure 2, where the time position of the electron bunch is marked in orange vertical lines, the RIL is present after the electron bunch, and the prompt response from Cherenkov radiation is obtained during the electron bunch.

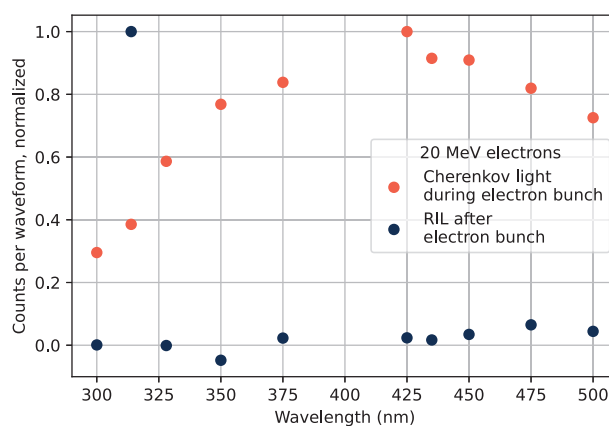


Figure 3. RIE spectra from 20 MeV electrons at a normal incidence angle without any water equivalent material above the sample. The luminescence detected after the electron bunches is shown in blue, and the prompt radiation response during the electron bunch in orange.

The prompt response spectral shape marked with orange dots in Figure 3 is similar to what was observed in, e.g., [20] for Cherenkov radiation. In the figure, the PMT spectral sensitivity was accounted and corrected for. The Cherenkov emission spectrum commonly described by the Frank–Tamm formula [21,22] predicts a continuously growing emission at shorter wavelengths. This is not observed, as the material absorbance at shorter wavelengths in the UV spectrum is high [23]. The suppression of the short wavelengths of Cherenkov spectra is further discussed in, e.g., [24,25].

The RIL spectrum shown in blue in Figure 3 presents the expected dominating emission of the Gd^{3+} -ions at the datum point at 314 nm. Further tendencies of emissions can be seen in the 450 nm–500 nm spectral region. This emission will be investigated and further discussed in Section 3.5.

3.2. Dose as a Function of Depth in Acrylic

The deposited dose as a function of depth in acrylic is shown in Figure 4. The response to 20 MeV electrons is shown in Figure 4a, and for 6 MeV electrons in Figure 4b. The gold-colored lines in the figures represent measurements taken using a reference parallel plate ionization chamber dosimeter IBA PPC40 [26], and the blue lines are from measurements with the tested sample, where the monochromator was set to 314 nm to select the Gd^{3+} luminescence signal. The figure legends contain information of the depth of maximum dose (maximum signal level) z_{max} measured by each method, as well as the fraction of dose (signal strength) at 0 cm of acrylic compared to that at z_{max} , denominated as the surface dose $D_{surface}$.

The same procedure as described for Figure 3 was used to separate the luminescence response after the electron bunch from the prompt signal caused by Cherenkov radiation. The RIL at 314 nm from the Gd^{3+} -ions is able to represent the dose as a function of depth in water in a manner very similar to the reference dosimeter. The Cherenkov radiation induced in the sample has a different shape, caused by the increased scattering of the electrons at larger angles as the depth increases, which is also shown and discussed in [10]. Some parts of the prompt signal might originate from other sources than Cherenkov radiation, but the shape of the depth profile of the prompt emissions in Figure 4 and the wide emission spectrum in Figure 3 suggest that a large majority of the light originates from Cherenkov radiation.

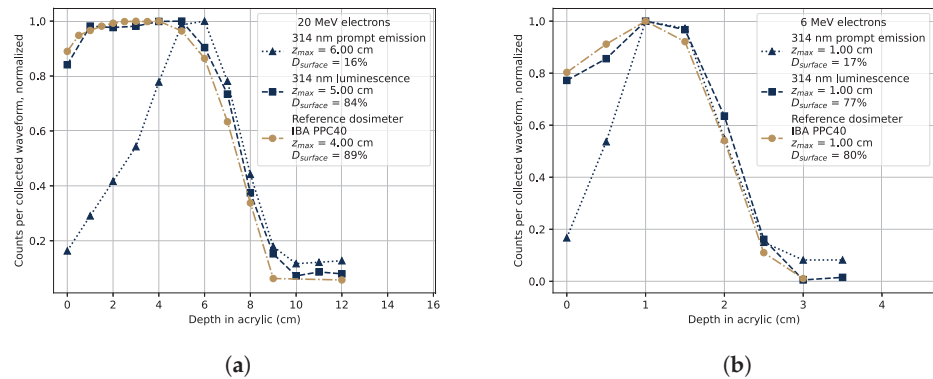


Figure 4. Generated light intensity in the sample as a function of depth in acrylic at 314 nm. The RIL after the electron pulse (squares) and the prompt light signal (triangles) were separated as in Figure 3. The response of a reference dosimeter, an IBA PPC40, is included in the figures as a gold dash-dotted line. The figure legends display the depth at which the maximal dose was recorded, Z_{max} , and the surface dose (0 cm depth) fraction relative to the maximum dose as $D_{surface}$. (a) 20 MeV electron beam. (b) 6 MeV electron beam.

The light output from the sample as a function of depth in acrylic was also analyzed using a spectrometer, by obtaining emission spectra with various thicknesses of acrylic covering the sample. The procedure used for separating the RIL at 314 nm (3.95 eV) from the Cherenkov background is shown in Figure 5, where the measured RIL peak is approximated as a Gaussian, the Cherenkov spectrum in the narrow region around the RIL peak is approximated as a straight line, and the total signal is fitted to the sum of those two components.

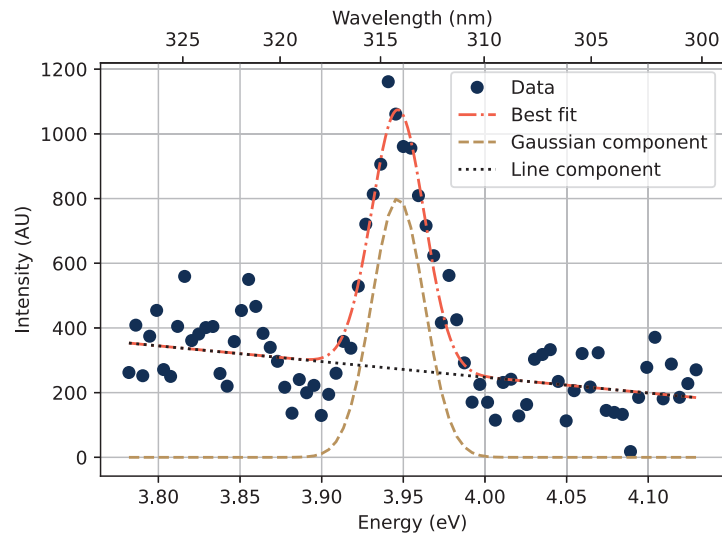


Figure 5. The wavelength region with the 314 nm emission peak from the Gd^{3+} -ions as measured under 4 cm acrylic and 12 MeV electrons. The emission peak was approximated as a Gaussian over the Cherenkov radiation background, which in turn was approximated with a straight line in the region shown in the figure.

The dose–depth curve of 12 MeV electrons is shown in Figure 6. Results from measurements with an optical spectrometer is included, where the size of the RIL peak at 314 nm is extracted as the signal above the Cherenkov background in measured emission spectra at each tested depth of acrylic, by the procedure exemplified in Figure 5. The Cherenkov radiation component is approximated as the total amount of detected light which is not

in the 314 nm peak, in the full measurement interval of the spectrometer from 180 nm to 875 nm.

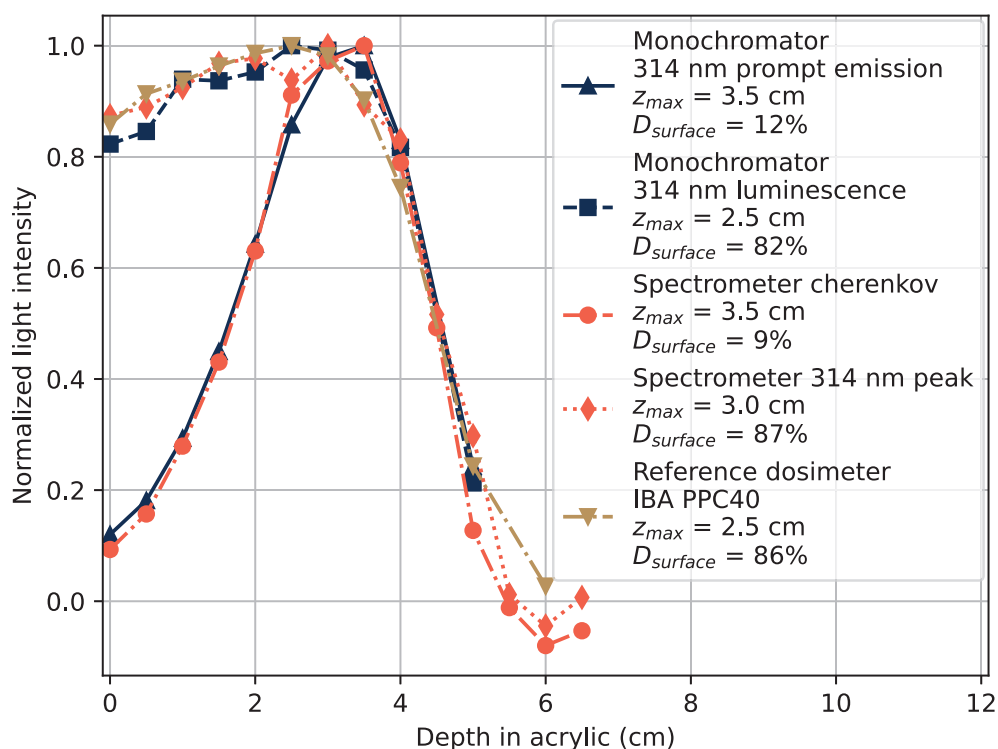


Figure 6. Dose–depth curves in acrylic of 12 MeV electrons obtained with the digitized PMT signal and monochromator set to 314 nm as shown in blue, using optical spectrometer in orange, and IBA PPC40 dosimeter in gold.

Both methods of light detection and separation between Cherenkov light and RIL from Gd^{3+} -ions, using a spectrometer and monochromator, show that the Gd^{3+} luminescence well represents the deposited dose in the material. They also show that Cherenkov radiation is present and needs to be taken into account, since the radiation profiles by Cherenkov radiation do not follow the profile of deposited dose.

3.3. Beam Tilting Tests

For further investigation of the Cherenkov component of the emitted light, irradiation with a tilted beam was performed. The beam tilting was performed by rotating the accelerator gantry around the sample, in the direction away from the transport fiber as described further in Section 2.4. By this procedure, the Cherenkov radiation through the transport fiber should increase with the beam angle ϕ , up to a maximum emission located at the Cherenkov emission angle $\theta = 90^\circ - \phi_{max}$, when the induced emission is directed along the transport fiber. The Cherenkov emission angle can be calculated as

$$\cos \theta = \frac{1}{\beta n(\lambda)}, \quad (1)$$

where β is the relative velocity of the charged particle inducing the Cherenkov radiation, and $n(\lambda)$ is the refractive index of the material, which varies with the wavelength λ of the emitted light. This relation is discussed further in, e.g., [22].

All electrons do not arrive in a parallel orientation at the sample, since the beam is narrow as it leaves the accelerator and spreads with an opening angle towards the irradiated sample. The electrons will thus have a distribution of angles in relation to the sample and transport fiber orientation. This angular distribution of electrons will cause a broadening of

the peak around the Cherenkov emission angle in the detected light intensity as a function of the beam tilting angle. Further broadening of the peak around the Cherenkov angle will be caused by the acceptance angle of the fiber, since photons in a range of scattering angles will be transmitted through the fiber.

The effect of the electron beam tilt angle on the light output is shown in Figure 7 using a 12 MeV electron beam. Similarly to Figure 6, Figure 7 shows the results from the measurements with both the optical spectrometer and the monochromator set to 314 nm. The effects of rotation on the different path-lengths of electrons in the sample and transport fiber, and variations in the beam window size were taken into account and corrected for in the figure.

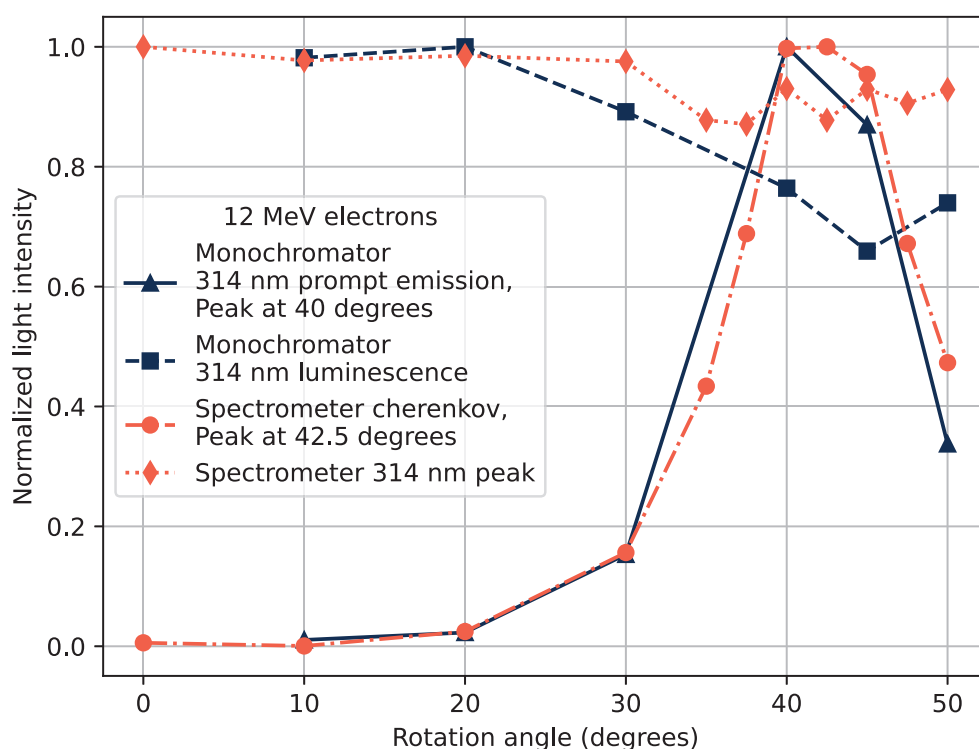


Figure 7. Detected light intensity as a function of the beam tilting angle of a 12 MeV electron beam obtained with digitized PMT signal and monochromator set to 314 nm shown in blue, and with optical spectrometer shown in orange.

The measured Cherenkov emission angle θ is related to the beam tilt angle ϕ so that $\theta = 90^\circ - \phi_{peak}$. The beam tilt angle of maximum Cherenkov emission was measured to be approximately 42.5° , corresponding to a Cherenkov emission angle of 47.5° . The expected Cherenkov emission angle according to Equation (1) is 47° for 12 MeV electrons in silica with $n \approx 1.47$ (using the refractive index at around 314 nm), which corresponds well to the measured peak emission.

In Figure 7, the emission peak luminescence is also shown at 314 nm, corrected for the loss of electrons due to beam tilting, as well as the increased path-length of the electrons in the material. The 314 nm RIL is thus expected to be fairly constant over all tested angles with those corrections in place. This is true within 20% for the measurements with the Ocean Optics spectrometer, and 35% with the monochromator. The decrease in observed luminescence at 314 nm for larger beam tilting angles remains not fully explained. There are some geometric effects that can play a role in the transmitted signal, such as the sample not being perfectly cylindrical or the doping profile not being perfectly homogeneous throughout the sample rod.

The emission spectra acquired by the Ocean Optics spectrometer at different tilt angles are shown in Figure 8. The large increase in light emission due to Cherenkov radiation when the beam is tilted can be clearly seen, with a maximum in emission at approximately 42.5° . The exact shape of the measured optical spectra depends on many factors, where the response of the photon sensor is an important part. The radiation-induced attenuation (RIA) is also something that has an effect, since RIA has a spectral dependence and will modulate the measured emission spectra.

The emission structure at 0° in the region from 400 nm to 500 nm, which could also be discerned in Figure 3, has not previously been reported in the previous studies of this type of sample [1,3]. The tested sample in this study is the same one as was tested in [3], where very little emission can be seen in the region from 400 nm to 500 nm in the emission spectrum. This emission structure is further discussed in Section 3.5.

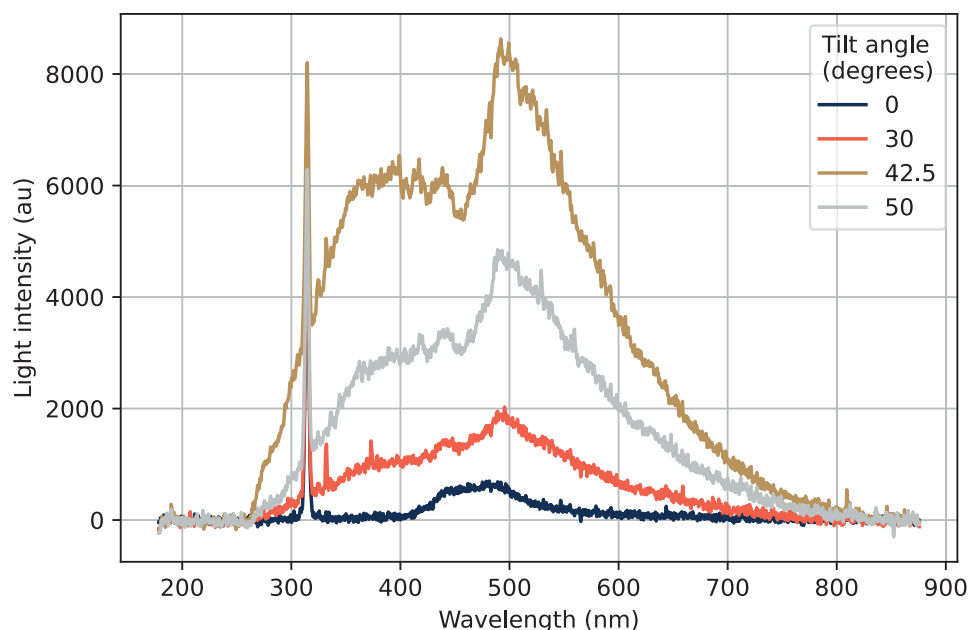


Figure 8. Emission spectra at different tilt angles, with the sharp emission peak of Gd^{3+} at 314 nm, as well as a wide Cherenkov emission spectrum with a maximum intensity at 42.5° .

3.4. RIL at 314 nm

The main luminescence peak at 314 nm in Gd^{3+} -doped silica glasses has a decay time measured around 1.35 ms in [1] and 1.80 ms in [5]. Fitting the measured luminescence signal after the electron pulse at 314 nm to an exponential decay function results in the fitted data shown in Figure 9a. The fit function was

$$I(t) = Ae^{-t/\tau} + B, \quad (2)$$

where $I(t)$ is the emitted light intensity as a function of time t , A is a constant scaling the amplitude of the light emission intensity, τ is the decay time of the luminescence, and B is a constant corresponding to the background signal level. The fitted value of the decay time is 1.33 ms, which is very similar to the decay time found in [1].

The fit is, however, not entirely satisfactory at times close after the electron pulse, where an increase in light emission is seen before the exponential decrease in light intensity is observed. A fit with a term accounting for the luminescence buildup is used instead to account for this behavior according to

$$I(t) = C(e^{-t/\tau_1} - e^{-t/\tau_2}) + B, \quad (3)$$

where I , t , and B are described in connection with Equation (2), C is a constant governing the amplitude of the signal, τ_1 is the decay time of the luminescence, and τ_2 is the characteristic time constant describing the initial luminescence buildup. The data fitted to Equation (3) are shown in Figure 9b.

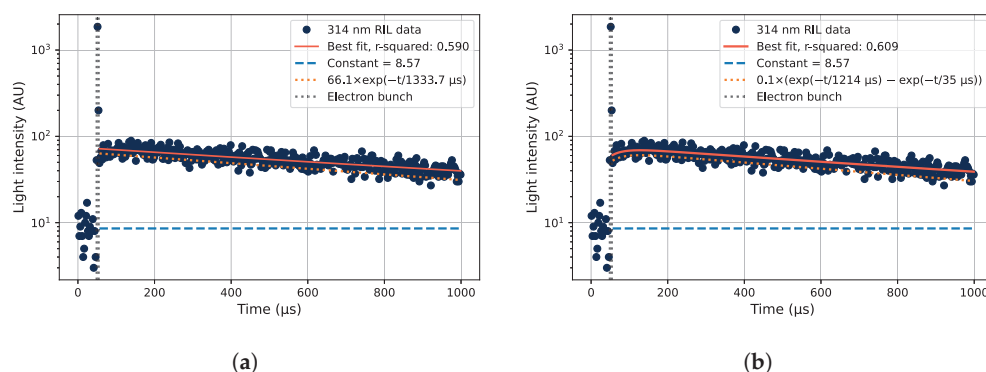


Figure 9. Measured decay curves of the 314 nm RIL of the Gd^{3+} -doped sample, using 12 MeV electrons at a depth of 2 cm in acrylic. The time of the electron pulse is also shown. (a) Data fitted to one exponential decay component (orange dotted line) plus a constant representing the background level (blue dashed line), according to Equation (2). (b) The data fitted with one exponential decay component with an additional term to account for the initial increase in light emission intensity over time shortly after the electron bunch, described in Equation (3).

An interpretation of Equation (3) is that the luminescence of the decay described by the time τ_1 is suppressed by a transient mechanism with diminishing strength described by a time constant τ_2 . This mechanism can be a transient radiation-induced attenuation (RIA), which strongly attenuates the induced light directly after the radiation pulse, then less after longer times. The transient absorption band at 4.2 eV caused by STEs covers the 314 nm emission line [6], and can well explain the luminescence attenuation at times shortly after the electron bunch has hit the sample.

From the data in Figure 9, one can approximate the transient RIA behavior. As a first-order approximation of the RIA strength after the electron bunch, we assume that the luminescence described by τ_1 is correct (although it might also be affected by a longer lasting time-dependent RIA). One can then extrapolate the fitted line in Figure 9b dominated by τ_1 to the end of the electron bunch. The unattenuated (extrapolated) signal is then found to be $\approx 1.23 \times$ the attenuated (measured) signal there. Assuming a fiber length of 8 cm in the beam where RIA is induced, this corresponds to an initial RIA of approximately 11 dB/m after the end of the electron pulse for the case in Figure 9b.

Fits according to Equation (3) were made for 6, 12, and 20 MeV electrons at the different tested depths of acrylic. For 12 MeV electrons, the characteristic decay times are shown in Figure 10, with error bars signifying the estimated standard deviation of the fitted parameters based on the covariation matrix formed during the fitting procedure. The average values on the tested depths as indicated in Figure 10 are shown for all tested electron energies in Table 1. The calculated average values of the initial RIA are also shown in the table.

A further note is that the luminescence increase after the electron bunch is more pronounced at the depth of the maximum dose in acrylic than without any material over the sample, as well as more pronounced than points deeper in the acrylic. The reason for this could be that the transient RIA is dose-rate-dependent, so that the higher dose rate on the sample at the depth of the maximum dose in the material corresponds to a larger initial RIA. The trend of measured RIA strengths as a function of depth in acrylic does not, however, strictly follow the shape of the dose–depth curves. This could be masked by uncertainties in the individual fits, which could distort the shape of RIA curves as a function of depth. The measured values of τ_2 and the RIA strengths rather vary around

a specific level, which motivates the use of the average value in Table 1 to represent the generally observed trends.

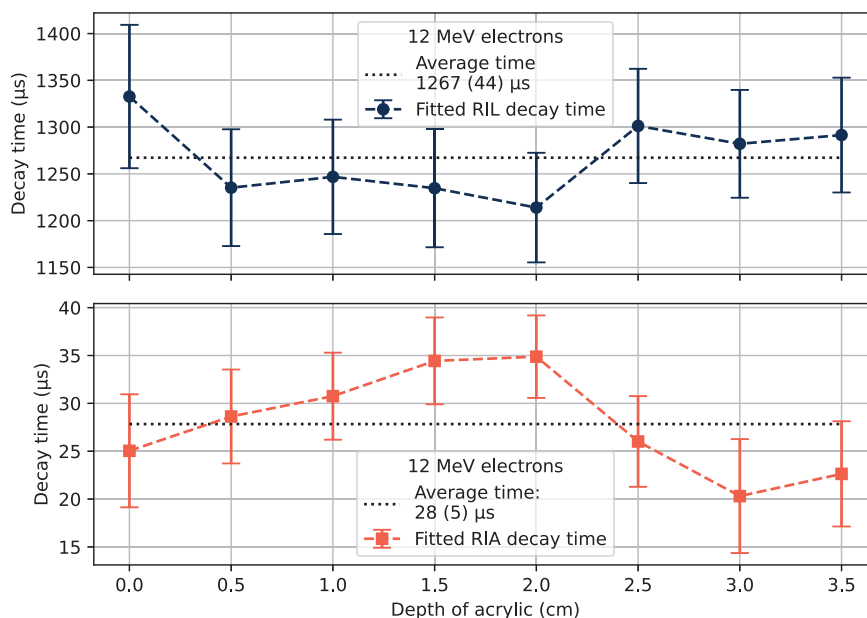


Figure 10. Fitted luminescence decay times (top), and transient RIA decay (luminescence buildup) times (bottom) at different depths of acrylic for 12 MeV electrons, with the estimated standard deviation of the fitted variable value as the error bars. The average of the measured values is shown with dotted lines, with the estimated standard deviations of the averages in parentheses.

Table 1. Decay times of the luminescence at the main Gd^{3+} -ion RIL at 314 nm under irradiation with electrons at a normal incidence angle. Fitted decay time values, transient RIA time constant, and RIA strength after the electron bunch are listed. The presented values are the average of the fitted ones at different depths of acrylic, with the estimated standard deviation in parentheses.

Electron Energy (MeV)	RIL Decay Time τ_1 (μ s)	Transient RIA Decay Time τ_2 (μ s)	Initial RIA Strength (dB/m)
6	1257 (43)	22 (4)	4.3 (2.1)
12	1267 (44)	28 (5)	7.2 (2.7)
20	1257 (44)	22 (9)	5.3 (2.4)

3.5. RIL between 400 and 600 nm

The optical emission structure seen at 0° in Figure 8 is further investigated in this section. The photon emission as a function of time, as measured using the monochromator setup at 450 nm, is shown in Figure 11, with the decay time $\tau = 16.7 \mu$ s when fitted to Equation (2) (one decay component). Other fitted decay times in the same wavelength region are shown in Table 2, where the best fits to the luminescence curves gave values from 10 μ s to 15 μ s.

The sum of detected photons in the region marked as *Luminescence region* in Figure 11 is compared, for the tested wavelengths, with the spectrum measured with the spectrometer. This is shown in Figure 12, where the emission spectrum from the spectrometer is the 0° spectrum from Figure 8. The 0° spectrum and the sum of detected photons in the *Luminescence region* coincide well with each other from 400 nm to 500 nm, suggesting that emissions in the luminescence region seen in Figure 11 are causing the peak observed using the spectrometer in Figure 12.

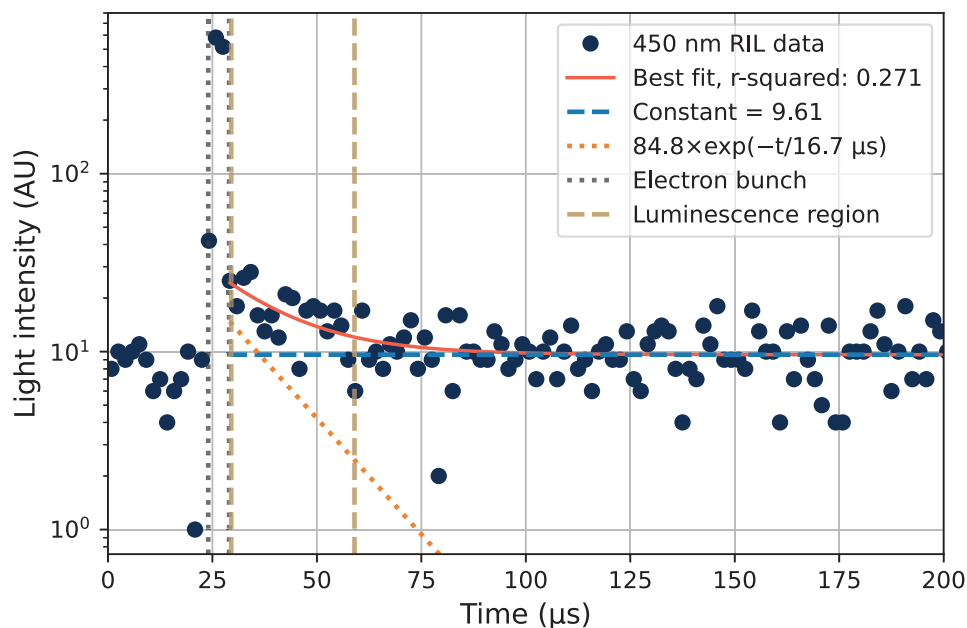


Figure 11. Luminescence decay measured at 450 nm, relative to the electron bunch time. The data were fitted to one exponential decay (orange-dotted line) plus a constant representing the background level (blue-dashed line), as given by Equation (2).

Table 2. Decay times of luminescence at different wavelengths in the emission region 425 nm to 500 nm during irradiation with 20 MeV electrons at a normal incidence angle without acrylic cover.

Wavelength (nm)	Decay Time (μs)
425	12.6
450	16.7
475	11.5
500	8.3

The measured peak is rather asymmetric, and likely does not consist of one static emission band. The spectrometer data were fitted to a sum of three Gaussian components in Figure 12, with a wide distribution centered at 2.53 eV (490 nm), and narrower peaks at 2.59 eV (479 nm), and 2.81 eV (441 nm). The position of the emission structure in the energy spectrum coincide well with previous measurements of the emissions from STEX centers, at, e.g., 2.4 eV in [6] and 2.8 eV in [9].

The blue-shift of the luminescent decay of the STEX were in [6] at 80 K found to be such that the luminescence peak center after 10 μs was observed at approximately 2.05 eV (605 nm), then shifting towards 2.4 eV (517 nm) over the course of tens of microseconds. This blue-shift in the STEX decay can cause some of the broadening and structure of the observed emission in Figure 12. Also note that the experiments in this study were performed at the ambient room temperature and not in a cooled down configuration.

In Table 2, a slight shift to longer decay times for shorter wavelengths could be estimated, but the fits made to the collected data in this experiment do not provide enough confidence to support such a blue shift. Further studies would be needed to confirm whether the emission peak observed in Figure 12 is composed of an emission center experiencing a blue-shift over time in the tested sample.

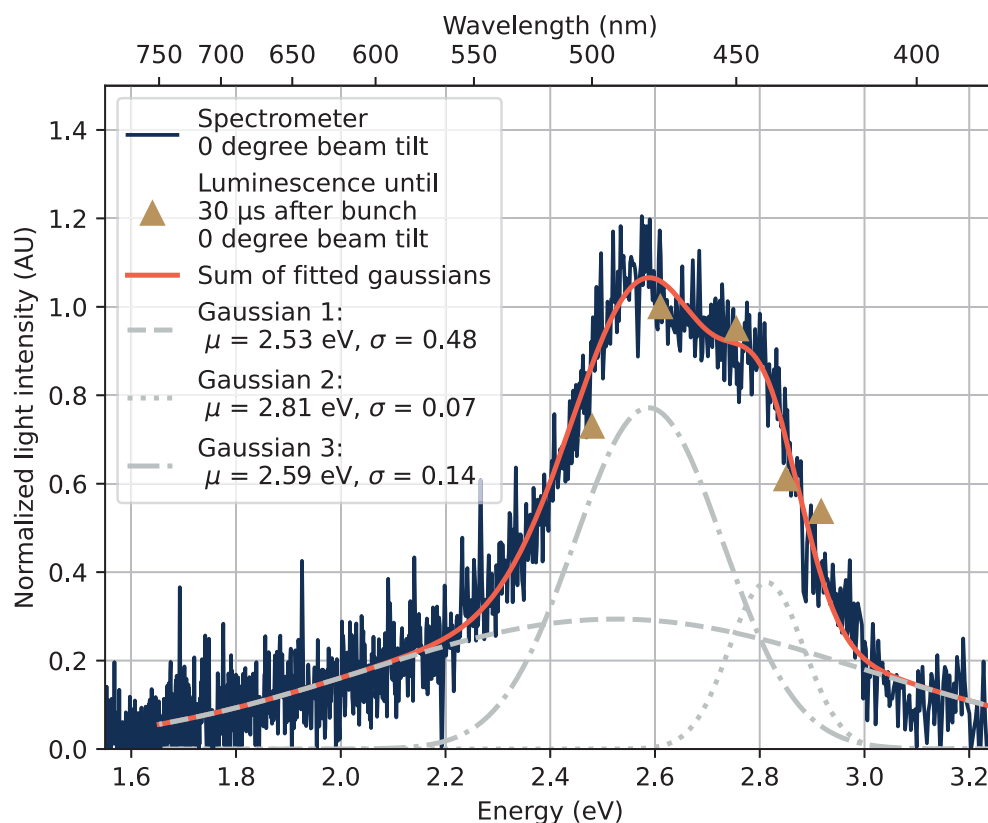


Figure 12. The observed peak in the optical emission spectrum between 400 nm and 600 nm. The structure is reproduced with an optical spectrometer as the blue line, and by summing the detected photons in the luminescence time region marked in Figure 11 by gold-dashed lines, resulting in the points marked by gold triangles in this figure. The spectrometer measurement was also fitted to a sum of three Gaussian components to recreate the peak shape.

4. Conclusions

Sol-gel silica glass doped with Gd^{3+} -ions shows great promise for applications in dosimetry as a point dosimeter using the RIL from ionizing radiation, which has an intensity proportional to the rate of deposited dose. In this study, the properties of the RIE under electron irradiation were studied under different irradiation conditions, allowing for the novel measurements of dose–depth curves, RIL decay times, transient RIA properties, and RIE spectra in this type of sample.

The RIL at 314 nm was found to be proportional to the deposited dose as a function of depth in acrylic for electron beams at 6, 12, and 20 MeV. The luminescence at 314 nm followed the dose–depth profile measured with a reference parallel plate ionization chamber dosimeter, while the Cherenkov radiation induced in the sample follows a different depth profile. To accurately represent the dose at varying depths in materials, it is thus necessary to only select the 314 nm RIL component.

The light emission was also investigated at a varying incidence angle of the beam, confirming a large presence of Cherenkov radiation in the measured RIE. A clear dominance of the Cherenkov light over the 314 nm RIL component was found for the angles allowing maximum Cherenkov light injection through the transport fiber.

The experiments were performed with two different setups: a commercial spectrometer and a monochromator with a PMT for light detection, which provided complementary data to each other. The systems offered different methods of discriminating the Cherenkov background, and only selecting the desired 314 nm RIL component.

With the monochromator and PMT setup, the decay time of the luminescence at selected wavelengths could be investigated. An emission band between 400 nm and 600 nm, with decay times of approximately 10 μ s to 15 μ s was observed. These emissions can be ascribed to the luminescent decay of STEX centers caused by the radiation on the sample. These emissions were not clearly observed in earlier tests with the same sample, which suggests an increase in these emissions with an increasing dose history. This should be further studied by obtaining emission spectra from this type of sample at increasing dose levels.

At the main emission line from Gd^{3+} -ions in silica glass at 314 nm, the RIL intensity was found to first increase after the end of the impinging electron pulses. This is likely due to a transient RIA caused by the pulsed electron beam, which has a large instantaneous dose rate of approximately 280 Gy/s, attenuating the RIL signal at times close to the electron bunch. The characteristic decay time of the transient RIA was found to be approximately 20 μ s to 30 μ s. The transient RIA is ascribed to the STEX absorption centers observed in previous studies at 4.2 eV.

The decay time of the 314 nm RIL was measured to be approximately 1.3 ms for 6, 12, and 20 MeV electrons at various depths of acrylic, with some fluctuations in the exact fitted value. This decay time value is comparable with previously reported values of 1.35 ms in [1] and 1.80 ms in [5].

Further research into the formation of STEX centers, and the link to the property of increasing luminescence from the STEX-center decay as a function of radiation history on the sample, is needed. A study of the properties of the emission bands which form the RIE structure from 400 nm to 600 nm is also of interest.

Author Contributions: Conceptualization, D.S., H.K. and S.G.; methodology, D.S., O.T., H.K. and R.K.; software, D.S. and O.T.; validation, A.M., Y.O., H.E.H., B.C., M.B. and S.G.; formal analysis, D.S.; investigation, D.S., O.T. and H.K.; resources, H.K., R.K., A.J., H.E.H., B.C., G.B., M.B. and S.G.; data curation, D.S. and O.T.; writing—original draft preparation, D.S.; writing—review and editing, D.S., O.T., H.K., R.K., A.M., H.E.H., B.C., M.B. and S.G.; visualization, D.S.; supervision, H.K., A.J. and S.G.; project administration, D.S., H.K., A.J. and S.G.; funding acquisition, H.K., A.J. and S.G. All authors have read and agreed to the published version of the manuscript.

Funding: The results presented herein were conceived within the RADSAGA ITN, which received funding from the European Union's Horizon 2020 Research and Innovation Programme under the Marie Skłodowska-Curie Grant Agreement No 721624. This work was also supported by the European Space Agency (ESA) under contract 4000124504/18/NL/KML/zk, by the ANR: LABEX CEMPI (ANR-11-LABX-0007), the Equipex Flux (ANR-11-EQPX-0017), by The Ministry of Higher Education and Research, and the Hauts-de-France Regional Council and the European Regional Development Fund (ERDF) through the Contrat de Projets Etat-Region (CPER Photonics for Society P4S).

Institutional Review Board Statement: Not applicable.

Informed Consent Statement: Not applicable.

Data Availability Statement: The dataset that was analyzed to produce this publication is found in <https://doi.org/10.23729/e7988ecf-d719-472e-9ad7-c66d0f7c427a>.

Acknowledgments: This work was supported by the IRCICA Institute and the FiberTech Lille platform of the University of Lille.

Conflicts of Interest: The authors declare no conflict of interest.

References

1. El Hamzaoui, H.; Bouwmans, G.; Capoen, B.; Cassez, A.; Habert, R.; Ouerdane, Y.; Girard, S.; Di Francesca, D.; Kerboub, N.; Morana, A.; et al. Gd^{3+} -doped sol-gel silica glass for remote ionizing radiation dosimetry. *OSA Contin.* **2019**, *2*, 715–721. [[CrossRef](#)]
2. Hoehr, C.; Morana, A.; Duhamel, O.; Capoen, B.; Trinczek, M.; Paillet, P.; Duzenli, C.; Bouazaoui, M.; Bouwmans, G.; Cassez, A.; et al. Novel Gd^{3+} -doped silica-based optical fiber material for dosimetry in proton therapy. *Sci. Rep.* **2019**, *9*, 16376. [[CrossRef](#)]

3. Söderström, D.; Kettunen, H.; Morana, A.; Javanainen, A.; Ouerdane, Y.; El Hamzaoui, H.; Capoen, B.; Bouwmans, G.; Bouazaoui, M.; Girard, S. Radioluminescence Response of Ce-, Cu-, and Gd-Doped Silica Glasses for Dosimetry of Pulsed Electron Beams. *Sensors* **2021**, *21*, 7523. [CrossRef] [PubMed]
4. He, J.; Wang, Y.; Steigenberger, S.; Macpherson, A.; Chiodini, N.; Brambilla, G. Intense ultraviolet photoluminescence at 314 nm in Gd³⁺-doped silica. In Proceedings of the Conference on Lasers and Electro-Optics: Applications and Technology 2016. Optical Society of America, San Jose, California, USA, 5–10 June 2016; p. JTh2A.86. [CrossRef]
5. Di Martino, D.; Chiodini, N.; Fasoli, M.; Moretti, F.; Vedda, A.; Baraldi, A.; Buffagni, E.; Capelletti, R.; Mazzer, M.; Nikl, M.; et al. Gd-incorporation and luminescence properties in sol-gel silica glasses. *J. Non-Cryst. Sol.* **2008**, *354*, 3817–3823. [CrossRef]
6. Tanimura, K.; Itoh, C.; Itoh, N. Transient optical absorption and luminescence induced by band-to-band excitation in amorphous SiO₂. *J. Phys. C Solid State Phys.* **1988**, *21*, 1869. [CrossRef]
7. Girard, S.; Kuhnhen, J.; Gusarov, A.; Brichard, B.; van Uffelen, M.; Ouerdane, Y.; Boukenter, A.; Marcandella, C. Radiation Effects on Silica-Based Optical Fibers: Recent Advances and Future Challenges. *IEEE Trans. Nucl. Sci.* **2013**, *60*, 2015–2036. [CrossRef]
8. Ismail-Beigi, S.; Louie, S.G. Self-Trapped Excitons in Silicon Dioxide: Mechanism and Properties. *Phys. Rev. Lett.* **2005**, *95*, 156401. [CrossRef]
9. Tanimura, K.; Tanaka, T.; Itoh, N. Creation of Quasistable Lattice Defects by Electronic Excitation in SiO₂. *Phys. Rev. Lett.* **1983**, *51*, 423. [CrossRef]
10. Beddar, A.S.; Mackie, T.R.; Attix, F.H. Cerenkov light generated in optical fibres and other light pipes irradiated by electron beams. *Phys. Med. Biol.* **1992**, *37*, 925–935. [CrossRef]
11. Styrdom, W.; Parker, W.; Olivares, M. *Radiation Oncology Physics: A Handbook for Teachers and Students*; Electron Beams: Physical and Clinical Aspects; International Atomic Energy Agency: Vienna, Austria, 2005; Chapter 8.
12. Andreo, P.; Seuntjens, J.P.; Podgorsak, E.B. *Radiation Oncology Physics: A Handbook for Teachers and Students*; Calibration of Photon and Electron Beams; International Atomic Energy Agency: Vienna, Austria, 2005; Chapter 9.
13. El Hamzaoui, H.; Courthéoux, L.; Nguyen, V.N.; Berrier, E.; Favre, A.; Bigot, L.; Bouazaoui, M.; Capoen, B. From porous silica xerogels to bulk optical glasses: The control of densification. *Mater. Chem. Phys.* **2010**, *121*, 83–88. [CrossRef]
14. El Hamzaoui, H.; Bouwmans, G.; Capoen, B.; Ouerdane, Y.; Chadeyron, G.; Mahiou, R.; Girard, S.; Boukenter, A.; Bouazaoui, M. Effects of densification atmosphere on optical properties of ionic copper-activated sol-gel silica glass: Towards an efficient radiation dosimeter. *Mater. Res. Express* **2014**, *1*, 026203. [CrossRef]
15. Kronholm, R.; Kalvas, T.; Koivisto, H.; Tarvainen, O. Spectroscopic method to study low charge state ion and cold electron population in ECRIS plasma. *Rev. Sci. Instrum.* **2018**, *89*, 043506. [CrossRef] [PubMed]
16. Hamamatsu. *Metal Package Photomultiplier Tube R9880U Series*; Hamamatsu Photonics K.K.: Shizuoka, Japan, 2022. Available online: https://www.hamamatsu.com/content/dam/hamamatsu-photonics/sites/documents/99_SALES_LIBRARY/etd/R9880U_TPMH1321E.pdf (accessed on 15 August 2022).
17. CAEN. N6751; CAEN S.p.A.: Viareggio, Italy, 2022. Available online: <https://www.caen.it/products/n6751/> (accessed on 15 August 2022).
18. Ocean Optics, Inc. *USB2000+ Fiber Optic Spectrometer Installation and Operation Manual*; Ocean Optics, Inc.: Dunedin, FL, USA, 2010. Available online: <https://www.oceaninsight.com/globalassets/catalog-blocks-and-images/manuals--instruction-old-logo/spectrometer/usb2000-operating-instructions1.pdf> (accessed on 26 August 2021).
19. Kettunen, H. *Varian Clinac Linear Accelerator*; University of Jyväskylä: Jyväskylä, Finland, 2020. Available online: <https://www.jyu.fi/science/en/physics/research/infrastructures/research-instruments/miscellaneous-instruments/clinac> (accessed on 19 March 2021).
20. Lambert, J.; Yin, Y.; McKenzie, D.R.; Law, S.; Suchowerska, N. Cerenkov light spectrum in an optical fiber exposed to a photon or electron radiation therapy beam. *Appl. Opt.* **2009**, *48*, 3362–3367. [CrossRef] [PubMed]
21. Frank, I.; Tamm, I. Coherent Visible Radiation of Fast Electrons Passing Through Matter. *Dokl. Acad. Sci. URSS* **1937**, *14*, 109–114.
22. Jelley, J.V. Čerenkov radiation and its applications. *Br. J. Appl. Phys.* **1955**, *6*, 227–232. [CrossRef]
23. Siegel, G.H., Jr. Ultraviolet spectra of silicate glasses: A review of some experimental evidence. *J. Non-Cryst. Sol.* **1974**, *13*, 372–398. [CrossRef]
24. Fülöp, F.; Biró, T. Čerenkov Radiation Spectrum. *Int. J. Theor. Phys.* **1992**, *31*, 61–74. [CrossRef]
25. Kremers, C.; Chigrin, D.N.; Kroha, F. Theory of Čerenkov radiation in periodic dielectric media: Emission spectrum. *Phys. Rev. A* **2009**, *79*, 013829. [CrossRef]
26. IBA. *DETECTORS For Relative and Absolute Dosimetry—Ionization Chambers and Diode Detectors*; IBA Dosimetry GmbH: Schwarzenbruck, Germany, 2018. Available online: https://www.iba-dosimetry.com/fileadmin/user_upload/products/02_radiation_therapy/_Detectors/Detectors-RD--AD_Rev.3_0718_E.pdf (accessed on 1 October 2020).